REPORT DOCUMENTATION P

AD-A240 641

oved
704-0188

1a REPORT SECURITY CLASSIFICATION	1b
UNCLASSIFIED	

2a SECURITY CLASSIFICATION AUTHORITY	3
SEP 23 1991	Approved for public release; distribution unlimited.
2b DECLASSIFICATION / DOWNGRADING SCHEDULE	

4 PERFORMING ORGANIZATION REPORT NUMBER(S)	5 MONITORING ORGANIZATION REPORT NUMBER(S)
N00014-85-C-0141-TR11	

6a NAME OF PERFORMING ORGANIZATION	6b OFFICE SYMBOL (If applicable)	7a NAME OF MONITORING ORGANIZATION
Washington State University		Office of Naval Research

6c. ADDRESS (City, State, and ZIP Code)	7b ADDRESS (City, State, and ZIP Code)
Department of Physics Washington State University Pullman, WA 99164-2814	Physics Division Code 1112 Arlington, VA 22217-5000

8a. NAME OF FUNDING / SPONSORING ORGANIZATION	8b OFFICE SYMBOL (If applicable)	9 PROCUREMENT INSTRUMENT IDENTIFICATION NUMBER
		N00014-85-C-0141

8c. ADDRESS (City, State, and ZIP Code)	10 SOURCE OF FUNDING NUMBERS			
	PROGRAM ELEMENT NO	PROJECT NO.	TASK NO.	WORK UNIT ACCESSION NO
	61153N	4126934		

11 TITLE (Include Security Classification) Wavefields Near Transverse Cusp Caustics Produced by Reflecting Ultrasonic Transients and Tone Bursts from Curved Surfaces.

12 PERSONAL AUTHOR(S)
Frederickson C. K.

13a TYPE OF REPORT	13b TIME COVERED	14. DATE OF REPORT (Year, Month, Day)	15 PAGE COUNT
Technical	FROM 880516 TO 910731	910816	XV + 231 = 246

16 SUPPLEMENTARY NOTATION This is the Ph.D. dissertation of Carl King Frederickson. The contract P. I. was P. L. Marston, Telephone (509) 335-5343 or 335-9531.

17	COSATI CODES		18. SUBJECT TERMS (Continue on reverse if necessary and identify by block number)
FIELD	GROUP	SUB-GROUP	Acoustical Scattering, Diffraction Catastrophes, and Caustics
20	01		
20	06		

19 ABSTRACT (Continue on reverse if necessary and identify by block number)

Ultrasonic wavefields reflected from curved surfaces were studied in the vicinity of caustics. Acoustical and optical transverse cusp diffraction catastrophes produced by reflections from a curved metal surface in water were imaged by displaying the amplitude or intensity in an observation plane transverse to the general direction of propagation. The optical image was used to located the cusp point in the observation plane. Acoustical diffraction patterns for sine waves, described by the Pearcey function, were

20 DISTRIBUTION / AVAILABILITY OF ABSTRACT	21 ABSTRACT SECURITY CLASSIFICATION
☒ UNCLASSIFIED/UNLIMITED ☐ SAME AS RPT ☐ DTIC USERS	UNCLASSIFIED

22a NAME OF RESPONSIBLE INDIVIDUAL	22b TELEPHONE (Include Area Code)	22c OFFICE SYMBOL
L. E. Hargrove	(703) 696-4221	ONR Code 1112

DD Form 1473 JUN 86   *Previous editions are obsolete*   SECURITY CLASSIFICATION OF THIS PAGE

UNCLASSIFIED

19. ABSTRACT (continued)

calculated with the parameters determined by the experimental setup leaving no adjustable scaling parameters. The calculated and experimental acoustical diffraction pattern showed good agreement near the cusp point. The acoustical diffraction pattern showed the expected mirror symmetry about an axis. The pattern was shown to scale properly with frequency.

The transverse cusp caustic separates space into region with three rays and a region with one ray. Inside the caustic there are three rays, on the curve two of the rays merge and disappear leaving one ray outside. Transient signals reflected from curved surfaces exhibited the merging and disappearance of rays on the caustic. Relative arrival times for signals in calculated and recorded time traces agree well. The relation to the wavefront parameters of the temporal orientation of the travel time surface is discussed. The general shape of the travel time surface is that of the swallow tail caustic surface.

The temporal shape of the transient echoes was seen to be generally that of the incident signal or of its Hilbert transform. The Hilbert transform shape identifies the signals the have touched the caustic. The observed arrival sequence of the transient signals was shh inside the caustic and one h outside, where s stands for a signal with the general shape of the incident signal and h for its Hilbert transform. The relation between the surface and wavefront parameters and the arrival sequence is given.

91-11216

UNCLASSIFIED

9 1

i

WAVEFIELDS NEAR TRANSVERSE CUSP CAUSTICS PRODUCED BY REFLECTING ULTRASONIC TRANSIENTS AND TONE BURSTS FROM CURVED SURFACES

By

CARL KING FREDERICKSON

A dissertation submitted in partial fulfillment of the requirements for the degree of

DOCTOR OF PHILOSOPHY

WASHINGTON STATE UNIVERSITY
Department of Physics

AUGUST 1991

Accession For

NTIS

By

Dist

A-1

To the Faculty of Washington State University:

The members of the Committee appointed to examine the dissertation of CARL

KING FREDERICKSON find it satisfactory and recommend that it be accepted.

Philip L. Marston
Chair

Michael Muller

M. Howard Miles

ACKNOWLEDGEMENTS

I am grateful to the faculty of the Physics Department for the personal nature of the graduate program at Washington State University. My special thanks goes to my advisor for the last four years Professor Philip L. Marston for his guidance and patience as my laboratory skills grew. I would like to thank the late Paul Bender for his advice recommending an experimental dissertation. For their support and fellowship during the last five years I am grateful to my fellow graduate students especially Steven G. Kargl and Harry J. Simpson my office mates during the period in which I completed my research.

For her support of both myself and my wife before the birth of our son and especially afterwards (babysitting), and the use of her house for a week and a half I thank Lori Finch the organizer of barbecues and general social gatherings that keep a graduate student sane. The office staff upstairs including, Lori Finch and Mickey Daniels, also deserves recognition for helping with the business end of being a graduate student.

For her support and love through the last five years when she has been without a husband for long periods of time I am grateful to my wife Kim Frederickson.

I am also grateful for the financial support of this research by the Office of Naval Research .

WAVEFIELDS NEAR TRANSVERSE CUSP CAUSTICS PRODUCED BY REFLECTING ULTRASONIC TRANSIENTS AND TONE BURSTS FROM CURVED SURFACES

Abstract

by Carl King Frederickson, Ph. D.
Washington State University
August 1991

Chair: Philip L. Marston

Ultrasonic wavefields reflected from curved surfaces were studied in the vicinity of caustics. Acoustical and optical transverse cusp diffraction catastrophes produced by reflections from a curved metal surface in water were imaged by displaying the amplitude or intensity in an observation plane transverse to the general direction of propagation. The optical image was used to locate the cusp point in the observation plane. Acoustical diffraction patterns for sine waves, described by the Pearcey function, were calculated with the parameters determined by the experimental setup leaving no adjustable scaling parameters. The calculated and experimental acoustical diffraction patterns showed good agreement near the cusp point. The acoustical diffraction pattern showed the expected mirror symmetry about an axis. The pattern was shown to scale properly with frequency.

The transverse cusp caustic separates space into a region with three rays and a region with one ray. Inside the caustic there are three rays, on the curve two of the rays merge and disappear leaving one ray outside. Transient signals reflected from curved surfaces exhibited the merging and disappearance of rays on the caustic. Relative arrival times for signals in calculated and recorded time traces agree well. The relation to the wavefront parameters of the temporal orientation of the travel time surface is discussed. The general shape of the travel time surface is that of the swallow tail caustic surface.

The temporal shape of the transient echoes was seen to be generally that of the incident signal or of its Hilbert transform. The Hilbert transform shape identifies the signals that have touched the caustic. The observed arrival sequence of the transient signals

was shh inside the caustic and one h outside, where s stands for a signal with the general shape of the incident signal and h for its Hilbert transform. The relation between the surface and wavefront parameters and the arrival sequence is given.

TABLE OF CONTENTS

LIST OF TABLES

LIST OF ILLUSTRATIONS

Dedication

This work is dedicated to my wife for her understanding and support over the last five

years.

CHAPTER ONE

INTRODUCTION AND OVERVIEW

This study is applicable to the simplest class of nontrivial three-dimensional caustic surfaces produced by reflecting sound from curved surfaces. It is also relevant to the understanding of the temporal and frequency dependence of wavefields where the strength of the focusing is limited by the shape of the initial wavefront instead of its aperture or spatial extent. This is commonly the situation in naturally produced caustics such as those produced when light is refracted by a rippled surface[1]. This dissertation describes experiments conducted to study wavefields in the vicinity of a particular structurally stable caustic: the transverse cusp caustic. The caustic was formed in an observation plane by reflecting ultrasonic tone bursts and transients in water from a surface with the generic local shape given by previous predictions[2] $h(x,y) = h_1x^2 + h_2xy^2 + h_3y^2$. Tone bursts were used to approximate steady state signals in order to image the diffraction pattern, given by the Pearcey function [3], that decorates the transverse cusp caustic. Transient signals were used to study the merging of signals associated with the merging of rays as the caustic is crossed. The temporal shape of the transient echoes was used to identify in the arrival sequence which echoes touch the caustic and which echoes do not.

Some background information pertinent to the transverse cusp caustic will now be reviewed. An important and unique aspect of the present experimental study is the use of high frequency sound to produce the wavefield such that both the steady state wavefield pattern and transient behavior could be observed for the same reflection geometry. The transverse cusp caustic can be observed in a uv observation plane that is transverse to the general direction of propagation of the wavefront that produces the caustic. A shear free transverse cusp caustic is described by a cubic cusp curve in the observation plane [3], $D_T(u - u_c)^3 = v^2$, where u and v are transverse coordinates and the cusp point is located at $(u_c,0)$. The wavefront that forms a shear free caustic, the caustic and the associated diffraction pattern have a mirror symmetry about a horizontal axis. The

transverse cusp caustic separates space into a region with three rays from the wavefront and a region with one ray from the wavefront. On the transverse cusp caustic two of the rays merge (are focused) and disappear outside the caustic.

Previously a particular example of an optical transverse cusp was observed that was embedded in the hyperbolic umbilic diffraction catastrophe[4]. Away from the most singular section of the hyperbolic umbilic, a transverse cusp diffraction catastrophe is evident as part of the unfolding of the hyperbolic umbilic. Though this transverse cusp observed by Marston and Trinh was imaged at infinity, from consideration of these observations the local shape of the outgoing wavefront was described that forms a transverse cusp in a finite observation plane as well as the farfield[2]. This result motivated the form of the reflecting surface h(x,y) mentioned above. The diffraction pattern that decorates this caustic was shown to be the Pearcey function that describes the field near the cusp associated with the cylindrical aberration [5].

Chapter 2 describes experiments to image the diffraction pattern associated with the transverse cusp caustic. A wavefront with the local shape that forms a transverse cusp was produced by reflecting sound from an appropriately curved surface. The wavefront and associated diffraction pattern thus produced were studied in the lab in an observation plane transverse to the direction of propagation. To study the transverse cusp caustic, computer software was developed to record the amplitude of a reflected acoustical signal in a transverse observation plane and display this information in a gray scale picture. This provided a picture of the diffraction pattern produced by the reflection of an approximately steady state signal from the curved surface. The pictures were then used to compare the imaged diffraction patterns to the theoretical calculations of the patterns.

There were no scaling parameters used in the comparison of the experimental data and theory. The reflecting surface was measured to find the local surface height in the region that produced the cusp point of the caustic. The location of the cusp point in the observation plane was given by gray scale pictures of the wavefront reflected when an

optical source and receiver were used in place of the acoustical source and receiver. The small wavelength of the optical source produced a bright transition across the caustic (due to the focusing of the two rays on the caustic). In the comparisons of the acoustical data and theory the location of the optical cusp point was used as a guide for the placement of the theoretical overlay on the acoustical picture. The differences between the location of the optical cusp point and the acoustical cusp point, found by finding the location of best agreement between the experimental and theoretical diffraction patterns near the cusp point, were very small and could be accounted for as a small difference in the horizontal and vertical positions of the optical and acoustical sources. The effect of the sign of h_1, the coefficient of x^2 in the shape of the surface, being positive is discussed in reference to the region where the opening rate of the transverse cusp caustic diverges.

In Chapter 3 the merging of the rays on the transverse cusp caustic are studied. There is a finite path difference for signals propagating along different rays from the wavefront. When transient (very short) source signals are used, the length of the ray paths define a sequence of arrival for the associated signals. As the caustic is approached from inside, two of these arrivals should merge as the rays merge, and be lost outside the caustic as the rays are lost. The arrivals of the signals in the observation plane can be described by a three dimensional travel time surface having the general shape of the singular surface of the swallow tail catastrophe [6]. The axes of the travel time surface are given by the transverse axes in the observation plane and time. The travel time surface can be used as a tool to locate caustics by the merging of rays.

Experiments are described in Chapter 3 in which the travel time surface of a transverse cusp caustic formed by reflecting sound from a curved surface in water was imaged. Travel time traces were recorded at equispaced vertical positions along vertical cuts through the observation plane both inside and outside the caustic. These time traces could be displayed in a waterfall format to show the travel time curve associated with the horizontal position of each cut. The travel time curves of each vertical cut display the

swallow tail shape associated with the travel time surface of the cusp caustic along with a slowly varying contribution associated with propagation to the observation plane from the exit plane. An optical gray scale picture of the wavefront reflected when the acoustical source and receiver were replaced by an optical source and receiver was used as a reference for the location of each time trace. As the observation point moves up into the cusp curve, signals appear slightly before the cusp curve is reached due to a tunnelling of the acoustical signal outside the caustic that can be associated with a ray having a complex phase [7] (complex point of origin). The signal that appears near the caustic reaches a maximum on the caustic and then splits into two distinct signals after crossing the caustic. This represents the merging of rays on the caustic and the appearance or disappearance of rays as the caustic is crossed moving from outside or inside the caustic.

The information contained in the travel time surface is discussed in the later part of Chapter 3. In the frequency domain, the diffraction pattern contains information about the shape of the wavefront in the shape of the maxima and minima of the pattern. The widths of the maxima and minima of the pattern are controlled by the carrier frequency of the source signal. In the time domain there is more information available through the added dimension of time. The sequence of the arrivals in the observation plane is controlled by the shape of the wavefront giving information not directly available in the diffraction pattern. The travel time surface in the observation plane gives a picture of the local shape of the wavefront after propagating from the exit plane to a region of the observation plane. This local shape of the wavefront near the caustic can be associated with the shape of the wavefront near the exit plane through the classification of the caustic surface. This classification gives the general form of the distance function for the wavefront.

Echoes from the reflecting surface may have touched the caustic at some point prior to arriving in the observation plane. These echoes will have distorted temporal shapes relative to the temporal shape of the source signal. The distorted shape are described by the Hilbert transform of the temporal shape of the source signal [8,9,10]. Chapter 4 shows the

arrival sequence of the distorted and nondistorted signals for the transverse cusp caustic formed by reflecting sound from a curved surface in water. For the reflecting surface used the arrival sequence inside the caustic was predicted to be shh, where s represents a signal with the general temporal shape of the source pulse and h represents the general temporal shape of the Hilbert transform of the source pulse. Outside the caustic the single arrival was predicted to be an h arrival. Time records showing the arrivals at equispaced horizontal positions along the symmetry axis of the transverse cusp caustic are analyzed. The arrival sequence shown in the time records agrees with the predicted arrival sequence of shh inside the caustic and h outside. The surface parameters and their relation to the arrival sequence are discussed along with some of the consequences of the distorted temporal shape of the echoes that touch the caustic.

References

1)   M. Berry, "Beyond rainbows," Current Science, **59**, 1175-1191, (1990).

2)   P. L. Marston, "Surface shapes giving transverse cusp catastrophes in acoustic or seismic echoes," in *Acoustical Imaging* vol 16, ed. L. W. Kessler, (Plenum, New York, 1988), 579-588.

3)   P. L. Marston, "Transverse cusp diffraction catastrophe: Some pertinent wavefronts and a Pearcey approximation to the wave fields," J. Acoust. Soc. Am. **81**, 226-232, (1987).

4)   P. L. Marston and E. H. Trinh, "Hyperbolic umbilic diffraction catastrophe and rainbow scattering from spheroidal drops," Nature (London) **312**, 529-531 (1984).

5)   T. Pearcey, "The structure of an electromagnetic field in the neighbourhood of a cusp of a caustic," Philos. Mag. **37**, 311-317, (1946).

6)   G. Danglemayr and W. Güttinger, "Topological approach to remote sensing," Geophys. J. R. astr. Soc.,**71**,pp 79-126, (1982).

7)   F. J. Wright, "The Stokes set of the cusp diffraction catastrophe," J. Phys. A: Math. Gen., **30**, (1980), 2913-2928.

8)   M. G. Brown, "The transient wave fields in the vicinity of cuspoid caustics," J. Acoust. Soc. Am. **70**, 1427-1436 (1986).

9)   D. P. Hill, "Phase shift and pulse distortion in body waves due to internal caustics," Bull. Seism. Soc. Am., **64**, 1733-1742, (1974).

10)   G. L. Choy and P. G. Richards, "Pulse distortion and Hilbert transformation in multiply reflected and refracted waves," Bull. Seism. Soc. Am. **65**, 55-70 (1975).

This page is intentionally blank.

CHAPTER TWO

THE TRANSVERSE CUSP DIFFRACTION CATASTROPHE PRODUCED BY THE REFLECTION OF TONE BURSTS FROM A CURVED METAL SURFACE IN WATER

2.1 INTRODUCTION

When sound propagates through an inhomogeneous medium or is reflected or refracted by curved surfaces caustics may be formed. Caustics describe focal envelopes for the rays traveling from a wavefront. Geometrical acoustics predicts unphysically divergent amplitudes at caustics. Catastrophe theory relates the diffraction patterns of the caustics to canonical diffraction integrals, removing the divergence at the caustic[1].

The simplest focal envelope is the fold or Airy caustic[1,2,3] formed by a wavefront curved along only one direction. The fold caustic marks the transition from a region with two distinct rays from the wavefront (the bright region) to a region where there are no rays from the wavefront (the shadow region). On the Airy caustic itself the two rays merge to come from the same point on the wavefront. The canonical diffraction integral that describes the diffraction pattern near a fold caustic has same form as the Airy function.

The next more complicated envelope of rays is the axial (longitudinal) cusp caustic[1,2,3]. The axial cusp is a cubic cusp curve of the form $D(z - z_{cp})^3 = x^2$, where z is along the direction of propagation, $(z_{cp}, 0)$ is the location of the cusp point, and x is a position transverse to the direction of propagation. The wavefront that forms the axial cusp caustic is also curved along only one direction, however, this focal envelope marks a boundary between a region with three rays from the wavefront and a region with one ray from the wavefront. Inside the cusp curve there are three distinct rays from the wavefront to each point. On the cusp curve two of the rays merge to come from the same point on the wavefront. Outside the cusp curve only one ray is directed from the wavefront to each point. The diffraction pattern decorating the cusp caustic was studied by Pearcey[4] in

connection with the axial cusp caustic associated with the cylindrical aberration. Pearcey was able to show that the diffraction pattern near the cusp point could be described by the Pearcey function, Eq.(12) below. The Pearcey function has the general form of the canonical diffraction integral for the cusp caustic[1,2].

A transverse cusp caustic (TCC) is a cubic cusp curve that opens roughly transverse to the direction of propagation. The general shape of the wavefront that forms an axial cusp caustic has cylindrical symmetry, that is, it is only curved along one direction. A wavefront curved along two directions transverse to the initial direction of propagation is needed to form a TCC. The TCC shown in Fig. 1 is a cusp caustic without any shear distortion opening transverse (perpendicular) to the general direction of propagation of the initial wavefront. The generic shape of the wavefront in the exit plane that produces a TCC without shear distortion in an observation plane proposed by Marston[5,6] is given by Eq. (1) below. A paraxial approximation of the propagation integral associated with this wavefront gives a relation for the pressure in the observation plane proportional to the Pearcey function, Eq. (9)[5,6]. This wavefront, like that of the axial cusp caustic without shear, is symmetric about the direction of propagation. However, unlike the axial wavefront, the TCC wavefront is not a cylindrical wavefront. The caustic produced by the TCC wavefront is an intrinsically three-dimensional caustic. An example is the general surface shape shown in Fig. 2. Cuts through this surface in uv planes perpendicular to the z axis exhibit the same general diffraction pattern in the transverse uv observation plane as an axial cusp caustic exhibits in a longitudinal observation plane.

TCC's are often embedded in more complicated caustics. An example of a more complicated caustic exhibiting a TCC is the asteroid caustic[7] formed by the smooth joining of four TCC's with the cusp points pointing away from the center of the caustic pattern. Dong and Adler were able to detect the TCC as part of an asteroid caustic produced by diffraction into the near-field shadow region of an elliptical disk[8]. Using high frequency
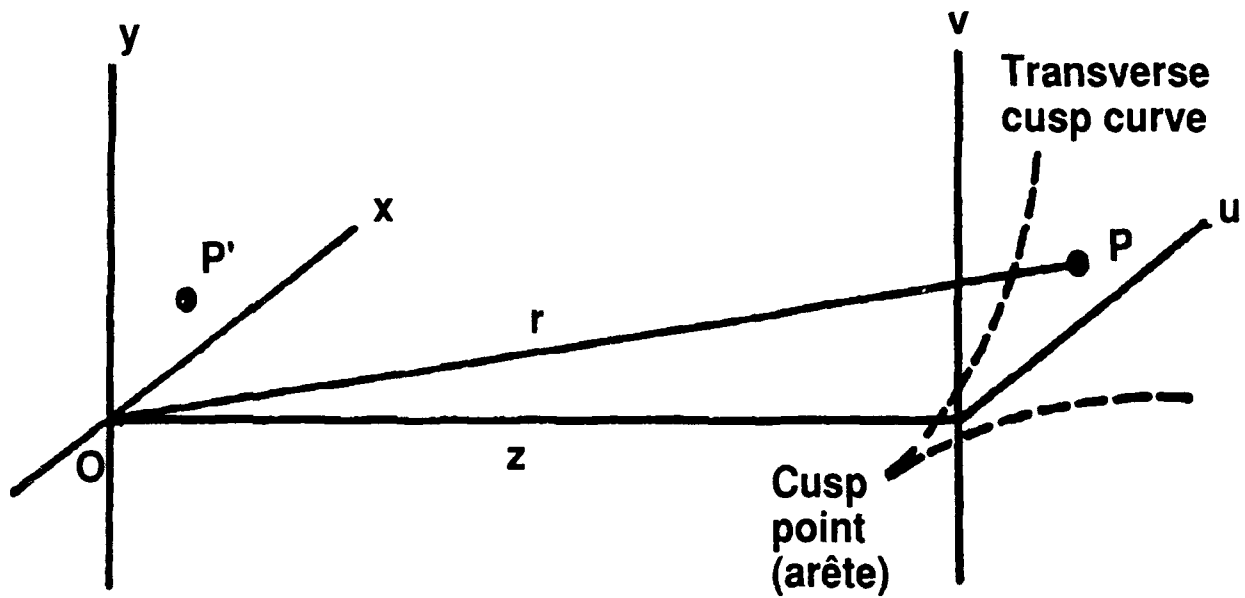
Figure. 1 Geometry of the transverse cusp diffraction catastrophe. The wavefront in the

exit plane (x,y) propagates to form a shear free TCC in the observation plane (u,v).
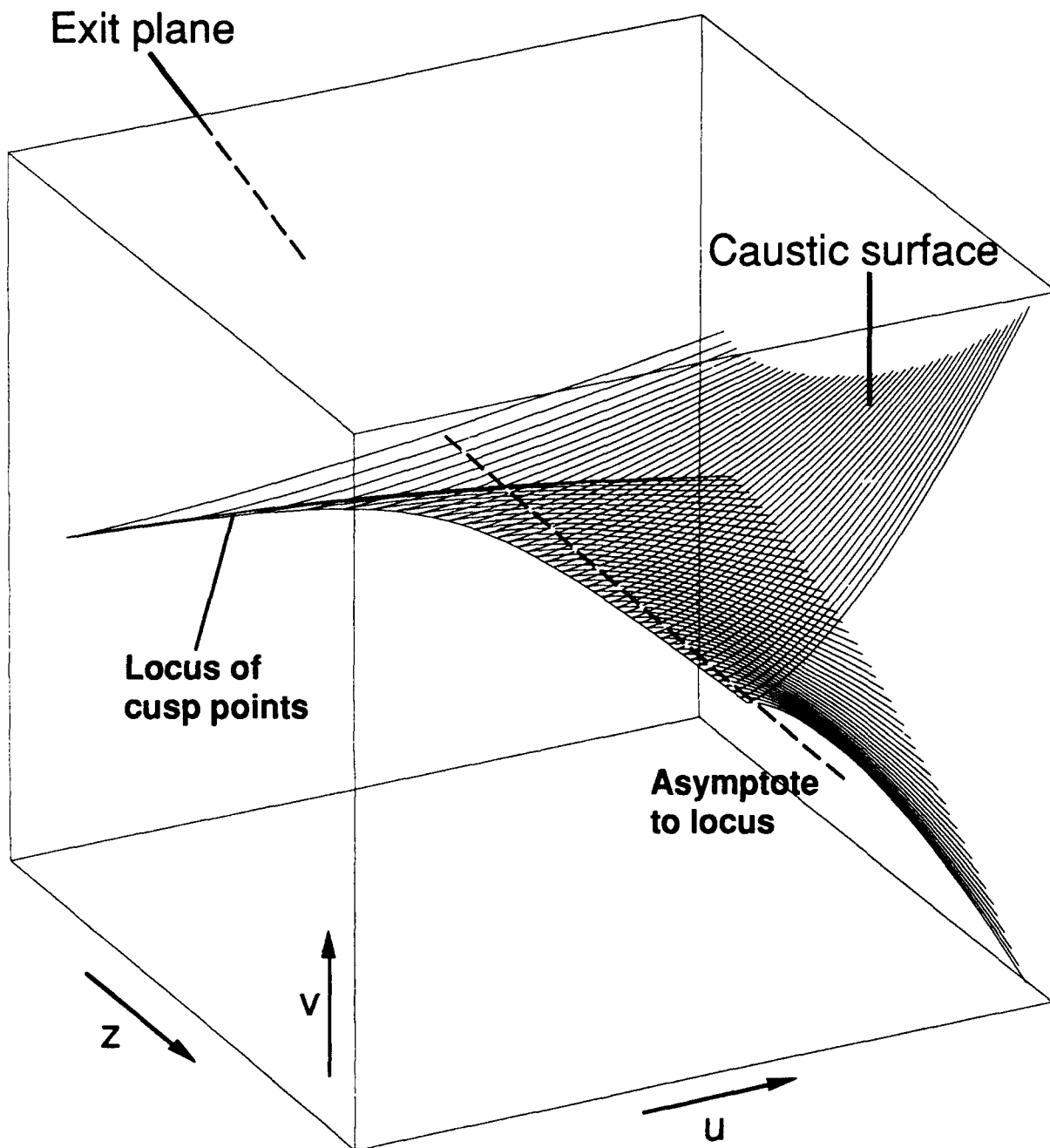
Figure. 2 The TCC forms a caustic surface in space. Cuts through this surface along

planes perpendicular to the direction of propagation exhibit the two-dimensional TCC. The

locus of cusp points in consecutive planes forms the rib of the caustic surface.

sound (5MHz) Dong and Adler were able to observe the shape of the caustic curve but indicated they were unable to resolve the diffraction pattern that should decorate the caustic.

Another example of a more complicated caustic that contains a TCC is the hyperbolic umbilic away from its most singular section. The hyperbolic umbilic contains a TCC along with a fold caustic. Photographs taken by Marston and Trinh of the light scattered into the rainbow region by a levitated water drop clearly show the TCC embedded in the hyperbolic umbilic caustic[9]. The diffraction pattern decorating the TCC is evident in the optical data taken by Marston and Trinh. The local shape of the region of a wavefront that produces an embedded TCC in a higher order caustic should be that given in Eq. (1). The wavefront proposed by Marston, Eq. (1), has been used by Dean and Marston to study the opening rate of the TCC associated with the hyperbolic umbilic away from its most singular section[10].

The wavefields that form specific caustics can be produced by reflecting sound from surfaces having generic shapes. The diffraction pattern decorating the caustic can be imaged if steady-state conditions are simulated while the impulse catastrophe will be evident for a pulsed source[2]. In a homogeneous medium the shape of the reflected wavefront is determined by the shapes of the incident wavefront and of the reflecting surface. Thus for steady-state signals, the diffraction patterns decorating the caustics can be studied by producing the wavefront that forms the caustic by reflecting sound from a surface with the proper shape. This chapter will describe an experiment to image and study the acoustical diffraction pattern of a transverse cusp caustic produced by reflecting long ultrasonic tone bursts (approximating steady-state sound) from a curved metal surface, with the local shape given by Eq. (3) below, in a homogeneous medium (deionized water). Section 2.2 of the paper gives a review of the wavefront that produces the TCC in subsection 2.2.A. Subsection 2.2.B is a list of the characteristics of the TCC which can be observed in experimental data and used for comparisons to theoretical calculations. Section 2.3 describes the experimental setup and method used to image the diffraction pattern.

Section 2.4 compares experimental and calculated diffraction patterns and gives the results

of the experiment. Section 2.5 discusses the results and concludes chapter 2. Appendix

2.A shows the derivation of the effective coordinate system that is used to relate the

theoretical calculations to the positions of the source and receiver. Appendix 2.B outlines

the experimental method for finding the quadratic approximation for the phase of the

acoustical source in the plane containing the reflecting surface. Appendix 2.C describes the

method used to approximate the acoustical reflection coefficient of the reflecting surface.

2.2 THEORY

A. A REVIEW OF A GENERAL WAVEFRONT THAT PRODUCES A TRANSVERSE CUSP CAUSTIC ON PROPAGATION FROM AN EXIT PLANE TO A DISTANT OBSERVATION PLANE

The generic shape of the wavefront that propagates from the exit plane, in Fig. 1

containing the point P', to an observation plane producing a TCC without shear is

locally[5,6]

$$W(x,y) = - (a_1 x^2 + a_2 xy^2 + a_3 y^2 + a_4 x + a_5 y).$$ (1)

The coefficients necessary for the formation of a TCC are a_1 and a_2. Coefficients a_1 and a_2

control the shape of the caustic. Coefficient a_3 affects the location of the caustic by

translating the wavefront along the x axis. To show that a_3 acts only to translate the caustic

consider a translation of the origin along the x axis, $x = x' - b$,

$$W(x',y) = -[a_1 x'^2 + a_2 x'y^2 + (a_3 - ba_2)y^2 + (a_4 - 2ba_1)x' + a_5 y],$$ (2)

for $b = a_3/a_2$ the y^2 term is eliminated. Terms linear in x and y only shift the location of the

cusp point (u_c) and may be set to zero by a proper choice of origin. This wavefront is a

two-dimensional wavefront; requiring the coefficient a_2 be nonzero means that the

wavefront is not a cylindrical wavefront. The caustic formed by this wavefront has the

reflection symmetry about the u axis in the observation plane shown in Fig. 1.

The relevance of the wavefront having the form of Eq. (1) to the production of a shear free transverse cusp was also noted by Nye et. al.[11]. Generally the wavefront and associated cusp caustic need not have the reflection symmetry implicit in Eq. (1). Such a lack of symmetry gives rise to a sheared cusp which displaces the caustic away from the symmetric caustic shown in Fig. 1[12,13]. The shear displacement vanishes as the cusp point is approached. The wavefront shape in Eq. (1) was previously applied to the scattering of light from an oblate drop of water by Dean and Marston[10]. This shape was found to describe the local shape of the wavefront that propagates to produce an optical transverse cusp caustic within the unfolded hyperbolic umbilic diffraction catastrophe[9].

The generic $W(x,y)$ in Eq. (1) may be produced by the reflection of a signal produced by a point source of sound from a surface of height[14]

$$h(x,y) = h_1 x^2 + h_2 xy^2 + h_3 y^2, \tag{3}$$

where linear terms may be included, though they only produce linear terms in the reflected wavefront. The source is located in the source plane a distance z_s from the exit plane, and a TCC is formed in an observation plane a distance z from the exit plane. Figure 3 shows the relative positions of the reflector, source, and receiver planes. A paraxial approximation of the shape of the reflected wavefront gives

$$W(x,y,u_s,v_s) \approx 2h(x,y) + (x\,\frac{u_s}{z_s} + y\,\frac{v_s}{z_s}) - \frac{x^2 + y^2}{2z_s}\,. \tag{4}$$

where u_s, v_s, and z_s give the location of the source point. The validity of the use of the paraxial approximation for classifying the TCC is discussed in Appendix D.

Using the effective coordinates given in Eqs. (A10), the reduced distance function for the TCC used in the phase of the diffraction integral, Eq. (12), is

$$\phi(x,y,U_e,V_e) = -2h(x,y) - (U_e x + V_e y) + \frac{x^2 + y^2}{2z_e}\,. \tag{5}$$

The two-dimensional diffraction integral Eq. (A12) may be evaluated to give the the pressure in an observation plane proportional to the Pearcey function[5,6,14]

$$p(u,v) = \frac{k^{1/4}\,p_0\,\xi}{i r_s \sqrt{2\pi}\,|b_1'|^{1/2}|a_2'|}\,e^{-ik(r\,+\,r_s)}\,e^{-(\pm i\pi/4)}\,e^{-(ikU_e^2/4b_1')}\,P_{\pm}(w_2,w_1) \tag{6}$$
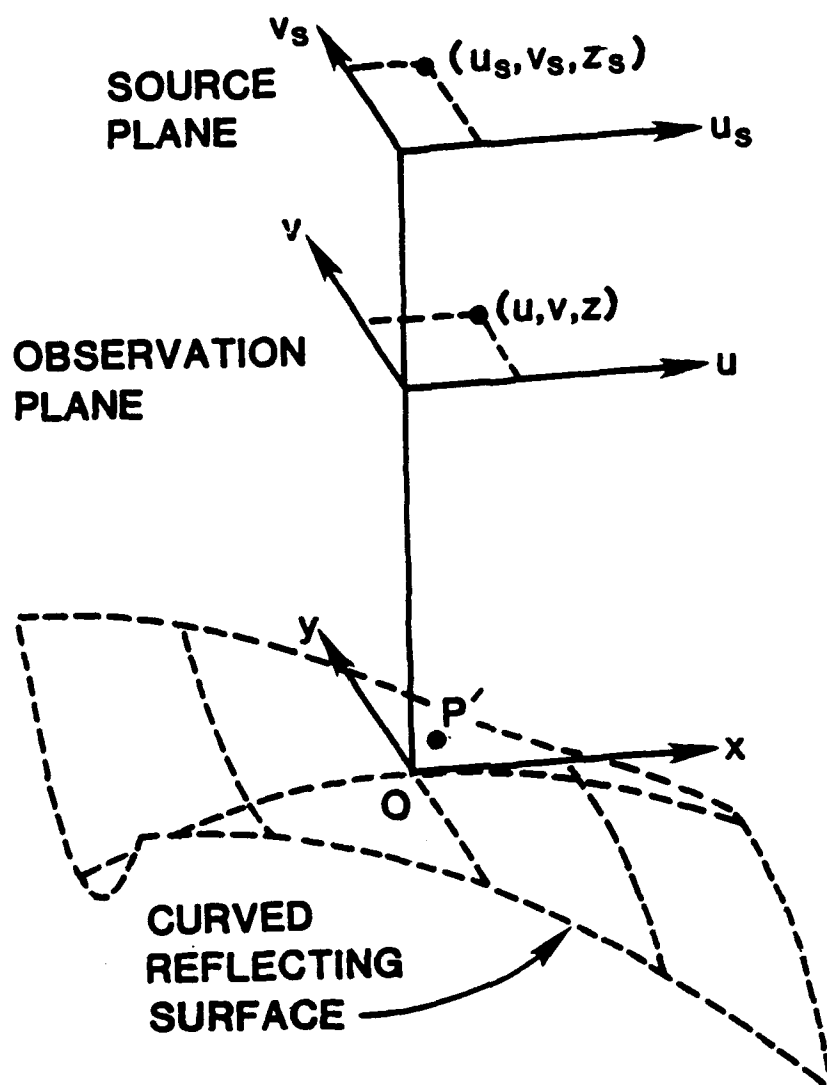
Figure. 3 Geometry for producing a TCC by reflecting the signal of a point source from a curved metal surface. The point source is located at (u_s, v_s, z_s) while the reflected wavefront is sampled in the observation plane at the point (u, v, z).

where r and r_s are shown in Fig A1, ξ is the acoustical reflection coefficient, p_o is the source strength, $a_2' = -2h_2$, $b_1' = -2h_1 + 1/(2z_e)$, $P_\pm(w_2,w_1)$ is given by Eq. (9), and the upper (lower) sign is taken when $b_1' < 0$ ($b_1' > 0$). The Pearcey function has the form of the canonical diffraction integral of catastrophe theory that describes the diffraction pattern of a cusp caustic[1,2]. The control parameters of the Pearcey function are related to the effective coordinates by[5,6,14]

$$w_2 = -\left(\frac{k}{|b_1'|}\right)^{1/2} [U_e - U_{ec}]\, \mathrm{sgn}(a_2'), \tag{7}$$

and

$$w_1 = k^{3/4} |b_1'|^{1/4} \left(\left|\frac{2}{a_2'}\right|\right)^{1/2} V_e\, \mathrm{sgn}(b_1'). \tag{8}$$

Plots of $|P(w_2, w_1)|$ can be used to represent the diffraction pattern of the TCC[5,6].

B THE CHARACTERISTICS OF THE TRANSVERSE CUSP CAUSTIC AND THE ASSOCIATED DIFFRACTION CATASTROPHE

The diffraction pattern of a cusp caustic is described by the Pearcey function

$$P_\pm(w_2,w_1) = \int_{-\infty}^{\infty} \exp\left[\pm i\left(\frac{s^4}{4} + w_2\frac{s^2}{2} + w_1 s\right)\right] ds, \tag{9}$$

where w_2 and w_1 are the control parameters of the catastrophe and for the TCC are given by Eqs. (7) and (8). Figure 4 shows a contour plot of $|P(w_2, w_1)|$ for $w_1 > 0$. The diffraction pattern, $|P(w_2, w_1)|$, produced by the symmetric wavefront of the unsheared TCC has the same reflection symmetry about the horizontal axis in the observation plane as does the TCC wavefront. The contours of $|P(w_2,w_1)|$ for $w_1 < 0$ would be given by reflecting the plot in Fig. 4 through the w_2 axis. The contour plot in Fig. 4 of $|P(w_2, w_1)|$ for $w_1 > 0$, shows that the minima of the diffraction pattern are located symmetrically about the horizontal axis. None of the minima of the pattern are located on the axis.

Figure. 4 A contour plot of $|P(w_2, w_1)|$. The solid line leaving the origin to the left is the cusp curve. To the right of the origin, the dotted line is the Stokes set. Note the minima located outside but near the cusp curve. These minima are due to the interference of the real and complex rays in this region.

$|P(w_2, w_1)|$

Stokes set

cusp curve

w_2

w_1
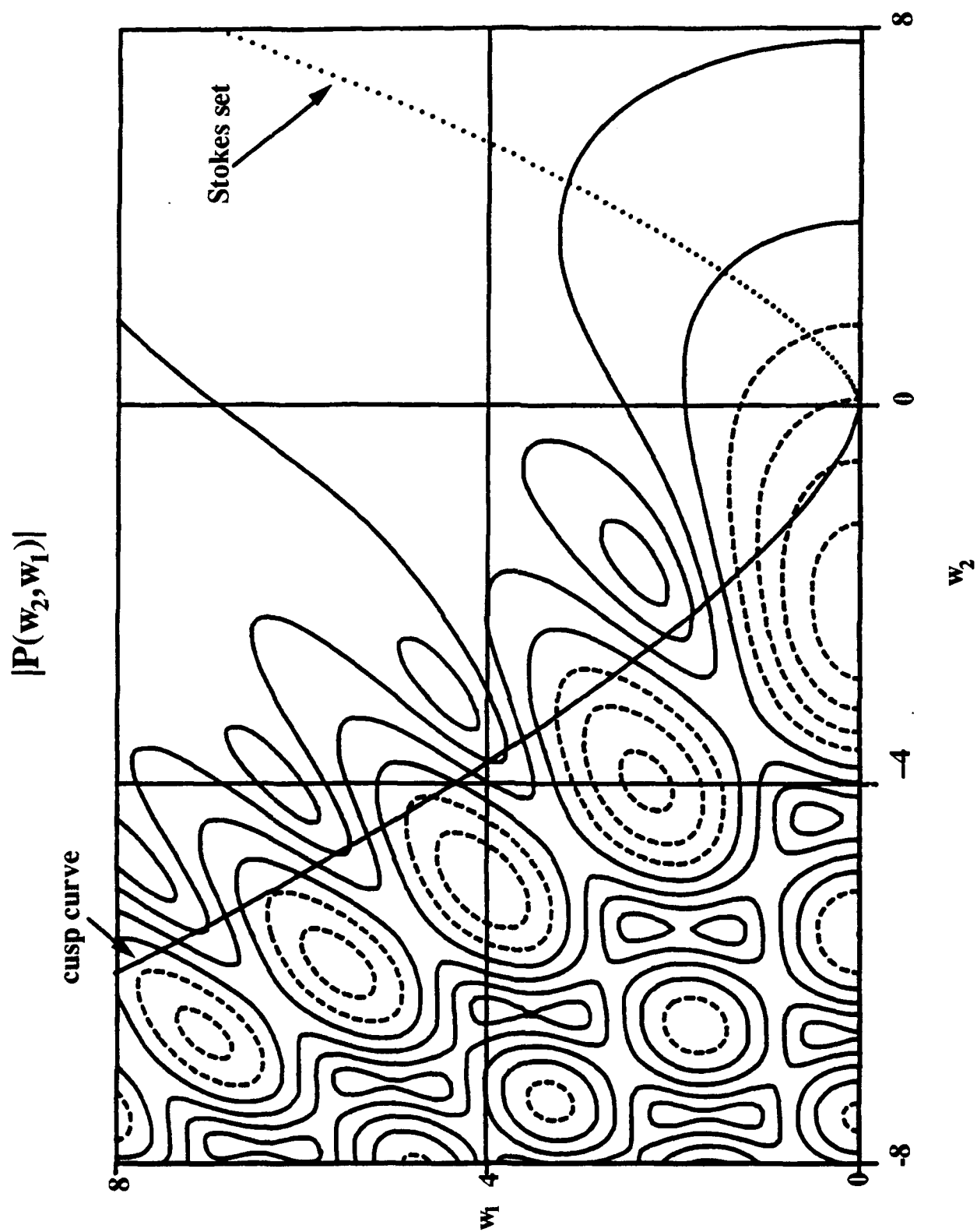
Our calculation of $P(w_2,w_1)$ is based on an algorithm received from F. J. Wright[15]. The Pearcey function has a highly oscillatory phase outside the central region containing the stationary phase points. For this reason the integral is split into three separate integrals[16]. The middle finite integral contains all the stationary points and is calculated numerically. The two outer infinite integrals are approximated using an asymptotic series keeping only the first three terms. This approximation works well near the cusp point. Comparisons of contours of $|P(w_2,w_1)|$ calculated using this method and those calculated by Pearcey and others agree well[4,17,18].

The geometrical acoustics approximation of the field in the observation plane is recovered by using the stationary phase approximation to evaluate the diffraction integral. The field in the observation plane is given by the sum of the contributions from rays that originate on the wavefront. The contribution of each ray is proportional to the reciprocal of the square root of the Hessian[5,6]

$$p(u,v) \propto \left(\frac{1}{H}\right)^{1/2},$$ (10)

where

$$H(x,y,U_e,V_e) = \frac{\partial \phi^2}{\partial x^2}\frac{\partial \phi^2}{\partial y^2} - \left(\frac{\partial \phi^2}{\partial x \partial y}\right)^2$$ (11)

evaluated at the stationary points of the phase of the diffraction integral

$$\frac{\partial \phi}{\partial x} = 2b_1'x + a_2'y^2 - U_e = 0,$$ (12)

$$\frac{\partial \phi}{\partial y} = 2y(a_2'x + 2b_3') - V_e = 0,$$ (13)

which define the rays to the observation plane. When the Hessian goes to zero the geometrical approximation to the amplitude diverges. Simultaneous solution of Eqs (11) and (12) with $H(x,y,U_e,V_e) = 0$ defines the cusp curve in terms of the effective and actual coordinates respectively [5,6,14]

$$D_T (U_e - U_{ec})^3 = V_e^2, \qquad d_T(u - u_{cp})^3 = (v - v_{cp})^2, \qquad (14a,b)$$

$$D_T = \frac{4a_2'}{27b_1'^2}, \quad U_{ec} = \frac{-2b_1'b_3'}{a_2'}, \quad d_T = \frac{-32h_2z}{27(1 + \frac{z}{z_c} - 4h_1z)^2}, \qquad (15a,b,c)$$

where $u_{cp} = z(U_{ec} - u_s/z_s)$ and $v_{cp} = z(v_s/z_s)$ give the actual location in the observation plane of the cusp point, and d_T is the actual opening rate in the observation plane having units of 1/distance. The opening rate of the cusp curve is given by Eq. (15a) and the effective cusp point location is $(U_{ec}, 0)$. There is a divergence in the opening rate, Eq. (15a), of the TCC for surfaces with $h_1 > 0$ at a particular value of z_e. This divergent opening rate can make comparison of theoretical calculations and experimental data difficult.

For observation points inside the cusp curve there are three real and unequal solutions to the stationary phase conditions, Eqs. (12) and (13). Real solutions of the stationary phase conditions locate the real rays passing through an observation point. As the observation point approaches the cusp curve from the inside, two of the real solutions merge at the cusp curve to form a doubly degenerate real solution. When the simultaneous solution of Eqs. (12), (13), and H = 0 is done graphically the merging of the rays on the caustic is evident. For observation points outside the region bounded by the cusp curve, there are one real and two complex conjugate solutions.

Figure 5 shows the graphical solution of Eqs. (12), (13), and H = 0, for $b_1' = 0.0118$ cm^{-1}, $a_2' = 0.00236$ cm^{-2}, $U_e = 0.05$, and $V_e = 0.001, 0.0177$, and 0.05. Equation (12) is represented by the parabola opening to the left, Eq. (13) by the rectangular hyperbola, and H = 0 by the parabola opening to the right. The parabola representing the zeros of the Hessian does not depend on U_e or V_e. The intersection of the two parabola give the location in the exit plane of the degenerate rays to the cusp curve. As the observation coordinate along the symmetry axis moves outside the cusp curve (U_e becomes negative), the parabola opening to the left, Eq. (12), moves further to the left. At the cusp
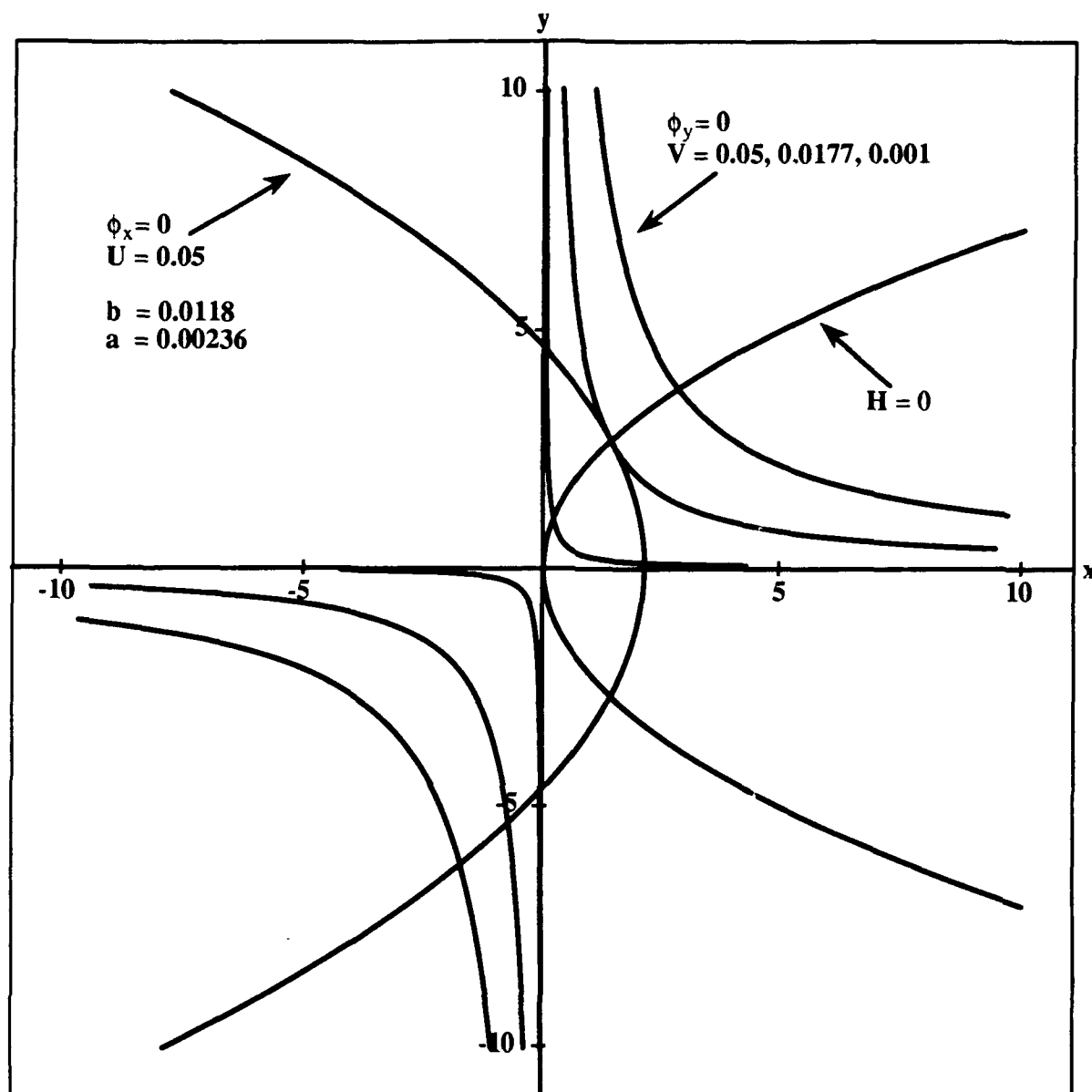
Figure. 5 An example of the graphical solution to the stationary phase conditions to locate rays in the exit plane. The intersections between the parabola opening to the left and the two branches of the hyperbola locate real rays in the exit plane which interfere at a point inside the cusp curve. The intersections of the two parabola locate degenerate rays in the exit plane which interfere on the cusp curve itself.

point, $U_e = 0$, the two parabola will be tangent to each other at the origin where there will be a triply degenerate solution to the three equations.

The hyperbola in Fig. 5 represent Eq. (13) for three different vertical positions. When $V_e = 0.001$ the observation point is inside the cusp curve. The two branches of the hyperbola intersect the parabola of Eq. (12) at three distinct places, representing the three distinct ray locations in the exit plane. Moving up to $V_e = 0.0177$ the observation point is on the cusp curve. the upper branch of the hyperbola is now tangent to the parabola of Eq. (12) where Eq. (12) and the parabola representing $H = 0$ intersect. The point where the upper branch of the hyperbola is tangent to the parabola gives the location of the doubly degenerate ray in the exit plane; the intersection of the lower branch of the hyperbola with the parabola gives the location of the single ray. As the observation point moves outside the cusp curve, $V_e = 0.05$, the branch of the hyperbola that was tangent to the parabola no longer intersects the parabola, leaving only the intersection of the lower branch and only one real ray location.

For observation points outside the cusp curve the steepest decent contour used in the asymptotic approximation of $P(w_2, w_1)$ must be moved off the real axis[19,20]. The contour passes through the one real solution on the real axis but can only pass through one of the complex conjugate solutions. A complex ray can be associated with the complex saddle point that contributes to the amplitude outside the cusp curve[20]. This complex ray contribution decays exponentially as the observation point moves away from the cusp curve. However, near the cusp curve this ray is strong enough to interfere destructively with the real ray and cause nulls in the cw wavefield. A line of minima can be seen in Fig. 4 just outside of the cusp curve. These minima are due to the interference between the real ray and the complex ray[20]. The region where no complex rays contribute to the wavefield is marked by the Stokes set of the Pearcey function[20]

$$\frac{5 + \sqrt{27}}{27} w_2{}^3 = w_1{}^2. \tag{16}$$

Between the Stokes set and the cusp curve there is one real and one complex ray

contributing to the wavefield. Outside of the Stokes set only the real ray contributes to the

wavefield. There is no more interference evident outside of the Stokes set. The three

regions of space defined by the cusp curve and Stokes set are shown in Fig. 6.
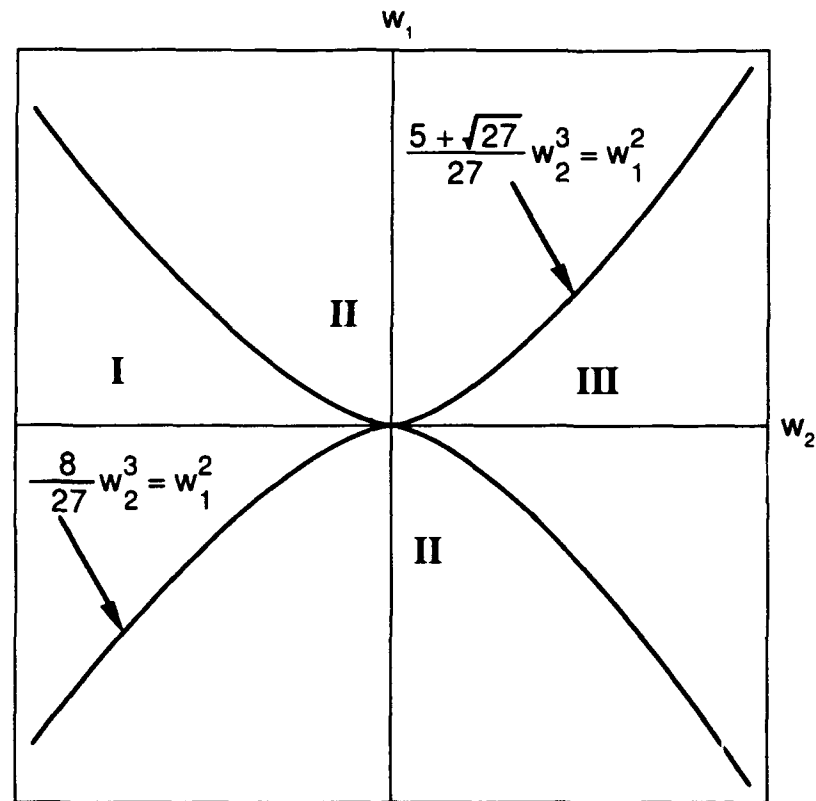
Figure. 6 A plane containing a TCC is divided into three regions by the cusp curve and the
Stokes set. I) Inside the cusp curve there are three real rays to any point in the plane.

II) Between the two curves there is one real ray and one imaginary ray to any point.

III) Inside the Stokes curve there is only one real ray to any point.

2.3 AN EXPERIMENT TO IMAGE THE TRANSVERSE CUSP DIFFRACTION CATASTROPHE FORMED BY REFLECTION FROM A CURVED METAL SURFACE IN WATER

Experiments were performed to image the wavefield reflected by a surface having the local shape given by Eq. (3). These experiments were carried out in a water tank 230 cm long, 57 cm wide, and 50 cm deep. A source was located at one end of the tank and the signal was reflected by a curved metal surface at the other end of the tank. A receiver was mounted on a two-axis positioner located near the center of the tank to sample the reflected wavefield. A schematic of the experimental set up is shown in Fig. 7.

To image the acoustical wavefield the signal from the receiving hydrophone was amplified and rectified. A sample-and-hold circuit converted the amplitude of the the rectified acoustical signal to a proportional dc level. An analog to digital data acquisition board in a Macintosh II computer stored the dc level from the sample-and-hold as a twelve bit digital value. Once the digital level was stored, the position of the receiver was changed by the computer to build a raster picture of the reflected wavefield. The digital levels were displayed as a gray-scale picture using 256 gray-levels.

A Panametrics V302 focused transducer with a 1MHz resonant frequency was used in the acoustical experiments to approximate a point source. A quadratic approximation of the phase of the source signal in the exit plane was found by fitting the phase of the outgoing wavefront from the source transducer with an approximation for the phase of a spherical wavefront as shown in Appendix B. The quadratic approximation of the phase was used to determine z_s for the source signal in the exit plane. The acoustical receiver was a DAPCO (DAPCO Industries, Inc. 199 Ethan Allen Highway, Ridgefield, Conn. 06877) bent needle hydrophone. This hydrophone has a 90° bend in the needle allowing the active element to be pointed into the reflected wavefield. The outer diameter of the needle case is $\approx 1mm$. The hydrophone frequency response curve is fairly flat in the region from 0.5MHz up to 4MHz.

26
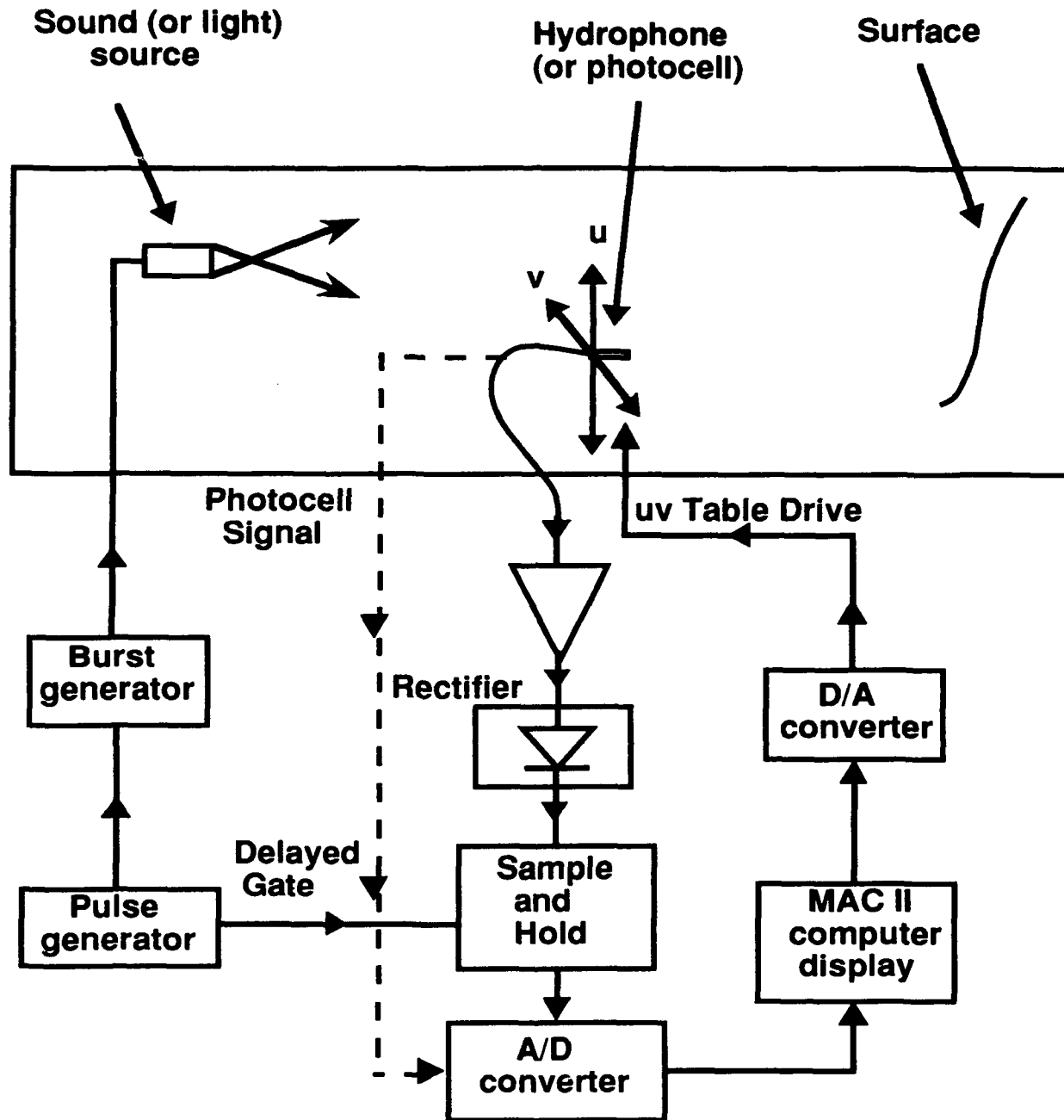
Figure. 7 A schematic diagram of the experimental set up.

TABLE I. Measured surface parameters used in theoretical calculations.

$h(x,y) = h_1x^2 + h_2xy^2 + h_3y^2 + h_4x + h_5y$		
Parameters	Surface 1	Surface 2
h_1	-0.000310 cm^{-1}	0.00431 cm^{-1}
h_2	-0.00117 cm^{-2}	0.00276 cm^{-2}
h_3	-0.01945 cm^{-1}	-0.0173 cm^{-1}
h_4	-0.154	-0.0645
h_5	-0.00301	-0.00169

Tone bursts were used to simulate a cw signal in the acoustical experiments. By using bursts the source signal could be separated from the reflection. Reflections from the sides and bottom of the tank and from the top of the water arrive at different times and could also be gated out. Bursts were long enough that end effects due to the finite difference in arrival times of the signals propagating along different rays were not sampled. The gate used to set the sample region of the reflected signal was positioned to gate out any spurious reflections from the tank. Figure 8 shows some representative scattered tone bursts. Note the build up at both ends of tone bursts 1, 2, 4, and 5 due to the finite difference in the arrival times of the different rays. Tone burst 3 does not show the same build up as it is from the one ray region of the diffraction pattern.

An HP9125A calculator plotter was modified to allow control of the plotter arm by two external analog sources. Mounted vertically over the water tank, the plotter was used as a two-axis positioner for the receiver sampling the reflected wavefield. The position of the receiver was controlled by connecting the analog inputs of the plotter to two digital to analog converters in the Macintosh II computer. A raster scan of the wavefield was produced by taking data on a grid of points in the observation plane and directly relating the grid points to pixels on the screen of the Macintosh. Each pixel was set to a gray level directly related to the amplitude of the reflected signal at the position in the observation plane represented by that pixel. Lighter gray levels represent larger amplitudes with white being the highest value and black the lowest.

In the experimental setup the acoustical source and receiver could be replaced with an optical source and receiver. The optical source was a HeNe laser attached to a small diameter (200 μm core diameter) optical fiber. A phototransistor was used as the optical receiver. The optical source was positioned at the focal point of the acoustical source, while the optical receiver was placed on the two-axis positioner. The phototransistor circuit provided dc signals proportional to the intensity of the reflected optical wavefield at each point in a raster scan. These signals were used to form a gray scale picture of the optical

Figure. 8 a) A gray-scale picture of the acoustical diffraction pattern in the observation plane with f = 809 kHz, z = 66.3 cm, and z_s = 116.6 cm. The white dots on the picture mark the position of the representative time traces shown in (b). b) Representative time traces of the bursts reflected from the surface. Trace three originates in a region with only one real ray. Trace one is in the region where there is one real ray and one imaginary ray. Traces two, four, and five contain three real rays. Traces two and four are along the symmetry axis where two of the rays arrive at the same time.

(b)

(a)

(c)
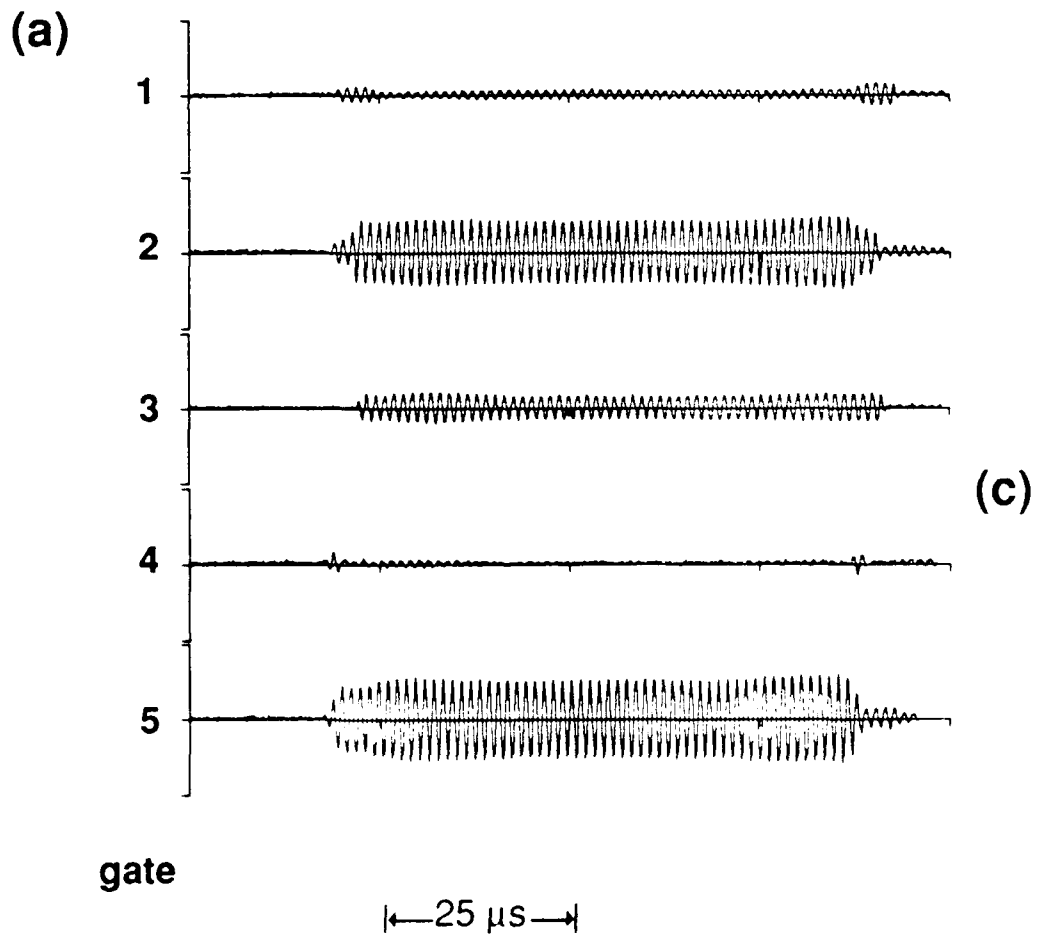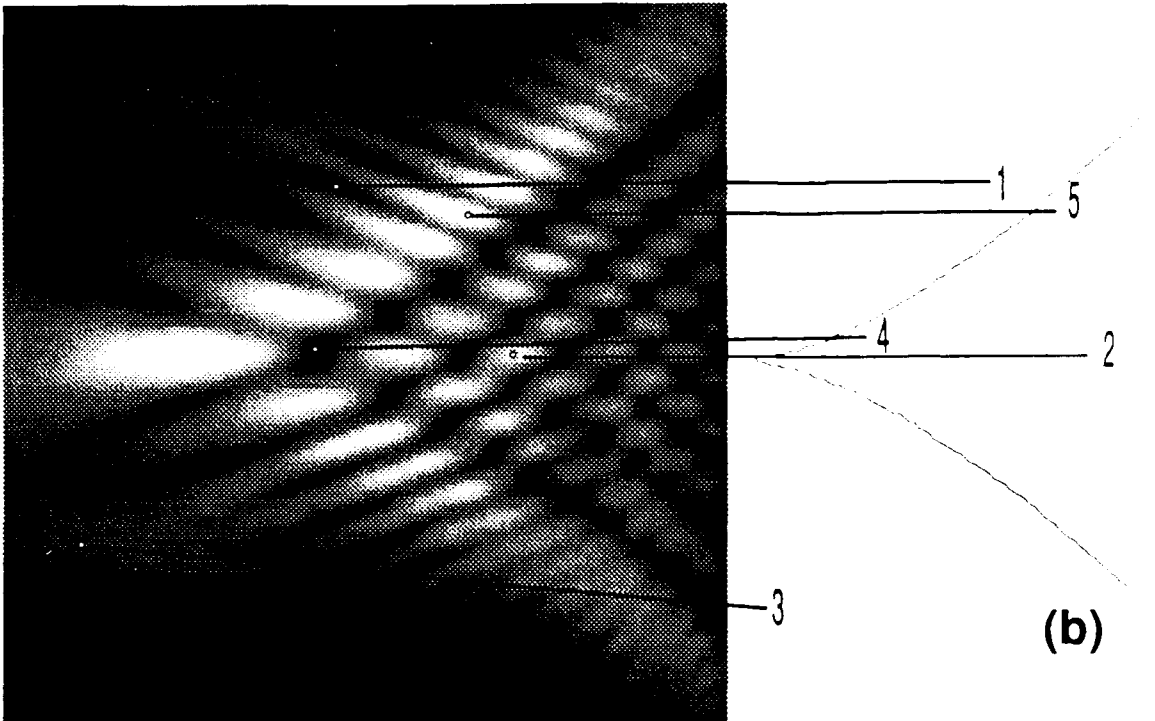
gate

|←— 25 μs —→|

wavefield in the same manner as in the acoustical experiments. The geometry of the optical and acoustical experiments was held constant allowing the imaging of the TCC for wavelengths separated by four orders of magnitude. Due to the short wavelength of the light in water ($\lambda \approx 430$ nm), the diffraction pattern is not observable in the optical experiments. However, the imaged optical wavefields do exhibit a sharp increase in intensity at the caustic that can be compared to calculated caustics.

The reflecting surface used was made of thin Apollo metal (Apollo Metals Ltd., 1001 14th Ave., Bethlehem, PA 18018) bent in the general shape given by Eq. (3). The sheet used for the surface was 15 mil thick. The acoustical reflection coefficient for the 15 mil Apollo metal in the frequency range from 0.5MHz to 2MHz is estimated in Appendix C to be between 0.8 and 0.95 thus the Apollo metal is a good acoustical mirror. Apollo metal has a polished surface making it a good optical as well as acoustical reflector. The Apollo metal was flexible enough to be bent into the desired shape.

A surface height measurement of the reflecting surface was made on a grid of points that included the area generating the cusp point. A mill with a digital readout showing the relative position of the mill bit in a plane was used to make the measurement. The vertical position was given by a dial indicator mounted to show the vertical position of the mill bed. With the surface mounted square on the mill bed, the vertical position was adjusted at each point on the grid until a reference indicator mounted in the bit holder read a preset reference value. The reference indicator assured that each vertical position could be directly related to a zero position on the surface. The surface was not deformed by the pressure of the reference indicator.

The data obtained in the surface measurement was fit to $h(x,y) = h_1 x^2 + h_2 xy^2 + h_3 y^2 + h_4 x + h_5 y$ to find the local shape of the surface. The linear terms were included in the fit to account for any linear offset or tilt in the surface. Though they have no bearing on the comparison of the data to the theory they can have a significant effect on the fit parameters. A multiple regression least squares fit was used on the data (the PROC GLM

routine of SAS; SAS Institute, Statistical Analysis System). The surface parameters found

for two different surfaces are given in Table I. A plot of the surface generated by the

values measured for the h_i of surface 1 is given in Fig. 9. The measured values of the

surface height parameters were used in comparing the theory to the data discussed below.
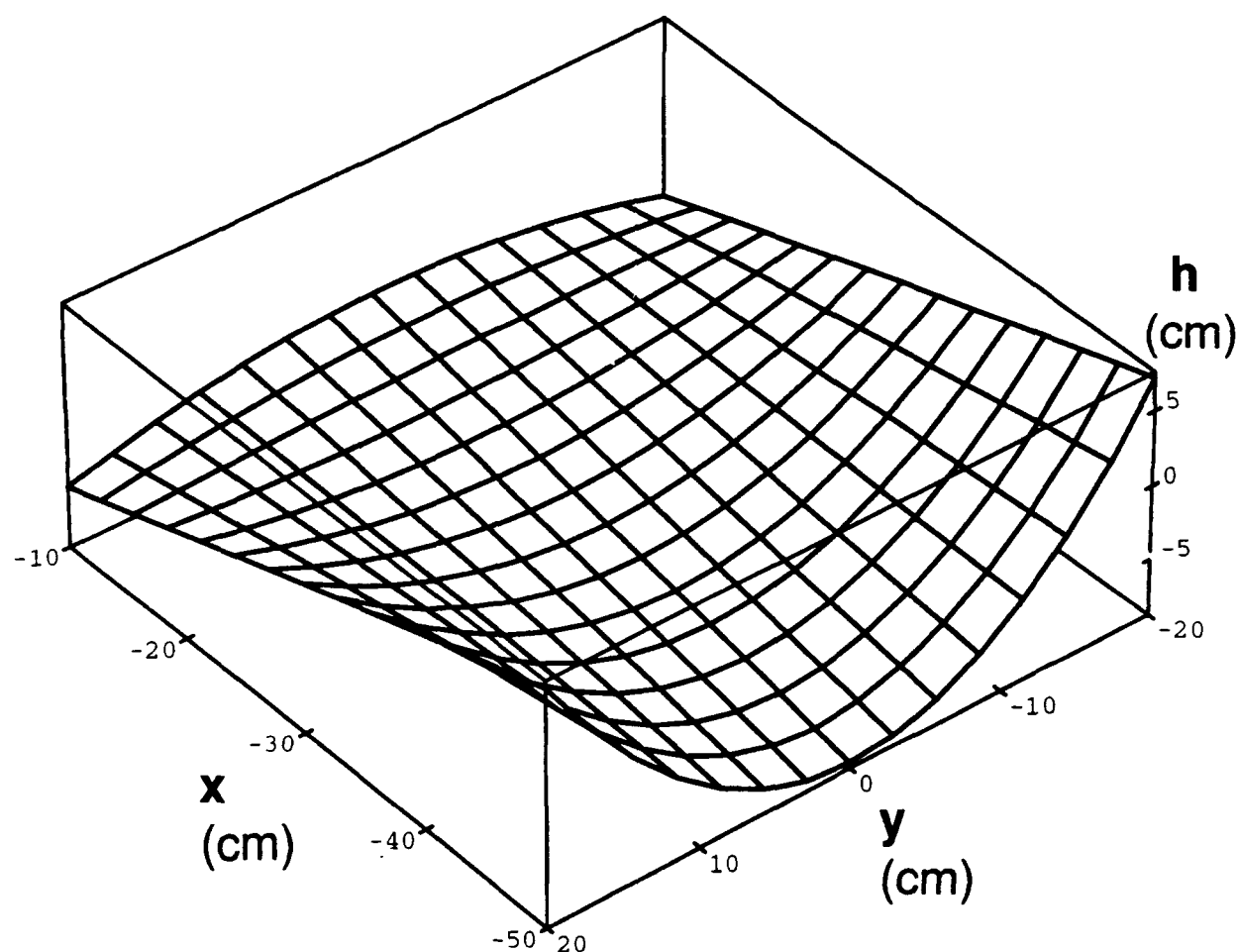
Figure. 9 The measured surface parameters h_1 - h_5 of surface 1 were used to produce a 3D

plot of the surface used in the experiment. The actual size of the surface was 35 cm long

and 20.5 cm wide.

2.4 RESULTS: COMPARISON OF THE ACOUSTICAL DIFFRACTION CATASTROPHE TO THEORETICAL CALCULATIONS OF THE EXPECTED DIFFRACTION PATTERN

A gray scale picture of the acoustical diffraction pattern produced by reflecting 1004kHz sound from surface 1 of Table I is shown in Fig 10a. The pattern exhibits the symmetry about the horizontal axis of a cusp caustic with no shear distortion. The contour plot of Fig. 10a in shown in Fig 10b. Note that none of the minima of the diffraction pattern are along the symmetry axis. This agrees with the location of the minima of the theoretical diffraction pattern $|P(w_2, w_1)|$ in Fig. 4. The shapes of the contours in Fig 10b are the same relative shapes as the corresponding contours in Fig 4. Thus the acoustical diffraction patterns exhibit the general characteristics of a cusp diffraction pattern.

Figure 11 shows a complimentary set of acoustical and optical data. The acoustical source is an 805kHz signal, and the reflecting surface is surface 1 of Table I. A contour plot of $|P(w_2,w_1)|$ was used in Fig 11b to compare a calculation of the theoretical diffraction pattern using the parameters defined by the experimental setup to the experimental picture. Using the measured surface parameters, the frequency, and the relative location in the raster scan, and Eqs. (7) and (8) a calculation of $|P(w_2,w_1)|$ could be scaled to give $|P(u,v)|$. The converted $|P(w_2,w_1)| \Rightarrow |P(u,v)|$ calculation was overlain on the acoustical pictures by shading pixels corresponding to given values of $|P(u,v)|$. A calculation of the cusp curve in terms of w_1 and w_2

$$-\frac{8}{27} w_2^3 = w_1^2, \tag{17}$$

is also overlain on the data to mark the transition from the three ray to the one ray region.

Outside but near the cusp curve shown in the acoustical overlay in Fig. 11b there is a line of minima in the acoustical data. These minima are due to interference between a complex ray and a real ray. Further away from the cusp curve the interference weakens as
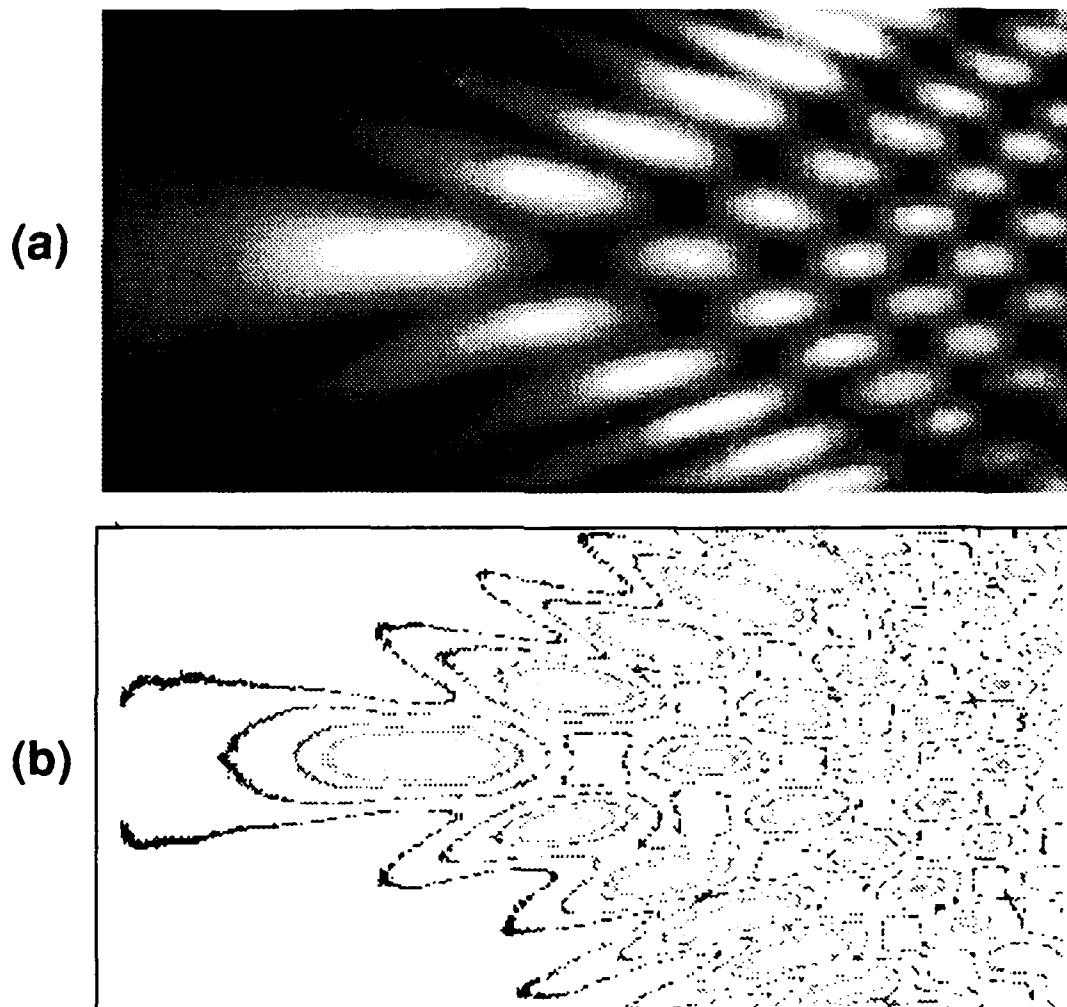
Figure. 10 a) A gray scale picture of the acoustical diffraction pattern in the observation plane due to scattering 1004kHz sound from surface 1 with $z = 80.5$ cm and $z_s = 113.2$ cm. The picture shows that the diffraction pattern has the expected symmetry about the horizontal axis of the cusp caustic. Note the line of minima along the outside of the acoustical diffraction pattern due to the interference between a real ray and an imaginary ray. b) A contour plot of the (a), note that the minima of the pattern are not located along the symmetry axis. There is general agreement between the shapes of the experimental contours and those of the theoretical diffraction pattern in Fig. 4.

the exponential decay of the complex ray starts to dominate. Outside the Stokes set drawn on the data there is no interference evident showing that only one ray exists in this region.

In the comparison of the theory to the data, the optical data in Fig 11c was evaluated first. The optical cusp was calculated using Eq. (14) with U_{ec} set to zero. Since the same source location was used for both the optical and acoustical data, the source coordinates are set to zero in the dimensionless coordinates U_e and V_e, as they will only shift the location of the cusp point. To calculate the cusp curve overlain on the optical data, Eq. (14) was evaluated and each point in the calculation scaled to correspond to pixels on the computer screen. Near the cusp point there is good agreement between the optical data and the overlain cusp curve. The location of the cusp point found in the optical comparison was used as a starting point for the acoustical comparison.

To evaluate the acoustical data in Fig 11a, $|P(u,v)|$ was overlain on the acoustical picture, Fig 11b. The location of the cusp point found in the optical comparison was used as a starting point for the acoustical comparison. In the acoustical comparisons the location of the acoustical cusp point is varied to get the best agreement near the cusp point between the maxima in the scaled Pearcey contours and the acoustical pictures. The location of the acoustical cusp point is different from that of the optical cusp point. The difference in the horizontal position is $\Delta u \approx 13$ mm and in the vertical direction $\Delta v \approx 4$ mm. This difference could be explained by differences in the location in the source plane of the acoustical and optical source points. The location of the acoustical focus is estimated to be along a line from the center of the transducer and a deviation of 2.5 cm in either direction can change the location of the cusp point in the observation plane by 1.5 cm. In the region where the calculation of $|P(w_2,w_1)|$ is best (near the cusp point), the separation of the maxima of the contours agrees well with the separation of the maxima in the acoustical data. Moving away from the cusp point the agreement deteriorates as in the optical comparison. This comparison of theory and data allowed only the location of the acoustical cusp point relative

Figure. 11 Gray-scale pictures of the acoustical and corresponding optical data for wavefronts reflected from surface 1. A contour plot of $P(w_2, w_1)$ is overlaid on the acoustical data showing good agreement between theory and experiment. The last picture is the optical data with the a calculated cusp curve overlain. The frequency of the acoustical source signal was 805kHz, $z = 67.3$ cm and $z_s = 111.7$ cm.

805 kHz data
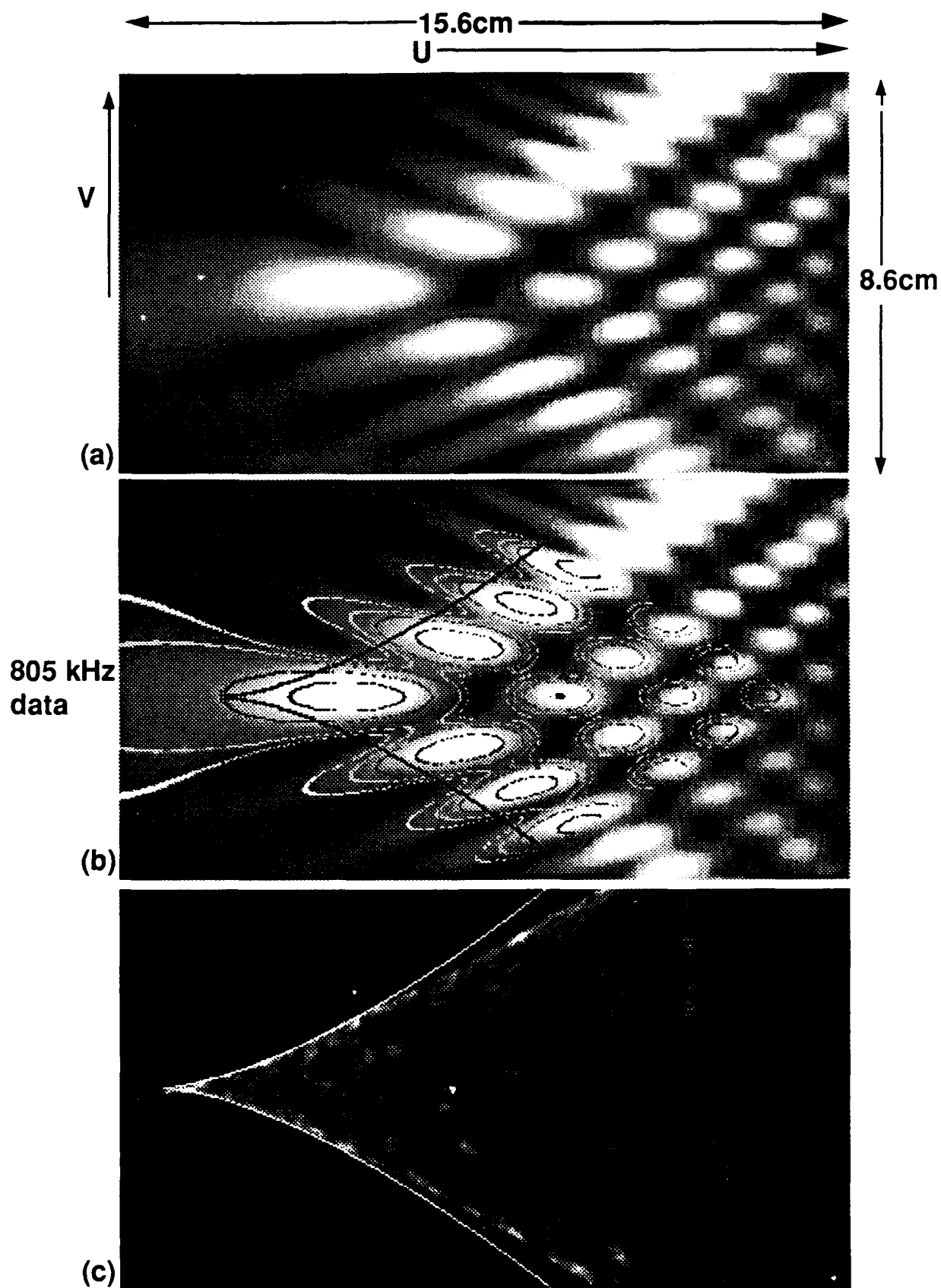
to the optical cusp point to vary, all other parameters in the calculation of the theoretical diffraction pattern were determined by the experimental setup.

To show that the wavefront produces a diffraction pattern that scales properly with frequency, the amplitude along the symmetry axis of two diffraction catastrophes produced by surface 1 with different frequencies are compared to a calculation of $|P(w_2,0)|$. The amplitude along the axis is normalized to the largest amplitude for each data set to account for any frequency response of the experimental equipment. Figure 12 shows plots of data for two frequencies, 1.5MHz and 1MHz, along with a calculation of $|P(w_2,0)|$. The cusp point is assumed to be at the origin in each of the plots. For the data plots, positions in the raster scan (u) are found using the location of the cusp point as the origin. Equation (7), the frequency, and h_1 are then used to relate the scan positions to w_2. Note that the positions and relative amplitudes of the first three maxima and minima of the data for both frequencies agree well with the calculation of $|P(w_2,0)|$.

When the surface parameter h_1 is positive, as for surface 2 of Table I, the opening rate of the caustic D_T, Eq. (15a), will diverge for a particular value of z_e. Figure 13 shows a plot of $|D_T|$ vs. receiver distance (z) for the two surfaces in Table I and $z_s = 110$ cm. The $|D_T|$ for surface 1 is well behaved for all receiver locations. Surface 1 has a negative h_1 parameter, thus $b_1' = -2h_1 + 1/(2z_e)$ is always nonzero for positive source and receiver positions. Surface 2, however, has a positive h_1 coefficient. This allows b_1' to go to zero for particular combinations of source and receiver plane distances. Figure 13 shows this divergence for surface 2. Using the value of h_1 in Table I for surface 2 and a source distance of $z_s = 110$ cm, b_1' goes to zero at $z = z_0 = 122.7$ cm. The opening rate goes as $1/(b_1')^2$ and diverges quickly as z approaches z_0.

Figure 14 shows an example of the acoustical diffraction pattern produced by reflection from surface 2. The source distance $z_s = 141.4$ cm and receiver distance $z = 67.6$ cm were constrained in the water tank, used for the experiment, to the region near where b_1' went to zero. From Fig. 13 it can be seen that a small error in z or conversely z_s

can produce a large error in D_T. The uncertainty in D_T makes a meaningful comparison of the acoustical data to a calculated diffraction pattern difficult.
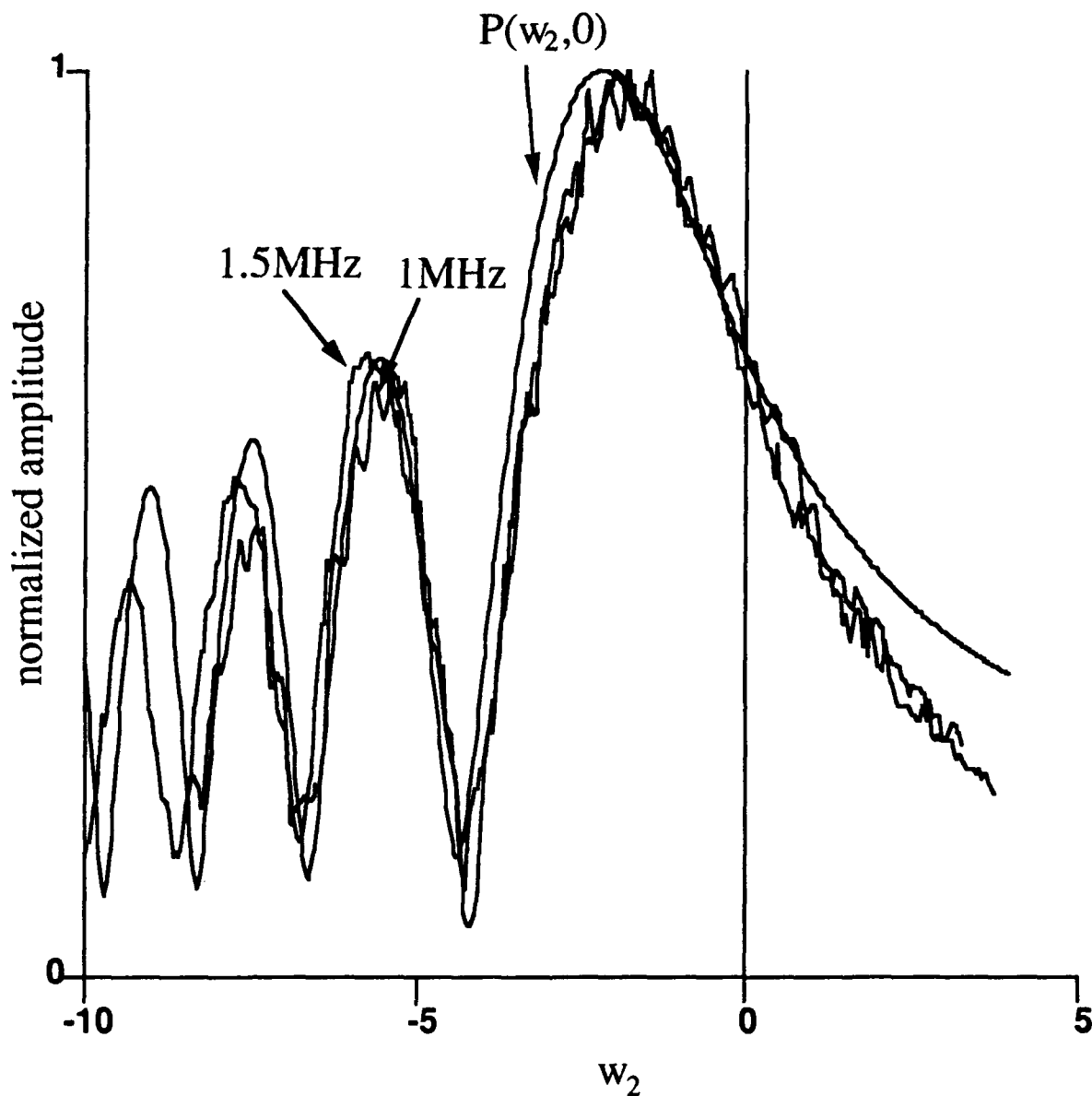
Figure. 12 The normalized amplitude along the symmetry axis of acoustical diffraction patterns for 1MHz and 1.5MHz and a calculation of $P(w_2, 0)$ are plotted vs. w_2. The position of the acoustical data is scaled using Eq. (13). The locations and relative amplitudes of the first three maxima and minima are in good agreement. The acoustical data was taken with $z = 73$ cm and $z_s = 110.5$ cm.
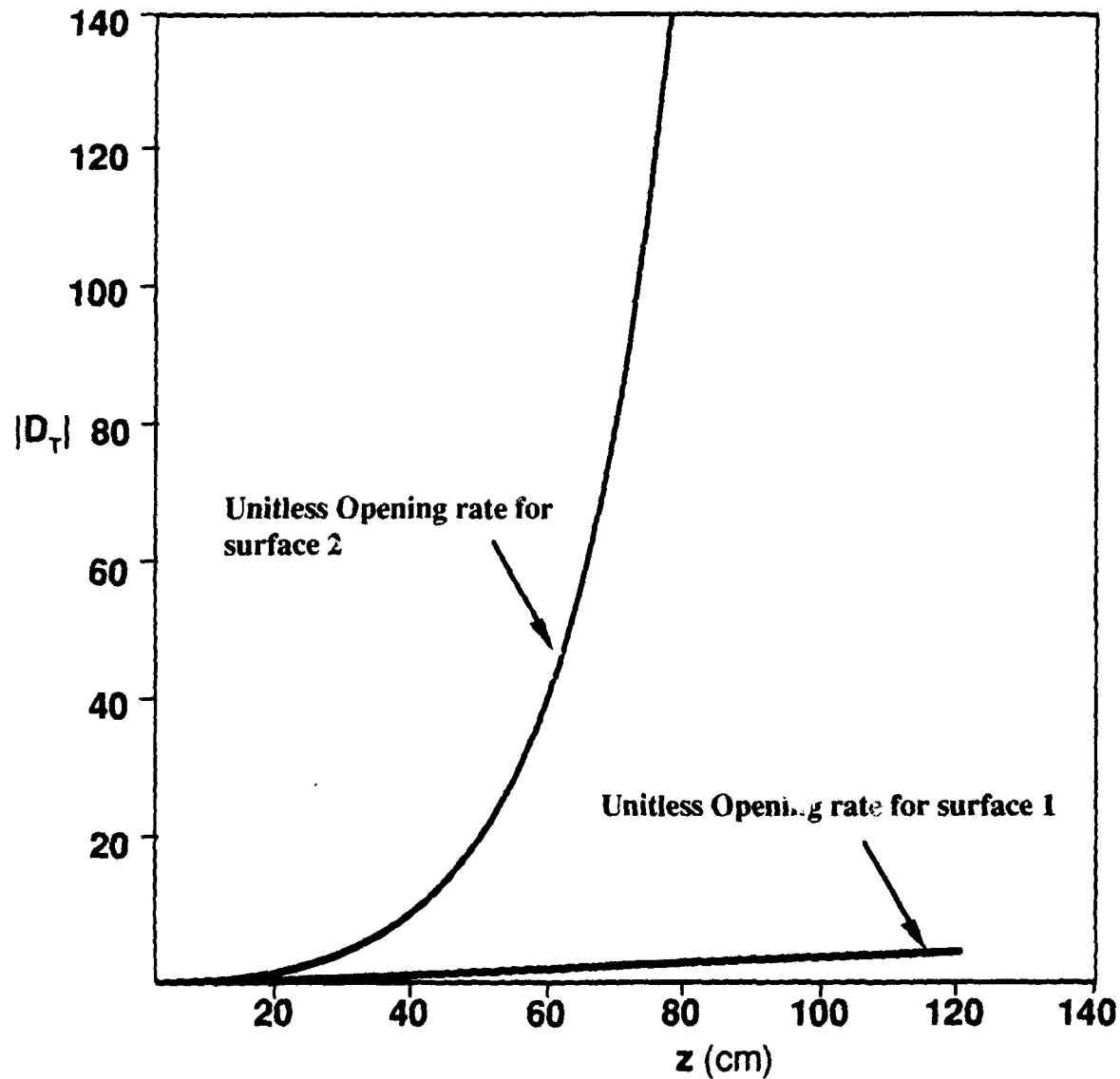
Figure. 13 Comparison of the unitless opening rate given in Eq. (22a) vs. observation distance z, for surface 1 and surface 2. The source distance used in the calculation was a typical source distance for the experimental setup $z_s = 110$ cm. Note that the rapid divergence of the opening rate for surface 2 with $h_1 > 0$ makes comparisons of theory and experiment very sensitive to errors in either the observation or source distances.
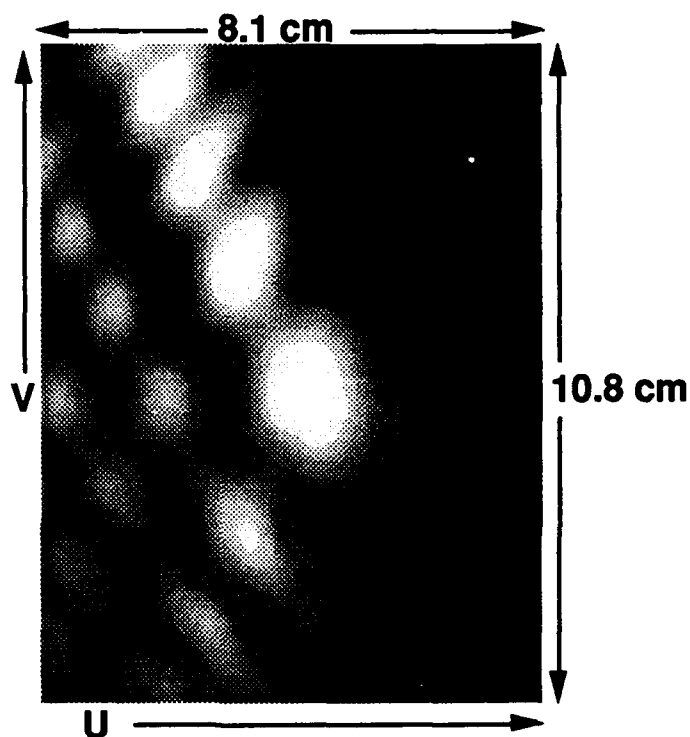
Figure. 14 A gray scale image of the acoustical diffraction pattern due to scattering of 1MHz sound from surface 2. The source and observation distances were z = 67.6 cm, z_S = 141.4 cm. The sensitivity of the calculated opening rate of this diffraction catastrophe made a meaningful comparison of the theory to the data difficult. The diffraction catastrophe is shown with the same horizontal and vertical scale as in Fig. 11.

2.5 CONCLUSION AND DISCUSSION

The wavefront that should form a TCC is given by Eq. (1). An evaluation of the propagation integral for this wavefront shows that the diffraction pattern produced is described by the canonical diffraction integral of catastrophe theory for a cusp caustic. Appendix A describes in general how the wavefront can be formed by reflection of a point source from a curved surface of local shape given by Eq. (3). The reflected wavefront should display the characteristics of the cusp caustic in an observation plane transverse to the direction of propagation.

In an observation plane the TCC exhibits the characteristics of a cusp caustic. The diffraction pattern is described by the Pearcey function, Eq. (9). The caustic curve, evident for large k, is given by Eq. (14) or Eq. (17). The separation of the maxima and minima along the symmetry axis scales with wave number like $k^{1/2}$. Just outside the caustic are interference minima that can be explained by interference between a real ray from the wavefront and a complex ray that decays exponentially away from the caustic. Inside a region marked by the Stokes set there will only be the real ray from the wavefront and therefor no interference.

Comparisons of theoretical calculations and experimental images of the diffraction pattern were made for surface 1 having the shape parameters listed in Table I. The caustic produced by the wavefront was imaged using an optical source (large k). Comparisons of the calculated cusp curve and the optical images agreed well near the cusp point as shown in Fig. (11c). With the cusp point located by the optical comparison there were no variable parameters for the acoustical comparison. The diffraction pattern seen in the acoustical images is described well near the cusp point by the Pearcey function, Fig. (11b). Interference nulls are evident outside but near to the caustic. Inside the Stokes set there are no interference nulls. Comparison of the locations and normalized amplitudes of the maxima and minima along the symmetry axis of acoustical images with different frequencies show the expected scaling of the diffraction pattern with frequency, Fig. (12).

The general agreement between the characteristics of the theoretical and experimental diffraction patterns confirms that the proposed wavefront produces a TCC in an observation plane transverse to the direction of propagation.

Some of the sources of uncertainties that may limit the quality of the agreement between the measured and theoretical diffraction patterns in Fig. (11b) will now be noted. The agreement worsens away from the cusp point as u increases. This degradation is also evident in Fig. (12). The following difficulties in the experiment are plausible causes of this problem: (i) The form of the fitted equation in Table I is only applicable to the region of the surface where rays are reflected to the region of the cusp point. Outside of this region, deviations in the surface from that form would cause deviations in the pattern predicted by Eq. (6). (ii) As evident from the phase measurements in Appendix B, the wavefront radiated from the source did not have phase properties identical to those of a true point source. This may be a consequence of some beam-like properties of the radiated wavefront. The measured phase properties suggest there may be some uncertainty in the true location of the effective source point. The analysis given in Appendix D suggests that the use of the paraxial approximation does not introduce significant error in the theory for the measurements shown.

APPENDIX A: DERIVATION OF THE DIFFRACTION INTEGRAL FOR THE REFLECTING OF SOUND PRODUCED BY A POINT SOURCE OFF OF A CURVED SURFACE OF HEIGHT h(x, y).

This appendix gives the general paraxial approximation of the field due to the reflection of a spherical source signal from a surface of height h(x,y). The geometry for this general reflection problem is shown in Fig. A1. For a point source in the source plane the incident pressure in the exit plane is given by Eq (A1)[21]

$$p_s(x,y) = p_0 \frac{e^{ikR_s}}{R_s},$$
(A1)

where p_0 is the strength of the source, k is the wavenumber ($k = 2\pi/\lambda$), and R_s is the distance from the point source to a point in the exit plane. The Fresnel approximation to the phase and denominator of Eq. (A1) is given by Eqs. (A2) and (A3) respectively

$$kR_s \approx kr_s - k\left(\frac{u_s}{z_s} x + \frac{v_s}{z_s} y\right) + k \frac{x^2 + y^2}{2z_s},$$
(A2)

$$R_s \approx r_s,$$
(A3)

where r_s is the distance from the source point in the source plane to the origin in the exit plane. Paraxially the phase delay for the propagation from the exit plane to a reflecting surface and back to the exit plane is given by the distance straight down from the exit plane to the surface and straight back up from the surface to the exit plane

$$\Delta\phi(x, y) \approx -2h(x,y),$$
(A4)

where h(xy) is the height of the reflecting surface in the exit plane. In the exit plane the portion of the wavefront reflecting from the lower areas of the surface will be phase advanced, due to a longer propagation distance to and from the surface, relative to the portions reflecting from the higher parts of the surface. If h(xy) is considered positive when it is in front of the exit plane and negative when it is behind, a signal that reflects from a positive region of the surface will have a propagation distance, relative to the
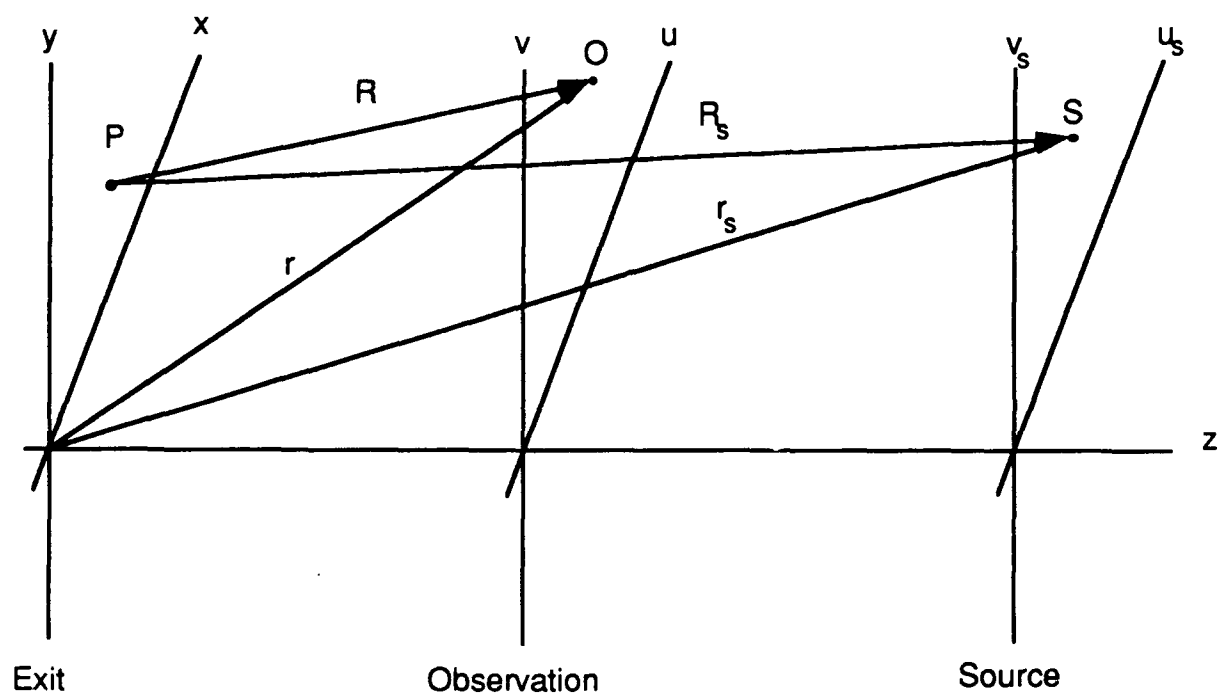
Figure. A1 The geometry used in the analysis of the diffraction produced by reflection of a point source at S from a curved surface in the exit plane. The observation point is O.

propagation distance to the exit plane, that is shorter by $-2h(x,y)$ while a signal that reflects from a negative portion of the surface will have a longer propagation distance by $2|h(x,y)| = -2h(x,y)$, thus the minus sign in Eq. (A4). Using Eqs. (A1) through (A4) the reflected pressure is paraxially approximated by

$$p_r(x,y) \approx p_0 \xi \frac{e^{-ikr_s}}{r_s} \exp\left[-ik\left\{ \frac{u_s}{z_s} x + \frac{v_s}{z_s} y - \frac{x^2 + y^2}{2z_s} + 2h(x,y) \right\} \right], \qquad (A5)$$

where ξ is the acoustical reflection coefficient for the reflecting surface.

The Rayleigh-Sommerfeld integral relates the pressure in the observation plane to p_r in the exit plane through

$$p(u,v) = -\frac{1}{2\pi} \int_{-\infty}^{\infty} \int_{-\infty}^{\infty} p_r(x,y) \frac{\partial}{\partial z} \left[\frac{\exp(-ikR)}{R} \right] dxdy. \qquad (A6)$$

where R is the distance from a point in the exit plane to a point in the observation plane, $R = \sqrt{z^2 + (x-u)^2 + (y-v)^2}$. This integral may be approximated in the far field by

$$p(u,v) \approx \frac{k}{2\pi i} \int\int p_r(x,y) \cos\chi \frac{e^{ikR}}{R} dxdy, \qquad (A7)$$

where χ is the angle between the z axis and R. The paraxial approximation is valid for wavefronts travelling approximately parallel to the z axis, thus $\cos\chi$ can be approximated by unity. Using the Fresnel approximation for the phase and denominator due to the propagation to the observation plane gives

$$\frac{e^{ikR}}{R} \approx \frac{e^{ikr}}{r} \exp\left[-ik\left\{ \frac{u}{z} x + \frac{v}{z} y - \frac{x^2 + y^2}{2z} \right\} \right], \qquad (A8)$$

where r is the distance from a point in the observation plane to the origin of the exit plane. The pressure in the observation plane is now given by

$$p(u,v) \approx p_0\,\xi\,\frac{k}{2\pi i}\,\frac{\exp[ik(r + r_s)]}{r r_s} \int\int \exp\left\{ -ik\left[\left(\frac{u}{z} + \frac{u_s}{z_s}\right)x + \left(\frac{v}{z} + \frac{v_s}{z_s}\right)y \right.\right.$$

$$\left.\left. -\frac{x^2 + y^2}{2}\left(\frac{1}{z} + \frac{1}{z_s}\right) + 2h(x,y) \right] \right\}\,dxdy. \tag{A9}$$

A set of effective coordinates related to the source and observation plane positions by [14]

$$z_e = \left(\frac{1}{z} + \frac{1}{z_s}\right)^{-1}; \quad U_e = \frac{u}{z} + \frac{u_s}{z_s}; \quad V_e = \frac{v}{z} + \frac{v_s}{z_s}, \tag{A10a,b,c}$$

can be used to describe the reflected wavefield. In terms of the effective coordinates the pressure is

$$p(U_e, V_e) \approx p_0\xi\frac{k}{2\pi i}\,\frac{e^{-ik(r+r_s)}}{r r_s}$$

$$\times \int\int \exp\left[-ik\{ U_e x + V_e y - \frac{x^2 + y^2}{2z_e} + 2h(x,y) \} \right]\,dxdy, \tag{A11}$$

where U_e, V_e, and z_e are given by Eqs. (A10a,b,and c).

The above result for the pressure in an observation plane due to the reflection from a surface of height $h(x,y)$ can now be specialized to a surface with $h(x,y)$ given by Eq. (3). For $h(x,y)$ with a small slope Eq. (A11) becomes

$$p(U_e, V_e) \approx p_0\xi\frac{k}{2\pi i}\,\frac{e^{-ik(r+r_s)}}{r r_s} \int\int e^{ik\phi}\,dxdy, \tag{A12}$$

where the reduced distance function ϕ is given by Eq. (5). This is in the same form as Eq. (5) of reference 6 and the relation to the Pearcey function follows from the steps outlined in Sec. II of reference 6. The result gives Eq. (6) which was originally derived in summary form in Ref. 14.

APPENDIX B: A QUADRATIC APPROXIMATION OF THE PHASE OF THE SIGNAL PRODUCED BY THE SOURCE TRANSDUCER USED TO ESTIMATE THE EFFECTIVE SOURCE DISTANCE z_s

The analysis given in Appendix A assumes a point source. However, in the experiments discussed in section 2.3 a point source was not available and a focused source was used to approximate a point source. The location of the focus of the source transducer was used as the source location in the acoustical experiments. In order to find the focal length z_f of the transducer, the phase of the outgoing wavefront was recorded at different points along an axis in an observation plane a distance z_T from the transducer and then fit to a quadratic approximation for the phase of a spherical wavefront along a line. Figure B1 shows the experimental setup for this measurement. Assuming that the focus of the transducer is a point focus, the outgoing wavefronts of constant phase will be spherical. Figure B2 shows a schematic of the outgoing wavefronts and the axis along which the phase measurements are taken. Assuming an $exp(-i\omega t)$ time convention, the spatial phase of the outgoing spherical wavefronts is given by $exp(i\psi)$, where $\psi = kr$. Along the x axis in Fig B2, a quadratic approximation of ψ may be obtained using the first two terms of a binomial expansion of $r = (z_s^2 + x^2)^{1/2}$

$$\psi = k\sqrt{z_s^2 + x^2} \approx kz_s + \frac{k}{2z_s} x^2 + O(x^4) \cdot \qquad (B1)$$

where it is assumed that $z_s \gg x$.

The first term, kz_s, in the expansion of ψ can not be used to find z_s. The phase of the wavefront found is given on an interval from $-\pi$ to π thus any common phase delay due to a common path length (for instance z_s) will be lost in the measurement. Only the variation of the phase caused by the changing path length along the x axis can be used to find z_s. If the phase is not collected symmetrically about the z axis it will introduce a term linear in x in the phase approximation. To show this, replace x in Eq (B1) with $x = x_0 + x'$, the phase is then given by
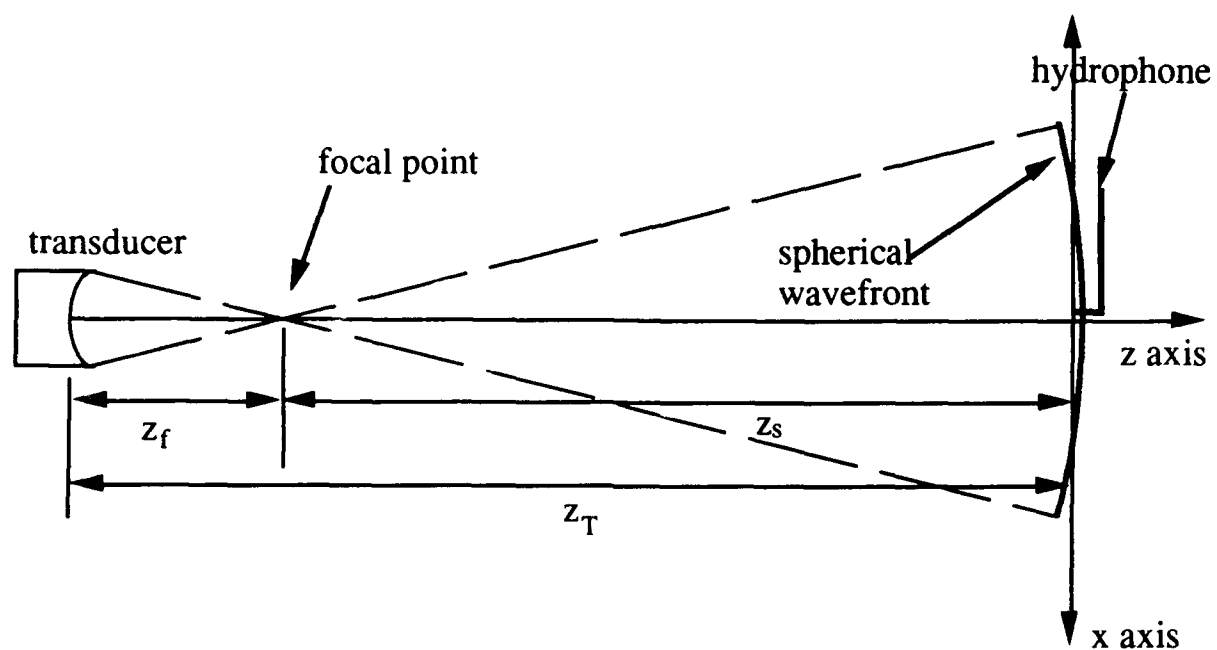
Figure B1 The experimental set up for estimating the focal length z_f of a transducer focused to a point.
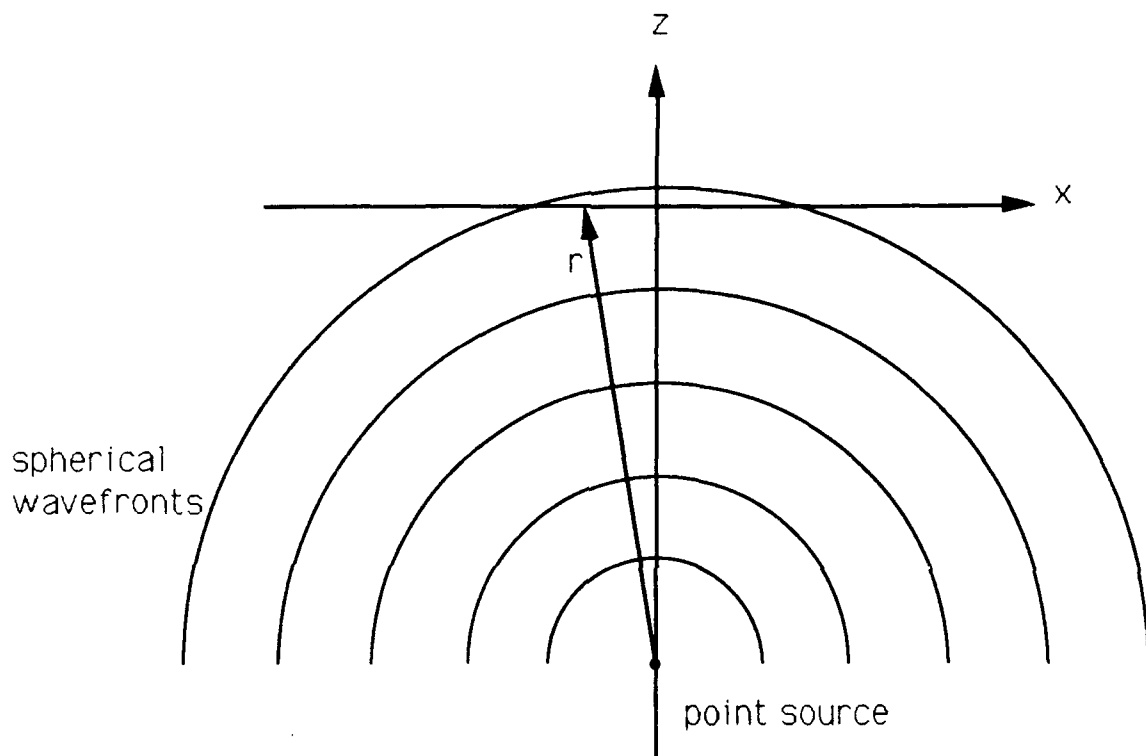
Figure. B2 To find the position of the focus of the source transducer, the phase of the outgoing wavefront from the transducer was measured along a line. The phase data was fit to an equation that was quadratic in the position along the line. The coefficient of the quadratic term in the fit equation gives the distance to the focus from the observation plane.

$$\psi \approx kz_s + \frac{k}{2z_s}x_0^2 + \frac{kx_0}{z_s}x' + \frac{k}{2z_s}x'^2, \qquad (B2)$$

where the coefficient of x'^2 is used to find z_s. Knowing z_s the focal length of the transducer is given by $z_f = z_T - z_s$.

Experiments to locate the focus were carried out using the geometry shown in Fig. B1. A long, 1MHz tone bur st was sampled in a region of the burst where the signal approximated a steady state signal. Tone bursts were used to separate the direct signal from scattered signals that had different arrival times at the hydrophone. Using the travel time of the front edge of the burst and the speed of sound in water at $18°$ C, the distance z_T to the transducer was $z_T = c/t$, where $c = 0.148 \times 10^6$ cm/s. A time record of the sampled region of the tone burst was recorded on an Analogic® Data Precision® Data 6000 (D6000). The D6000 was programmed to take a Fast Fourier Transform of the data and save the phase of the 1MHz frequency component at each position along the x axis. Thus the trend of the phase of the incident wavefront along the x axis could be recorded. Note that the phase data on the D6000 forms an inverted parabola due to use of the $\exp(+i\omega t)$ time convention. For the $\exp(-i\omega t)$ time convention the data shown in Fig. B3 forms an upright parabola. The phase data from the D6000 was transformed to the $\exp(-i\omega t)$ [the phase was multiplied by -1] time convention and fit with a quadratic equation in x. The fits of the phase data for four different values of z_T are shown in Table B1. The phase data and corresponding fit for the $z_T = 117.4$ cm is shown in Fig. B3. When the values for z_f from Table B1 were fit with a straight line they give a relation for the effective location of the focal point of the source transducer for an observation plane a distance z_T away, z_f (cm) $\approx$ 5.825 cm + 0.0928 z_T (cm). This relation was used to approximate the focal length, z_f, of the source transducer for the signal radiated to a given distance, z_T. The distance z_T was taken to be the distance from the transducer to the reflecting surface. The effective focal point was then used to approximate the effective point source distance in the evaluation of the acoustical data, $z_s = z_T - z_f$. The weak dependance of the apparent focal length z_f on z_T

is evidence that the wavefront leaving the focus does not fully simulate the wavefront leaving a point source. This may be a consequence of the directionality or beam-like properties of the source.

TABLE B1. Results of quadratic fits to the phase of the outgoing wavefront produced by the source transducer locating the focus.

$\psi = a + bx + cx^2$					
z_T (cm)	z_s (cm)	z_f (cm)	a	b (cm^{-1})	c (cm^{-2})
37.1	27.88	9.22	0.137	4.193	−0.761
85.8	71.82	13.98	−2.018	2.832	−0.233
105.6	91.20	14.40	−0.209	2.525	−0.233
117.4	100.68	16.72	−8.238	2.499	−0.211
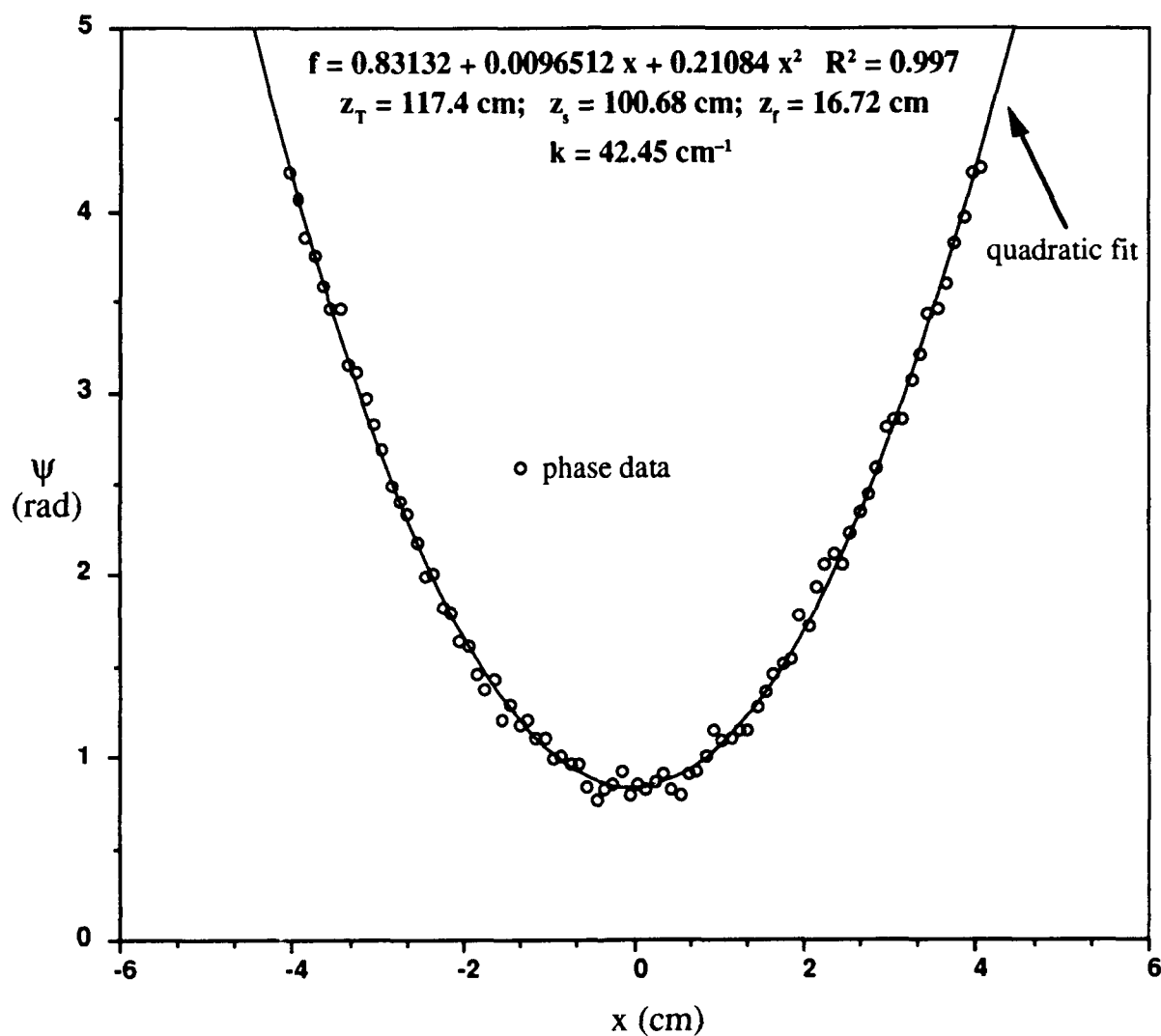
Figure B3 The experimentally measured phase of the outgoing wavefront from the
transducer located z = 117.4 cm from the observation plane. A quadratic, shown overlain
on the data, was fit to the data to find the distance from the observation plane to the
effective focal point.

APPENDIX C: ESTIMATION OF REFLECTION COEFFICIENT FOR THE METALLIC SHEET

The acoustical reflection coefficient of the reflecting surface was estimated by considering only the inertial impedance of the surface to the incident wavefront[22]. The acoustical reflection coefficient is the ratio of the reflected pressure to the incident pressure $r = |p_r|/|p_i|$. This is related to the power reflection coefficient $\mathcal{R}$ by $\mathcal{R} = r^2$. For a lossless plate the sum of the reflected power and the transmitted power must equal the incident power, thus $\mathcal{R} + \tau = 1$, where $\tau = |p_t|^2/|p_i|^2$ is the power transmission coefficient. For a slab that is bounded on both sides by water the plane wave transmission loss is given by[22]

$$\tau(\Theta_i) = \left(\left| 1 + \frac{1}{2}\frac{Z_{sl}}{\rho c} \cos \Theta_i \right| \right)^{-1}, \tag{C1}$$

where Z_{sl} is the acoustic impedance of the slab approximated below, $\rho = 0.9986$ gm/cm^3 and $c = 0.148 \times 10^6$ cm/s are the density and speed of sound in water at 18° C, and Θ_i is the angle of incidence of a plane wave. Thus the reflection coefficient is

$$\mathcal{R}(\Theta_i) = 1 - \left(\left| 1 + \frac{1}{2}\frac{Z_{sl}}{\rho c} \cos \Theta_i \right| \right)^{-1}, \tag{C2}$$

using the relation between τ and $\mathcal{R}$. This approximation assumes that the thickness of the slab $l_{sl} \ll \lambda_{sl}/4$ and $[Z_{sl}/Z_{local}(\text{back})] \ll 2\pi(l_{sl}/\lambda_w)$, where λ_{sl} is the wavelength of sound in the slab, $Z_{local}(\text{back})$ is the local specific acoustic impedance $Z_{local}(\text{back}) = \rho_w c_w$, and λ_w, c_w, and ρ_w are the wavelength and speed of sound in water and the density of water respectively. The above assumptions give the components of the fluid velocity normal to the slab on each side of the slab equal to each other $v_{front} = v_{back} = v_{sl}$.

If the slab is considered to be a perfectly limp plate, the acoustic impedance of the slab Z_{sl} is due to the inertial resistance of the mass of the plate to the pressure of the sound field. From Newton's second law

$$m_{sl} \frac{\partial v_{sl}}{\partial t} = p_{front} - p_{back}, \qquad (C3)$$

where $m_{sl} = 0.317$ gm/cm^2 is the mass per unit area of the slab and v_{sl} is the velocity of the the slab due to the difference in pressure between the front face and the back face of the slab, $p_{front} - p_{back}$. With a time dependence of the form $\exp(-i\omega t)$ for the velocity, Eq. (C3) becomes, with $\omega = 2\pi f$

$$-i m_{sl} 2\pi f v_{sl} = p_{front} - p_{back}, \qquad (C4)$$

which defines the inertial impedance of the slab[22]

$$Z_{sl} = \frac{p_{front} - p_{back}}{v_{sl}} = -i 2\pi f m_{sl}. \qquad (C5)$$

The reflection power coefficient is now given by

$$\mathcal{R}(\Theta_i) = 1 - \left[\left| 1 + \frac{1}{2} \frac{-i 2\pi f m_{sl}}{\rho c} \cos \Theta_i \right| \right]^{-1}$$

$$= 1 - \left[1 + \left(\frac{2\pi f m_{sl}}{2\rho c} \right)^2 \cos^2(\Theta_i) \right]^{-1}. \qquad (C6)$$

At normal incidence $\Theta_i = 0$ the ratio of the incident to reflected pressure is $r = \mathcal{R}^{1/2}$

$$\mathcal{R}(\Theta_i = 0) = 1 - \left[1 + \left(\frac{2\pi f m_{sl}}{2\rho c} \right)^2 \right]^{-1}. \qquad (C7)$$

Figure C1 shows a calculation of r vs f using Eq. (C7). The acoustical reflection coefficient approximated in the manner described above is positive and goes to r = 1 as the frequency increases. For the frequency range used in the acoustical experiments the range of r approximated from the calculation is $0.8 \leq r \leq 0.95$. The approximation used was for a flat slab with normally incident acoustical plane waves. However, the reflecting surface was curved and the source was approximately a point source. This could bring the approximation into question. To test the validity of the approximations used to calculate r the incident signal and transmitted signals were measured for a 900 kHz tone burst. The incident signal was 1.4 Vpp while the transmitted signal was 0.15 Vpp giving a transmission coefficient t = 0.107. This is related to the

reflection coefficient by $r = (1 - t^2)^{1/2} = 0.994$. This measured value of r at 900 kHz is very near the value given in Fig. C1 for the approximation of the reflection coefficient, $r \approx 0.987$.
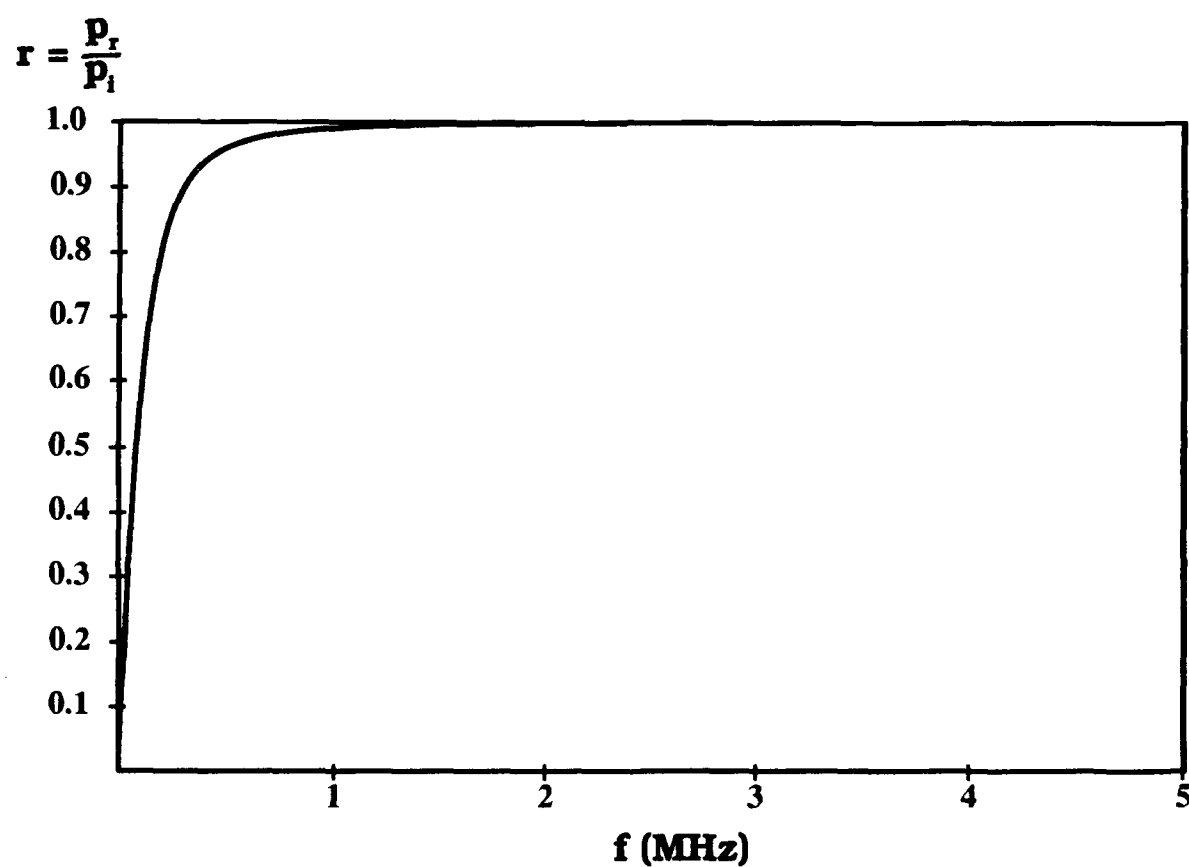
Figure C1 A plot of the reflection coefficient due to inertial impedance of the material used

to form the reflecting surface used in the experiments. Above 500kHz the reflection

coefficient is approximated by 1.

APPENDIX D: THE PARAXIAL APPROXIMATION AND QUANTITATIVE AND QUALITATIVE ERRORS

The analysis that classifies the caustic formed by W(x,y) in Eq. (1) or by the reflection of the wavefront produced by a point source of sound from a surface with the local shape given by Eq. (3) involves the paraxial approximation of the distance function $\Phi(x,y,u,v)$

$$\Phi(x,y,u,v) = \{ \ [z - W(x,y)]^2 + [u - x]^2 + [v \quad y]^2 \ \}^{1/2}. \tag{D1}$$

The distance function Φ represents the distance from a point on the wavefront (x,y) to a point in an observation plane (u,v) a distance z from the exit plane. The qualitative behavior of the wavefront in the observation plane is described by the caustic classified by the singularities of the mapping of the wavefront in the exit plane to the wavefront in the observation plane where the singularities are given by

$$\frac{\partial\Phi}{\partial x} = 0, \qquad \frac{\partial\Phi}{\partial y} = 0, \qquad \frac{\partial^2\Phi}{\partial x^2}\frac{\partial^2\Phi}{\partial y^2} - \left(\frac{\partial^2\Phi}{\partial x\partial y}\right)^2 = 0. \tag{D2}$$

The reduced distance function $\phi(x,y,u,v)$ is the paraxial approximation of $\Phi(x,y,u,v)$

$$\phi(x,y,u,v) = z - W(x,y) + \frac{(u-x)^2 + (v-y)^2}{2z}. \tag{D3}$$

Use of this approximation in Eq. (D2) yields the transverse cusp caustic surface given by Eq. (14) and Eq. (15).

Dangelmayr and Wright consider the paraxial approximation of the distance function that forms a hyperbolic umbilic caustic [23]. They show that the classification of the caustic given by the paraxial approximation of the distance function ϕ is the same as the classification found using the full distance function Φ. The transverse cusp caustic embedded in an hyperbolic umbilic is therefor also paraxially determined. Thus ϕ, the paraxial approximation of Φ, should give the same classification for the caustic as Φ itself and no qualitative information about the caustic surface is lost in the paraxial approximation.

The classification of the caustic is not affected by the size of the terms that are ignored in the paraxial approximation, however, for the paraxial approximation to be valid these terms must be small. For the distance function Φ of Eq. (D1) the paraxial approximation is given by the binomial expansion of Eq. (D1), with $W(x,y) / z \ll 1$, to first order in b where

$$b = \frac{(u - x)^2 + (v - y)^2}{2z}. \tag{D5}$$

and terms of order b^2 and higher are ignored. When the next higher order term in b is considered, the approximation to the distance function has the form

$$\Phi(x,y,u,v) \approx \phi(x,y,u,v) + \phi_c(x,y,u,v), \tag{D6}$$

where the leading correction term is

$$\phi_c(x,y,u,v) = -\frac{[(u - x)^2 + (v - y)^2]}{2z}$$

$$\times \left\{ \frac{[(u - x)^2 + (v - y)^2]}{4z^2} - \frac{W(x,y)}{z} \right\}, \tag{D7}$$

where terms of $O\{[W(x,y)/z]^2\}$ have been dropped as $W(x,y) / z \ll 1$. Conditions, from the form of ϕ_c, for the paraxial approximation to the distance function to lead to negligible error in the caustic location near the cusp point are noted below.

To show that this term ϕ_c is small consider the wavefront given in Eq. (1). The wavefront produced by reflecting a spherical wavefront from a surface with the local shape of Eq. (3) has the local shape of Eq. (1) if the source is located at the origin ($u_s=0$, $v_s=0$). With a distant source, the paraxially approximated reflected wavefront is

$$W(x,y) = a_1 x^2 + a_2 x y^2 + a_3 y^2. \tag{D8}$$

where

$$a_1 = -2h_2 + \frac{1}{2z_s}, \qquad a_2 = -2h_2, \qquad a_3 = -2h_3 + \frac{1}{2z_s}. \qquad (D9a,b,c)$$

The location in the exit plane of the rays to the cusp point is (x_{cp}, y_{cp}) with $y_{cp} = 0$ and $x_{cp} = -b_3 / a_2$, where

$$b_i = a_i + \frac{1}{2z}. \qquad (D10)$$

The location of the cusp point in the observation plane is given $v = 0$ and Eq. (15b) with b_i' $\rightarrow b_i$ and $a_2' \rightarrow a_2$, and $u_{cp} = -2zb_1b_3/a_2$. With the cusp point as defined above, the correction term to the reduced distance function at the cusp point is

$$\phi_c(x_{cp}, y_{cp}, u_{cp}, v_{cp}) = -\frac{(u_{cp} - x_{cp})^2}{z} \left[\frac{(u_{cp} - x_{cp})^2}{4z^2} - \frac{W(x_{cp},0)}{z} \right]. \qquad (D11)$$

It has been argued[13] that this correction will be negligible if each of the terms in the square bracket is $\ll 1$. At the cusp point $W(x_{cp},0) / z$ is given by

$$\left| \frac{W(x_{cp},0)}{z} \right| = \left| \frac{a_1 b_1^2}{z a_2^2} \right| \ll 1. \qquad (D12)$$

The second term in the square bracket in Eq. (D11) can be written

$$\frac{(u_{cp} - x_{cp})^2}{4z^2} = \left(\frac{-2zb_1b_3}{a_2} + \frac{b_3}{a_2} \right)^2 (4z^2)^{-1} = \left(\frac{2zb_3}{a_2} \right)^2 (-b_1 + \frac{1}{2z})^2 (4z^2)^{-1}$$

$$= \left(\frac{b_3 a_1}{a_2} \right)^2 \ll 1. \qquad (D13)$$

For surface 1 in Table I and the representative source and receiver distances $z = 68$ cm and $z_s = 110$ cm the inequalities in Eqs. (D12) and (D13) are seen to hold with $a_1 b_1^2 / z a_2^2 = 0.0357$ and $(b_3 a_1 / a_2)^2 = 0.0125$. Thus for the distances used in the experiment the paraxial approximation ϕ of the distance function Φ is a valid approximation.

In addition to these geometric conditions, if the phase of the wavefield is to be accurately approximated, it is necessary for $k\phi_c \ll 1$ with x and y corresponding to the rays to the observation point (u,v,z).

References

1)   M. V. Berry and C. Upstill, "Catastrophe optics: Morphologies of caustics and their diffraction patterns," in *Progress in Optics*, ed E. Wolf (North Holland, Amsterdam, 1980), Vol. 18, pp 257-346.

2)   M. G. Brown, "The transient wave fields in the vicinity of cuspoid caustics," J. Acoust. Soc. Am. **70**, 1427-1436 (1981).

3)   M. G. Brown and F. D. Tappert, "Catastrophe theory caustics and traveltime diagrams in seismology," Geophys. J. R. astr. Soc. **88**, 217-229 (1987).

4)   T. Pearcey, "The structure of an electromagnetic field in the neighbourhood of a cusp of a caustic," Philos. Mag. **37**, 311-317 (1946).

5)   P. L. Marston, "Directional caustics in acoustics and light scattered from bubbles," in *Proceedings of the 12th International Congress on Acoustics*, (Beauregard Press, Toronto Canada, 1986), pp I1-1.1/1.2.

6)   P. L. Marston, "Transverse cusp diffraction catastrophe: Some pertinent wavefronts and a Pearcey approximation to the wave fields," J. Acoust. Soc. Am. **81**, 226-232 (1987).

7)   W. P. Arnott and P. L. Marston, "Unfolding axial caustics of glory scattering with harmonic angular perturbations of toroidal wave fronts," J. Acoust. Soc. Am., **85**, 1427-1440 (1989).

8)   R. Dong and L. Adler, " Observations of diffraction caustics for ultrasound," J. Appl. Phys. **54**, 2832 (1983).

9)   P. L. Marston and E. H. Trinh, "Hyperbolic umbilic diffraction catastrophe and rainbow scattering from spheroidal drops," Nature (London) **312**, 529-531 (1984).

10)   C. E. Dean and P. L. Marston, "Opening rate of the transverse cusp diffraction catastrophe in light scattered by oblate drops," Appl. Opt. **30**, xxxx-xxxx, (1991).

11)   J. F. Nye, D. R. Haws and R. A Smith, "Use of diffraction gratings with curved lines to study the optical catastrophes D_6^+ and D_6^-," J. Modern Optics, **34**, No. 3, 407-427, (1987).

12)   J. F. Nye and J. H. Hannay, "The orientations and distortions of caustics in geometrical optics," Opt. Acta. **31**, 115-130, (1984).

13)   P. L. Marston, "Geometrical and catastrophe optics methods in scattering," for *High Frequency and Pulsed Scattering*, Physical Acoustics **20** or **21**, ed. R. N. Thurston and A. D. Pierce, (Academic Press).

14)   P. L. Marston, "Surface shapes giving transverse cusp catastrophes in acoustic or seismic echoes," in *Acoustical Imaging* vol 16, ed. L. W. Kessler, (Plenum, New York, 1988), pp. 579-588.

15)   F. J. Wright (private communication).

16)   M. V. Berry, J. F. Nye, and F. J. Wright, "The elliptic umbilic diffraction catastrophe," Philos. Trans. R. Soc. London, Ser. A **291**, 453-484 (1979).

17)   J. J. Stamnes and B. Spjelkavik, "Evaluation of the field near the cusp of a caustic," Optica. Acta., vol 30, no 9, 1331-1358 (1983).

14)   J. N. L. Connor, "Semiclassical theory of molecular collisions: Three nearly coincident classical trajectories," Molecular Physics **26**, no 5, 1217-1231 (1973).

19)   M. V. Berry and C. J. Howls, "Stokes surfaces of diffraction catastrophes with codimension three," Nonlinearity, 281-291 (1990).

20)   F. J. Wright, "The Stokes set of the cusp diffraction catastrophe," J. Phys. A: Math. Gen. **13**, 2913-2928 (1980).

21)   A. D Pierce, *Acoustics, An Introduction to its Principles and Applications*, (McGraw-Hill, New York, 1981) pp. 159-162.

22)   Ref. 21, pp. 143-144.

23)   G. Dangelmayer and F. J. Wright, "On the validity of the paraxial eikonal in catastrophe optics," J. Phys. A: Math. Gen. **17**, 99-108, (1984).

CHAPTER THREE

OBSERVATION OF THE TRANSIENT CHARACTERISTICS AND THE MERGING OF RAYS FOR THE WAVEFIELD FORMING THE TRANSVERSE CUSP CAUSTIC

3.1 INTRODUCTION

Wavefronts reflected or refracted by curved surfaces can form caustics that are the focal envelopes of rays from the outgoing wavefront. As a caustic is crossed from the bright side in an observation plane to the dark side at least two rays from the wavefront merge and are lost. When a transient source is used, the arrivals of the transient signals associated with merging rays also merge and disappear after the caustic is crossed [1]. The more commonly investigated situation is the use of catastrophe theory to associate structurally stable caustics with canonical diffraction integrals for steady state wavefields [2]. The structural stability of the caustics means that the classification of the caustic survives small perturbations of the curved surface or the propagating medium. The emphasis of the present chapter is on the merging of transient signals for one example of a structurally stable caustic: a transverse cusp caustic. The signals are associated with reflections from a curved metal surface in water. The investigation of the merging of such echoes may prove useful for inferring the local shape of the reflecting surface.

Prior to considering transverse cusps, the merging of transient arrivals for a simpler situation, a longitudinal cusp, will be discussed. Figure 1 shows a longitudinal cusp caustic and the wavefront that propagates to form the caustic. This figure will be used to illustrate the merging of rays on the caustic. The longitudinal (axial) cusp caustic was studied by Pearcey in connection with the cylindrical aberration[3]. The cusp caustic associated with the cylindrical aberration opens parallel to the direction of propagation of the wavefront and is described by the general equation

$$D_L(z - z_{cp})^3 = x^2, \qquad (1)$$

where D_L is the opening rate of the cusp curve with units of 1/distance and x and z are shown in Fig. 1. The wavefront that produces the longitudinal cusp caustic is curved along one direction[4]. This wavefront is mirror symmetric about an axis along the direction of propagation and forms a caustic that is also mirror symmetric along the same axis. The wavefront in Fig. 1 is given by $W(x) = W_\infty x^2/[x^2 + (W_\infty/\beta)]$ where β and $W_\infty > 0$. The cusp curve formed by the wavefront $W(x)$ is described by Eq. (1) above with $z_{cp} = 1/(2\beta)$ and $D_L = 8/(27Kz_{cp})$, where $K = 1 + 1/(\beta W_\infty)$ is the coefficient of cylindrical abberation. In the bright region inside the cusp curve, point **A**, there are three rays from the wavefront and outside the cusp curve in the dark region, point **C**, there is only one ray from the wavefront. In the center of the caustic at point **A** the three rays from the wavefront are d, e, and f. Ray paths d and f represent the same path lengths to the observation point **A** which are shorter then ray path e. Moving to the left from **A** to **C** along the cut through the caustic shown in Fig. 1, on the cusp curve, point **B**, there are two rays b and c where ray c, the longer of the two, is the result of the merging of rays e and f on the caustic. As the observation point moves from **A** inside the caustic to **B** on the caustic the locations of both the rays e and f on the wavefront $W(x)$ move toward the location of ray e on the wavefront. After crossing the wavefront, point **C**, the rays that merge on the cusp curve are lost leaving only one ray.

Consider transient signals propagating along the rays shown in Fig. 1 at a speed c. To reach the point along the cut shown in Fig. 1 where the ray the signal is propagating along crosses the cut, it will take each signal a time $t_i = r_i/c$ where r_i is the distance along the ray from the wavefront to the cut. Inside the cusp curve there will be three arrivals times t_i i=1,2,3 associated with the three ray paths to each point. On the cusp curve there are only two arrival times as two of the rays have merged to come from the same point on the wavefront. Outside the cusp curve there is only one arrival time as there is only one ray path through each point. When the arrival times are displayed along consecutive lines
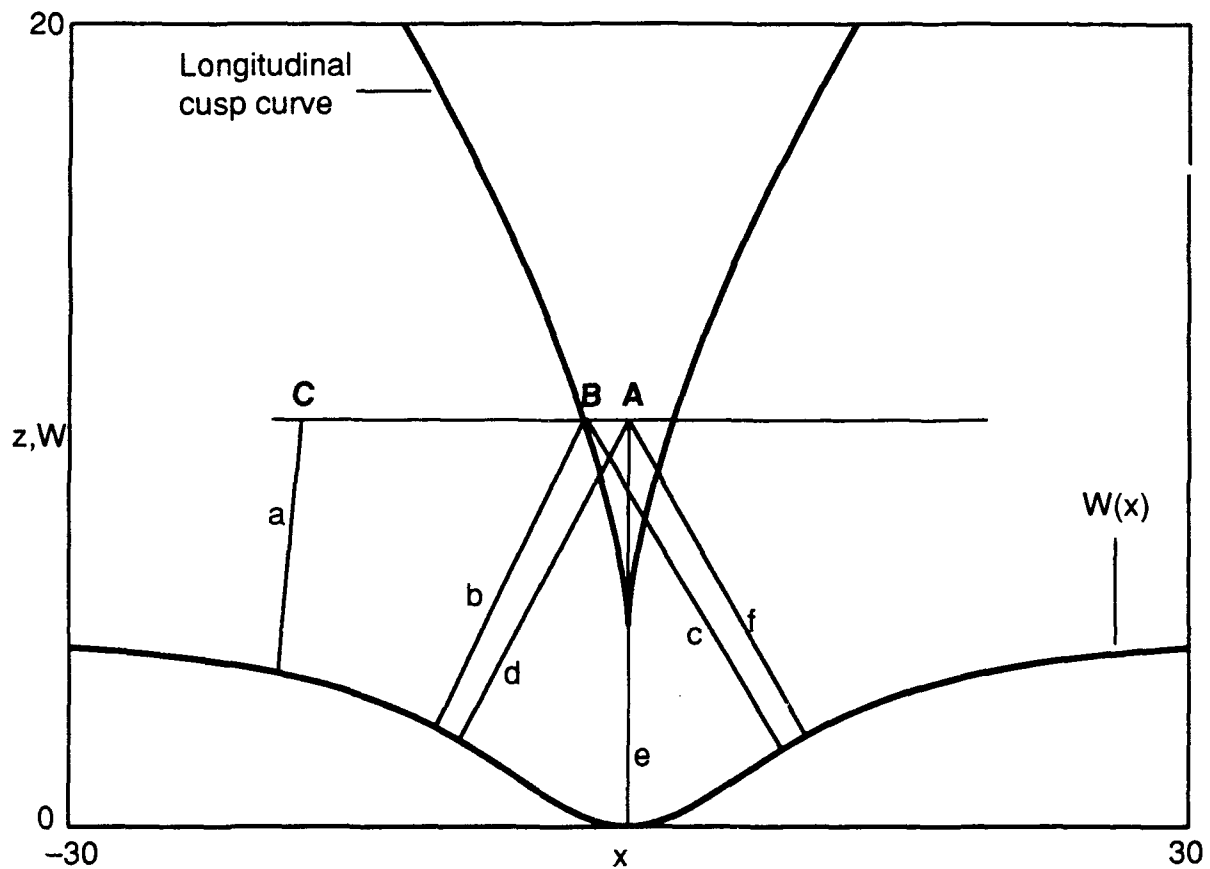
Figure 1) A calculation showing the wavefront $W(x) = W_\infty x^2 / [x^2 + (W_\infty/\beta)]$ where $W_\infty = 1$ and $\beta = 0.001$. For large values of x, $W(x) = W_\infty$, while for small values of x, $W(x) \approx \epsilon x^4 + \beta x^2$ where $\epsilon = -\beta^2/W_\infty$. The local shape of this wavefront forms a longitudinal cusp caustic described by Eq. (1). The location of the cusp curve for the wavefront shown is also. Outside the cusp curve (C) there is only one ray passing through each point. On the cusp curve (B) there are two rays passing through each point, one of which is due to the merging of two rays on the cusp curve that are lost outside the cusp curve. Inside the cusp curve (A) there are three distinct rays passing through each point.

corresponding to equispaced positions along a cut similar to the one shown in Fig. 1, the arrival time surface has the general form shown in Fig. 2. In Fig. 2 the horizontal axis represents the position of a hypothetical receiver in a receiver array of 41 receivers placed along the cut shown in Fig. 1 with the center receiver at point **A**. The arrival times of the signals propagating along rays from the wavefront are designated by the points in Fig. 2 with time increasing along the vertical axis. Positions 1-7 and 35-41 in Fig. 2 are outside the cusp curve and there is only one arrival time shown. The two receivers positioned on the cusp curve are at positions 8 and 34. There are two arrival times shown for positions 8 and 34 in Fig.2, the first is the single ray that was left outside the cusp curve and the second is due to the two rays that merge on the cusp curve. Moving inside the cusp curve at positions 9-33 there are three arrival times shown for each position. Position 21 shows only two arrivals, however the first arrival is the simultaneous arrival of two signals that travel along ray paths of equal length and thus arrive at the same time, point **A** in Fig. 1.

The symmetric transverse cusp caustic (TCC) is a cusp caustic that opens roughly perpendicular (transverse) to the general direction of propagation of the wavefront. This caustic is mirror symmetric along an axis perpendicular to the direction of propagation and is defined by Eq. (12) below. The wavefront that produces the TCC, described by Eq. (10) below[5], is curved along two directions and has the same mirror symmetry as the TCC. This wavefront forms a caustic surface in space similar to the surface shown in Fig. 3. The TCC observed in the observation plane is a cut through this surface in a uv plane a distance z from the exit plane. The diffraction catastrophe exhibited by the TCC is the same as that of the axial cusp caustic. The diffraction pattern has been used (in Chapter 2) to demonstrate that the wavefront given by Eq. (10) exhibits the characteristics of the wavefront in catastrophe theory that produces a cusp caustic.

In the frequency domain each catastrophe is associated with a diffraction pattern and caustic. The association of the caustics to the diffraction patterns is through the distance function used in the phase of the diffraction integral as in Eq. (2) below. Ray locations on
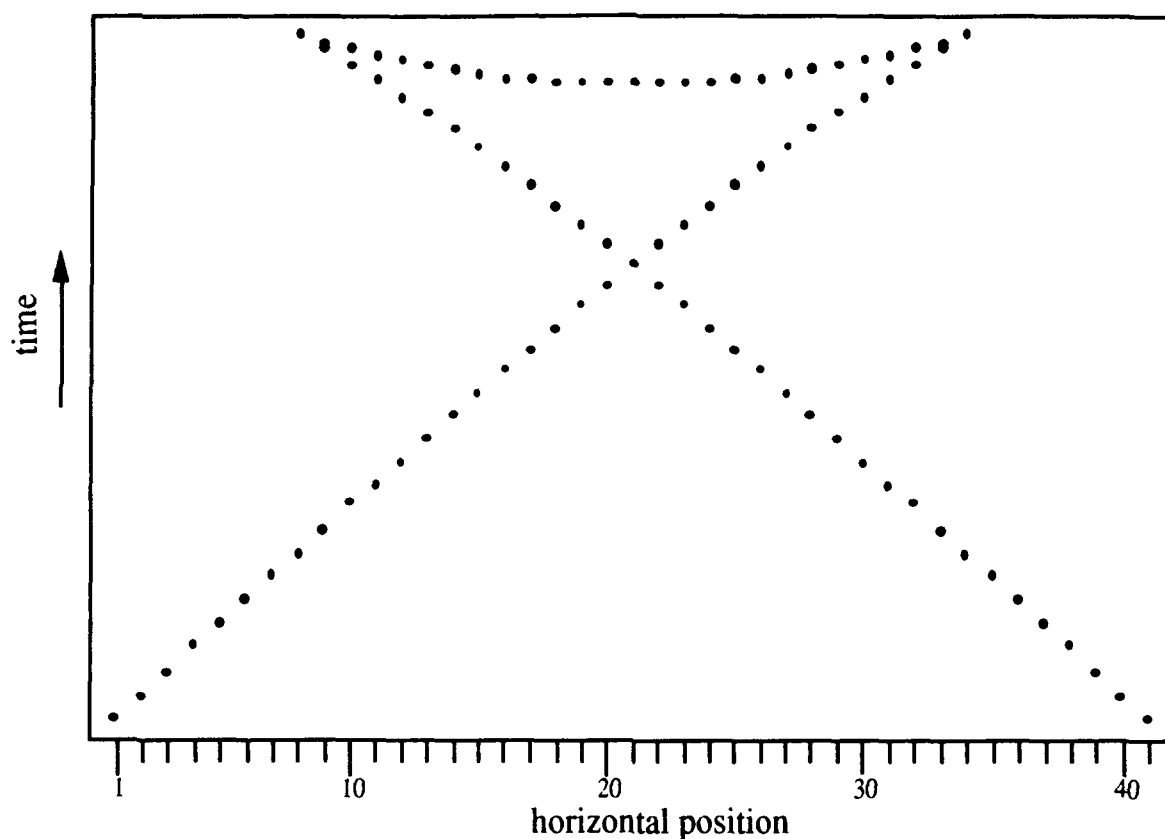
Figure 2) An example of the general shape of the travel time curve associated with the longitudinal cusp caustic for a horizontal cut that passes through a cusp curve. The points in the figure represent the arrival times of signals that propagate to different positions along a horizontal cut through a cusp curve similar to that shown in Fig. 1. This travel time curve can be related to Fig. 1, assuming a uniform sound speed c, by dividing the distance, r_i, along the ray paths from the wavefront W(x) to the horizontal cut, by c ($t = r_i/c$). Positions 1-7 are outside the cusp curve like point **C** in Fig. 1. As the observation position moves toward the cusp curve the ray path, marked a in Fig. 1, becomes longer and the arrival time of the signal propagating along this ray path is later. On the cusp curve, position 8 in Fig. 2 and (**B** in Fig. 1), there are two arrivals, rays b and c, the later of which is due to two rays that merge on the cusp curve. Moving inside the cusp curve, positions 9-33, there are three separate arrivals where at position 21 the early arrival is due to the simultaneous arrival of two signals that travel along different ray paths that have the same length (**A** in Fig. 1).
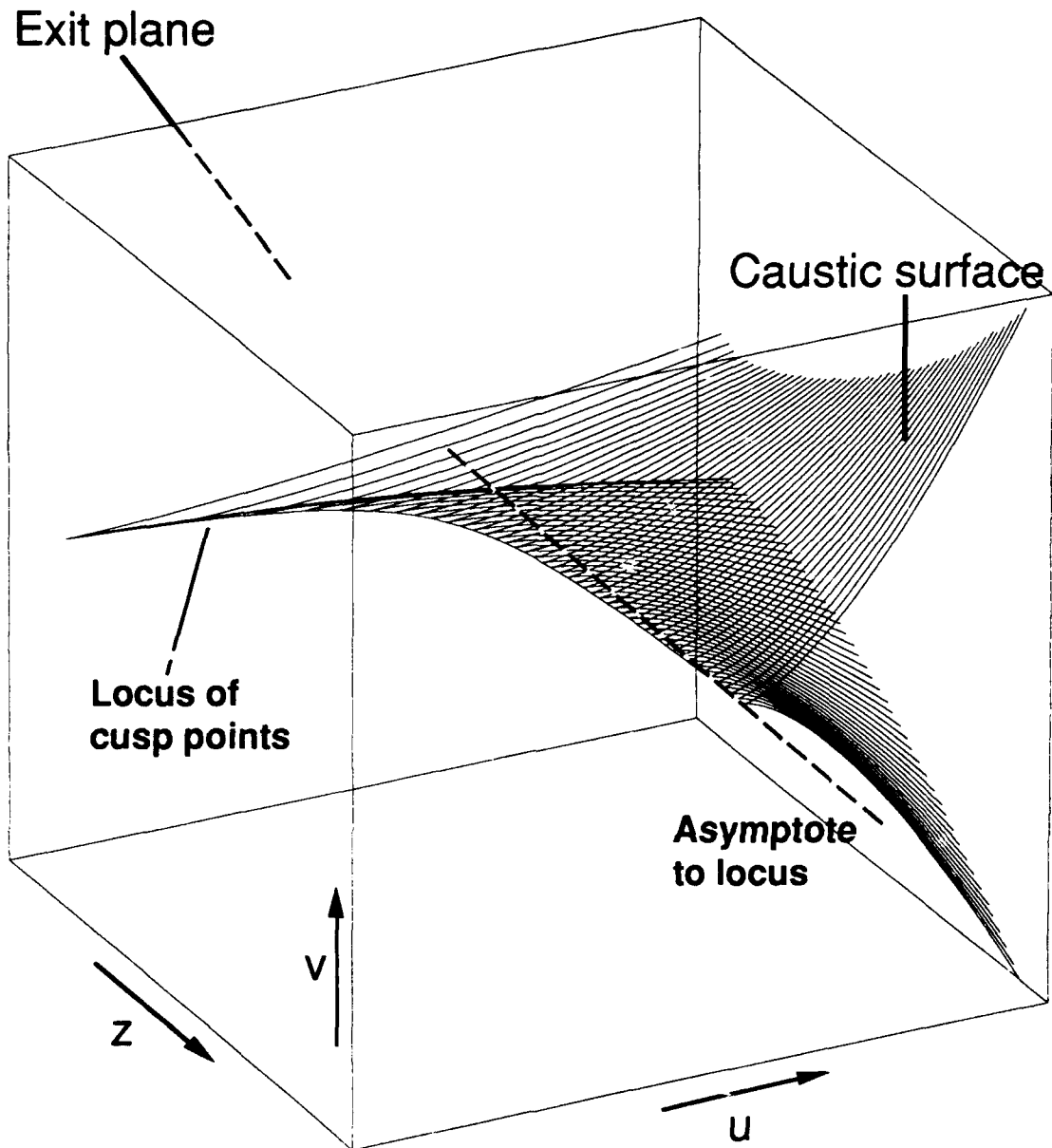
Figure 3) The caustic surface formed by a wavefront with the general shape in the exit

plane given by Eq. (10). A transverse cusp caustic described by Eq. (12) is formed in a uv

plane that cuts through the caustic surface a distance z from the exit plane. The rib of the

caustic surface is formed by the locus of cusp points in consecutive uv planes cutting

through the surface. There is only one ray path to each point outside the surface, while

inside the surface there are three ray paths to each point. On the caustic surface two of the

ray paths merge to come from the same point in the exit plane and are subsequently lost as

the caustic surface is crossed moving outside.

the wavefront are given by the ray condition for the distance function of the diffraction integral, Eq. (5) below. The ray location can be used in the distance function Φ to find the distance r a signal travels along a ray path to an observation point. Thus the distance function that classifies a caustic also classifies the associated travel time surface that displays the merging and disappearance of signals on the caustic.

Many scattering problems do not lend themselves to the use of long (many cycle) source signals. One example is seismography. In seismography short single cycle bursts from a point source are scattered by boundaries and sound speed gradients in the earth's crust and the scattered field is measured at the surface. The scattered signals are collected at the surface by either an array of receivers or by positioning the source along an array of points and using the source as the receiver also. The collected signals are displayed vs surface position and arrival time [6] in a manner similar to Fig. 2. This displays cuts through the travel time surface of the wavefield scattered from the boundary. The travel time surface displays the arrival times of all the rays from the wavefront to an observation plane adding an extra dimension, time, to provide information about the wavefront. Seismic signals scattered from curved boundaries form travel time surfaces that can be categorized in terms of the structurally stable caustics [7]. Figure 2 shows the general shape of the travel time surface associated with a common boundary shape similar to the shape of the wavefront in Fig. 1 when the surface is buried sufficiently deep [6,8]. In the vocabulary of seismology, the travel time surface shown in Fig. 2 is an example of a triplication [9,10]. Identification of triplications is thought to be useful for inferring the local shape of the reflecting surface [6-9].

Chapter 3 describes experiments to image the travel time surface in a transverse observation plane associated with a TCC. The wavefront shape given by Eq. (10) below, was produced by reflection of signals from a transient ultrasonic source. Section 2.A reviews the general theory relating the travel time surfaces and the caustic surfaces. The specific case of a TCC is formulated in section 2.B. Section 3 describes the experimental

set up and technique used to image the travel time surface. Section 4 gives a calculation of the travel time surface of the TCC and compares this to the results of the experiments. Section 4 discussions the different orientations of the travel time surfaces for different reflecting surfaces. Appendix A shows the method used to calculate the travel time surface and location in the exit plane of the rays to the observation plane.

3.2 THEORY REVIEW

A) GENERAL ASPECTS OF TRAVEL TIME SURFACES ASSOCIATED WITH CUSPOID CAUSTICS

Catastrophe theory uses canonical diffraction integrals to describe the diffraction patterns near caustics. The general form of the diffraction integral is[1,2,11]

$$\Psi(C,k) = \int_{-\infty}^{\infty} dx \; b(a,C) \; \exp[\; ik\Phi(a,C)], \qquad (2)$$

where $\Phi(x,C)$ is the distance function associated with a particular catastrophe, $b(a,C)$ is a slowly varying amplitude function, and k is the wave number of the signal $k = 2\pi/\lambda$. The state variables $a = (a_1, a_2, a_3, ...)$ and control parameters $C = (C_1, C_2, ...)$ in Φ are the confined in this paper to be the exit and observation plane coordinates respectively. With the state variables a and control parameters C as defined above the distance function $\Phi(a,C)$ gives the total distance traveled by a signal that propagates from a source to the reflecting surface then to a receiver[7]. The diffraction patterns described by Eq. (2) are often referred to as diffraction catastrophes. When ray theories are used to describe the catastrophes there is a divergent amplitude occurring on the associated caustic of each catastrophe. The caustics are focal envelopes of rays originating on the wavefronts that produce the diffraction catastrophes.

The catastrophes are classified by the number of state variables needed to describe the most singular section of the catastrophe, the corank N; and the number of control parameters needed to describe the caustic, the codimension K. Cuspoid catastrophes are the simplest of the catastrophes as the most singular section of the caustic surface associated with the catastrophe can be described by a single state variable[1]. Thus there is only one state variable necessary to describe a cuspoid catastrophe $\mathbf{a} = (x)$ and the corank of cuspoid catastrophes is N = 1. For cuspoid catastrophes , the distance function of the diffraction integral $\Phi(x,C)$ has the general form[1,9]

$$\Phi(x, C) = \frac{x^{K+2}}{K+2} - C_K \frac{x^K}{K} - C_{K-1} \frac{x^{K-1}}{K-1} - \ldots - C_1 x, \quad K = 0, 1, 2, \ldots , \tag{3}$$

where K is the codimension of the catastrophe. Away from the caustic, the amplitude of the diffraction pattern may be approximated using the stationary phase approximation of Eq. (2). In the stationary phase approximation $\Psi(C,k)$ is proportional to $|H(x,C)|^{-1/2}$ where

$$H(x,C) = \frac{\partial^2 \Phi}{\partial x^2} , \tag{4}$$

and is evaluated at each of the stationary points of $\Phi(x_i,C)$ defined by the ray condition

$$\frac{\partial \Phi}{\partial x}\bigg|_{x_i} = 0, \tag{5}$$

where the x_i are the locations of the rays in the exit plane. The caustic surface of each catastrophe is defined by the singularities of the stationary phase approximation of $\Psi(C,k)$ where $H(x_i,C) = 0$. Figure 4 shows the caustic surfaces in control space of the first three cuspoid catastrophes. The diffraction pattern is exhibited when continuous or very long (many cycle) source signals are used.

When short single cycle signals are used to produce the wavefield, the temporal response of the wavefield can be studied. This adds an extra dimension, time, unavailable in the frequency domain diffraction pattern. The temporal response of the wavefield can be
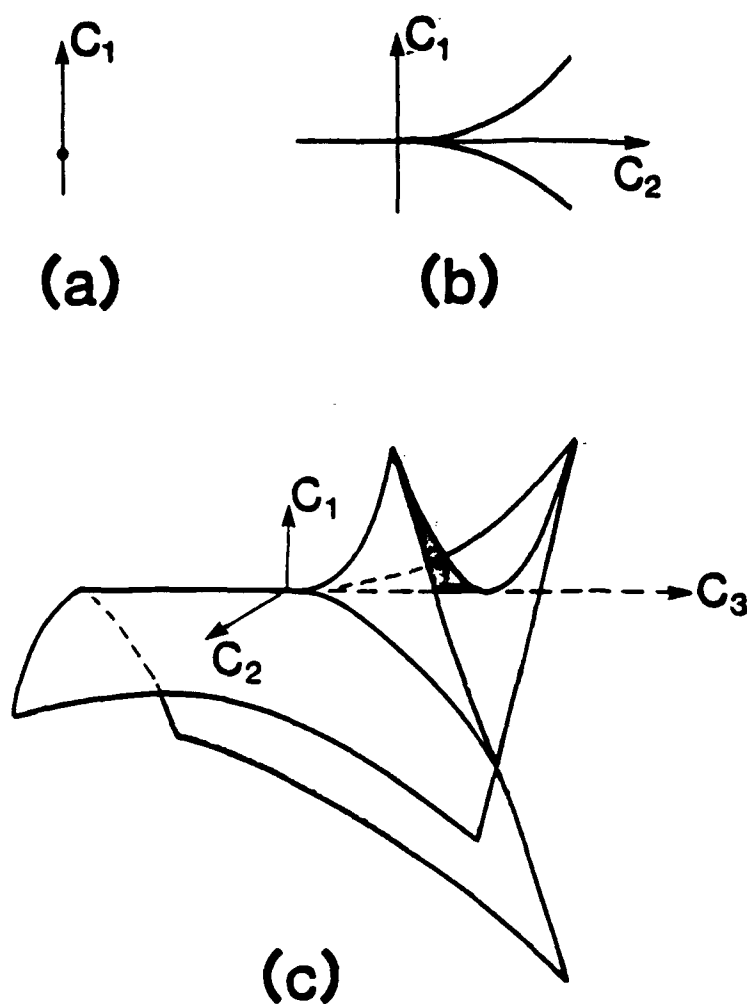
Figure 4) The caustic surfaces of the first three codimension cuspoid caustic (a) fold

caustic K=1 is described by a single control parameter and thus is represented by a point,

(b) the cusp caustic K=2 is described by two control parameters and is given by a curve in

a plane, and (c) the swallow tail caustic K=3 described by three control parameters forming

a surface in three dimensional space. The travel time surface of a cuspoid catastrophe of

codimension K has the same form as the caustic surface of codimension K+1.

found using the ray condition Eq. (5) to locate the rays in the exit plane. The location of the rays in the exit plane can be used in the distance function of the canonical diffraction integral to find the distance along a ray path to a point in the observation plane. The time it takes for a signal from a wavefront that forms a cuspoid caustic to reach the observation plane is

$$t_i = \Phi(x_i, C) / c, \tag{6}$$

where c is the speed of sound in the propagating medium and the x_i are the locations in the exit plane of the ray paths that pass through the observation point given by C.

Equation (6) along with the ray condition Eq. (5) define a parametric equation for the travel time surface associated with the caustic corresponding to $\Phi(x,C)$. Using Eq. (3), the caustic surface of the cuspoid catastrophe of codimension K is defined by the simultaneous solution of the ray condition for a cuspoid caustic

$$\frac{\partial\Phi}{\partial x} = x^{K+1} - C_K x^{K-1} - C_{K-1} x^{K-2} - \dots - C_1 = 0, \tag{7}$$

and Eq. (4)

$$\frac{\partial^2\Phi}{\partial x^2} = (K+1)x^K - C_K x^{K-2} - C_{K-1} x^{K-3} - \dots - C_2 = 0. \tag{8}$$

The travel time surface of the cuspoid caustic of codimension K is defined by the simultaneous solution of the Eq. (6) for a cuspoid caustic

$$\Phi(x,C) - t = \frac{x^{K+2}}{K+2} - C_K\frac{x^K}{K} - C_{K-1}\frac{x^{K-1}}{K-1} - \dots - C_1 x - t = 0, \tag{9}$$

and the ray condition Eq. (7). Comparing Eqs. (7) through (9), the parametric definition of the travel time surface given by Eqs. (7) and (9) has the form of the equations that define the catastrophe surface for the cuspoid of codimension K+1 with t becoming the control parameter C_1 for the travel time surface[7]. The parametric equations given by Eqs. (7) - (9) for the travel time and caustic surfaces of the cuspoid caustic of codimension 2 (the cusp caustic) are given in Table I. The more general scaling relationship between the control

TABLE I. Defining equations for the travel time surface of the cusp caustic (K=2) and the caustic surface of the swallow tail caustic (K=3).

	Travel time surface defining equations for codimension K=2 (cusp caustic)
$\Phi - t = 0$	$\dfrac{\partial \Phi}{\partial x} = \dfrac{x^4}{4} - C_2 \dfrac{x^2}{2} - C_1 x - t = 0$
ray condition	$\dfrac{\partial \Phi}{\partial x} = x^3 - C_3 x - C_2 = 0$
	Caustic surface defining equations for codimension K=3 (swallow tail caustic)
ray condition	$\dfrac{\partial \Phi}{\partial x} = x^4 - C_3 x^2 - C_2 x - C_1 = 0$
Hessian = 0	$\dfrac{\partial^2 \Phi}{\partial x^2} = 4x^3 - 2C_3 x - C_2 = 0$

TABLE II. Relation of the parameters defining the cuspoid catastrophe of codimension K+1 to the parameters defining the travel time surface of the cuspoid catastrophe of codimension K.

codimension K + 1	codimension K
$C_{K+1} K/(K+2)$	C_K
$C_K(K-1)/(K+2)$	C_{K-1}
$\vdots$	$\vdots$
$C_2/(K+2)$	C_1
$C_1/(K+2)$	t
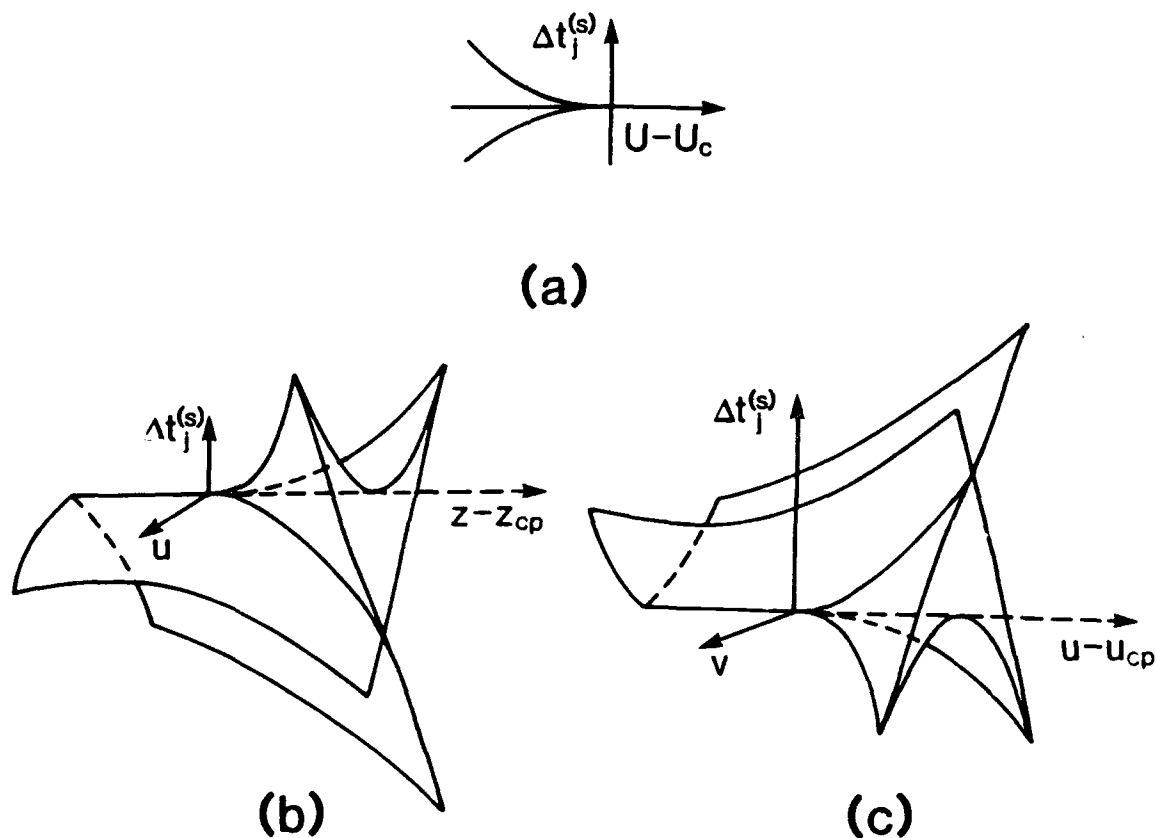
Figure 5) The singular part of the travel time surfaces for the (a) fold caustic, (b) longitudinal cusp caustic (Fig. 1), and (c) the transverse cusp caustic. (a) The travel time surface of the fold caustic ($K = 1$) has two effective control parameters Δt_j and $U - U_c$, where Δt has two values when $U < U_c$ (the caustic has not been crossed). (b) The travel time surface of the longitudinal cusp caustic similar to that shown in Fig. 1 has three control parameters: Δt_j, u (a coordinate transverse to the direction of propagation of the wavefront), and $z - z_{cp}$. When inside the cusp caustic, $z > z_{cp}$, there are three values of Δt for each point (u, z). (c) The travel time surface for a transverse cusp caustic similar to that of the cusp caustic formed by a transverse cut through the surface shown in Fig. 3. There are three effective control parameters Δt_j, v. and $u - u_{cp}$, with three values of Δt_j when inside the caustic $u > u_{cp}$.

parameters of the caustic and the travel time surfaces for a cuspoid caustic of codimension K are given in Table II.

The analysis given above shows that for the cusp catastrophe (K=2) the travel time surface should have the general form of a swallow tail caustic (K=3). Figure 5 shows the travel time surfaces for the fold, K=1, (Fig. 5a) longitudinal cusp, K = 2, (Fig. 5b) and transverse cusp (Fig. 5c) catastrophes. The fold caustic can be described with only one control parameter and appears as a point in Fig. 4. The cusp caustic is defined by two control parameters and the swallow tail requires three control parameters. The travel time surface of the fold catastrophe requires the single control parameter C_1 of the fold caustic and the arrival time of the transient source signal. Thus the travel time surface of the fold catastrophe has two effective control parameters and has the general shape of the cusp caustic, Fig. 5a. Similarly the travel time surface of the cusp catastrophe requires the two control parameters of the cusp caustic, C_1 and C_2, and the arrival time giving three effective control parameters for the travel time surface of the cusp catastrophe, Fig. 5b and 5c. Marston [12] illustrates the above result for the fold caustic.

B) TRAVEL TIME SURFACE OF THE TRANSVERSE CUSP CAUSTIC

The transverse cusp caustic (TCC) is a cusp caustic that opens roughly transverse to the general direction of propagation of the wavefront producing the caustic. Unlike the wavefront that produces the axial or longitudinal cusp associated with the cylindrical aberration [3], the TCC wavefront is curved in two directions [5]. The general shape of the wavefront that produces a TCC is given in the exit plane by

$$W(x,y) = - (a_1x^2 + a_2xy^2 + a_3y^2 + a_4x + a_5y), \qquad (10)$$

where the last three terms only affect the location of the cusp in the observation plane. This wavefront can be produced by the reflection of the signal produced by a point source of sound, from a surface with the general shape[13,14]

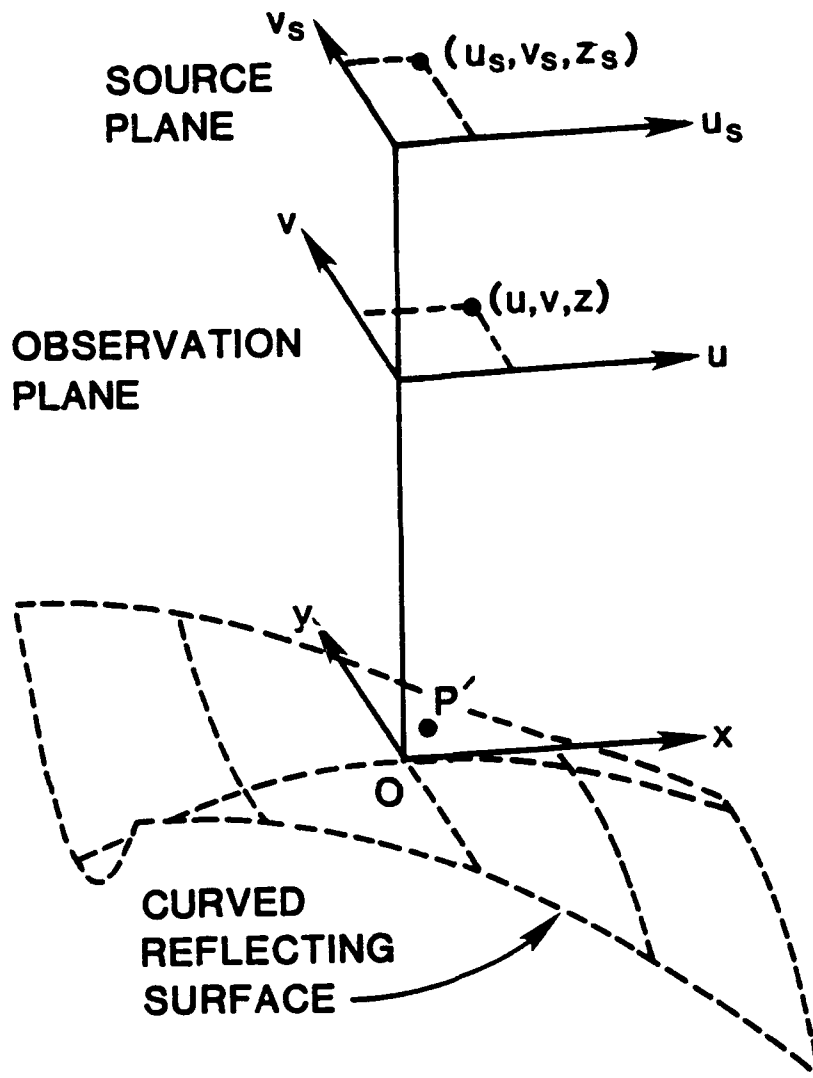Figure 6) Geometry for the reflection of the signal produced by a point source of sound

from a curved surface to produce the wavefront that propagates to form a transverse cusp

caustic. The distance function Φ for the propagation of the source signal from the point

(u_s,v_s,z_s) in the source plane to the P' on the reflecting surface and then to the point (u,v,z)

in the observation plane is given paraxially by Eq. (15).

$$h(x,y) = h_1x^2 + h_2xy^2 + h_3y^2 + h_4x + h_5y, \tag{11}$$

where the linear terms produce linear terms in the scattered wavefront and may be set to zero by a proper choice of origin. The wavefront defined in Eq. (10) produces a cusp caustic in an observation plane transverse to the direction of propagation defined by

$$D_T(U_e - U_{ec})^3 = V_e^2, \tag{12}$$

where U_e, V_e, U_{ec}, and D_T are defined below in terms of the source, and receiver coordinates and the surface parameters h_i. Figure 6 shows the geometry for the reflection of the spherical source signal from the curved surface.

The propagation integral that gives the scattered field in a distant observation plane can be approximated paraxially by[5,13]

$$p(u,v) \approx \frac{kq\xi}{2\pi i r r_s} e^{ik(r + r_s)} \int_{-\infty}^{\infty} \int_{-\infty}^{\infty} e^{-ik\phi(U_e,V_e,x,y)} \, dx \, dy, \tag{13}$$

where q is the strength of the source, r and r_s are the distances from the origin in the exit plane to the observation point (u,v) and the source point (u_s,v_s), ξ is the reflection coefficient of the surface, and k is the wavenumber of the wavefront $\left(k = 2\pi/\lambda = \omega/c\right)$. The paraxial reduced distance function ϕ is given by

$$\phi(U_e,V_e,x,y) = b_1'x^2 + a_2'xy^2 + b_3'y^2 + U_ex + V_ey, \tag{14}$$

where $b_i' = -2h_i + 1/2z_e$, $a_2' = -2h_2$, $U_e = u/z + u_s/z_s$, $V_e = v/z + v_s/z_s$, and $z_e = \left(1/z + 1/z_s\right)^{-1}$. The coordinates (u, v, z) and (u_s, v_s, z_s) give the location of the source and receiver. The complete distance function of the TCC is

$$\Phi(x,y;U_e,V_e) = \phi_0(U_e, V_e) + \phi(x, y, U_e, V_e), \tag{15}$$

where $\phi_0 = r + r_s$ is a slowly varying function of the source and receiver positions and does not depend on the exit plane coordinates x and y, thus it may be pulled out of the diffraction integral Eq. (13). Using Eq. (14), Eq. (13) can be evaluated to give the pressure in an observation plane as

$$p(u,v) \approx \frac{k^{\frac{1}{4}} q\xi}{irr_s\left(2\pi|b'_1|^{1/2}\,|a'_2|^{1/2}\right)^{1/2}} \exp\left(ik(r+r_s) - (\pm\frac{i\pi}{4}) - \frac{ikU_e^2}{4b'_1}\right) P_{\pm}(w_2,w_1), \qquad (16)$$

where the upper (lower) sign is used when $b'_1 < 0$ ($b'_1 > 0$)[5,13]. In a distant observation plane the diffraction catastrophe associated with the TCC is proportional to the Pearcey function [3] $P(w_2,w_1)$

$$P_{\pm}(w_2,w_1) = \int_{-\infty}^{\infty} \exp[\pm i\Phi_p(s,w1,w2)]\,ds \cdot \int_{-\infty}^{\infty} \exp[\pm i(\frac{s^4}{4} + w_2\frac{s^2}{2} + w_1 s)]\,ds. \qquad (17)$$

The control parameters w_2 and w_1 are related to the observation plane coordinates by

$$w_2 = \left(\frac{k}{|b'_1|}\right)^{\frac{1}{2}} (U_e - U_{ec})\,\mathrm{sgn}(a'_2), \qquad (18a)$$

$$w_1 = \left(k^2\,|b'_1|\right)^{\frac{1}{4}} \left(\frac{2}{|a'_2|}\right)^{\frac{1}{2}} V_e\,\mathrm{sgn}(b'_1), \qquad (18b)$$

where $U_{ec} = u_c/z + u_s/z_s = -2b'_1 b'_3/a'_2$, u_c is the horizontal location of the cusp point, and $k = 2\pi/\lambda$ is the wave number of the source signal.

The distance function of the diffraction integral of the TCC contains two variables x and y, however the integral can be evaluated to give the TCC diffraction catastrophe in terms of the Pearcey function which has only one state variable. The evaluation of the TCC diffraction integral amounts to a smooth coordinate transformation to the Pearcey function[13]. Note the phase of the Pearcey function in Eq. (17) has the form

$$\Phi(s,C) = \frac{s^{K+2}}{K+2} - C_2\frac{s^K}{K} - C_1 s, \qquad (19)$$

where $K = 2$ and for the TCC $C_1 = -w_1$ and $C_2 = -w_2$, thus the Pearcey function is in the general form of the cusp catastrophe diffraction integral. The diffraction pattern and associated caustic of the TCC have the same general form as the diffraction pattern and associated caustic of the cuspoid caustic of codimension $K = 2$ (the longitudinal cusp caustic). The merging and disappearance of the rays of the the $K = 2$ cuspoid caustic in a

longitudinal observation plane are described by a travel time surface with the general shape of the cuspoid caustic of codimension K = 3. A TCC will have rays merging and disappearing on a cusp caustic similar to the longitudinal cusp caustic except in a transverse plane. Thus the transverse travel time surface should have the same general shape in a transverse observation plane as the longitudinal travel time surface in a longitudinal observation plane, the swallow tail caustic surface Fig. 4c.

To calculate the travel time surface of the TCC, the ray condition for the reduced distance function of the diffraction integral $\phi(x,y;U_e,V_e)$ can be used. The location in the exit plane of the rays from the wavefront is given by the ray conditions for the two dimensional TCC diffraction integral

$$\frac{\partial \phi}{\partial x}\Big|_{(x_i,y_i)} = 0 ; \quad \frac{\partial \phi}{\partial y}\Big|_{(x_i,y_i)} = 0, \tag{20a,b}$$

where the location of the ray in the exit plane is (x_i,y_i). When the observation point is inside the cusp curve there will be three real ray locations in the exit plane. When the observation point is on the curve two of the rays will have merged, and outside the cusp curve there is only one real ray from the wavefront. Equations (20a,b) and Eq. (14) give the locations of rays in the exit plane as the simultaneous solutions of

$$\frac{\partial \phi}{\partial x}\Big|_{(x_i,y_i)} = 2b_1'x_i + a_2'y_i^2 - U_e = 0 \tag{21a}$$

$$\frac{\partial \phi}{\partial y}\Big|_{(x_i,y_i)} = 2y_i (a_2'x_i + b_3') - V_e = 0. \tag{21b}$$

The solution of Eq. (21a) for x_i can be used in Eq. (21b) to give a cubic equation in y_i

$$y_i^3 - \frac{y_i}{a_2'} \left(U_e - U_{ec}\right) + \frac{b_1'}{a_2'^2} V_e = 0. \tag{22}$$

The solution shown in Appendix A, of Eq. (22) for y_i and then Eq. (21a) for x_i gives the location in the exit plane of the ray or rays to the point in the observation plane given by U_c and V_e. The total distance traveled along a ray path that passes through a point in the

Figure 7) The calculated travel time surface of the transverse cusp caustic. (a) The slowly varying contribution of the form ϕ_0/c in Eq. (25). (b) The term due to the reduced distance function of the diffraction integral ϕ,Eq. (14). This contribution has the general shape of the travel time surface of the transverse cusp shown in Fig. 5c. (c) The sum of the two contributions shown in a and b giving the complete travel time surface of the transverse cusp caustic.
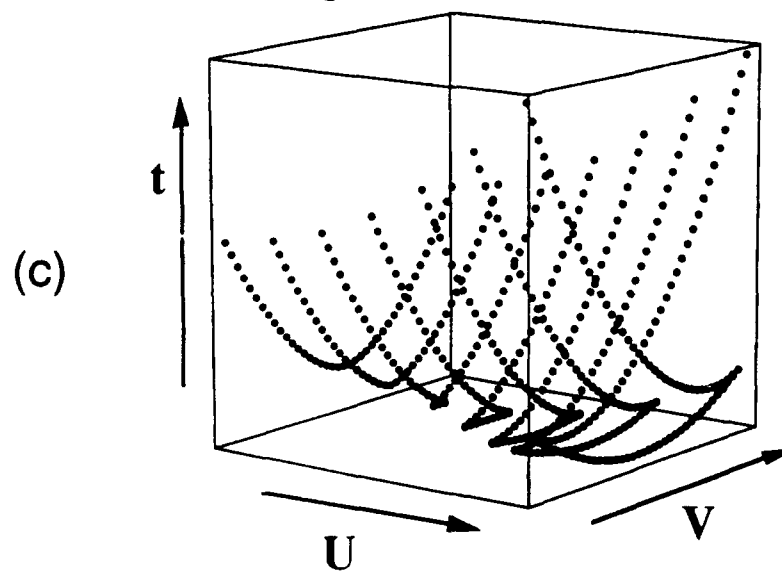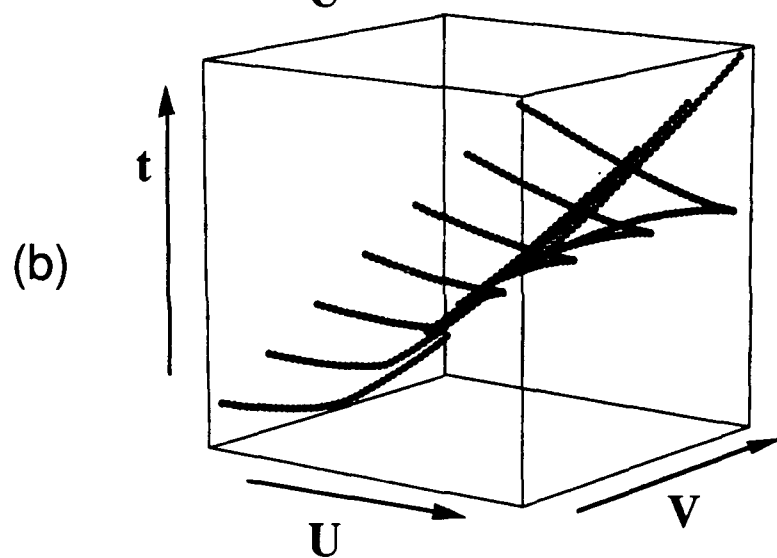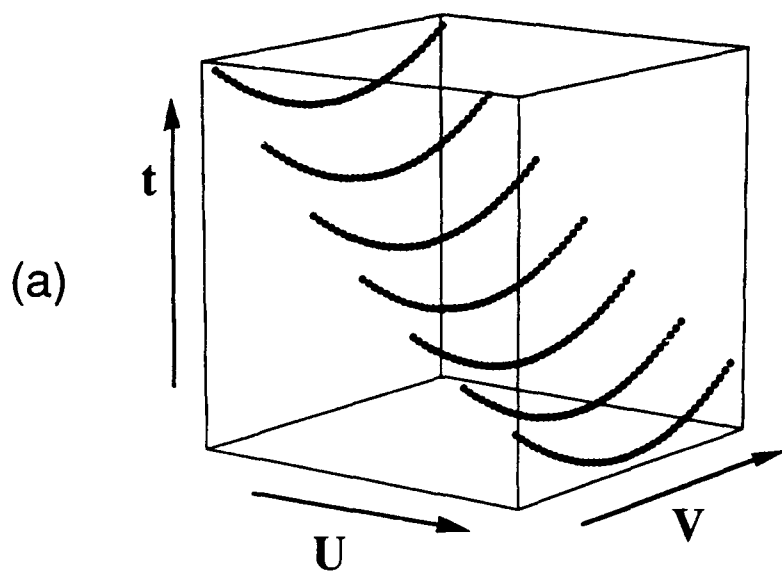
observation plane is given by the complete distance function $\Phi(x,y;U_e,V_e)$, the distance from the source to the reflecting surface plus the distance from the reflecting surface to the observation plane. In Fig. 6 this distance is the distance from (u_s,v_s,z_s) to P' on the surface plus the distance from P' to (u,v,z) in the observation plane.

The paraxial distance function for reflecting from the curved surface that forms a TCC is given by Eq. (15). For a uniform medium with a constant sound speed c, the travel time surface of the TCC is given by

$$\Delta t_i = \frac{\Phi(x_i,y_i;U_e,V_e)}{c} , \qquad (23)$$

where (x_i,y_i) is the location in the exit plane of the ray paths that pass through (U_e,V_e). For observation points in the observation plane inside the cusp curve there will be three real values of Δt_i. On the cusp curve there will be two real values of Δt_i, one associated with the two ray paths that have merged to come from the same point on the wavefront. Outside the cusp curve there will only be one real value of Δt_i. The arrival time surface given by Eqs. (15) and (23) can be written in two parts, one a slowly varying portion ϕ_0 that does not describe the merging of the rays on the caustic and the other depending on the reduced distance function ϕ of the wavefront in the exit plane which will describe the swallow tail characteristics of the travel time surface due to the of merging rays on the caustic. Thus Δt_i may be written

$$\Delta t_i = \frac{\phi_0(U_e,V_e)}{c} + \frac{\phi_c(x_i,y_i;U_e,V_e)}{c} , \qquad (24)$$

$$\phi_0(U_e,V_e) = r + r_s = \sqrt{z^2 + v^2 + u^2} + \sqrt{z_s^2 + v_s^2 + u_s^2} . \qquad (25)$$

Equation (25) gives the paraxial approximation to the travel time surface due to the reflection of the spherical point source from the origin in the exit plane. The reduced distance function $\phi(x,y;U_e,V_e)$ describes the contribution to the travel time surface due to the shape of the reflecting surface.

Figure 7a shows a calculation of ϕ_0/c, using the parameters given below, that gives

the dependence of the travel time surface on the distance from the source point to the

reflecting surface plus the distance from the reflecting surface to points in the observation

plane. This carries no information about the surface other then the distance of the source

and receiver points from the surface. Characteristics of the travel time surface due to the

shape of the reflecting surface are shown in Fig. 7b. The travel time surface shown in Fig.

7b, calculated using ϕ/c and the parameters given below, has the general form of the

singular surface of the swallow tail catastrophe shown in Fig. 4c with $C_1 \leftrightarrow t$, $C_2 \leftrightarrow V_e$,

and $C_3 \leftrightarrow (U_e - U_{ec})$. The complete travel time surface is shown in Fig. 7c; this is the

combined contributions shown in Figs. 7a and 6b, $\Phi/c = \phi_0/c + \phi/c = t$. The interesting

features of the complete travel time surface (Φ/c) are the swallow tail features describing the

merging of rays on the caustic. Figures 7a-c show travel time surface contributions ϕ_0/c,

ϕ/c, and the travel time surface Φ/c calculated using Eqs. (21)-(23). The values of the

parameters used in the calculations were $b_1' = 0.0118$ cm^{-1}, $a_2' = 0.00236$ cm^{-2}, $b_3' =$

0.0491 cm^{-1}, $z = 68$ cm, $z_s = 170$ cm, $u_s = -15.0$ cm, $v_s = 0$, and the horizontal positions

relative to the cusp point of the cusp curve for each cut through the travel time surface

shown are $U_e - U_{ec} = (u - u_c)/z = -0.0397, 0.0, 0.0397, 0.0794, 0.1191, 0.1588,$

0.1985. These values correspond to experimental values for the experimental data to be

discussed later.

The distance function $\Phi(x,y;U_e,V_e)$ depends on $U_e = u/z + u_s/z_s$ and $V_e = v/z +$

v_s/z_s which are symmetric in the source and receiver coordinates, thus the travel time

surface can be mapped by scanning the source and holding the receiver fixed. Figure 7c

could have been calculated using a fixed value of u and v in the observation plane and

incremental values of u_s and v_s in the source plane. The measured travel time surface due

to the reflection of a point source by a surface curved into a shape locally described by Eq.

(11) should exhibit the same general shape as Fig. 7c when either the receiver or the source

is scanned while the other is held fixed.

3.3 AN EXPERIMENT TO MAP THE TRAVEL TIME SURFACE OF THE TRANSVERSE CUSP CAUSTIC

Experiments were performed to map the travel time surface of the wavefield generated by reflecting a high frequency single cycle burst from a curved metal surface in water. The local shape of the metal surface was given by

$$h_m(x,y) = m_1 x^2 + m_2 xy^2 + m_3 y^2 + m_4 x + m_5 y, \qquad (26)$$

comparing Eq. (26) to Eq. (11) the metal surface had the proper local shape to produce a TCC when it scattered the signal from a point source. A measurement of the surface height $h_m(x,y)$ was made and fit to Eq. (26) giving the parameters m_i of the reflecting surface shown in Table III. Fig. 8 shows a plot of the surface shape calculated using the values of the surface parameters in Table III.

The acoustical source and receiver were 0.25 in diameter non-focused transducers with a 10 MHz resonance frequency manufactured by Sonic Instruments Incorporated (Sonic Instruments Inc. transducer type CBA 10-1). One transducer was placed in a source plane approximately 170 cm from the reflecting surface. The pulsed source was assumed to approximate a point source and the source distance was the distance to the reflecting surface from the source transducer. The receiving transducer was mounted on the uv positioner shown in Fig. 9 about 68 cm from the surface. The receiving transducer could be positioned at different points in the observation plane to map the travel time surface. In order to map the travel time surface, 20.48 μs time traces of the reflected signal were recorded on a Data Precision Data 6000® (DATA 6000) along vertical cuts through the observation plane at seven different horizontal positions relative to the cusp curve. Figure 10 shows how the cuts were positioned relative to the cusp curve. Vertical time traces were 5.4 mm apart while there were 27 mm between the horizontal cuts. Time traces

TABLE III. The measured surface parameters for the metal reflecting surface.

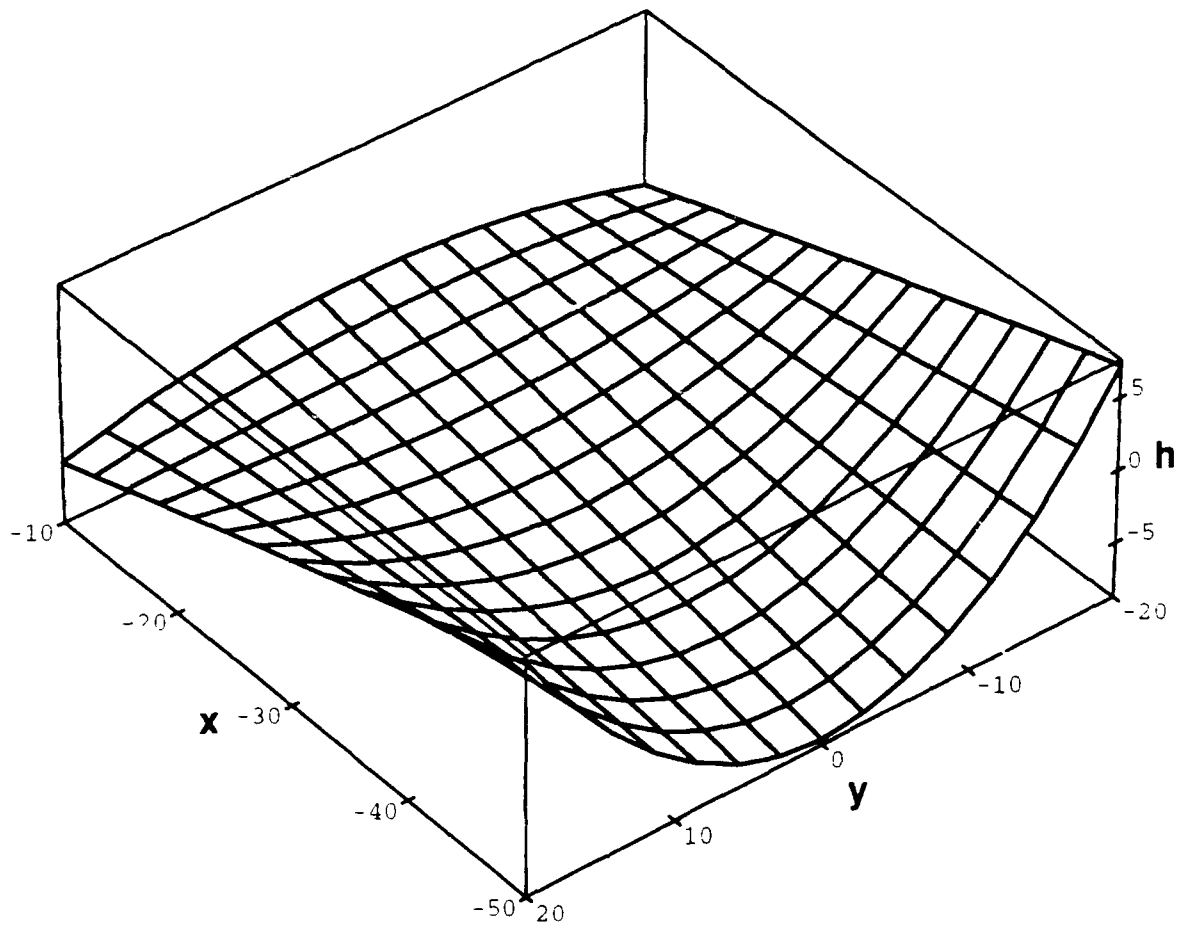| m_i	measured value
m_1	-0.000310 cm^{-1}
m_2	-0.00117 cm^{-2}
m_3	-0.0194 cm^{-1}
m_4	0.154
m_5	-0.00301

Figure 8) A plot of the reflecting surface used in the travel time experiments calculated using the surface parameters given in Table III. The wavefront given in Eq. (10) has the same general shape.
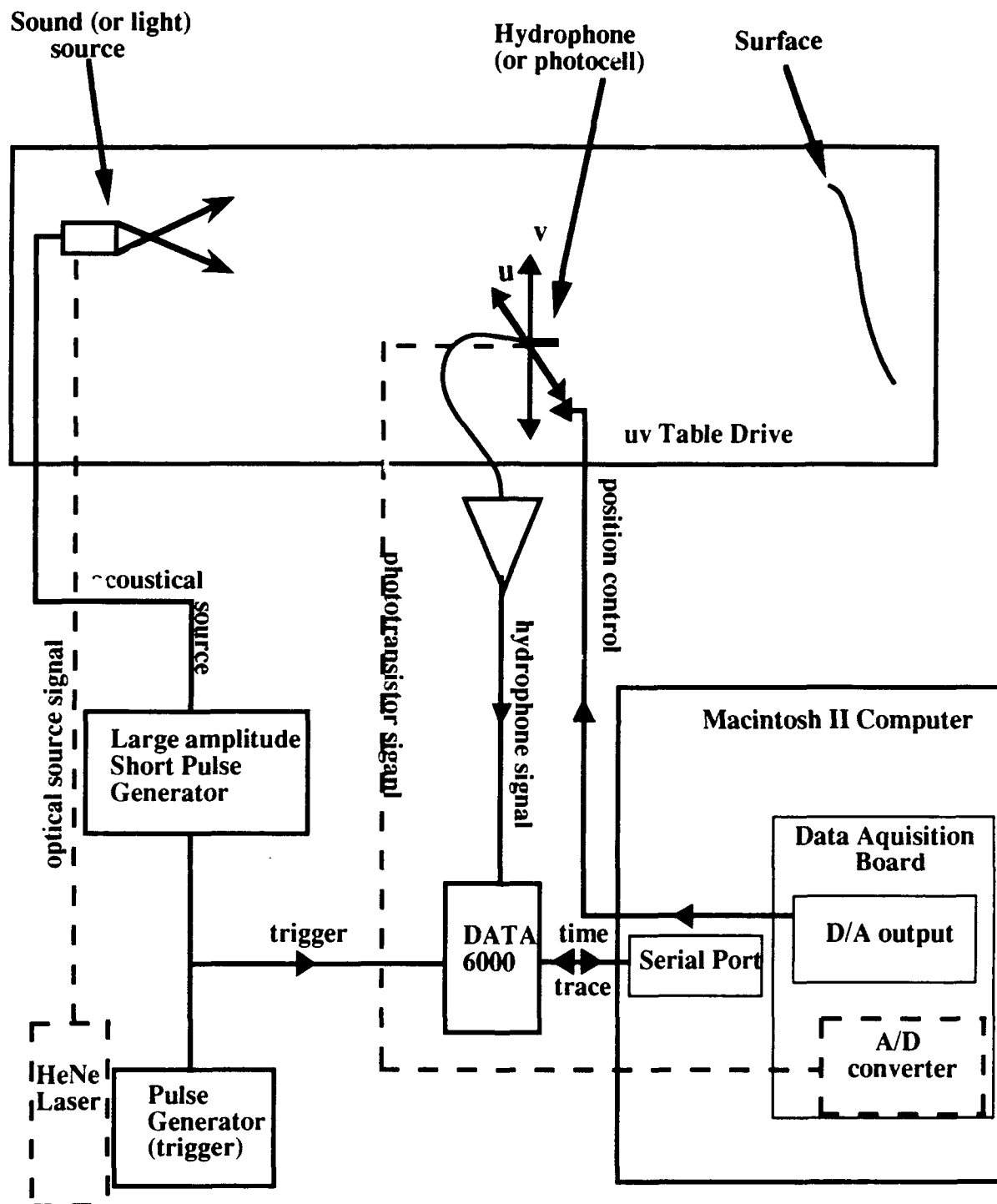
Figure 9) Schematic diagram of the travel time experiment. Both the optical and acoustical

experiments are diagramed with the optical experiment shown in dashed lines.

were recorded along each of the cuts and transferred to a Macintosh II computer where they were displayed in a waterfall format to show the corresponding cuts through the travel time surface. Figure 11 shows a scan well inside the of the caustic, the vertical position of the receiver corresponds to the vertical position of each time trace in the Fig. 11 while the horizontal axis represents increasing time to the right.

The source for the pulses used in the experiment was a Smith Kline Instruments (SKI) medical ultrasound driver modified to allow it to be triggered at a slow rep-rate. The SKI driver provided a unipolar pulse of approximately ~ 70 V in amplitude with a rise time on the order of nanoseconds and an approximately 3 μs exponential tail. This short spike produced an approximately 1MHz single cycle pulse from the source transducer in the far field. The bipolar shape of the source pulse was due to the direct signal from the transducer face and the inverted signal from an effective ring source lying around the transducer perimeter15. A representative source pulse, measured by rotating the receiver transducer so that it pointed at the source transducer approximately 1 m away, is shown in Fig. 12. Note that there was little ringing in the source transducer signal, the bipolar shape is due to the diffraction effects discussed above. A sharp source signal was necessary to allow the resolution of the different arrival times in the observation plane.

Equations (16) and (23) depend on the source and receiver coordinates in the same manner through U_e and V_e. U_e and V_e are symmetric in the source and receiver coordinates $U_e = u/z + u_s/z_s$ and $V_e = v/z + v_s/z_s$, thus it should be possible to image either the diffraction catastrophe or the travel time surface by scanning the source transducer while holding the receiver fixed. The source and receiver transducers were symmetric for the travel time surface experiments, in that both source and receiver were the same type of transducer. This allowed for switching the source and receiver transducers in order to map the travel time surface by scanning the source transducer and holding the receiving transducer fixed. The source-receiver switch was done by connecting the transducer on the uv positioner (the old receiver) to the SKI driver and the fixed transducer, at the back of the
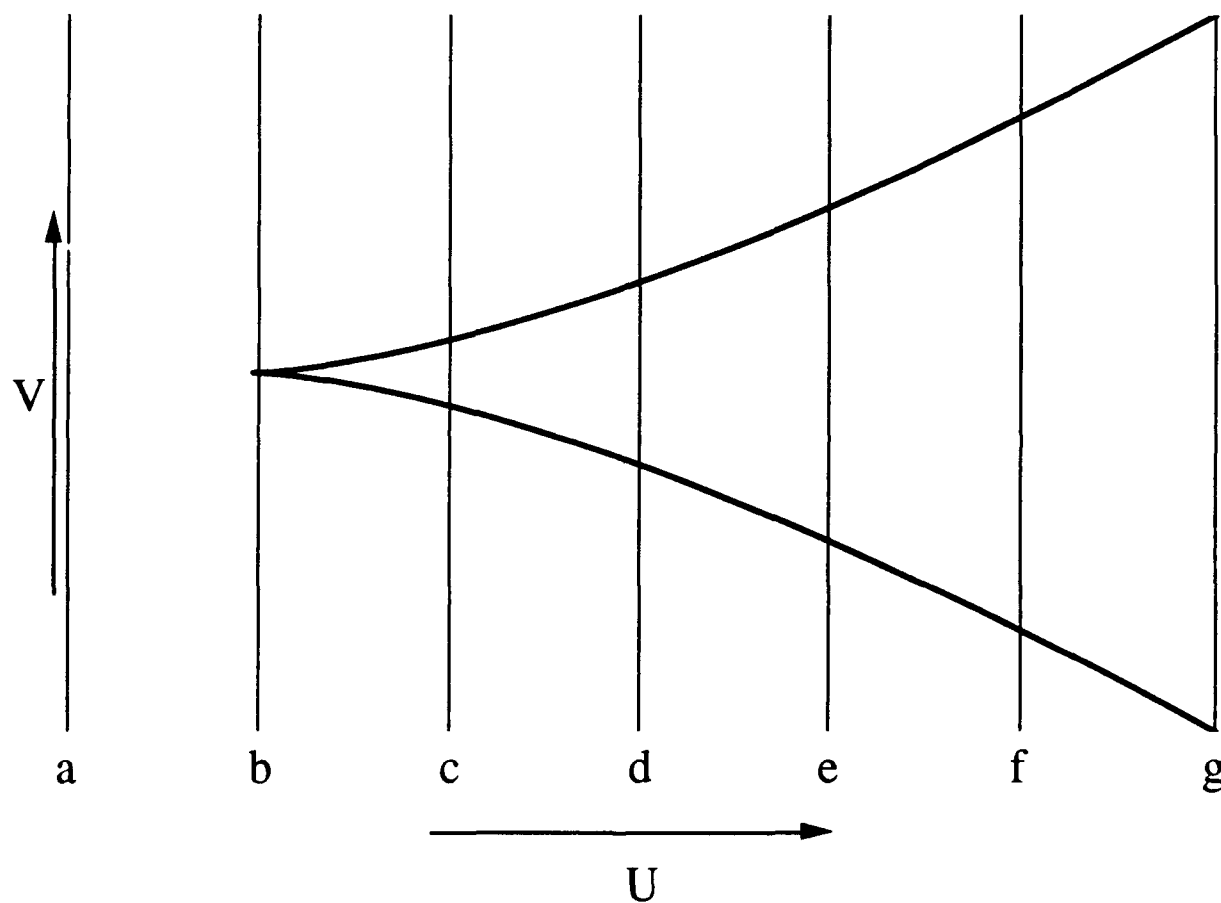
Figure 10) Location of the travel time cuts relative to the cusp curve in the observation plane. The time traces were taken along the vertical cuts at horizontal positions relative to the cusp point given the horizontal positions marked a-g.
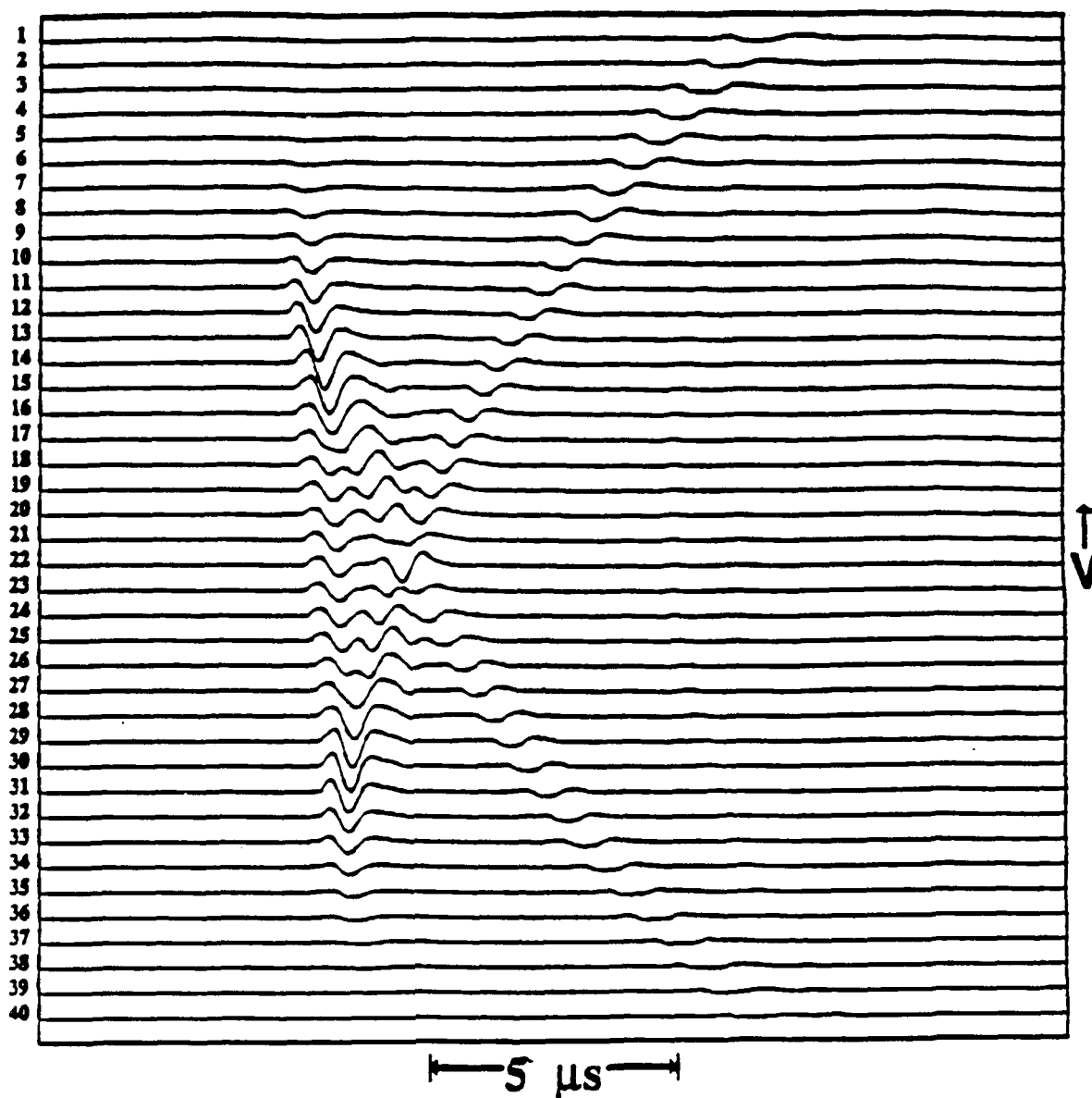
Figure 11) A representative travel time cut well inside the caustic. The cut displays arrival times for the signals froi ` the wavefront that form a travel time curve similar to the one shown in Fig. 2.

Source signal for travel time experiments
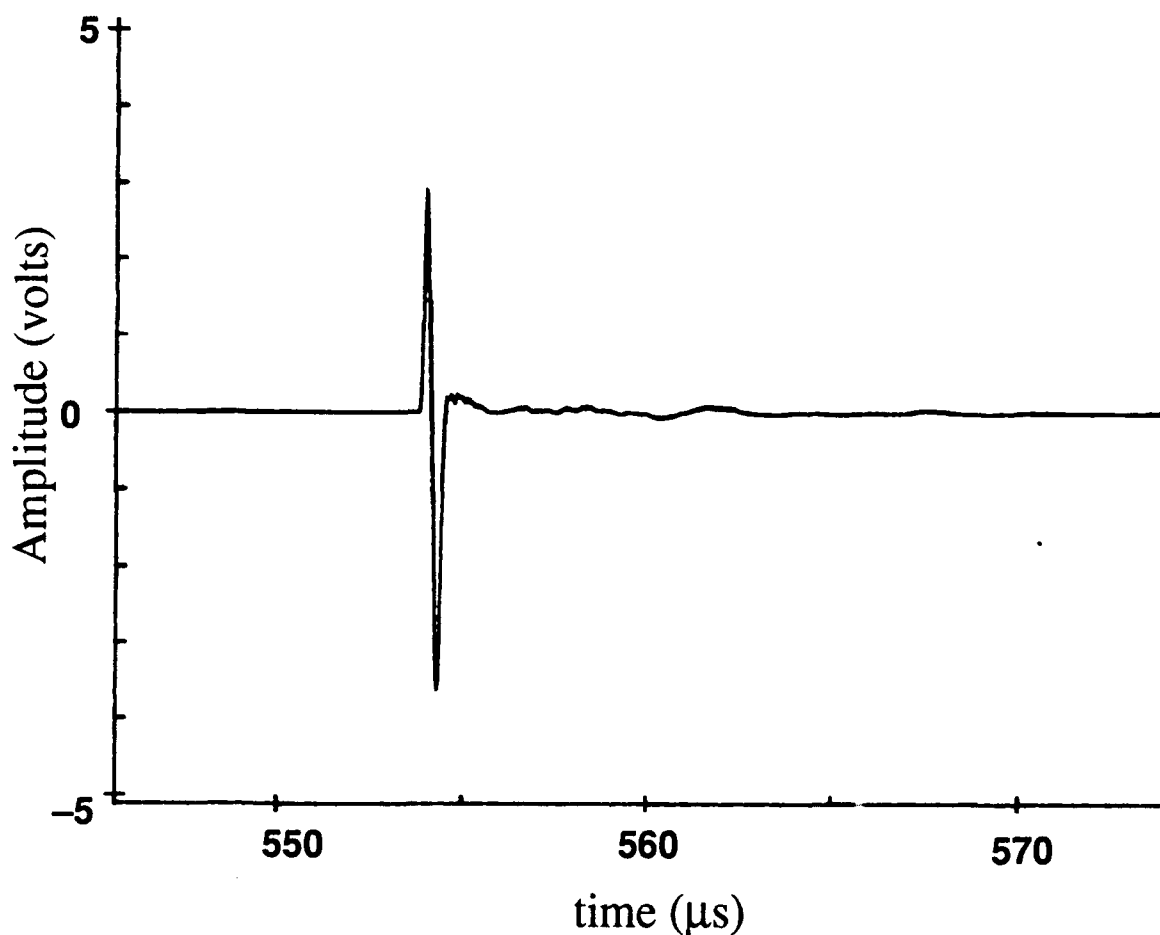
Figure 12) The receiving transducer was pointed directly at the source transducer with a separation of approximately 1m to collect a time trace of the source pulse. The shape of the source pulse used in the time traces was bipolar due the a contribution form the planar face of the transducer and an effective ring source lying on the perimeter of the transducer. The source transducer used was a heavily damped transducer thus the high amplitude spike used to drive the transducer produced very little ringing allowing for a high resolution of the reflected signals.

tank (the old source), to the DATA 6000. With this set up the source transducer could be scanned while the receiving transducer was held fixed. The travel time surface mapped with this set up was displayed in the same manner as described above.

Gray scale pictures of the optical cusp curve were used as a reference for the acoustical time traces. A small diameter (200 µm core diameter) optical fiber attached to a HeNe laser ($\lambda \approx 430$ nm in water) was the optical source. In Fig. 9 the optical schematic is shown by the dashed lines. The short wavelength of the optical source did not allow for the resolution of the diffraction pattern. However, because of the short wavelength, there was a sharp transition from the bright three ray region inside the cusp curve to the dark one ray region outside the cusp curve. The location of the optical source and receiver in the optical experiments was approximately the same as the location of the acoustical source and receiver in the acoustical experiments. Thus the cusp curve imaged in the optical experiments is the cusp curve associated with the acoustical travel time surface. This provides a good picture of the cusp curve in the observation plane that can be used as a reference for the location of the acoustical time traces.

A phototransitor mounted on the uv positioner was used to acquire a raster scan of the optical wavefield in the observation plane. The signal from the phototransitor, which is proportional to the intensity of light at that point, was associated with the gray scale of a pixel on a Macintosh II computer screen. Each pixel on the computer screen corresponded to a position in the raster scan of the observation plane, thus a picture of the cusp curve in the observation plane could be produced. Positions in the observation plane at which the acoustical time traces were taken corresponded to pixels in the optical raster picture. These pixels were marked along the bottom and left sides of the optical picture forming a grid of points where the acoustical time traces were taken. Figure 13 shows an optical gray scale picture that corresponds to an acoustical data set. The squares along the left side of Fig. 13 mark the vertical position of each time trace, while the squares along the bottom mark the horizontal position of each vertical cut through the travel time surface.
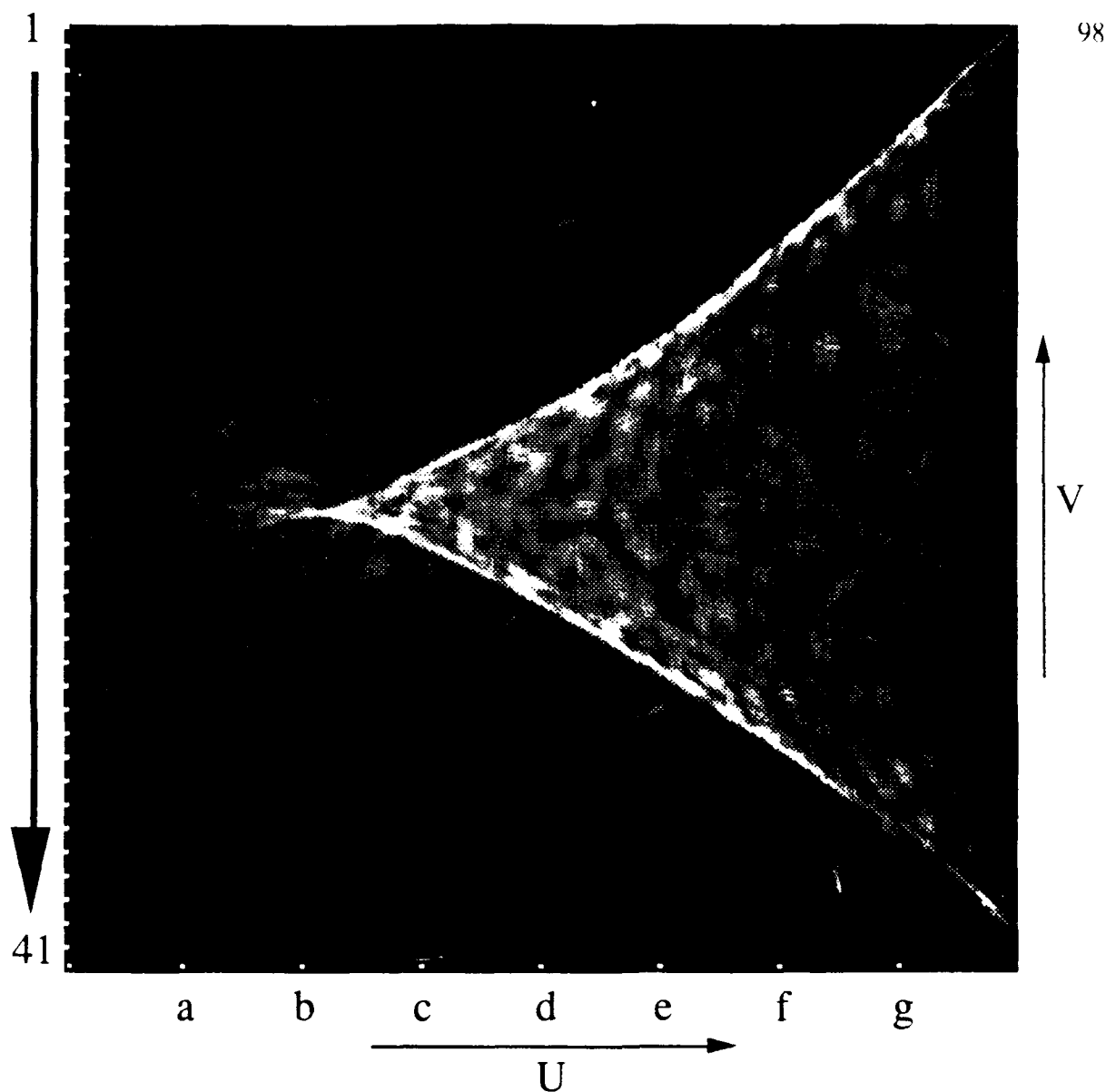
Figure 13) Optical raster picture used as a reference for the location of the travel time cuts shown in Figs. 16 and 17. The small squares on the left side of the picture show the vertical location of each of the time traces along each horizontal cut. The small squares along the bottom of the picture labeled a-g show the horizontal location of each of the cuts. Relative to the horizontal position of the cusp point the horizontal positions are $u - u_c = -27mm$, 0.0, 27mm, 54mm, 81mm, 108mm, 135mm , the vertical positions relative to the vertical position of the cusp point are $v - v_c = -108mm$ to 108mm by 5.4mm steps.

3.4 RESULTS: THE CALCULATED TRAVEL TIME CURVES AND TRAVEL TIME SURFACES IMAGED BY REFLECTING SOUND FROM A CURVED METAL SURFACE IN WATER

A) CALCULATED TRAVEL TIME CURVES FOR THE TRANSVERSE CUSP CAUSTIC

Figures 14a-g show cuts through the travel time surface (Φ/c) calculated at horizontal positions relative to the cusp point ($U_e - U_{ec}$) of the cusp curve corresponding to positions a-g in Fig. 13. Each figure consists of the calculated arrival times associated with the real rays originating on the wavefront and passing through a given point in the observation plane (u,v). There are 41 vertical positions v in each cut with position 21 being on the symmetry axis of the cusp curve. The horizontal axis of each figure represents increasing time going to the right and is 20.48 μs long. Relative to the cusp point of the cusp curve, the horizontal location of the cut in 13a is outside the cusp curve, 13b is on the cusp point, and 13c-g are inside the cusp curve. The relative horizontal positions of each calculation from a-g are $U_e - U_{ec} = (u - u_c)/z = -0.0397, 0.0, 0.0397,$ 0.0794, 0.1191, 0.1588, 0.1985. Figures 15a-g show the reduced travel time surface due to $\phi(x,y;U_e,V_e)$. The travel time surface cuts in Figs. 14a-g are a superposition of the cuts in Figs. 15a-g (ϕ/c) and ϕ_0/c of Eq. (24). Figure 14 should represent the actual measured travel time surface while in Fig. 15 the slowly varying background function ϕ_0/c has been subtracted off to more clearly show the swallow tail properties of the travel time surface of the TCC.

In Figs. 14a and 14a there is only one arrival at each of the vertical positions and the curve is smooth through the center time trace. Figures 14b and 15b also only have one arrival at each vertical position, however at the cusp point the travel time curve is less smooth as seen at the origin in Fig. 4c. At the cusp point, represented by the twenty first vertical position in Figs. 14b and 14b, all three rays from the wavefront have merged to

Figure 14) Calculated travel time cuts of the transverse cusp caustic using the total distance function $t = \Phi/c = \phi/c + \phi_0/c$ [Eq. (24)]. The horizontal positions correspond to the positions labeled a-g in Fig. 13. Cut (a) is the smooth travel time curve outside the cusp curve. The horizontal position of cut (b) is on the cusp point and the cusp curve is slightly pointed. Cuts (c)-(g) are inside the cusp curve and show the increasing width of the tail as the effective horizontal positions of the cuts move further inside the caustic.

(a)

(b)

(c)

(d)

103
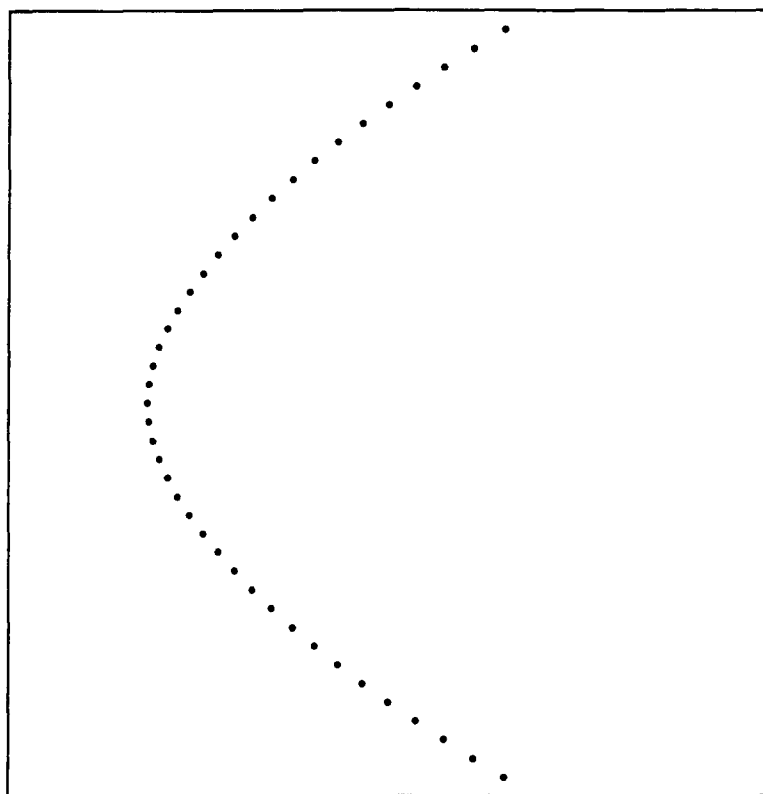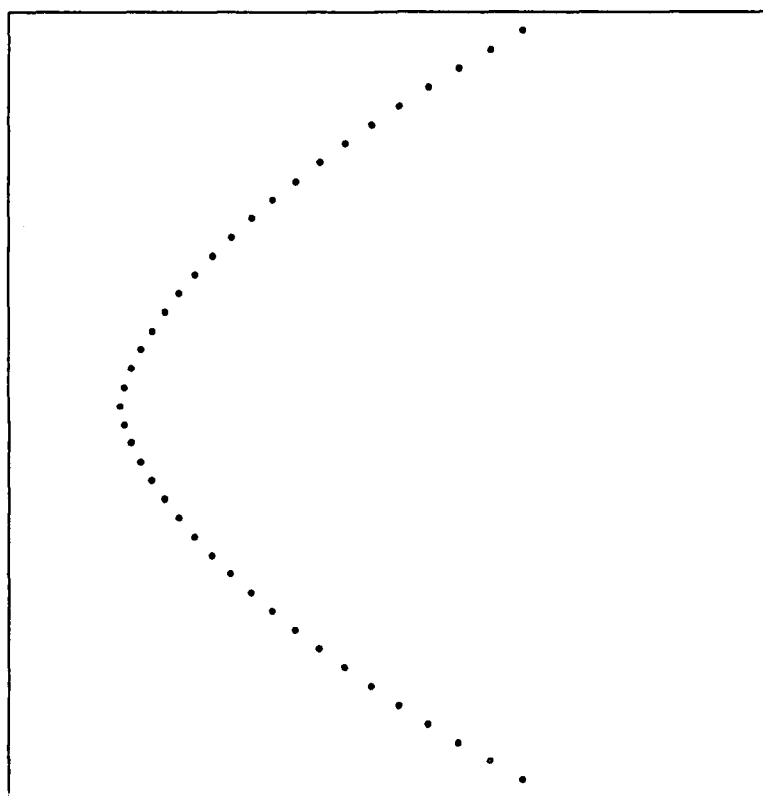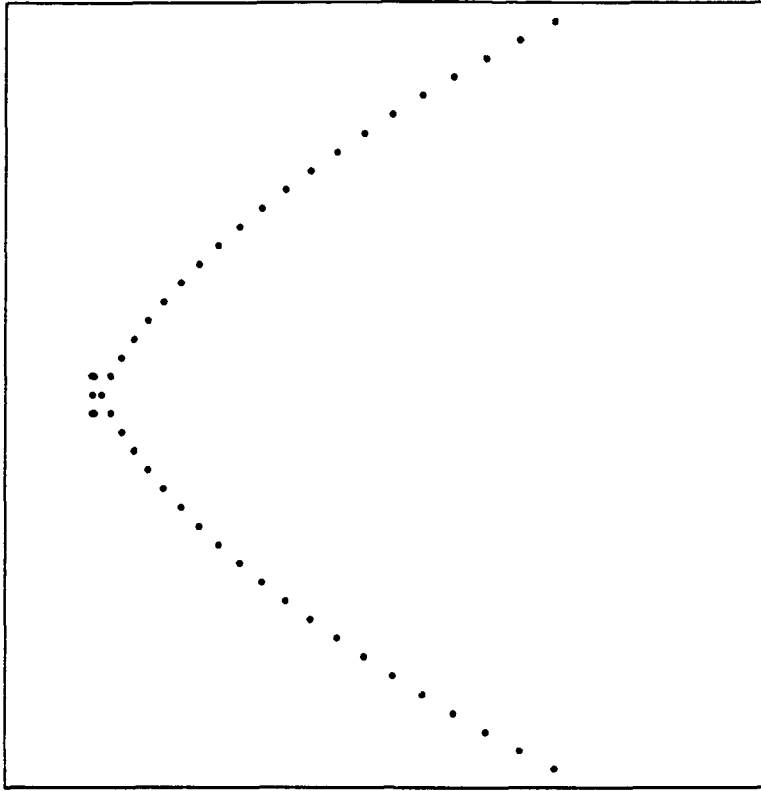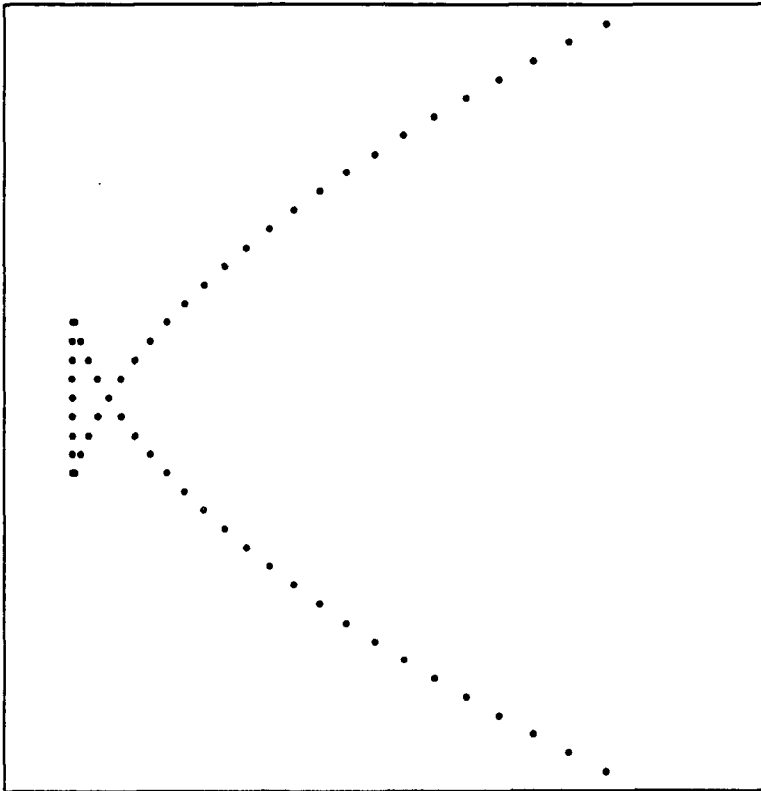
(e)
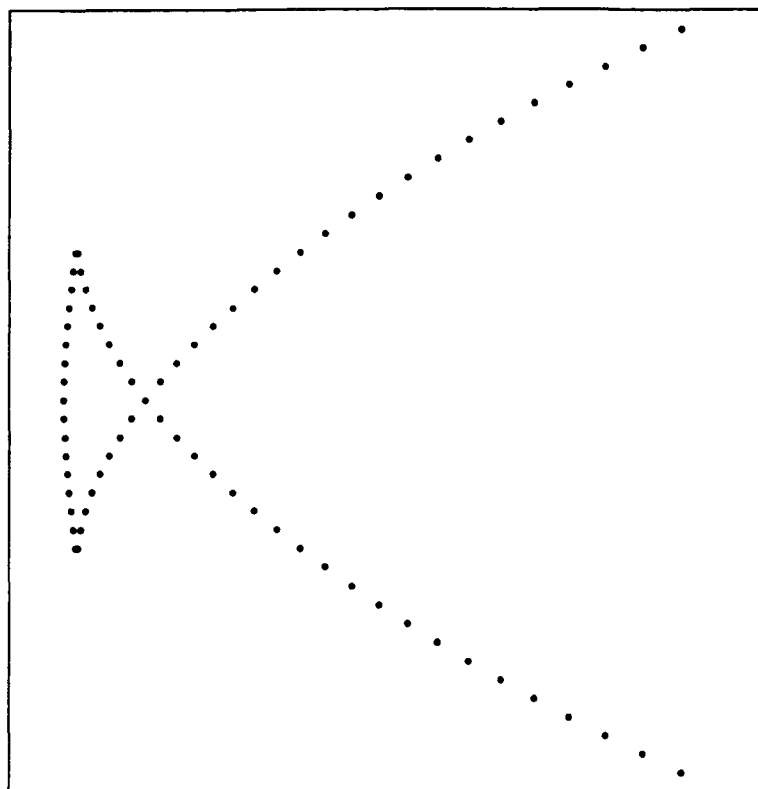
(f)
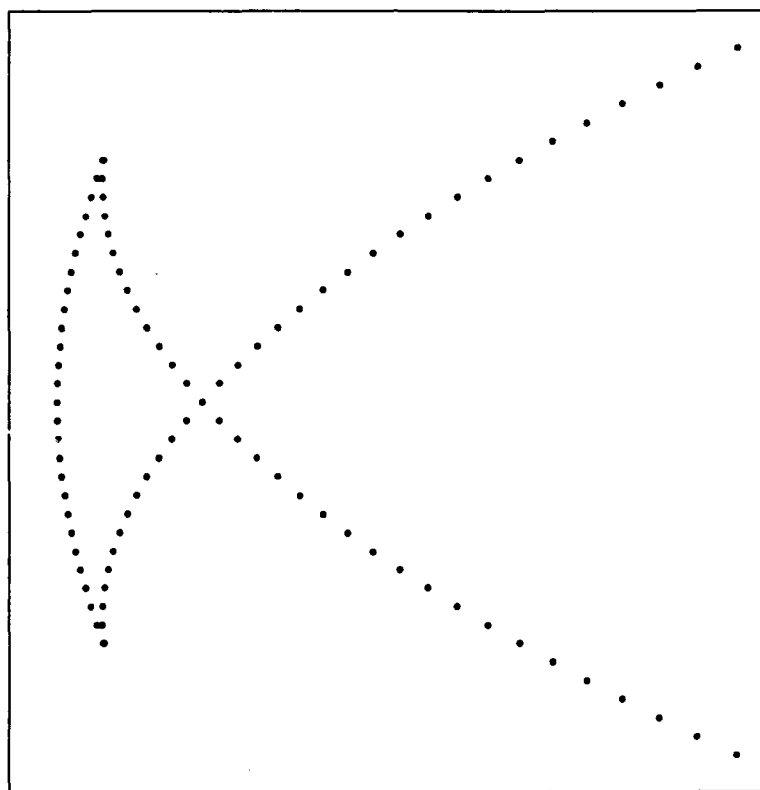
(g)
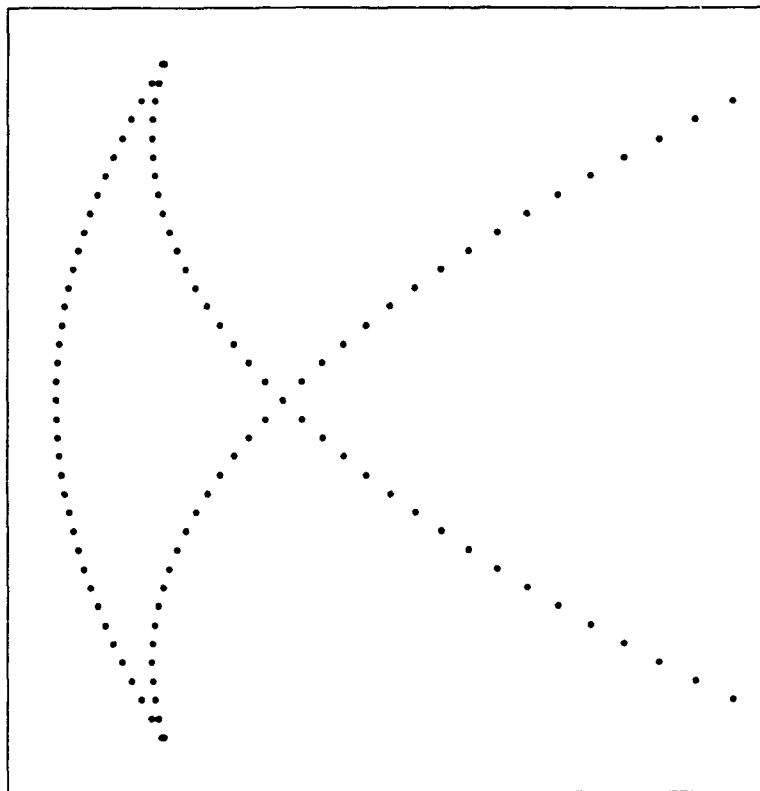
Figure 15) The travel time surface contribution due to the reduced distance function of the wavefront ϕ/c. The effective horizontal locations are the same as in Figs. 13 and 14. Cut (a) is the smooth cut outside the cusp curve. Cut (b) shows the unsmooth form of the travel time curve through the cusp point better the 14b as it is not smoothed by the slowly varying contribution from ϕ_0/c. Cuts c-g are inside the caustic showing the widening of the tail as the horizontal cut location moves further into the cusp curve. This travel time surface has the general shape of the swallow tail caustic which is the general travel time surface of the cusp caustic. Figure 14 should represent the data better as it contains the contribution of the slowly varying term ϕ_0/c.

(a)
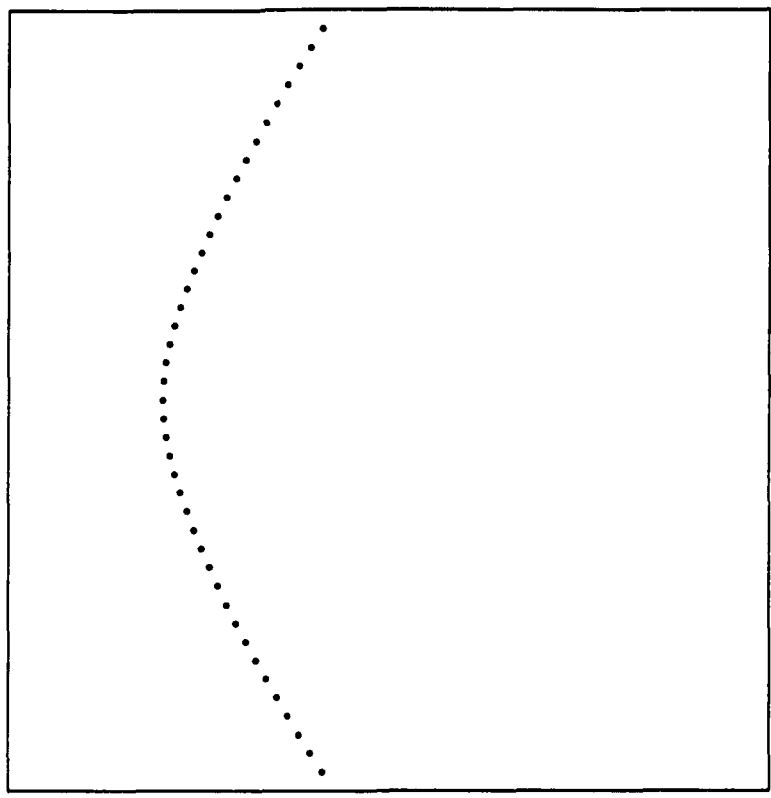
(b)
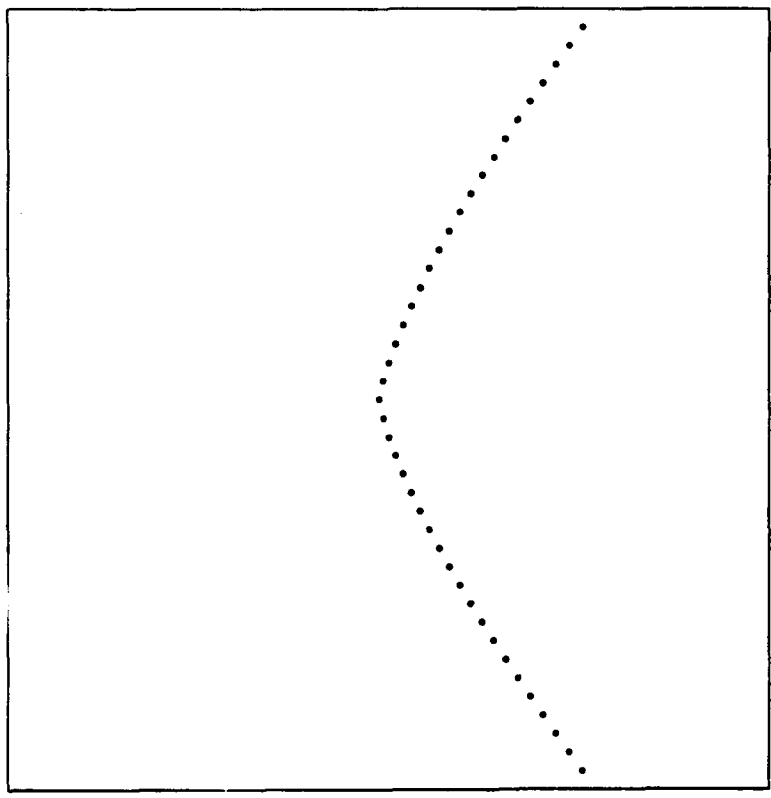
(c)
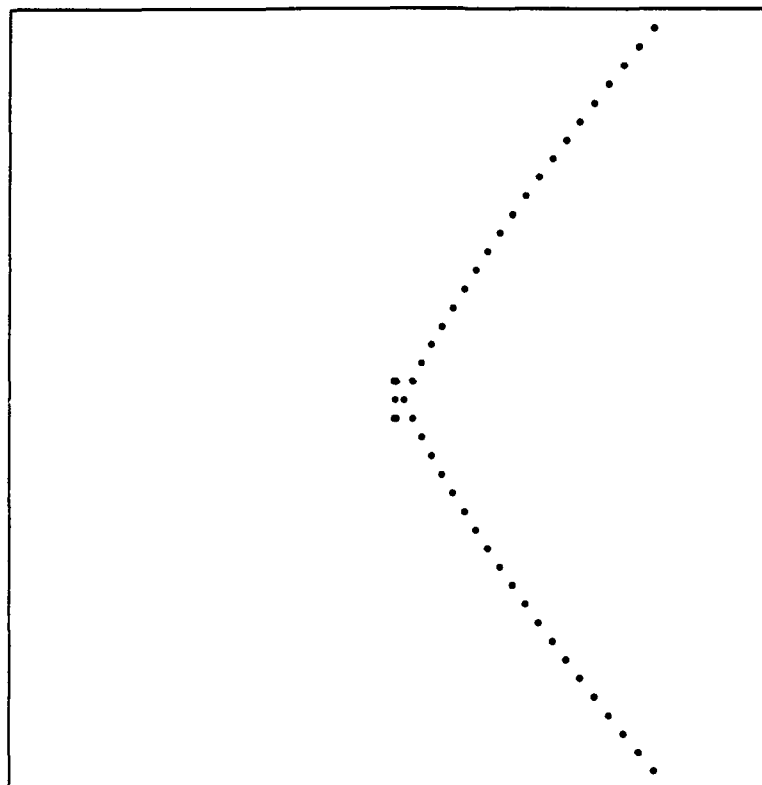
(d)
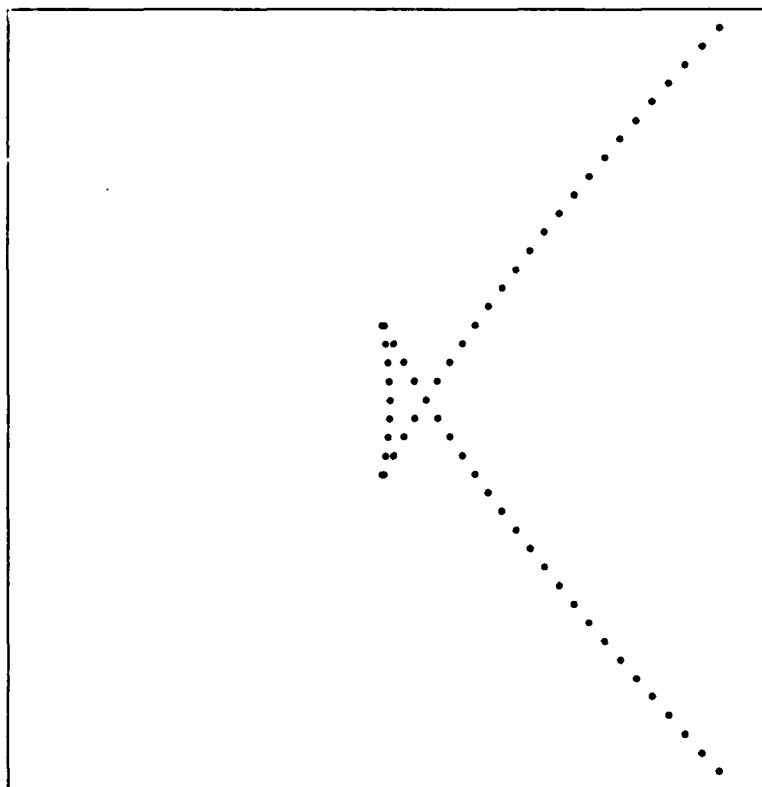
(e)
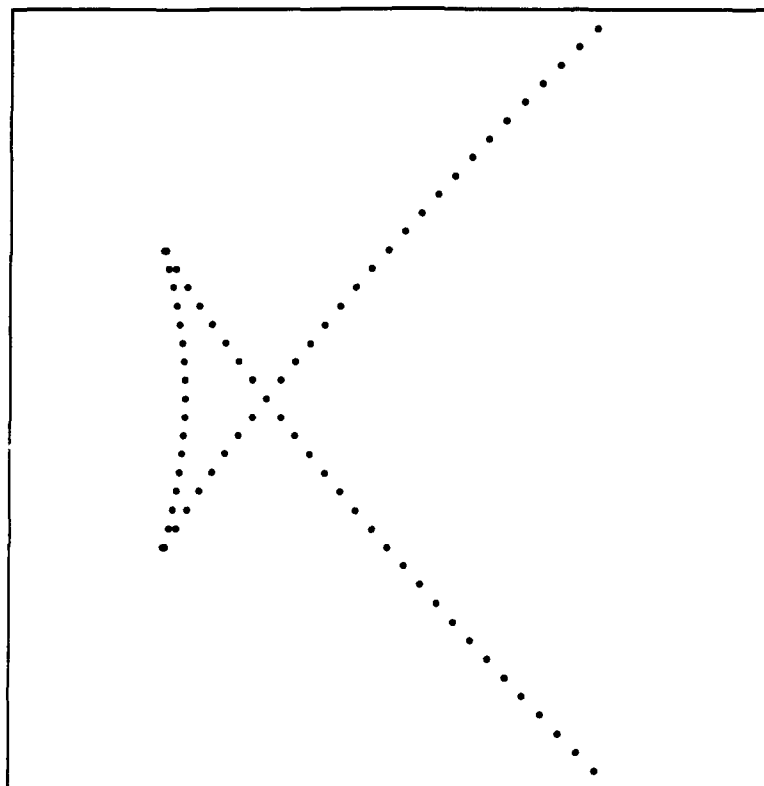
(f)
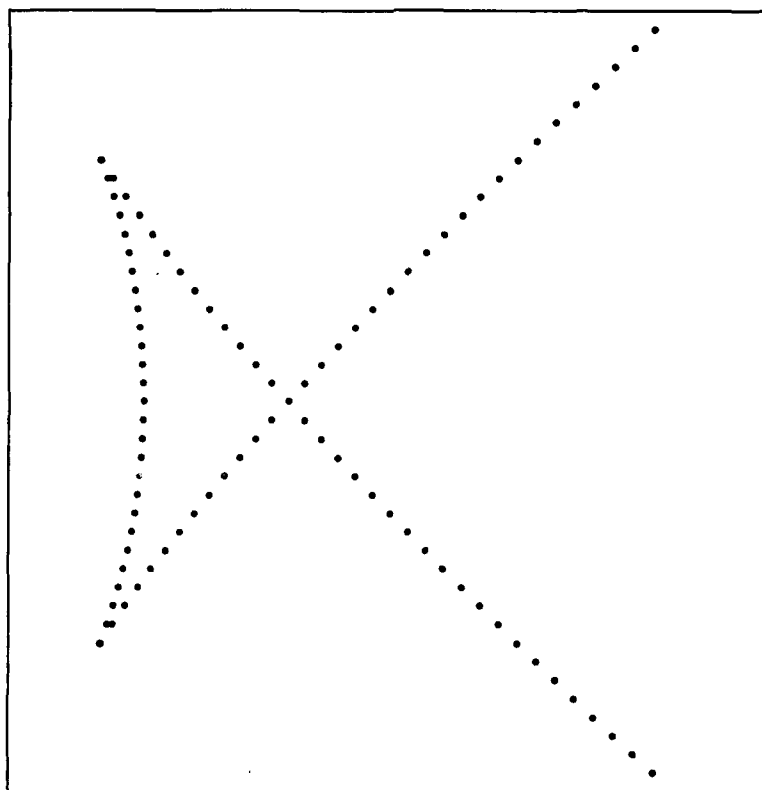
(g)
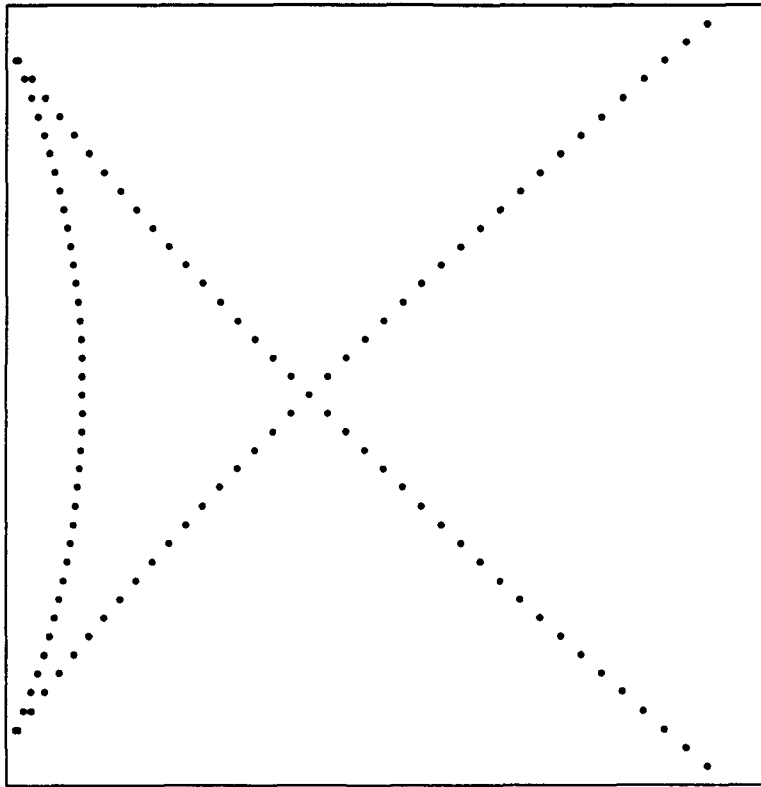
come from the same point. The pointed shape of the travel time surface at the cusp point is more apparent in Fig. 15b as it is not softened by the contribution to the travel time surface due to ϕ_0 in Eq. (24). In Thom's description of the swallow tail surface[16], at the origin (for the travel time surface $U_e = U_{ec}$) the rib lines of the curvilinear tail of swallow tail caustic come together in a cusp where at the origin the surface has a point of infinite curvature. This agrees with the less smooth shape of Figs. 14b and 14b.

Just inside the cusp curve Figs. 14c and 14c show what appear to be two arrivals in the middle three vertical positions. The upper and lower early arrivals are near the caustic curve and are due to the single arrival of the two rays that merge on the caustic. The central late arrival is on the symmetry axis of the caustic and due to the simultaneous arrival of two rays from different points on the wavefront that have the same acoustical path distance to the observation point. In each of the calculations along the symmetry axis with $U_e > U_{ec}$ there will be a simultaneous late arrival by two rays from different portions of the wavefront. These rays do not merge on the symmetry axis, they simply represent equal path lengths to the observation point. The merging rays are represented by the signals, located symmetrically about trace 21, that merge and disappear as the cusp curve is crossed. Notice that the width of the tails of the travel time curves in Figures 14c-g and 15c-g grows as the horizontal observation plane position moves through the cusp curve, while the later region of the surface (the wings) move closer together. The growth of the tail is a characteristic of the swallow tail caustic, Fig. 4c, moving along the positive C_3 axis[16]. Thus the calculated travel times for the TCC have the form of the swallow tail caustic surface plus a slowly varying background contribution of the form ϕ_0/c.

B) THE IMAGED TRAVEL TIME CURVES FOR A WAVEFRONT THAT FORMS A TRANSVERSE CUSP CAUSTIC, COLLECTED USING A FIXED SOURCE AND A SCANNING RECEIVER

Data taken with the receiver scanned in the observation plane as described in Sec. II is shown in Fig. 16. Each time trace is 20.48 μs long. The horizontal positions of the cuts shown in Fig. 16 correspond to the horizontal positions a-g in Fig. 13. In Fig. 16a there is only one arrival at each vertical position as would be expected outside the cusp curve. The travel time surface cut shown in 15a is a smooth curve corresponding to the swallow tail surface, in the Fig. 4c, when $C_3 < 0$. On or near the cusp point Fig. 16b shows an increase in amplitude near the central time trace. This cut is slightly pointed near the center similar to Fig. 14b which is the calculated travel time surface cut at the cusp point. As the horizontal observation location moves inside the cusp curve, Figs. 16c-g, the tail of the travel time surface grows while the wings move closer together as do the tail and wings of the corresponding calculations, Figs. 14c-g.

The general form of the travel time cuts shown in Figs. 16a-g agree well with the corresponding calculations in Figs 13a-g. A smooth background travel time contribution given by ϕ_0/c of Eq. (24) can be seen in the convex shape of the tails and the extra curvature in the wings that is also evident when Figs. 14a-g are compared to Figs. 15a-g. The contribution to the travel time surface due to the specific shape of the reflected wavefront is evident in the existence of the tail and wings for observation points inside the caustic. The tails represent the merging (focusing) and subsequent loss of rays on the cusp curve. The travel time surface displayed by these travel time cuts has the general shape of the swallow tail caustic surface associated with the cusp catastrophe, superposed on a slowly varying contribution from ϕ_0/c of Eq. (24).

For the calculations shown in Figs. 14 the relative horizontal positions used were the same as those of the data shown in Figs. 16. The parameters used in the calculation were also obtained from the experimental setup ($b_1' = 0.0118$ cm^{-1}, $a_2' = 0.00236$ cm^{-2},

$b_3' = 0.0491$ cm^{-1}, $z = 68$ cm, $z_s = 170$ cm, $u_s = -15.0$ cm, $v_s = 0$). Thus the calculations

in Figs. 14 should represent, up to a constant time delay, the travel time surface imaged

experimentally. To compare the calculations with the data, both were displayed with the

same scales and absolute length for the time and vertical axes. The calculations (Fig. 14)

were then overlain on the measurements (Fig. 16) using the arrival time of the early signal

along the symmetry axis (trace 21 in both the data and calculations) to compare the

calculated arrival time surface with the experimental arrival time surface. This comparison

does not attempt to compare the absolute arrival times: only the arrival times relative to the

other signals in the travel time curve are compared and thus the shapes of the surfaces.

The absolute distances z and z_s were not determined with sufficient precision to facilitate a

meaningful comparison of the absolute times. Each travel time curve is a slice through the

travel time surface at constant $U_e - U_{ec}$.

Comparing Figs. 14 and 15 as discussed above shows there is very good

agreement between the qualitative shape of the travel time surfaces of the calculations and

the data. The size and shapes of the tails and wings in Figs. 14c-13f and 15c-15f agree to

within approximately a $\pm 1\mu s$ error in the arrivals when the central trace is used as the guide

for the comparison. A $1\mu s$ error amounts to an error in the estimate of the propagation

length of approximately 1.5 mm. The size of the tail in Figs. 14g and 15g agrees well,

however, the experimental tail at this position is not as concave as the calculated tail.

Figures 14b-14c and 16b-16c do not have the distinct tails to use for the comparison but the

wings in each of the figures do show the same qualitative agreement between the relative

arrival times of the signals. For Figs. 14a and 15a the smooth shapes of both the

calculated and measured travel time curves outside the cusp curve agree to within $\pm 1\mu s$.

One source of the error in matching the calculated and measured travel time curves

is the distortion of the pulse occurring along ray paths that touch the caustic surface due to

the signal being phase advanced by $\pi/2$[1,9,17]. The shape of the phase advanced signal will

contain a precursor that arrives earlier then the elementary geometrical arrival time predicted

by propagation along a ray at speed c. In the calculation and comparison there were no arbitrary scaling factors used. The parameters used in the calculation were all determined by the measured surface parameters h_m and the experimental set up. Each of the calculated time traces is 20.48 μs long, the same as the measured time traces, and each uses a range of $V_e = v/z + v_s/z_s$ from –0.159 to 0.159 with $v_s = 0$, for the value of z in the experiment (z = 68 cm) a vertical scan in the observation plane of 21.6 cm.

In the tail of the travel time surface the two rays that merge on the caustic move closer in time as the observation point moves out toward the cusp curve. On the cusp curve these two rays merge to form a single ray with a signal that has a larger amplitude then each ray individually. Elementary geometrical acoustics predicts only a single arrival once the cusp curve is crossed, where the rays that merge on the cusp curve abruptly disappear outside of the cusp curve. In Figs. 16c-g the contributions from the rays that merge on the cusp curve do not abruptly disappear after the cusp curve is crossed but fade gradually. This tunneling of the acoustical signal into the shadow region of the TCC can be explained in terms of a complex ray. The complex ray has a phase that is complex giving an exponential decay to the contribution of the ray away from the caustic.

The complex phase of the ray can be associated with a complex distance function ϕ_c associated with the ray. This describes a ray that propagates in a complex space where the measured signal is due to the intersection of the complex ray path with the real plane[18]. The existence of the complex ray can be explained using the stationary phase approximation of the diffraction integral for steady state signals Eq. (13)[19]. Inside the cusp curve there are three real and distinct stationary points (rays) of the phase of the diffraction integral defined by Eqs. 21a and 21b. The contribution of each stationary point has the general form of a ray

$$p_i(u,v) \approx \sqrt{\frac{2\pi k}{|H|}} \, b(x_i,y_i) \, \exp[\, ik\phi(x_i,y_i;U_e,V_e) + \frac{1}{4} \, i\pi \, \text{sgn}(H)], \qquad (27)$$

where b is a slowly varying amplitude function, H is the Hessian [in two dimensions

$H = (\partial^2\phi/\partial x^2)(\partial^2\phi/\partial y^2) - (\partial^2\phi/\partial x\partial y)^2]$, and the location of the ray in the exit plane is (x_i,y_i). When the source point is complex the distance function ϕ also becomes complex $\phi = \phi_r + i\phi_i$. This gives the exponential in Eq. (27) of the form $\exp[-k\phi_i + ik\phi_r + (1/4)i\pi \, sgn(H)]$ which for positive ϕ_i has an exponential decay.

As the observation point moves onto the cusp curve two of the stationary points merge, and after the cusp curve is crossed these two real stationary points become complex conjugate stationary points. When the stationary points become complex the distance function $\phi(x_i,y_i,U_e,V_e)$ becomes complex in Eq. (27) giving a ray that has a complex source point. Inside the cusp curve the diffraction integral can be considered as a contour integral in the complex plane with the contour along the real axis. All three of the stationary phase points are along the real axis while the observation point is inside of or on the cusp curve. When the cusp curve is crossed, however, the two real stationary points that have merged move off the real axis and become complex conjugate stationary points. Only one of the complex stationary phase points contributes to the approximation of the diffraction integral outside the cusp curve[19]. The integration contour is deformed to pass through the real stationary point and only one of the complex stationary points. This complex stationary phase point contribution is in the form of a ray with a complex phase. The contribution of the complex ray near the cusp curve is strong enough to interfere destructively with the real ray causing a null in the amplitude of the wavefield but decays exponentially away from the cusp curve and thus contributes very little to the field far from the cusp curve.

As the observation point moves horizontally away from the caustic it eventually crosses into a region where the complex stationary point no longer contributes to the approximation of the diffraction integral. The region outside the caustic where only the one real ray contributes to the field is defined by the Stoke's set of the cusp caustic[19]. In Fig. 16a there is only one real ray and no complex rays as the horizontal location is well within the Stoke's set. The complex rays are most evident in Figs. 16c-g. As the caustic is

approached from the bright region the the two early rays are seen to merge in time giving a maximum on the caustic. As the caustic is crossed this maximum starts to decay away from the caustic as expected for the complex ray that tunnels into the shadow region of the TCC.

Figure 16) Time records of received signals collected at consecutive vertical positions of the receiving transducer along cuts through horizontal positions in the observation plane, displayed in a waterfall format to show the travel time curve for the vertical cut. The vertical positions in the displayed travel time curves correspond to the vertical positions in the observation plane at which that time record was collected. Relative to the horizontal position of the cusp point the horizontal positions are $u - u_c = -27$mm, 0.0, 27mm, 54mm, 81mm, 108mm, 135mm , the vertical positions relative to the vertical position of the cusp point are $v - v_c = -108$mm to 108mm by 5.4mm steps. Cut (a) shows the smooth travel time curve expected from Fig. 14a outside the cusp curve. The horizontal position of cut (b) is approximately on the cusp point and the cusp curve is slightly pointed. Cuts (c)-(g) are inside the cusp curve and show the increasing width of the tail as the horizontal positions of the cuts move further inside the cusp curve.

(a)

├─5 μs─┤

(b)

(c)

├──5 μs──┤

(d)

119

(e)

├─5 μs─┤

(f)

(g)

$\longmapsto$ 5 µs $\longmapsto$

C) THE IMAGED TRAVEL TIME CURVES FOR A WAVEFRONT THAT FORMS A TRANSVERSE CUSP CAUSTIC, COLLECTED USING A SCANNING SOURCE AND FIXED RECEIVER

Experiments were performed to image the travel time surface produced by scanning the acoustical source and holding the receiver fixed in the observation plane. In the experimental setup used, this amounted to reversing the roles of the source and receiver used to collect the data shown in Fig. 16. Through reciprocity it would be expected that the travel time surface imaged by scanning the source in this manner would be the same as that shown in Fig. 16. The results, though reciprocal to those shown in Fig. 16, still demonstrate that the travel time surface and similarly the TCC can be imaged by scanning a source and holding the receiver fixed. Figure 17 shows the cuts through the travel time surface obtained by scanning the source. Each of the horizontal positions of the cuts now refers to the horizontal location of the source as this controls the horizontal location of the cusp curve in the observation plane. The vertical location of each time trace is also referenced to the vertical position of the source as this moves the cusp curve up or down in the observation plane. The qualitative shape of each of the cuts in Fig. 17 is the same as the corresponding cut in Fig. 16. Comparison of the cuts in Fig. 17 with those in Fig. 16 and the calculated cuts in Fig. 14 show that the TCC in the observation plane can be mapped by scanning either the source or the receiver.

The experimental parameters used when the source was scanned were the same as those for the experiments when the receiver was scanned with the exception of the reversal of the roles of (u, v, z) and (u_s, v_s, z_s). This does not effect the calculations shown in Fig. 14 as the dependence of the location of the rays in the exit plane is on U_e and V_e. The only change in the calculation due to switching the source and receiver in the above manner would be to exchange r and r_s where now r will be fixed and r_s will change at each position of the source in the scan. Thus the calculations in Fig. 14 can be used to compare the theoretical travel time surface to the experimental surface shown in Fig. 17 for the scanned

source. When this comparison was done it showed that the smooth shape of the calculated travel time curve in Fig. 14a matches well the shape of the experimental travel time curve 16a, with all the calculated relative arrival times falling within $1\mu s$ of the measured arrival times. The wings in Figs. 17b and 16c also displayed the agreement seen in Fig. 17a with the calculated travel time curves. In Figs. 17d-16f the tail of the travel time curves agreed well with the tails of the calculated curves in size and shape. The relative arrival times of the signals forming the tail were within the $\pm 1\mu s$ error seen in the comparisons of the rest of the data to the theory.

123

Figure 17) Time records of received signals collected at consecutive vertical positions of the source transducer along cuts through horizontal positions in the source plane, displayed in a waterfall format to show the travel time curve for the vertical cut. The vertical positions in the displayed travel time curves correspond to the vertical positions in the source plane at which that time records were collected. Relative to the horizontal position of the cusp point the horizontal positions are $u - u_c = -27mm, 0.0, 27mm, 54mm, 81mm, 108mm, 135mm$, the vertical positions relative to the vertical position of the cusp point are $v - v_c = -108mm$ to $108mm$ by $5.4mm$ steps. Cut (a) shows the smooth travel time curve expected from Fig. 14a outside the cusp curve. The horizontal position of cut (b) is approximately on the cusp point and the cusp curve is slightly pointed. Cuts (c)-(g) are inside the cusp curve and show the increasing width of the tail as the horizontal positions of the cuts move further inside the cusp curve. These travel time curves show that the transverse cusp caustic can be observed by holding the receiver fixed and scanning the source.

(a)

⊢—5 μs—⊣

(b)

(c)

V

├─ 5 μs ─┤

(d)

V

(e)

5 μs

(f)

(g)

├──5 μs──┤
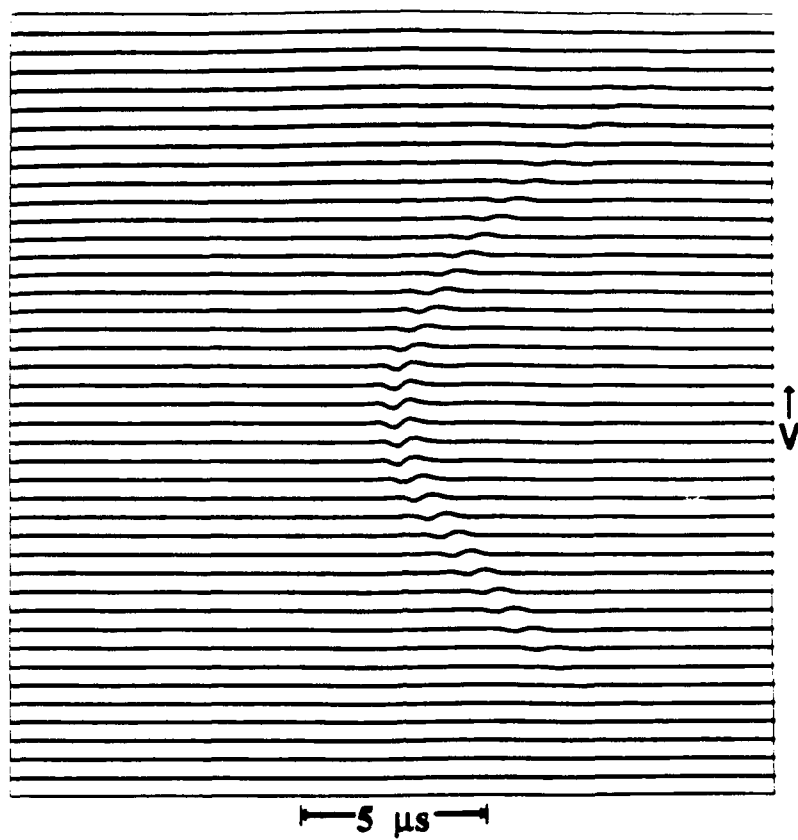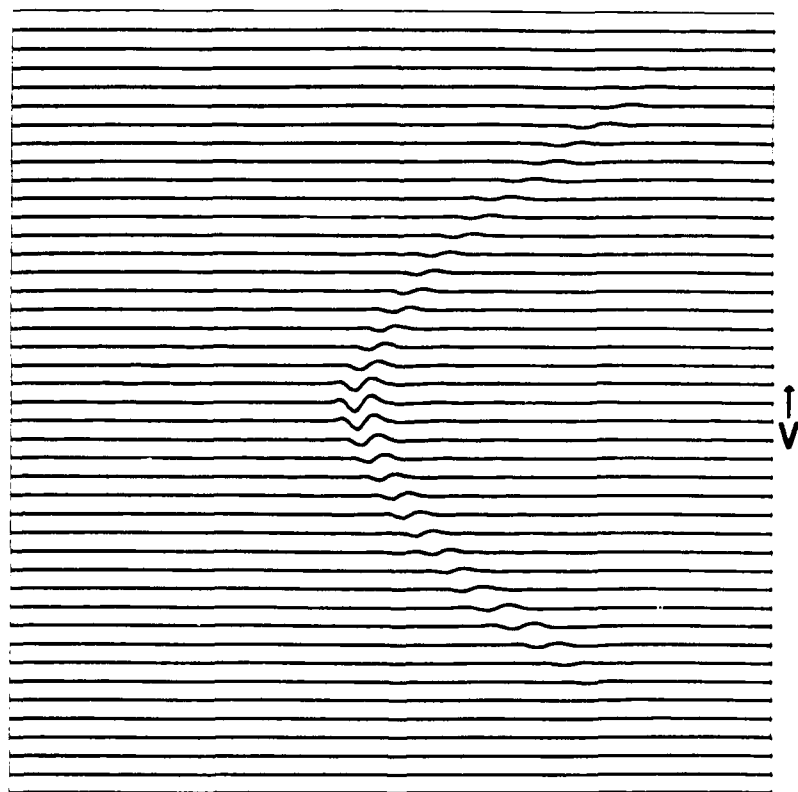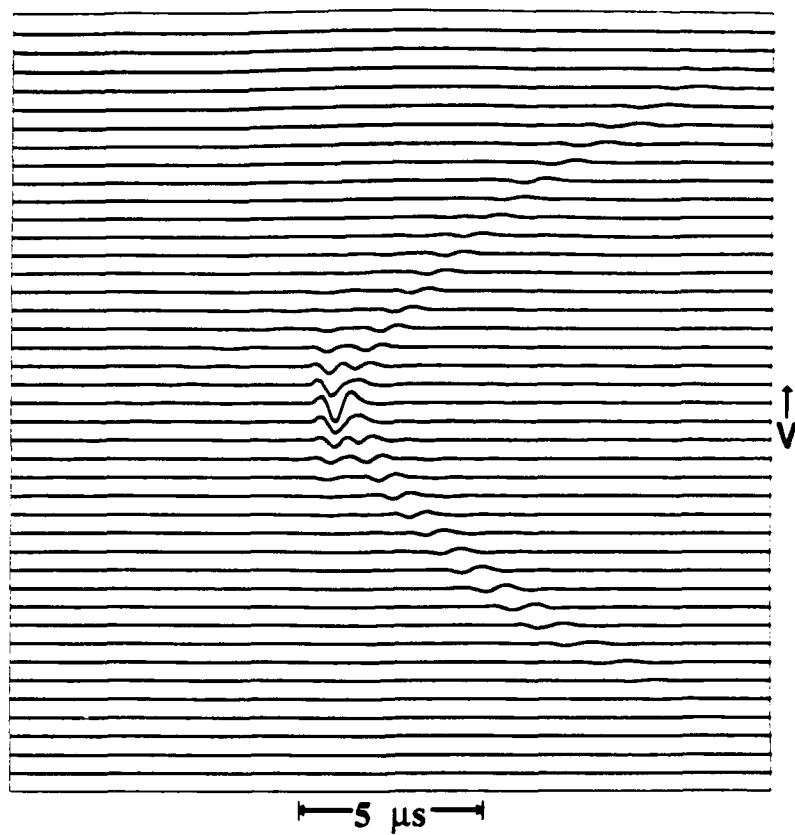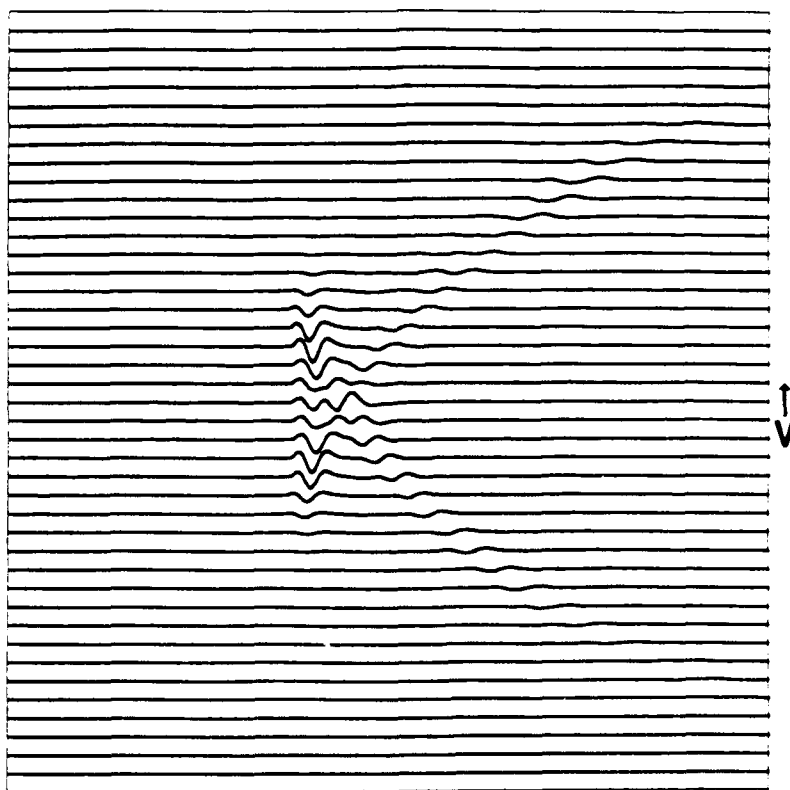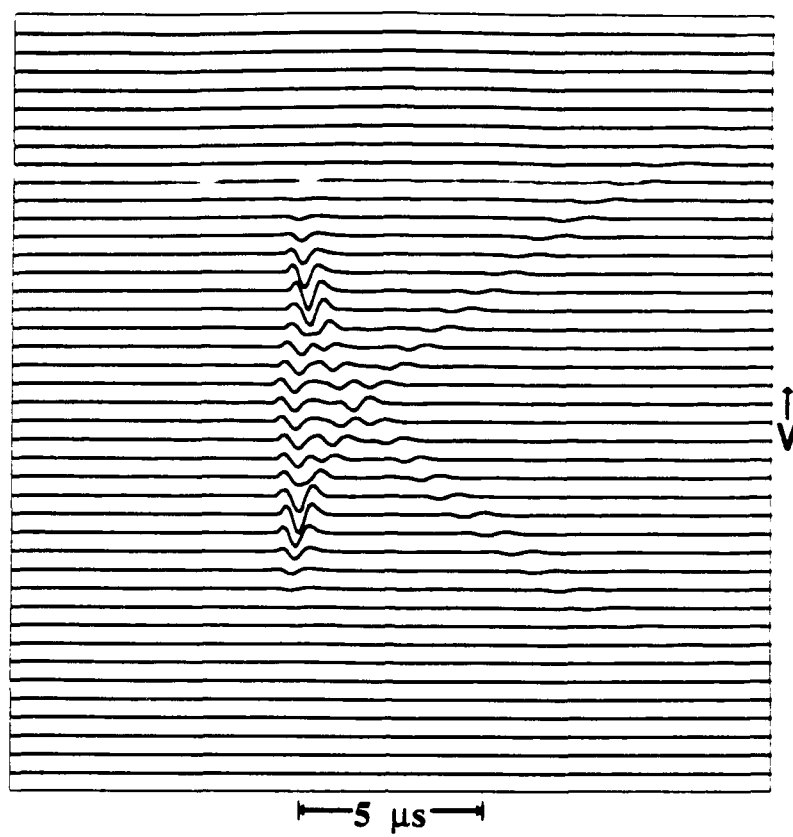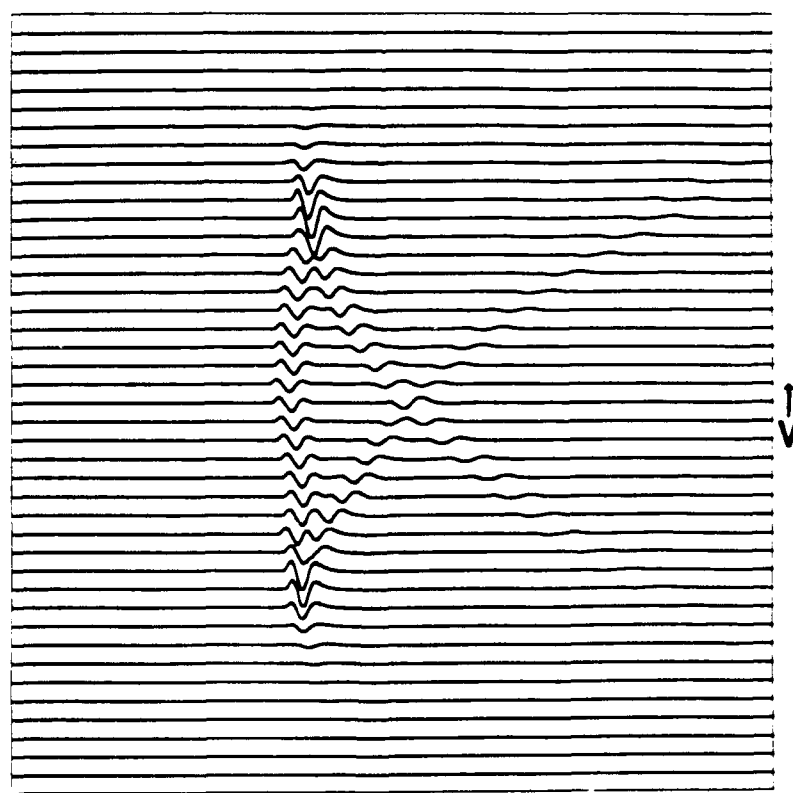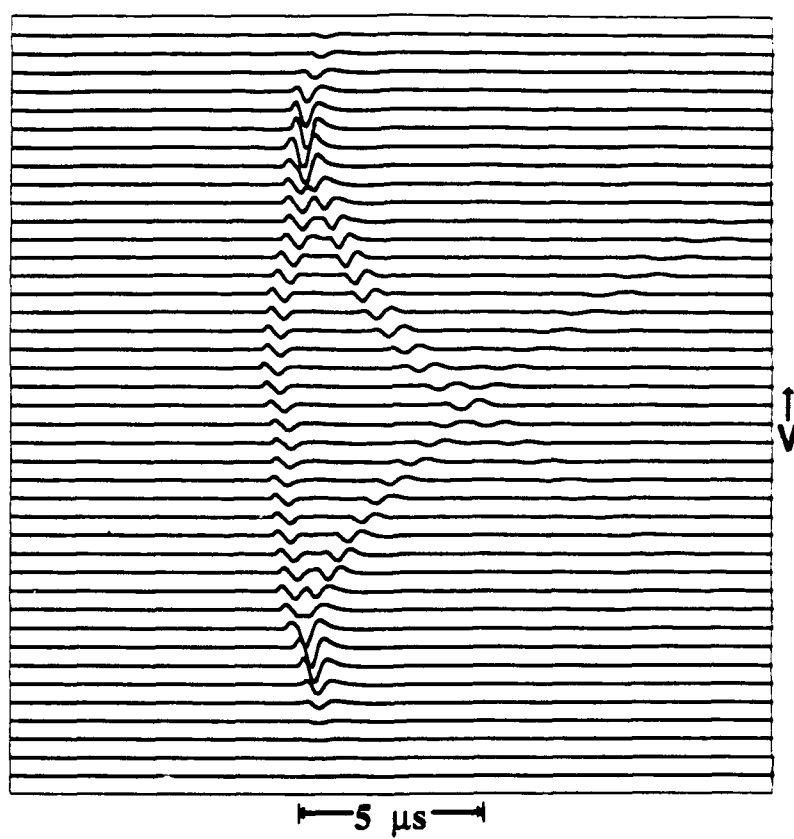
3.5 DISCUSSION OF THE RAY EVOLUTION AND ITS SENSITIVITY TO THE SURFACE PARAMETERS

The locations of the rays in the exit plane can give some insight into how the local wavefront shape in the exit plane forms the travel time surface in the observation plane. Figure 18a shows the locations of the rays in the exit plane associated with the travel time cut in Fig. 18b corresponding to the horizontal position of cut e in Figs. 13e - 17e. When the observation point is below the cusp curve, there is only one real ray path from the exit plane passing through the observation point. For example, there is only one ray path that passes through the point marked a in Fig. 18b originating in the exit plane at point a in Fig. 18a. Moving up the vertical cut from below the cusp curve in the observation plane the single arrivals are associated with the ray locations from the branch of the wavefront in the exit plane marked by the arrow 1. The arrow gives the general direction of migration for the rays from branch 1 of the wavefront in the exit plane as the observation point moves up in to the cusp curve. When the observation point reaches the cusp curve the two rays that merge on the lower branch of the cusp curve appear in the exit plane at the point marked "lower cusp curve". The migration of these two rays in the exit plane as the observation point moves through consecutive vertical locations up through the cusp curve is shown by the arrows marked 2 and 3 along branches 2 and 3 of the wavefront in the exit plane. When the observation point is on the symmetry axis rays 1 and 2 from the wavefront are located symmetrically about the x axis while the ray 3 is located on the x axis. Crossing the x axis and moving up toward the upper half of the cusp curve the original ray (ray 1) merges with ray 3 at the point marked "upper cusp curve" in Fig. 18a which correspond to the single arrival marked "upper cusp curve" in Fig. 18b. After crossing the upper half of the cusp curve only ray 2 is left moving down toward the lower left corner in Fig. 18a. The three branches of the wavefront in Fig. 18a correspond to the branches of the travel time surface in Fig. 18b.

Figure 18) (a) The location in the exit plane of rays to the observation plane for the travel time cut corresponding to Fig. 15e. Rays to the vertical cut in the observation plane originate on three branches of the wavefront in the exit plane labeled **1, 2,** and **3** in (a). The arrows indicate the migration of the rays along the branches as the vertical position in the observation plane moves up through the cusp curve. (b) Shows the corresponding travel time curve with the signals arriving along the three branches of the travel time curve associated with the locations of the rays from the three branches of the wavefront in the exit plane marked **1, 2,** and **3**. The arrows label the signal arrivals associated with the migrating rays in (a) indicating where the associated signals came from in the exit plane. As a guide there are four rays in (a) and the locations on the travel time curve of signals associated with these rays in (b) labeled a-d.
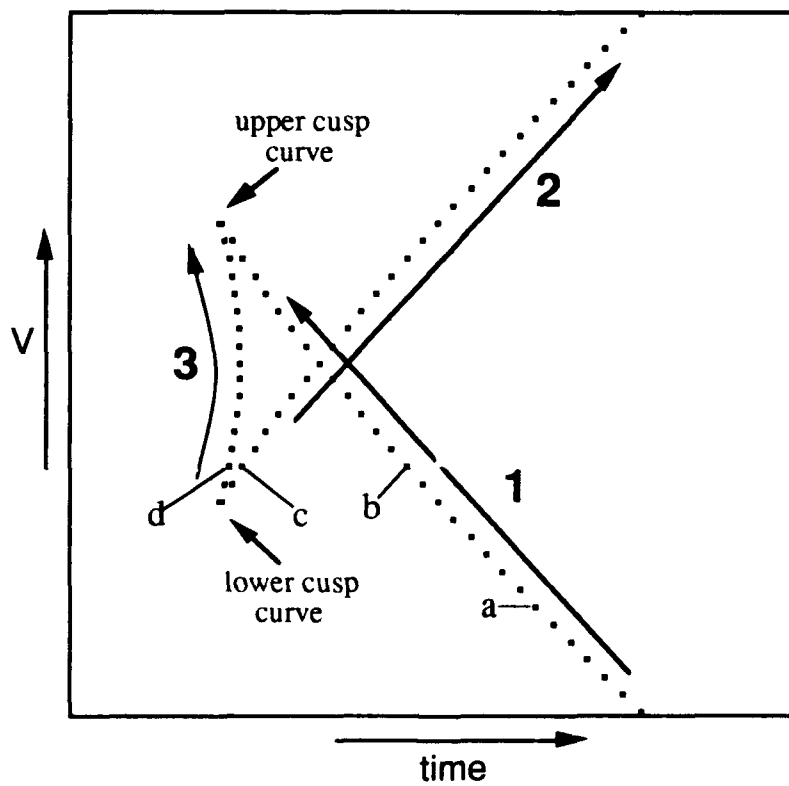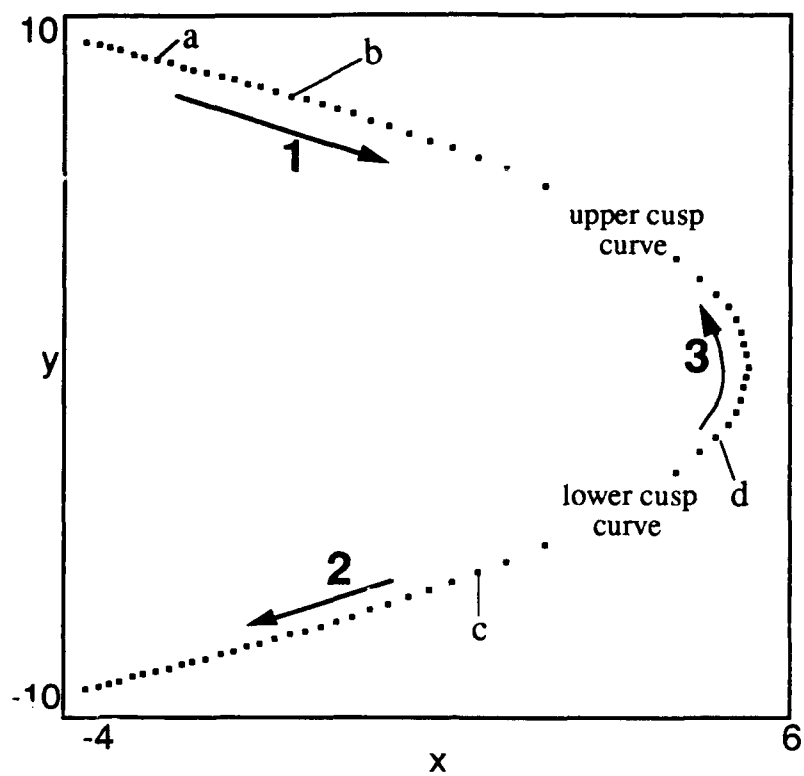
The rays located in the exit plane in Fig. 18a are normal to the wavefront at those points. The arrival times associated with these rays in the observation plane provide a picture of the local shape of the wavefront after propagating from the exit plane to the region containing the observation plane. In the exit plane the wavefront has the general shape given by Eq. (10) and shown in Fig. 8. After propagating to the region containing the observation plane the wavefront has the general shape of the appropriate singular surface described by the ray condition, Eqs. (20a) and (20b), and $\Phi/c - t = 0$. For the cusp catastrophe this is a surface given by the swallow tail caustic Fig. 4c. In Fig. 18a the shape of the wavefront in the exit plane is that of Fig. 8. After propagation to the observation plane the branch of the wavefront represented by **1** in 17a has folded over to **1** in 17b, branch **2** in 17a to **2** in 17b and **3** in 17a to **3** in 17b, where the arrows relate positions in the exit plane to positions in the observation plane. Figure 18b represents a slice through the wavefront in space after propagation to the region containing the observation plane and has the same general shape as a cut through the swallow tail caustic in Fig. 4c with $C_3 > 0$.

The ray locations for the TCC described above produce a caustic that opens along the positive u direction in the observation plane. In the three ray region of the caustic, rays from branch **3** of of the wavefront will be the first to arrive in the observation plane at a given vertical position. The important parameter in determining the arrival orientation of the signals propagating along the rays in Fig. 18 is $b_1' = 1/(2z_e) - 2h_1$. Parameter a_2' only affects the direction along which the cusp curve opens and a change in sign is effectively a reflection of the wavefront through the vertical axis. Figure 18 shows the general ray locations for a wavefront with $a_2' > 0$ and $b_1' > 0$. When h_1 is negative b_1' will always be positive and the caustic surface, Fig. 3, will be well behaved. However, when h_1 is positive there will be combinations of source and receiver distances that give $b_1' = 1/(2z_e) - 2h_1 = 0$. As b_1' goes to zero the opening rate of the caustic diverges. The position of branch **3** in the exit plane in Fig. 18a moves off to $x = +\infty$ while branch **3** in the observation plane goes to $t = -\infty$ as $b_1' \to 0$ from the positive side. When $b_1' = 0$ t

Figure 19) Calculated travel time curves at an effective horizontal position relative to the cusp point of $U_e - U_{ec} = 0.1191$, with $b_1' = 0.01, 0.001, 0.0001, 0.00001, -0.00001, -0.0001, -0.001, -0.01$ in a-j. As the value of b_1' goes to zero from the positive side the early arrival in the tail moves off to $t = -\infty$ while the two later arrivals go to $t = [U_e b_3'/a_2' \pm -V_e(U_e/a_2')^{1/2}]/c$. After b_1' goes through zero and becomes negative the travel time curve giving the outer boundary of the tail moves in from $t = \infty$ while the wings unfold from the limit given above. The orientation in time of the arrival of signals when b_1' is negative is opposite that for positive b_1'.

(c)

(d)

(e)

(f)

(i)

(j)
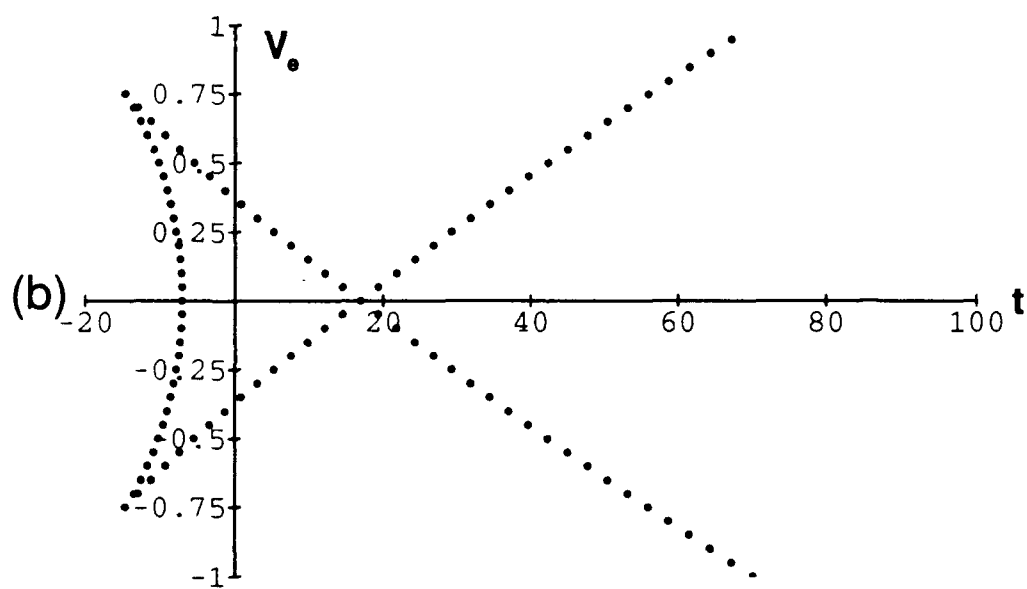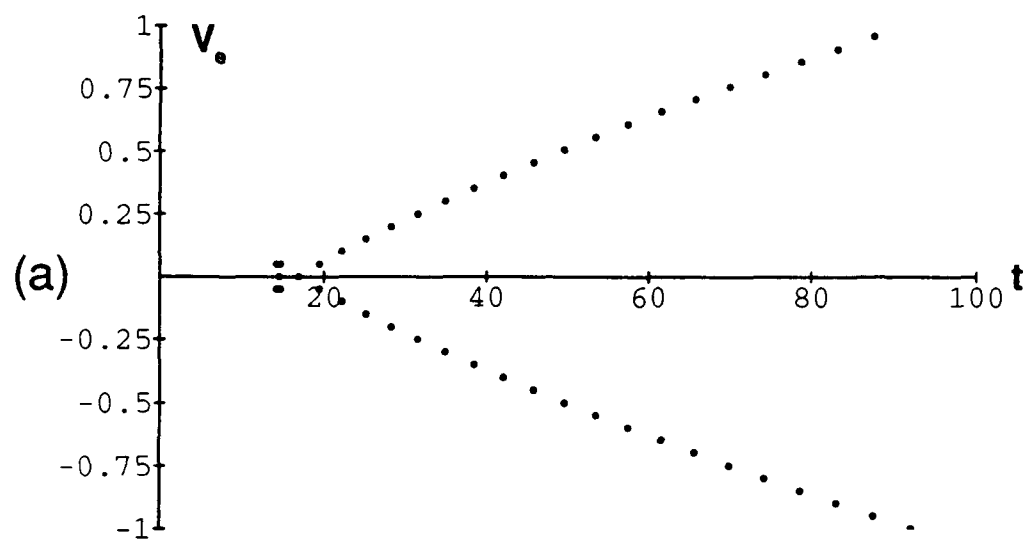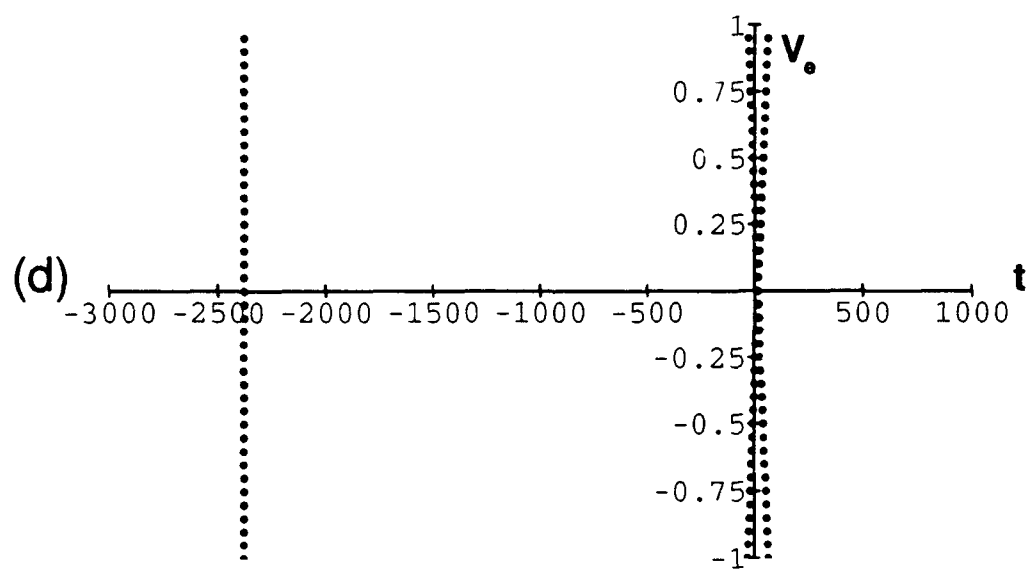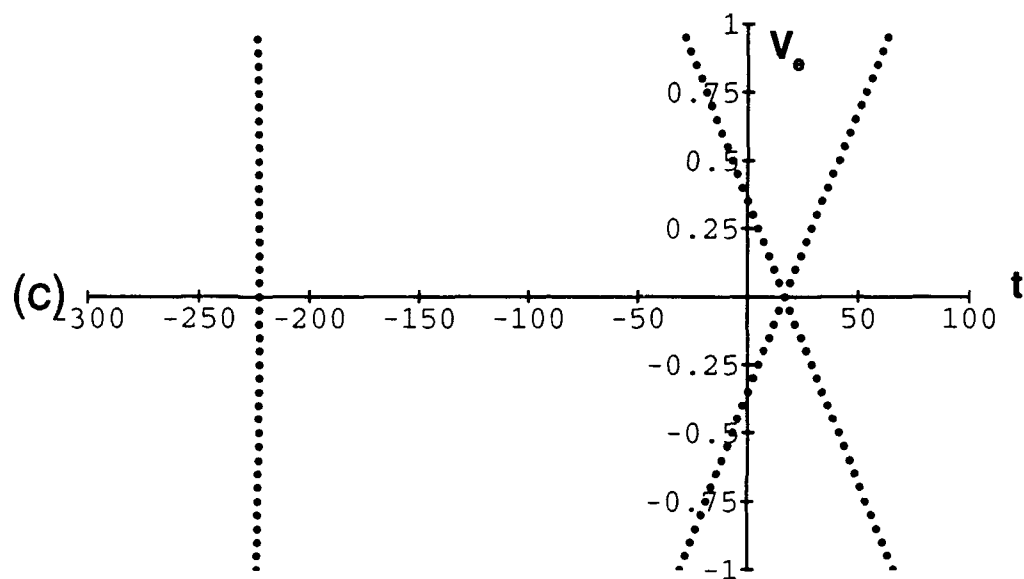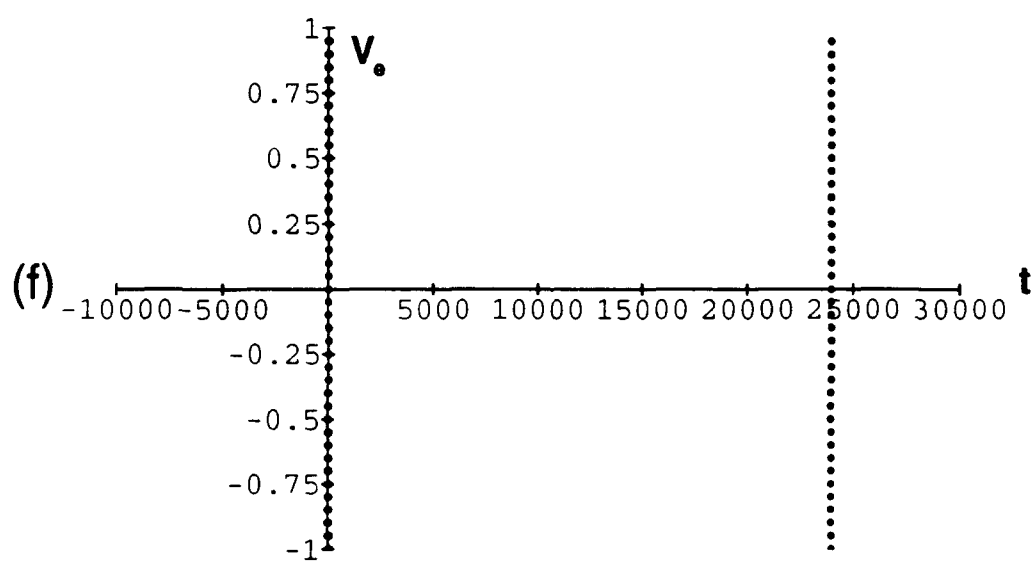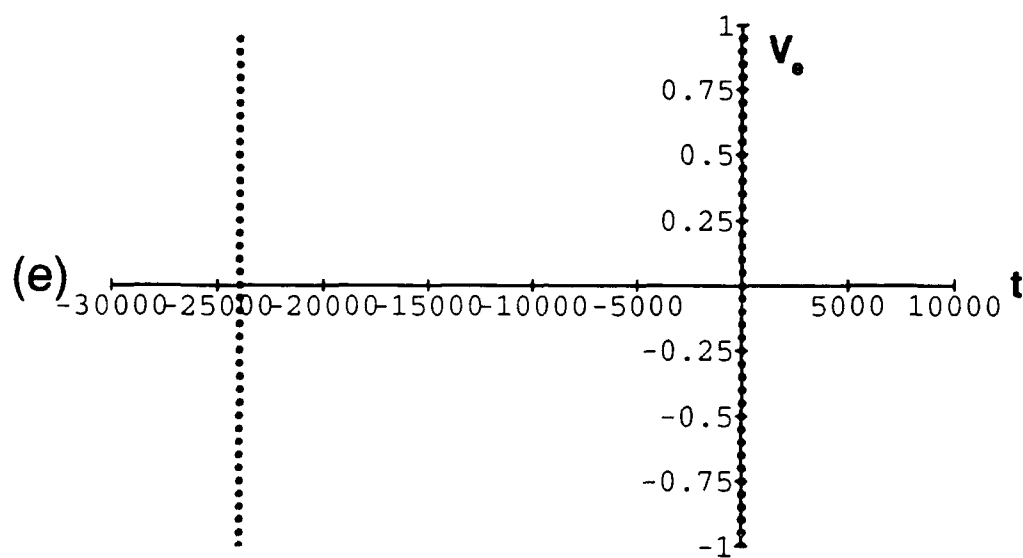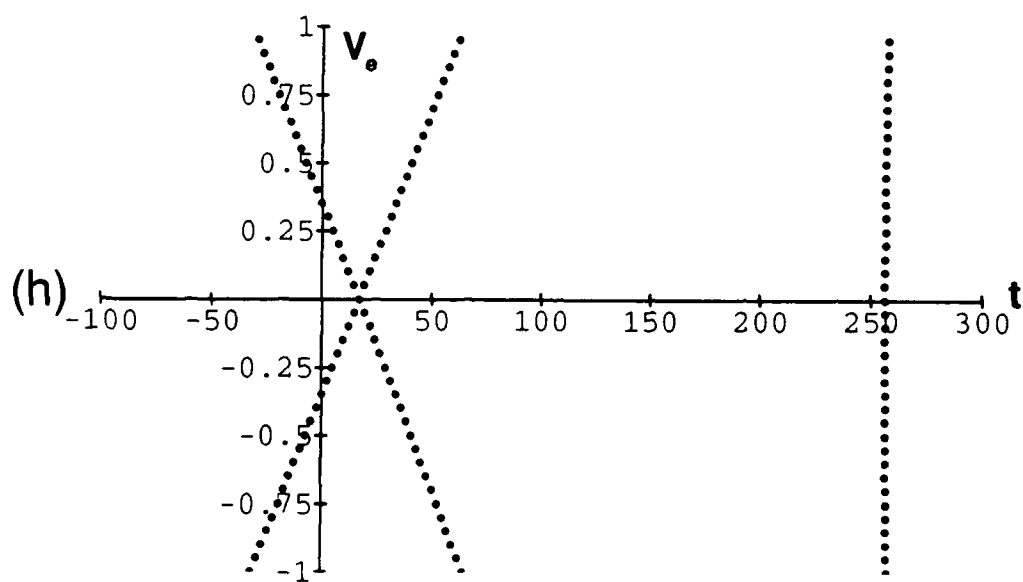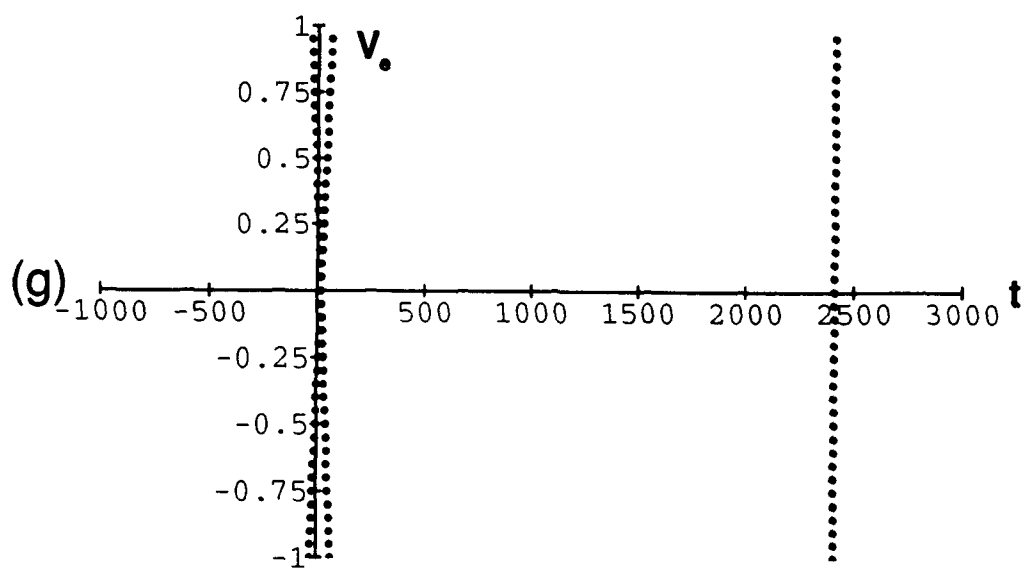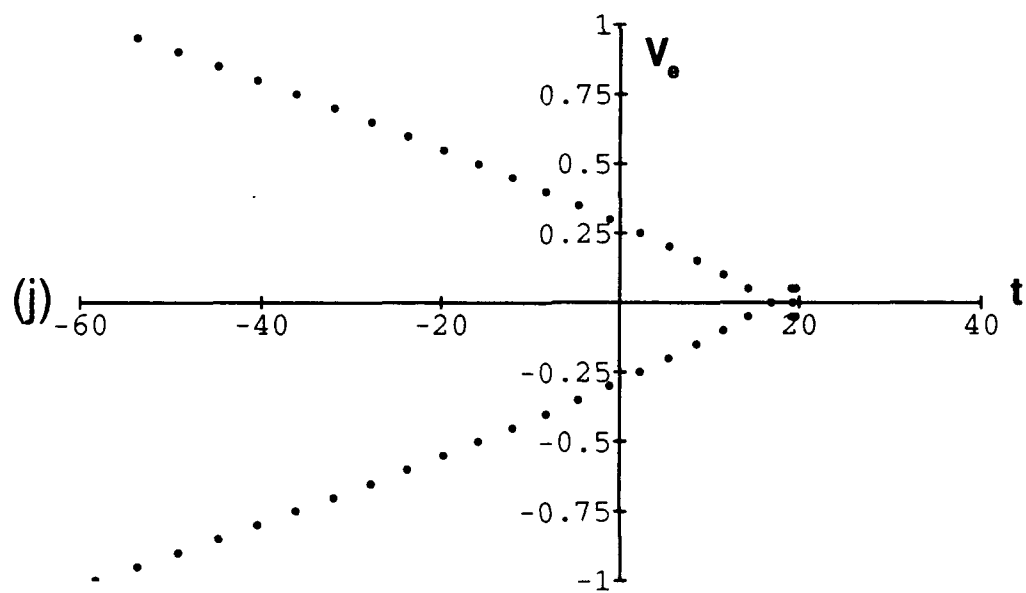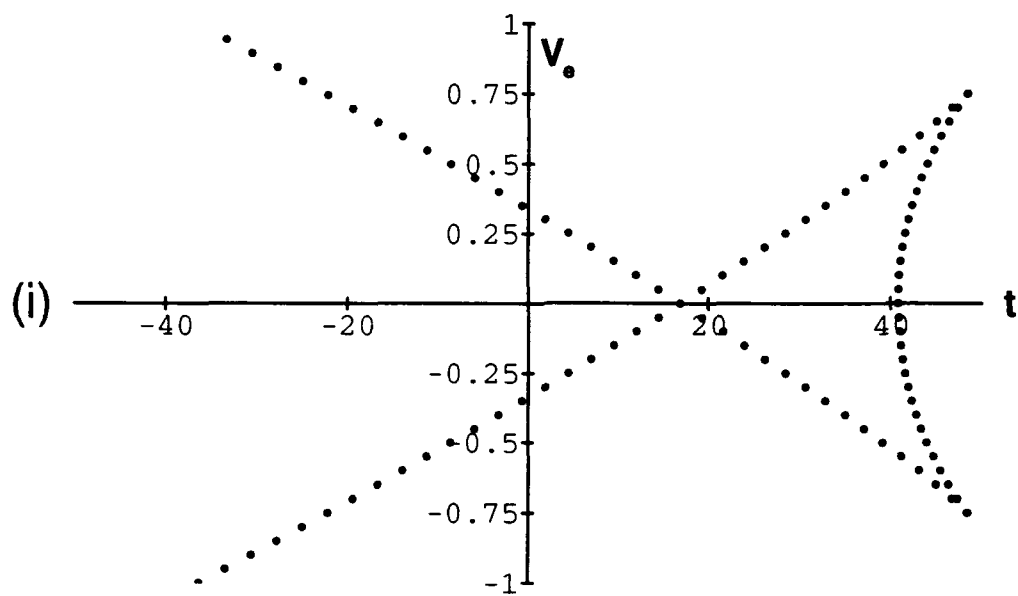
here are only two real finite solutions, corresponding to branches **1** and **2** in Fig. 18a, for

the location of the rays in the exit plane from Eqs. (21a) and (21b)

$$\frac{\partial \phi}{\partial x_i} = a_2'y_i^2 - U_e = 0, \quad \Rightarrow \quad y_i = \pm \sqrt{\frac{U_e}{a_2'}}, \tag{28a}$$

$$\frac{\partial \phi}{\partial y_i} = 2y_i\,(a_2'x_i + b_3') - V_e = 0 \Rightarrow x_i = \pm \frac{V_e}{a_2'}\sqrt{\frac{a_2'}{U_e}} - \frac{b_3'}{a_2'}. \tag{28b}$$

At the point where $b_1' = 0$ there are only two arrival times associated with signals

propagating along rays from the exit plane to the observation plane.

Figure 19 shows the evolution of the travel time cut as b_1' goes from 0.01 to

–0.01. As $b_1' \to 0$ from the positive side, Figs. 19a - 19e, the arrival time of the rays due

to the reduced distance function of the wavefront, $\phi(x,y;U_e,V_e)$, goes over to just two finite

arrival times. The two branches of the wavefront that form the wings (**1** and **2** in Fig. 18)

of the travel time cut remain finite while branch **3** moves to $t = -\infty$ at $b1' = 0$. As b_1'

becomes more negative branch **3** moves in from $t = +\infty$ to form the tail of the swallow tail

with branches **1** and **2** of the wavefront Figs. 19f - 19j.

Figure 20 shows the location of the rays in th xit plane and the travel time cut for

the same horizontal position in the observation plane relative to the cusp curve as in Fig.

18, but with $a_2' > 0$ and $b_1' = -|b_1'|$. Since a_2' and $|b_1'|$ are the same in both Figs. 18 and

19 the cusp curve and diffraction catastrophe are also the same. The only difference is in

the sign of b_1'. Note that the orientation of the travel time cut, with respect to time, in Fig.

20 is the opposite of that of Fig. 18. The orientation of the ray paths from the exit plane

that pass through points in the observation plane is also different. As the observation point

moves up from below the cusp curve, the single arrival below the cusp curve now comes

from the bottom half of the exit plane branch **1** of the wavefront in Fig. 20. The rays that

merge on the lower half of the cusp curve now originate in the upper half of the exit plane,

branches **2** and **3** in Fig. 20. Moving up through the cusp curve ray **3** moves down from

the top half of the exit plane and the signal propagating along this ray is always the last to arrive in the observation plane. Ray **1** now moves up to the left from the bottom in Fig. 20 and ray **2** moves up and to the right. Not only is the orientation with respect to time of the travel time cut different but the location of the rays in the exit plane is also changed.

Figure 20) (a) The location in the exit plane of rays to the observation plane for b_1' having the opposite sign as in Fig. 18. Rays to the vertical cut in the observation plane originate on three branches of the wavefront in the exit plane labeled **1**, **2**, and **3** in (a). The arrows indicate the migration of the rays along the branches as the vertical position in the observation plane moves up through the cusp curve. Note that the migration of the rays in the exit plane is counter clockwise which is opposite the direction of migration seen in Fig. 18a. (b) Shows the corresponding travel time curve with the signals arriving along the three branches of the travel time curve associated with the locations of the rays from the three branches of the wavefront in the exit plane marked **1**, **2**, and **3**. The arrows label the signal arrivals associated with the migrating rays in (a) indicating where the associated signals came from in the exit plane. As a guide there are four rays in (a) and the locations on the travel time curve of signals associated with these rays in (b) labeled a-d.
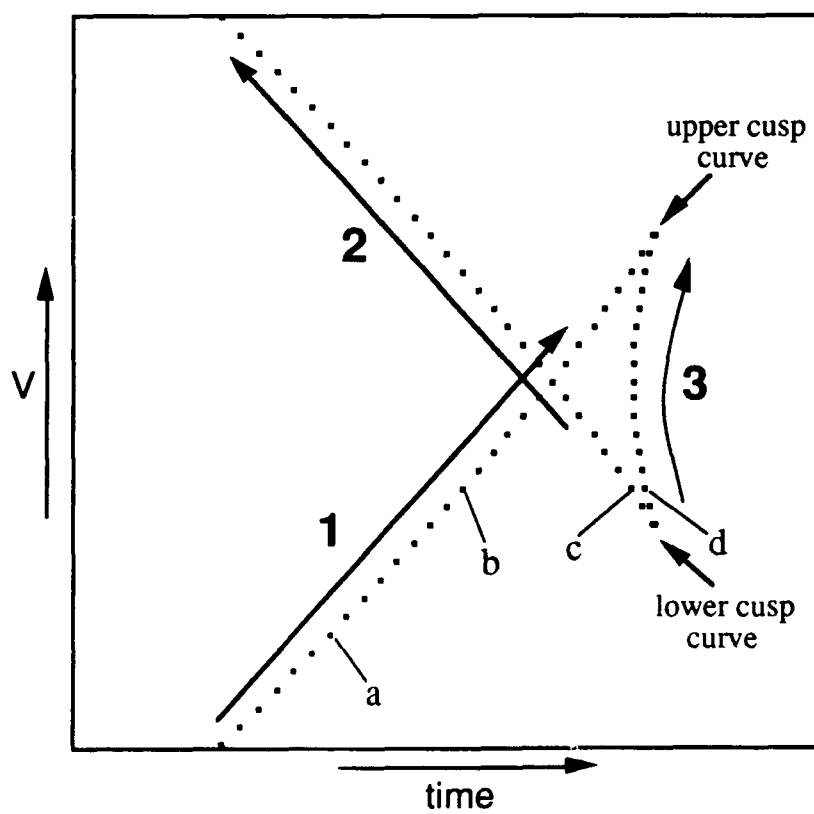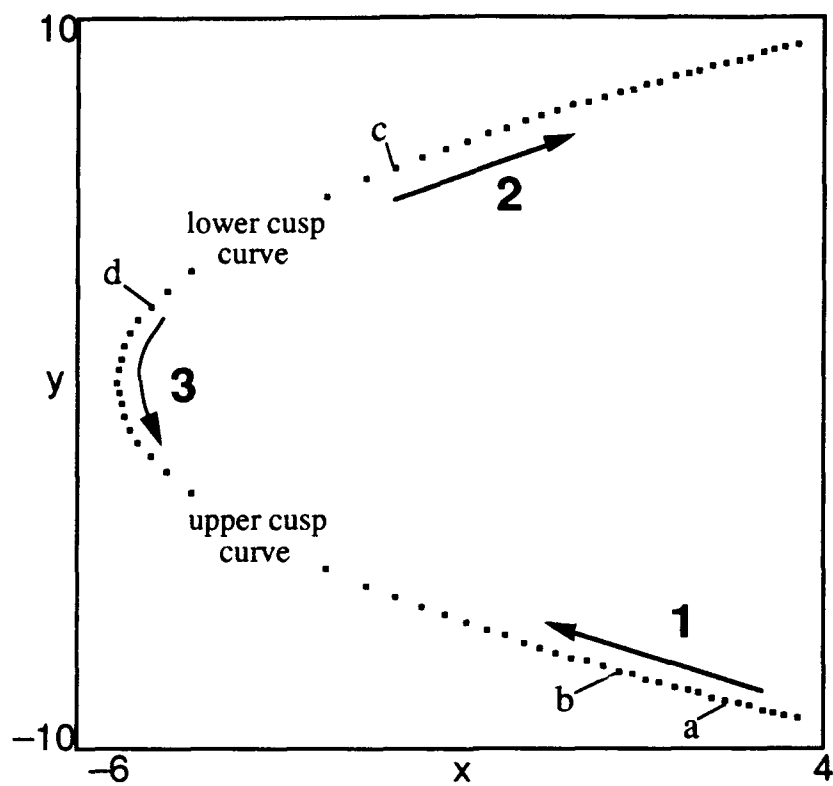
3.6 CONCLUSION

Short pulsed source signals were used to study the impulse characteristics of the wavefront that produces a TCC in a distant transverse observation plane. The travel time surface of a wavefront that forms a caustic displays the merging and disappearance of rays as an observation point crosses a caustic from the bright side to the shadow side. For the cuspoid catastrophes the travel time surfaces are described by the caustic surface of the next higher codimension catastrophe[7]. For the cusp catastrophe (for example the longitudinal cusp caustic) this means that the form of the travel time surface is the swallow tail caustic surface. The TCC, though produced by a wavefront curved in two dimensions, has the properties of the longitudinal cusp caustic. The expected travel time surface is then that of a swallow tail caustic. Calculations of the expected travel time surface from the distance function of the TCC display the expected swallow tail form superposed on a slowly varying contribution of the form ϕ_0/c where ϕ_0 is defined in Eq. (25).

Experiments to image the travel time surface were conducted using two methods for mapping the travel time surface in an observation plane. In the first method the travel time surface in the observation plane was mapped by holding the source fixed and scanning the receiver, while in the second the receiver was held fixed and the source scanned. The travel time surfaces imaged (Fig. 16) showed general agreement with the shapes of the calculated surfaces (Fig. 14). There were contributions evident of the form ϕ/c in Eq. (23) giving the expected swallow tail caustic surface and a slowly varying form ϕ_0/c from Eq. (24). To compare the shapes of calculated travel time surfaces to the experimentally measured surfaces, the travel time surface was calculated using the parameters defined by the experiment. These calculations were plotted using the same length and scale for the V_e and t axes as was used in the plots of the experimental data. With this format for displaying the data and calculations, the calculated travel time curves could be overlain on the experimental curves to compare the two. There were no scaling parameters used in the

comparison of the data and theory, only a constant offset in the initial arrival time was allowed to vary. The parameters used in the calculation were all determined by the measured surface parameters h_m and the experimental set up. When the calculated curves were overlain with the experimental curves they showed good qualitative agreement in the relative arrival times of the signals forming the travel time surfaces with a maximum difference of ± 1 μs. The comparisons, done for travel time surfaces measured using both the scanning source and the scanning receiver, showed that the measured travel time surfaces had the expected form for a cusp caustic: the swallow tail caustic form with a slowly varying contribution of the form ϕ_0/c due to the source.

In time traces that were just outside the cusp curve a tunneling ray was evident in the region inside the Stoke's set. This tunneling ray decays away from the cusp curve rapidly, agreeing with the expected exponential decay of this ray away from the cusp curve. The travel time surface was imaged using both a scanning receiver and a scanning source. This is possible due to the symmetry between the source and receiver coordinates in the description of the reflection problem. Though the experimental method used to produce the images of the travel time surface by scanning the source produced a reciprocal picture of the images produced by scanning the receiver; they none the less showed that the travel time surface and thus the diffraction catastrophe may be mapped with a moving source and a stationary receiver. The agreement between the travel time curves measured using the scanning source and the calculated travel time curves was as good as the agreement for the scanning receiver affirming the symmetry in the source and receiver coordinates of the theory describing the TCC.

The orientation with respect to time of the travel time surface is dependent on the parameter b_1' of the distance function. For $b_1' > 0$ the tail of the surface arrives first, with the ray from near the symmetry axis of the wavefront, branch **3** in Fig. (17), arriving earliest. When $b_1' < 0$ the tail arrives last and the ray from the center of the wavefront, branch **3** in Fig. (19), is the last arrival. In the frequency domain these two wavefronts

would produce the same diffraction catastrophe with only an offset in the cusp point of the cusp curve. In the time domain, the added dimension of time shows the difference between the two wavefronts by the orientation with respect to time of the travel time surfaces. The added dimension of time provides extra information that can be useful for classifying the wavefronts that produce caustics. The travel time surface provides a picture of the local shape of the wavefront after propagation from the exit plane to the region containing the observation plane.

APPENDIX A
THE CALCULATION OF THE LOCATION OF THE RAYS IN THE EXIT PLANE AND THE TRAVEL TIME SURFACE

The location of the rays in the exit plane is given by the solutions of Eqs. (21a) and (21b). Equation (21a) may be solved for x_i

$$x_i = \frac{U_e - a_2'y_i^2}{2b_1'}, \tag{A1}$$

where

$$U_e = \frac{u}{z} + \frac{u_s}{z_s}, \tag{A2}$$

and b_1' and a_2' are defined in Sec. I. Equation (A1) may be used in Eq. (21b) to get a cubic equation in y_i

$$y_i^3 - y_i \frac{1}{a_2'} (U_e + \frac{2b_1'b_3'}{a_2'}) + V_e \frac{b_1'}{a_2'^2} = 0, \tag{A3}$$

where

$$V_e = \frac{v}{z} + \frac{v_s}{z_s}. \tag{A4}$$

Equation (A3) can be rewritten as

$$y_i^3 - y_i\tilde{U} + 2\tilde{V} = 0, \tag{A5}$$

where

$$\tilde{U} = \frac{U_e}{a_2'} - \frac{U_{ec}}{a_2'}, \tag{A6}$$

$$\tilde{V} = V_e \frac{b_1'}{2a_2'^2}, \tag{A7}$$

and

$$U_{ec} = -\frac{2b_1'b_3'}{a_2'}. \tag{A8}$$

There will be three solutions to Eq. (A5). The three solutions to a cubic equation of the form of Eq. (A5) are[20]

$$y_1 = A + B, \quad y_2 = -\frac{A+B}{2} + \frac{A-B}{2}\sqrt{-3},$$

$$y_3 = -\frac{A+B}{2} - \frac{A-B}{2}\sqrt{-3}, \qquad (A9a,b,c)$$

where

$$A = \sqrt[3]{-\tilde{V} + \sqrt{\tilde{V}^2 + \frac{\tilde{U}^3}{27}}}, \qquad (A10)$$

and

$$B = -\sqrt[3]{-\tilde{V} + \sqrt{\tilde{V}^2 + \frac{\tilde{U}^3}{27}}}. \qquad (A11)$$

There will be three real and unequal solutions for y_i when $\tilde{V}^2 + \tilde{U}^3/27 < 0$ this corresponds to an observation point inside the caustic. There are three real solutions with two of the solutions equal when $\tilde{V}^2 + \tilde{U}^3/27 = 0$ this corresponds to an observation point on the caustic. When $\tilde{V}^2 + \tilde{U}^3/27 > 0$ there is one real solution and two complex conjugate solutions corresponding to an observation point outside the caustic.

A FORTRAN program was written to solve for the locations of rays in the exit plane. Since the solutions of Eqs. (A3) and (A5) depend on the location of U_e relative to the cusp point U_{ec} the initial value of U in the program was $U = U_e - U_{ec}$. The vertical position of the cusp point was taken to be zero in the observation plane so there was no need to alter V_e relative to the cusp point to solve for the rays. The cube roots in Eqs. (A10) and (A11) were calculated by simply raising the argument $-\tilde{V} + (\tilde{V}^2 + \tilde{U}^3/27)^{1/2}$ to the 1/3 power. There were complications as there are three different cube roots of the argument. The difficulty arose when the real part of the argument was negative and the root obtained was not along the proper branch cut of the cube root. A complex number can be expressed as $z = z_r + iz_i = re^{i\phi}$ where $r = (z_r^2 + z_i^2)^{1/2}$ is the magnitude of the complex number and ϕ is the phase $\phi = \tan^{-1}(z_i/z_r)$. The cube root of z is then

$$\sqrt[3]{z} = \sqrt[3]{z_r + iz_i} = \sqrt[3]{r}\exp\left[i\frac{\phi}{3}\right], \qquad (A12)$$

where the three roots of z are due to the phase ϕ being multivalued (ϕ can be ϕ, $\phi + 2\pi$, $\phi + 4\pi$, ..). Unique values of $z^{1/3}$ are obtained for $\phi = \phi$, $\phi + 2\pi$, and $\phi + 4\pi$. When z = -1 there are three cube roots: -1, $\cos(\pi/3) + i\sin(\pi/3)$, or $\cos(5\pi/3) + i\sin(5\pi/3) = \cos(\pi/3) - i\sin(\pi/3)$. When $(-1)^{1/3}$ is computed using standard VMS Fortran by raising the complex variable z = -1 to the 1/3 power it returns $\cos(\pi/3) + i\sin(\pi/3)$ which is the result if $z = -1 = 1e^{i\pi}$ however the desired root is $(-1)^{1/3} = -1$. This occurs because VMS Fortran assumes phases between $-\pi/4$ and $\pi/4$ thus all the results are along the positive real axis. As an example for z = -1 + i0, the computer gives a phase of $\phi = 0$ radians. In order to assure cube roots along the negative real axis were preserved, the algorithm developed used $(z)^{1/3} = -1(-z)^{1/3}$ when the real part of z was negative.

To find the arrival time of each ray, Eq. (24) was used with c = 0.148 cm/μs, the speed of sound for water at 18° C. The initial values of U_e and V_e used to find x_i and y_i were split into u and v using Eqs. (A2) and (A4) and a given source location. These values of u, v, u_s, and v_s were then used to find the source and receiver distances from the origin in the exit plane

$$r_s = \sqrt{z_s^2 + u_s^2 + v_s^2}, \qquad (A12)$$

and

$$r = \sqrt{z^2 + u^2 + v^2}, \qquad (A13)$$

respectively. This provided the slowly varying term ϕ_0 in Eq. (25). The ray locations (x_i, y_i) in the exit plane were used in $\phi(x_i, y_i, U_e, V_e)$ from Eq. (14) to calculate the travel time surface contribution due to the shape of the reflecting surface. The two travel time contributions could then be plotted separately as in Figs. 7a and 6b or summed to give the actual travel time surface as in Fig. 7c.

References

1)   M. G. Brown, "The transient wave fields in the vicinity of the cuspoid caustics," J. Acoust. Soc. Am. **79**(5), 1367-1384 (1986).

2)   M. V. Berry and C. Upstill, "Catastrophe optics: Morphologies of caustics and their diffraction patterns," in *Progress in Optics*, ed E. Wolf (North Holland, Amsterdam, 1980), Vol. 18, pp 257-346.

3)   T. Pearcey, "The structure of an electromagnetic field in the neighborhood of a cusp of a caustic," Philos. Mag. **37**, 311-317 (1946).

4)   P. L. Marston and C. K. Frederickson, "Wavefields of linear cusp caustics germane to nonlinear foci, " in *Frontiers of nonlinear acoustics, Proceedings of 12th ISNA*, ed M. F. Hamilton and D. T. Blackstock (Elsevier Science Publishers Ltd, London, 1990), pp 203-208.

5)   P. L. Marston, "Transverse cusp diffraction catastrophe: Some pertinent wavefronts and a Pearcey approximation to the wave fields," J. Acoust. Soc. Am. **81**, 226-232, (1987).

6)   F. J. Hilterman, "Seismic Imaging," in *Acoustic Imaging* **9**, ed. K. Y. Wang (Plenum Press, New York, 1990), pp 653-679.

7)   G. Danglemayr and W. Güttinger, "Topological approach to remote sensing," Geophys. J. R. astr. Soc.,**71**,pp 79-126, (1982).

8)   F. J. Hilterman, "Three-dimensional seismic modeling," Geophysics **35**, 1020-1037 (1970).

9)   M. G. Brown and F. D. Tappert, "Catastrophe theory, caustics and traveltime diagrams in seismology," Geophys. J. R. astr. Soc **88**, 217-229 (1986).

10)   G. L. Choy and P. G. Richards, "Pulse distortion and Hilbert transformation in multiply reflected and refracted waves," Bull. Seism. Soc. Am. **65**, 55-70 (1975).

11)   M. G. Brown, "On the singularity index and the unfolding of the diffraction catastrophes," Wave Motion **9**, 107-110 (1987).

12)   P. L. Marston, "Geometrical and catastrophe optics methods in scattering," for *High Frequency and Pulsed Scattering*, Physical Acoustics **20** or **21**, ed. R. N. Thurston and A. D. Pierce, (Academic Press).

13)   P. L. Marston, "Surface shapes giving transverse cusp catastrophes in acoustic or seismic echoes," in *Acoustical Imaging* vol 16, ed. L. W. Kessler, (Plenum, New York, 1988), pp. 579-588.

14)   C. K. Frederickson and P. L. Marston, "Transverse cusp diffraction catastrophes produced by reflecting ultrasonic tone bursts from curved metal surfaces," in *Elastic Waves and Ultrasonic Nondestructive Evaluation*, ed. S. K. Datta, J. D. Achenbach and Y. S. Rajapakse (Elsevier Science Publishers B. V., North-Holland, 1990), pp 411-413.

15) M. R. Layton, E. F. Carome, H. D. Hardy and J. A. Bucaro, "Effects of diffraction on stress pulse propagation," J. Acoust. Soc. Am., **64**, pp 250-256, (1978).

16) R. Thom, *Structural Stability and Morphogenesis An Outline of a General Theory of Models*, (W. A. Benjamin Inc., Reading, Mass., 1975), pp 64-67.

17) D. P. Hill, "Phase shift and pulse distortion in body waves due to internal caustics," Bull. Seism. Soc. Am., **64**, 1733-1742, (1974).

18) L. B. Felsen, "Evanescent waves," J. Opt. Soc. Am., **88**, pp 751-760, (1976).

19) F. J. Wright, "The Stokes set of the cusp diffraction catastrophe," J. Phys. A: Math. Gen., **30**, (1980), 2913-2928.

20) *CRC Standard Mathematical Tables 26th edition*, ed. W. H. Beyer (CRC Press, Boca Raton, Florida, 1984), p 9.

CHAPTER FOUR

SHAPES OF TRANSIENT ECHOES NEAR TRANSVERSE CUSP CAUSTICS PRODUCED IN REFLECTIONS FROM CURVED SURFACES

4.1 INTRODUCTION, REVIEW, AND OVERVIEW

As discussed in Chapters 2 and 3, transverse cusp caustic is formed by the reflection of sound from a surface with the local shape given by Eq. (9) below. In the vicinity of the caustic, the temporal shape of the signals arriving in the observation plane is seen to depend on position. This is evident from inspection of the data given in Chapter 3. The temporal shape of the reflected signals is either that of the incident signal or a distorted shape due to touching a caustic prior to arrival in the observation plane. The theoretical basis of this is discussed below. The principal objective of Chapter 4 is to identify which echoes have touched caustics and which echoes have not by examining their shape. While the emphasis is on reflection from a surface having the shape of Eq. (9), consideration is given to more general aspects of the problem of classifying transient arrivals.

When a ray touches a caustic (ie. is tangent to the curve describing the caustic not simply crossing the caustic) high frequency components of the signal propagating along the ray, after passing the point where the ray path touches the caustic, undergo a $\pi/2$ phase advance [1]. The phase advance affects each high frequency component of a signal that has passed a caustic thus distorting the shape of the signal. After touching the caustic, the shape of the distorted signal is given approximately by the Hilbert transform of the shape of the signal prior to touching the caustic. For a transient signal the Hilbert transform shape will contain an infinite precursor giving the distorted signal an arrival time [2,3,4,5] of $t = -\infty$. Though the precursor is not eliminated, it may be reduced to finite t by consideration of the frequency dependence of the phase advance due to touching the caustic [2].

Prior to discussing the transient formulation some relevant aspects of catastrophe theory will be reviewed. Structurally stable caustics have been organized and classified by

catastrophe theory according to the corank and codimension of an associated general distance function in the phase of a diffraction integral $\Phi(\mathbf{a},\mathbf{C})$[3,6,7]. The diffraction integral has the general form

$$P(C) = \int_{-\infty}^{\infty} b(\mathbf{a},\mathbf{C})\exp[ik\ \Phi(\mathbf{a},\mathbf{C})]\ d\mathbf{a}$$ where the a_i are state variables (ray parameters in the

ray approximation), the C_i are controls parameters (these could be characteristics of the media or coordinates in an observation plane), and $b(\mathbf{a},\mathbf{C})$ is a slowly varying amplitude function[3]. The codimension of a caustic K is the number of control parameters C_i needed to describe the caustic. The corank of a caustic N is the number of state variable a_i needed to describe the most singular section of the catastrophe associated with the caustic. The caustic itself is defined by the locus of points where the gradient map from state space to parameter space is singular[3,6], where the ray condition $\partial\Phi/\partial\mathbf{a} = 0$ and $\partial^2\Phi/\partial\mathbf{a}^2 = 0$.

The cuspoid caustics are the caustics with corank one (they only have one state variable). The distance function of a cuspoid caustic has the general form with $\mathbf{a} = x$ of $\Phi(x,C) = x^{K+2}/(K+2) - C_K x^K/K - C_{K-1}x^{K-1}/(K-1) - ... - C_1 x$, where $K = 0, 1, 2, ...$ is the codimension of the caustic. The longitudinal cusp caustic is a cuspoid caustic of codimension two that opens roughly parallel to the direction of propagation of the wavefront, as seen in Figs. 21 and 22 below. This caustic, also known as the axial cusp caustic, is formed by the smooth joining of two fold caustics (cuspoid caustics of codimension one) coming together at an arête[8]. The longitudinal cusp caustic, near the arête, has the general form given by Eq. (8) below with D_T replaced by D_L, a longitudinal opening rate with units of 1/distance. U_e and U_{ec} replaced by z and z_{cp}, the distance from the exit plane to the observation point and arête respectively, and V replaced by the distance x, the normal offset from the symmetry axis of the caustic. The distance function of the longitudinal cusp caustic has the general form $\Phi(x,\mathbf{w}) = x^4/4 - w_2 x^2/2 - w_1 x$, and the diffraction catastrophe decorating the caustic is given by the Pearcey function $P(w_2,w_1)$ where [9] $w_2 \propto z$ and $w_1 \propto u$.

A transverse cusp caustic (TCC), Fig. 6, is a cusp caustic, described by Eq. (8) below, opening roughly transverse to the direction of propagation[10]. Though the distance function of this caustic has two state variables [a = (x,y)], the TCC has all the properties in parameter space of the cuspoid caustic of codimension two (a longitudinal cusp caustic). Like the longitudinal cusp caustic the diffraction catastrophe that decorates the TCC is given by the Pearcey function[10] where now $w_2 \propto u$ and $w_1 \propto v$. The travel time surface of the TCC has the general form of the singular surface of the next higher codimension catastrophe the swallow tail catastrophe shown in Fig. 8. The signals propagating along the rays forming the TCC also should have the same arrival sequence as the signals that form the longitudinal cusp caustic. The number of ray paths through an observation point that have touched the caustic surface should depend on the orientation of the caustic surface relative to the locations of the rays in the exit plane in a manner similar to that of the longitudinal cusp caustic.

Chapter 4 gives a brief heuristic explanation of the $\pi/2$ phase advance associated with rays that touch caustics in Sec. 2.A. In 2.B the effect of the phase advance on the shape of the signal is discussed. Section 3 specializes to the rays that form the TCC with a brief review of the caustic and travel time surfaces in Sec. 3.A. In Sec. 3.B some data showing the sequence of signal arrivals when b_1' and a_2', as defined in 3.A, are greater then zero is analyzed. In Sec. 4 the relation of the parameters describing the wavefront that forms a TCC to the sequence of the signals arriving in the observation plane is discussed. Section 5 discusses the arrivals shown in Sec. 3.B as they relate to the expected arrivals given by Sec. 3.A and the sequence of arrivals for the longitudinal cusp caustic.

4.2 A REVIEW OF THE EFFECT ON SIGNALS PROPAGATING ALONG RAYS THAT TOUCH CAUSTICS AND THE HILBERT TRANSFORM

A. A HEURISTIC EXPLANATION OF THE PHASE CHANGE USING RAY TUBES

The $\pi/2$ phase advance of a ray that touches a caustic can be explained by looking at the behavior of a ray tube that touches a caustic. A ray tube consists of all the rays that pass through a small surface area transverse to the ray paths at x_0 as shown in Fig. 1. Moving along the ray paths, the cross-sectional area of the ray tube will increase or decrease depending on the curvature of the wavefront. For a wavefront that is curved in two directions there will be two principle radii ρ_1 and ρ_2 which describe the curvature of the wavefront. The time dependence used in the discussion below is $\exp(-i\omega t)$. In a small region around a given point, the wavefront shape may be approximated by[8] $W(x,y) \approx$ constant $- x^2/2\rho_1 - y^2/2\rho_2$, where the ρ_i are negative (for a concave surface along the direction of propagation) positive (for a convex surface) or of opposite sign (for a saddle shaped surface). Figure 2 shows a wavefront moving in the direction of $\hat{n}$. For the wavefront shown in Fig. 2 the principle radius is negative at x_0, goes to zero on the caustic at x_c, and is positive at x. The bounding rays of the ray tube, labeled 1 and 2, exchange positions on each side of the caustic due to the change in the curvature of the wavefront.

The amplitude along a ray tube is inversely proportional to the square root of the cross sectional area of the tube. If the amplitude at $x_0 = (x_0,y_0)$ is given by the complex pressure $P(x_0)$, then at $x = (x,y)$ the amplitude is given by[8]

$$P(x) = P(x_0) \sqrt{\frac{A(x)}{A(x_0)}} , \tag{1}$$

where $A(x)$ is the cross sectional area of the ray tube at x. The dependence of the amplitude on the area of the ray tube may also be described in terms of the principle radii of the wavefront at a given point in space. In terms of the principle radii the amplitude at x is[8]

$$P(x) = P(x_0) \sqrt{\frac{\rho_1 \rho_2}{(q+\rho_1)(q+\rho_2)}} \quad , \tag{2}$$

where $q = |x - x_0|$ is the distance along the ray tube from x_0 to x and ρ_1 and ρ_2 are the principle radii at x_0. The quantities $q + \rho_1$ and $q + \rho_2$ in Eq. (2) are the new principle radii of the wavefront after propagation from x_0 to x.

A caustic is formed when one of the local principle radii ($q + \rho_i$) goes to zero, as for example, when $\rho_1 < 0$ and $q = |\rho_1|$. From Eq. (2), the amplitude of the signal propagating along a ray tube diverges where the ray tube touches a caustic. Provided $q \neq -\rho_2$ at the same point, there will be a change in the sign of the ratio of the product of the principle curvatures $(\rho_1\rho_2)/[(q+\rho_1)(q+\rho_2)]$. This sign change gives a $(-1)^{1/2}$ factor to $P(x)$ due simply to touching the caustic. This factor can be represented by a phase change of $\pi/2$ for positive frequencies as $\exp[i\pi/2] = i = (-1)^{1/2}$. After touching the caustic the phase of the signal is $\exp[i(kq + \pi/2)]$, thus the signal is phase advanced by $\pi/2$.
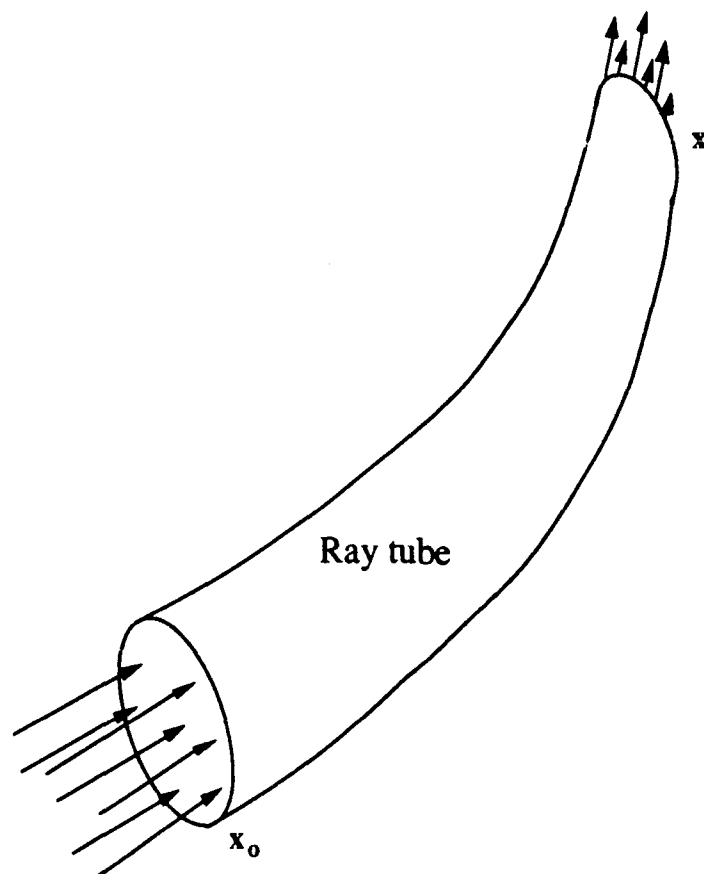
Figure 1) A ray tube that contains all the rays entering normal to the cross sectional area of the tube at x_0 and leaving normal to the cross sectional area of the tube at x. The amplitude of the signal propagating along the ray tube at any point along the tube is proportional to the cross sectional area of the tube at that point.
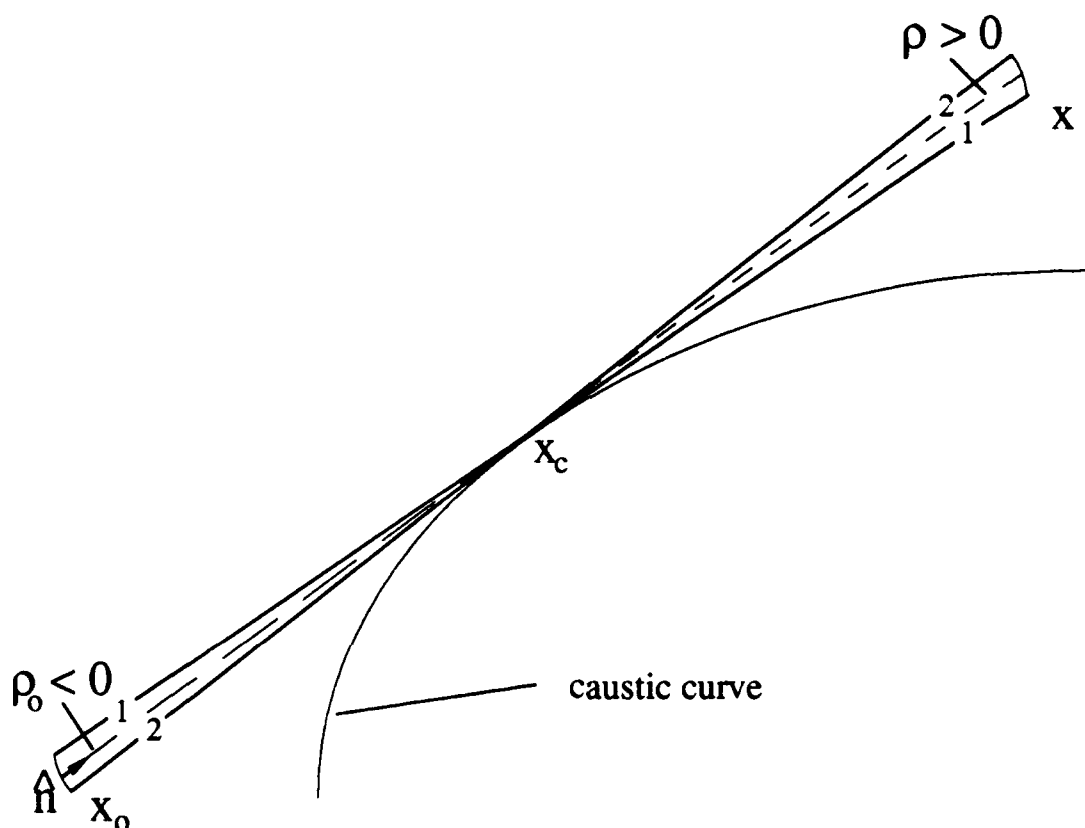
Figure 2) The change in the curvature of the wavefront after touching a caustic is shown at points x_0 and x. At x_0 the ray tube bounded by rays 1 and 2 is travelling along the direction given by the unit vector $\hat{n}$ towards the caustic with the principle radius $\rho_0 < 0$. At the caustic, x_c, both the area of the ray tube and the principle radius go to zero. After touching the caustic at the point x_c the positions of the rays 1 and 2 switch and the principle radius at x is $\rho > 0$.

B. EFFECT OF THE PHASE ADVANCE ON THE PULSE SHAPE

A transient signal propagating along a ray path that has touched a caustic will contain many frequency components each of which, in the high frequency approximation, is phase advanced by $\pi/2$. The phase advance produced by touching the caustic changes the shape of a transient signal. The shape of the phase advanced signal can be found by examining the effect of the phase advance on the Fourier transform of the signal, where for an initial signal with the shape $s(t)$

$$\underline{s}(\omega) = \frac{1}{\sqrt{2\pi}} \int_{-\infty}^{\infty} s(t) \, e^{-i\omega t} \, dt \, , \tag{3}$$

is the Fourier transform of $s(t)$. For real $s(t)$, $\underline{s}(-\omega) = [\underline{s}(\omega)]^*$ where the '*' means to take the complex conjugate. The phase advanced signal is represented by $h(t)$ and it's Fourier transform

$$\underline{h}(\omega) = \frac{1}{\sqrt{2\pi}} \int_{-\infty}^{\infty} h(t) \, e^{-i\omega t} \, dt. \tag{4}$$

The change in the pulse shape occurs due to the phase advance of each spectral component of the pulse. Thus the Fourier transforms of the initial and phase advanced signals are related by

$$\underline{h}(\omega) = \underline{s}(\omega) \exp[i\frac{\pi}{2} \, \text{sgn}(\omega)], \tag{5}$$

where $\text{sgn}(\omega) = \omega/|\omega| = \pm 1$. The $\text{sgn}(\omega)$ factor is necessary to assuring that the phase of the negative frequency components is phase advanced by adding a negative $\pi/2$ to the phase. The $\text{sgn}(\omega)$ term also assures that $h(t)$ is real by forcing $\underline{h}(\omega) = \underline{h}^*(-\omega)$.

Using Eqs. (3) and (5) and the inverse Fourier transform of $\underline{h}(\omega)$, the phase advanced signal is

$$h(t) = \frac{1}{\sqrt{2\pi}} \int_{-\infty}^{\infty} \underline{h}(\omega) \; e^{i\omega t} \; d\omega = \frac{1}{\sqrt{2\pi}} \int_{-\infty}^{\infty} \exp[i\frac{\pi}{2} \, \mathrm{sgn}(\omega)] \; \underline{s}(\omega) \; e^{i\omega t} \; d\omega$$

$$= \frac{1}{2\pi} \int_{-\infty}^{\infty} d\omega \int_{-\infty}^{\infty} \exp[i\frac{\pi}{2} \, \mathrm{sgn}(\omega)] \; s(t') \; e^{i\omega(t-t')} \; dt'. \tag{6}$$

Equation (6) may be rewritten using $\exp[i(\pi/2)\mathrm{sgn}(\omega)] = i$ for $\omega \geq 0$ and $-i$ for $\omega < 0$

$$h(t) = \frac{1}{\pi} \int_{-\infty}^{\infty} d\omega \int_{-\infty}^{\infty} s(t') \; \sin[\omega(t' - t)] \; dt'. \tag{7}$$

Equation (7) is called the allied integral of the Fourier integral and h(t) = H[s(t)] is the Hilbert transform (HT) of s(t) [2,5,11,12]. The HT is commonly written in terms of the principal [3,4,5,7,9,11,12] of convolution of the source signal with the impulse response of a caustic given by $-1/\pi t$. Some examples of HT pairs are given in Table I. The HT is said to be skew-reciprocal[12] in that if H[s(t)] = h(t) then H[h(t)] = −s(t). Performing two consecutive HT's on a function corresponds to a π phase advance of the function giving −1s(t) while four consecutive HT's corresponds to a 2π phase advance and the function is unchanged.

From Eq. (5) it is possible to calculate the HT of a sampled pulse s(t) by computing the Fourier transform $\underline{s}(\omega)$ multiplying it by i sgn(ω) and inverting the transform. A computer program was written to calculate the HT's of digitized time signals. The IMSL Fast Fourier Transform (FFT) routines were used. Table II shows a schematic of how the HT was calculated. An input signal s(t) was FFT'd giving $\underline{s}(\omega)$. The first half of $\underline{s}(\omega)$ was multiplied by i and the second half by −i, then inverse FFT'd to arrive at the HT of the input signal. The second half of the frequency spectrum represents negative frequencies thus the multiplication factor of −i to get the negative frequency components of the phase advanced spectrum. The inverse FFT of the phase advanced frequency spectrum gives the temporal form of the signal that has been phase advanced by a factor of $\pi/2$.

Table I Some functions [s(t)] and their Hilbert transforms [h(t)].

s(t)	h(t)
$\cos(t)$	$-\sin(t)$
$\dfrac{1}{1+t^2}$	$-\dfrac{t}{1+t^2}$
$\delta(t)$	$-\dfrac{1}{\pi t}$
$\exp[iat],\ a > 0$	$\exp[iat + \dfrac{i\pi}{2}]$

Table II The algorithm used to calculate the Hilbert transforms of digitized time traces.

(input signal)

$s(n\Delta t)$ n=1,N$\rightarrow$

$FFT[s(n\Delta t)] = \underline{s}(n\Delta\omega) \rightarrow$

for n=1,$\dfrac{N}{2}$ $\underline{h}(n\Delta\omega) = i\underline{s}(n\Delta\omega)$, for n=$\dfrac{N}{2}$ + 1,N $\underline{h}(n\Delta\omega) = -i\underline{s}(n\Delta\omega)\rightarrow$

$\dfrac{1}{N} FFT^{-1}[\underline{h}(n\Delta\omega)] = h(n\Delta t)$

(output signal)
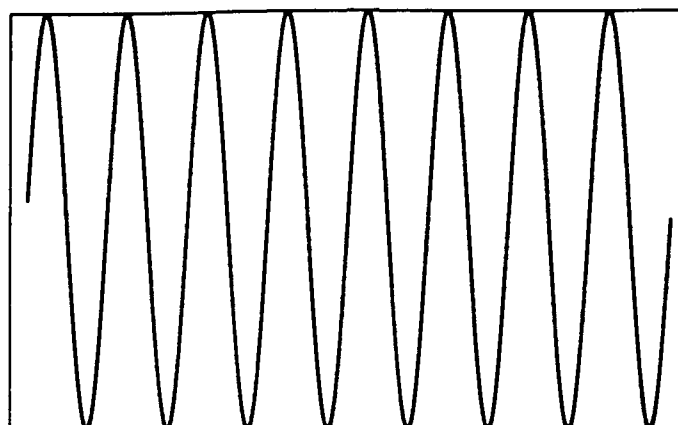
a
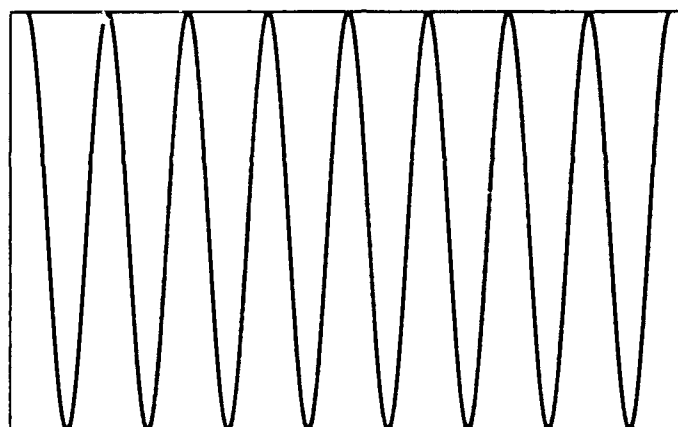
b

Figure 3)(a) A continuous sine wave of frequency 64, sin($2\pi t/64$). (b) The Hilbert

transform of (a). Since there is only one frequency component in (a) the Hilbert transform

can be written down directly as sin($2\pi t/64 + \pi/2$) = cos($2\pi t/64$). The signal in (a) was

used as a test for the Hilbert transform algorithm used to calculate the Hilbert transforms of

digitized time signals.

Figure 3 shows a trial input signal used in the computer program and it's resulting HT. In Fig. 3a $s(t) = \sin(2\pi t/64)$ and was used as a test of the algorithm used for calculating HT's. From Table I the HT of $\sin(t)$ can be found using the skew-reciprocal relationship between HT pairs. The HT of $\sin(t)$ is $H[\sin(t)] = H[-H[\cos(t)]] = -H[H[\cos(t)]] = --\cos(t) = \cos(t)$, as expected since there is only one frequency component and thus $H[\sin(t)] = \sin(t + \pi/2) = \cos(t)$. Figure 3b shows the HT of $\sin(2\pi t/64)$, $H[\sin(2\pi t/64)] = \cos(2\pi t/64)$, confirming that the HT algorithm was working correctly for the case considered.

Figure 4 shows the HT, computed by the above algorithm, of a single cycle sine burst of frequency $f = 1/64$ Hz. The dashed line is the input signal $s(t)$ and the solid line the HT, $h(t) = H[s(t)]$. Cron and Nuttall [13] analytically calculate the HT of a similar pulse. The results they obtain are the same for a $\pi/2$ phase advance with the $h(t)$ shape being symmetric about the center of the $s(t)$ shape and having the precursor and tail seen in Fig. 4. Consider that either $s(t)$ or $h(t)$ represents the signal propagating along a ray that originates on a hypothetical wavefront W in a uniform medium. If the ray path does not touch a caustic, the signal at the observation point will arrive with the shape shown by the dashed line in Fig. 4. The arrival time will be given by the distance along the ray path from the wavefront to the observation point, q, divided by the speed of sound, c, $t = qc$. If, however, W forms a caustic before arriving at the observation point and the ray path to the observation point touches this caustic the signal propagating along the ray path will arrive with the approximate shape given by solid curve in Fig. 4. Though this signal has travelled geometrically the same distance as the signal that does not touch the caustic, components of it appears to arrives at the observation point earlier then the geometrically expected arrival time.

For a signal to be causal it can not arrive at an observation point prior to the time it takes to propagate from the point of origin of the signal to the observation point. The precursor seen in Fig. 4 arrives at the observation point earlier then $t = q/c$. If the signal is
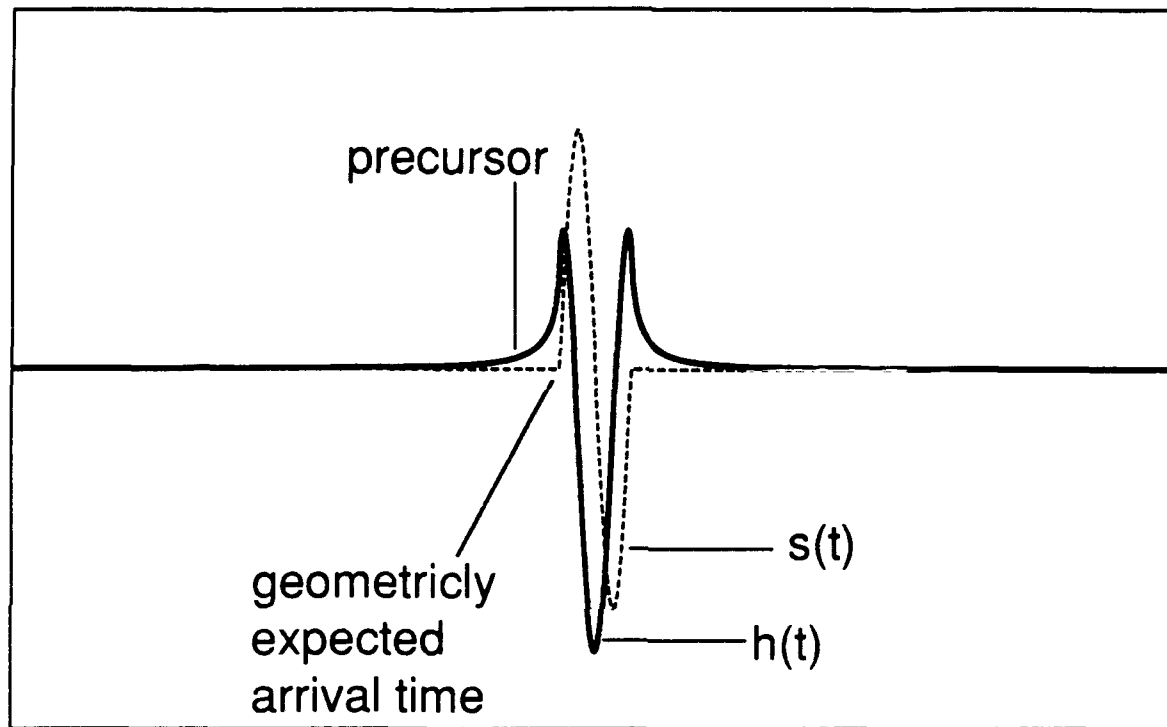
Figure 4) A single cycle sine burst s(t) (dashed curve) and its Hilbert transform h(t) (solid curve). The sine burst is a causal signal as it turns on abruptly at the arrival time of the ray. The Hilbert transform of s(t), h(t), is a noncausal pulse due to the precursor, shown in the figure, that arrives ahead of the expected arrival time of the ray.

assumed to have traveled along the ray path a distance q then the precursor in Fig. 4 is not causal. For an impulse signal the precursor seen in Fig. 4 would extend to [3] $t = -\infty$. Apparently noncausal precursors have been discussed in some vary different manners, though the final resolution with causality is perhaps most clearly seen in the analysis given by Hill [2] reviewed below.

Tolstoy [4] and Pierce [14] use the example of plane waves totally reflected by a half-space of higher sound speed. The totally reflected ray undergoes a $\pi/2$ phase advance ar.d has the Hilbert transform shape of the incident ray and thus the precursor. The infinite precursor in this situation is associated with a surface wave that travels in the higher sound speed media. The source is assumed to be at infinity so that plane waves are assumed. Tolstoy generalizes this explanation of the precursor to the caustic observed in the reflection of sound by a stratified half-space where the speed of sound increases uniformly with depth. The turning point of a stratified medium is analogous to the boundary between two uniform media, in that the turning point is the apparent depth at which plane waves incident past the critical angle for total reflection are totally reflected. When a point source is locatea above a stratified half-space a caustic is formed in the half-space by rays that are reflected back out of the half-space. Tolstoy shows that in the limit of the source point moving away to ∞ (the source signal becoming plane waves) the caustic formed in the half-space goes over to the turning point of the stratified media. Then the explanation given for the precursor is the same as that for the reflection of plane waves from a half-space given above.

To deal with the apparent noncausal nature of the phase advanced pulses at caustics, Brown and Tappert have developed a set of rules that are supposed to govern the formation of caustics by wavefronts that are not aperture limited[7,15]. To satisfy causality Brown and Tappert require that all noncausal signals be preceded by a causal signal and that the noncausal precursor not extend beyond the earlier causal arrival. Brown and Tappert state that for a general wavefront, defined by a function of position along a single direction

transverse to the direction of propagation (Figs. 21 and 22 are examples), to be causal it must be organized in terms of cuspoid caustics of even codimension. This requirement means that a fold caustic (K=1) must always be part of at least a cusp caustic (K=2), and a swallow tail caustic (K=3) must be at least part of a butterfly caustic (K=4). By requiring that two dimensional wavefronts, as described above, be organized in terms of cuspoid caustics with K even, there will always be an odd number of ray paths through an observation point. The order by which signals propagating along these ray paths can arrive at the observation point is further restricted. If the causal shape of the initial signal is given by s(t) and the HT noncausal signal shape is h(t), then Brown and Tappert require:

(I) The total number of arrivals N is odd. If N = 1 then this arrival must be a causal s(t) type arrival. When N > 1 there must be 1 more s(t) type arrival then h(t) type arrivals.

(II) When N > 1 each h(t) type arrival must be preceded by two s(t) type arrivals.

(III) When N > 1 the last arrival must an h(t) type arrival.

For caustics formed in three space dimensions, there are similar requirements along with an added signal type of –s(t).

(I) The same as I for two dimensions except that now the number of h(t) type arrivals must be one less then the total of s(t) and –s(t) type arrivals.

(II) Each –s(t) type arrival must be preceded by an s(t) and an h(t) type arrival.

(III) Each h(t) type arrival must be preceded by an s(t) type arrival.

(IV) The last arrival must be either an h(t) or –s(t) type arrival, precluding the trivial single s(t) type arrival.

The restrictions above allow for the arrival of noncausal h(t) type signals as long as they are preceded by causal s(t) type signals.

The precursor is in part an effect of the high frequency approximation used in ray theories. The $\pi/2$ phase advance produced in rays that touch caustics is a high frequency phenomenon, for low frequencies the phase advance tends to zero. In the HT all frequencies in the spectrum of s(t) are phase advanced by $\pi/2$ to produce h(t). This

introduces low frequency components into the precursor that may contribute to the noncausal shape[2]. Hill states that the shape of the actual pulse is modified by this frequency-dependent behavior of the phase shift, maintaining causality [2]. Hill compares the shapes of the calculation of the HT of a causal pulse shape and an exact numerical calculation of the pulse after propagation along a ray path that touches a caustic. The frequency response of the exact calculation is analyzed to show that as the frequency decreased the phase advance also decreased, tending to zero as the frequency went to zero. The shape of the HT pulse and the exact calculation were similar, although the exact calculation contained a shorter and more abrupt precursor. By including the frequency-dependence of the phase shift the precursor in the HT pulse no longer extends to $t = -\infty$.

The exact numerical calculation performed by Hill of the shape of a transient signal that has touched a caustic showed that the transformed pulse had a finite duration precursor. This precursor still arrives with energy prior to the arrival time predicted by propagation along the geometrical ray path. This apparently noncausal arrival may be explained if the signal actually travels along a different path that is shorter then the geometrical ray path as discussed below. Elementary ray theories use independent locally plane waves that propagate along the ray paths (straight lines in homogeneous media) to construct the wavefield. The field at any given point is then the superposition of these plane waves. Near a caustic, however, the independent plane-wave character of the fields is not applicable [16].

A method for dealing with ray fields near caustics is to use, instead of plane waves with real phases, plane waves with a complex phase (evanescent plane waves)[16,17,18]. The local tracking of evanescent plane-wave fields shows that signals near a caustic move along phase paths that are defined to be normal to the surfaces of constant phase [17]. For a Gaussian beam, which goes through a focus at its most narrow point (the beam waist), the phase paths are actually hyperbola centered around the beam waist. Components of the signals in a Gaussian beam travel along the hyperbolic phase paths as opposed to the

geometrical straight line rays that cross in the beam waist. The distance along the phase paths is shorter then the distance along the straight line rays. Boyd [19] has shown that the difference in the path lengths can account for the π phase advance of the signal after passing through the focus. Though the signals travel along trajectories given by the phase paths, the phase paths are not actual rays. A ray in a homogeneous medium is defined as a straight line with real direction cosines for a real ray. Phase paths in a homogeneous medium near a caustic are in general not straight lines. The direction cosines become complex for a complex ray where a complex ray is one that travels in a complex space [17]. For the evanescent waves used to describe the fields near caustics, a phase path in real (physical) space is the locus of points of the intersection of complex rays with the real plane [16,17,18]. Signals that travel along phase path trajectories near caustics, as opposed to along the straight line geometric ray paths, may actually travel a shorter distance and thus arrive earlier then the times predicted for travelling along the ray paths.

4.3 THE ARRIVAL SEQUENCE OF THE TRANSVERSE CUSP CAUSTIC

A. THE EXPECTED ARRIVAL SEQUENCE FOR A TRANSVERSE CUSP CAUSTIC PRODUCED BY REFLECTION FROM A CURVED SURFACE

The general wavefront shape in an exit plane given by $W(x,y) = a_1x^2 + a_2xy^2 + a_3y^2$ forms a three dimensional caustic surface similar to that shown in Fig. 5. An observation plane parallel to the exit plane some distance z away that cuts through this caustic surface exhibits a transverse cusp caustic, Fig. 6. The TCC is a cubic cusp curve given by

$$D_T(U - U_c)^3 = V^2, \qquad (8)$$

where D_T is a unitless opening rate and U and V are unitless observation coordinates given by u/z and v/z respectively. The caustic is symmetric about the u axis in the observation plane and the cusp point is located at $u_c = U_c z$, $v_c = 0$. The diffraction catastrophe that
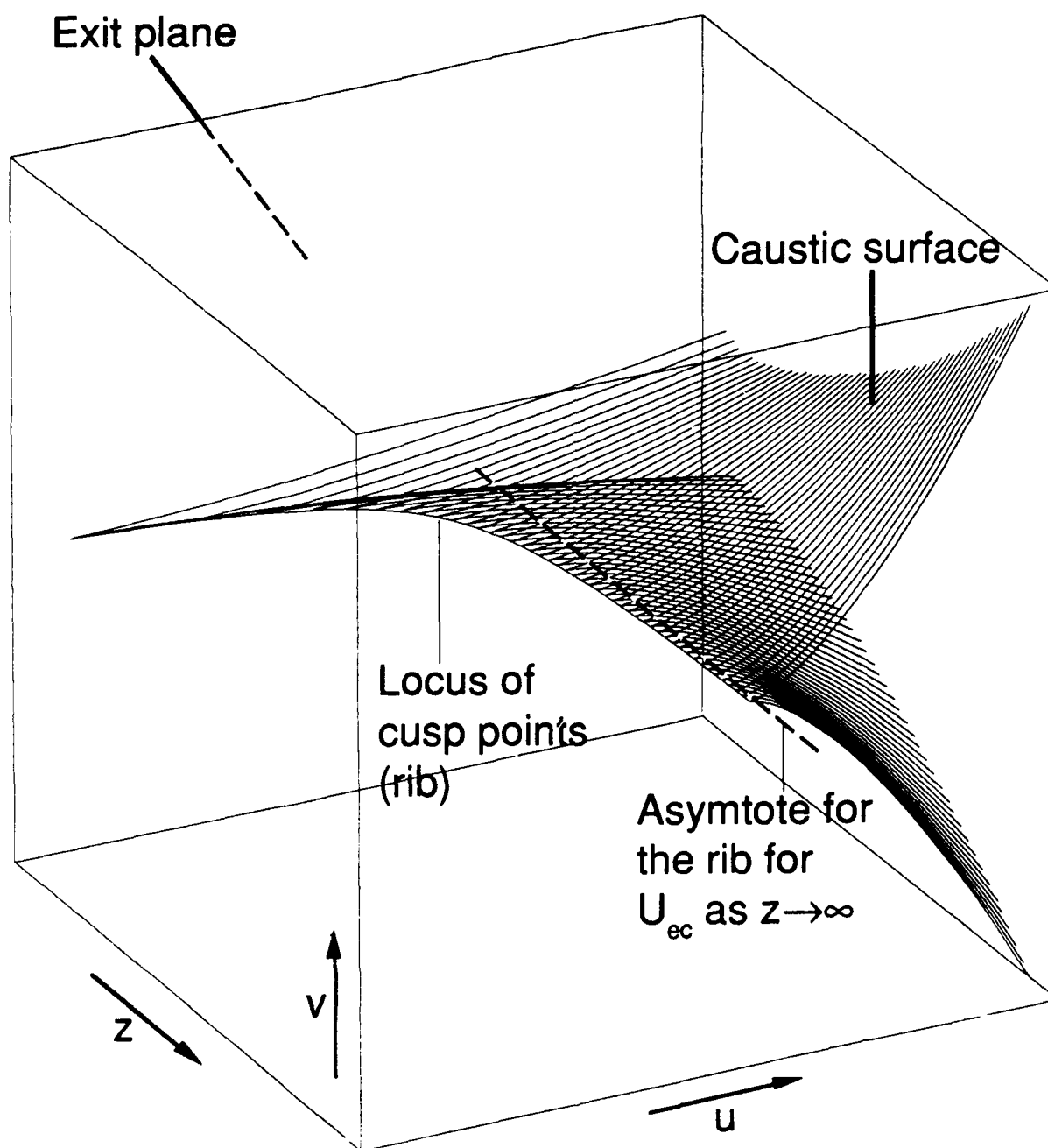
Figure 5) A three dimensional view of the caustic surface. Transverse cusp caustics are seen as uv cuts through this surface at a distance z from the exit plane. The locus of cusp points in adjacent uv planes defines the rib of the caustic surface.
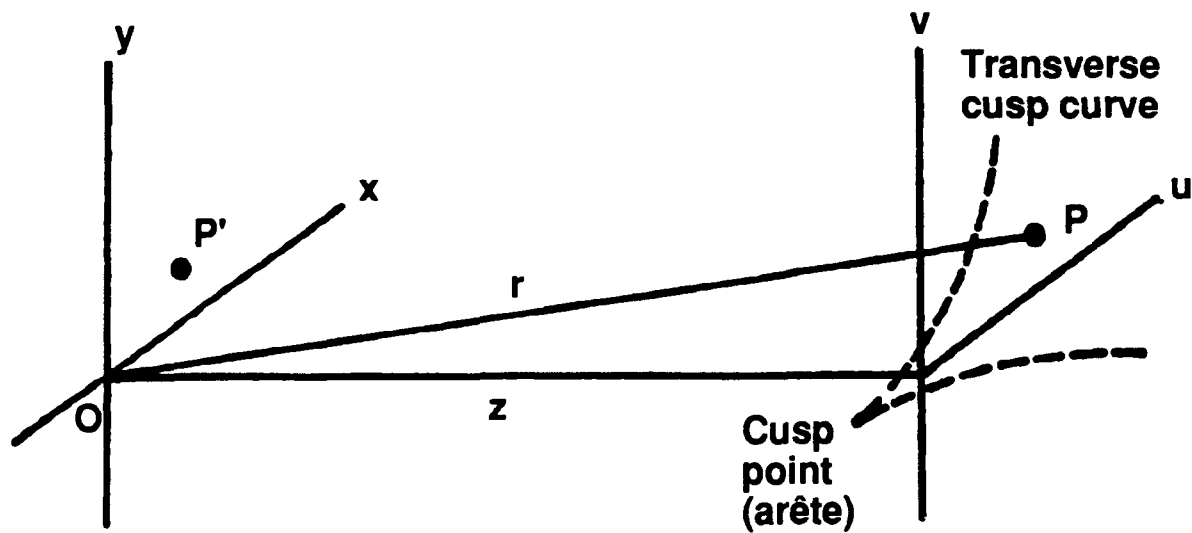
Figure 6) A transverse cusp caustic in a uv observation plane. The shape of the cusp curve

is given by Eq. (8). At the point P inside the cusp curve there are three distinct signal

arrivals, on the cusp curve there are two distinct signal arrivals, and outside the cusp curve

there is only one signal arrival.

decorates the TCC, produced by a steady state signal, is given by the Pearcey function [9] $P(w_2,w_1)$ where w_1 and w_2 vary as $k^{3/4}v$ and $k^{1/2}u$ respectively with $k = 2\pi/\lambda$ [10]. As discussed in Chapter 2 the wavefront $W(x,y)$ can be produced by scattering from a surface with the general shape

$$h(x,y) = h_1 x^2 + h_2 xy^2 + h_3 y^2. \tag{9}$$

The wavefront produced by scattering a point source of sound from a surface with local shape given by Eq. (9) is characterized in the observation plane by the reduced distance function

$$\phi(x,y,U_e,V_e) = b_1'x^2 + a_2'xy^2 + b_3'y^2 - U_e x - V_e y, \tag{10}$$

where $b_i' = -2h_i + 1/(2z) + 1/(2z_s)$, $a_2' = -2h_2$, z_s is the distance from the source plane to the exit plane, and U_e and V_e are dimensionless coordinates $u/z + u_s/z_s$ and $v/z + v_s/z_s$ respectively depending on both the source and observation locations. Using the parameters defined in the reduced distance function $\phi(x,y,U_e,V_e)$, Eq. (8) may be rewritten to describe the TCC formed by the reflected wavefront

$$D_T\left(U_e - U_{ec}\right)^3 = V_e^2, \tag{11}$$

where now

$$D_T = \frac{4a_2'}{27\, b_1'^2}, \tag{12}$$

and the horizontal location of the cusp point is given by

$$U_{ec} = \frac{u_c}{z} + \frac{u_s}{z_s} = -\frac{2b_1'b_3'}{a_2'}. \tag{13}$$

To show which of the rays touch the caustic, the complete distance function

$$\Phi(x,y,U_e,V_e) = r + r_s + \phi(x,y,U_e,V_e), \tag{14}$$

where $\phi(x,y,U_e,V_e)$ is given by Eq. (10) and the analysis given in Appendix A are used. This distance function is used in the diffraction integral to find the diffraction catastrophe in the observation plane. Rays are located in the exit plane by the simultaneous solution of the

ray conditions on the reduced distance function $\partial\phi/\partial x = 0$ and $\partial\phi/\partial y = 0$. The x

dependance of the distance function can be eliminated using the ray condition

$$\frac{\partial\phi}{\partial x} = 2b_1'x + a_2'y^2 - U_e = 0, \tag{15}$$

to find the horizontal location of the ray in the exit plane. The distance function now has

only y dependence. Using $s = (|a_2'|^2/4|b_1'|)^{1/4}y$ the distance function becomes

$$\phi'(s,U_eV_e) = -sgn(b_1')\,s^4 - sgn(a_2')\sqrt{|b_1'|}\left(U_e + \frac{2b_1'b_3'}{a_2'}\right)s^2$$
$$+ \left(\frac{4|b_1'|}{|a_2'|^2}\right)^{1/4}V_es - \frac{U_e^2}{4b_1'}, \tag{16}$$

where $sgn(g) = |g|/g = \pm 1$ and s has the same sign as y. The extrema of Eq. (16) will locate

the position of rays in the exit plane that pass through an observation point given by U_e and

V_e. Figure 7 shows a calculation of Eq. (16) for $b_1' > 0$, $a_2' > 0$, $U_e > 0$, $V_e > 0$. With

b_1' positive there are two maxima and there for two ray paths that touch the caustic prior to

reaching the observer. In Fig. 7 as the observation point moves outside the caustic, one of

the two maxima merges with the minimum leaving a curve with one extremum that is a

maximum. It follows from Fig. 7 the earliest arrival of the travel time surface for the TCC

inside the caustic will always be an s(t) type arrival and the last arrival will always be an

h(t) arrival. The fact that the rays touching a caustic are at a maximum of the ϕ' means that

these rays are always the last to arrive.

As shown in Ch. 3, the singular part of the travel time surface of the TCC, Fig. 8,

has the same form as the singular surface of the swallow tail catastrophe. The orientation

of this surface along the time axis of Fig. 8 will depend on the parameter b_1'. Figure 9a

shows a calculated cut through a travel time surface with $b_1' > 0$ at the relative horizontal

position inside the caustic given by $|U_e - U_{ec}| = 0.1191$. Each point in Fig. 9a represents

the geometrical arrival time at a point along a vertical cut through the observation plane

corresponding to the vertical posi ion of the point in the figure. Comparing Fig. 9a with

Fig. 7 shows that the two later arrivals are going to be at maxima of the distance function

and there for h(t) type arrivals while the early arrival is at a minima of the distance function and is an s(t) type arrival.

Form the analysis given above the expected sequence of arrivals for a surface that forms a TCC with b_1' and a_2' positive would be shh inside the caustic and a single h outside the caustic. A wavefront reflected from a surface with a negative h_1 term will always have a positive value of b_1'. Figure 10 shows a projection onto a plane, of the cusp curve in the observation plane and the location of the rays in the exit plane that pass through a vertical cut through the cusp curve. Moving up along the cut, outside the cusp curve there is only one arrival (ray 1). From the discussion following Fig. 7, this arrival is at a maximum of the distance function and is an h(t) type arrival. Crossing the cusp curve, inside the caustic there are three arrivals at each point along the cut (rays 1'-3'). From Fig. 7, two of these arrivals will be at maxima of the distance function while the third is at a minimum giving an arrival sequence of one s(t) type arrival then two h(t) type arrivals.
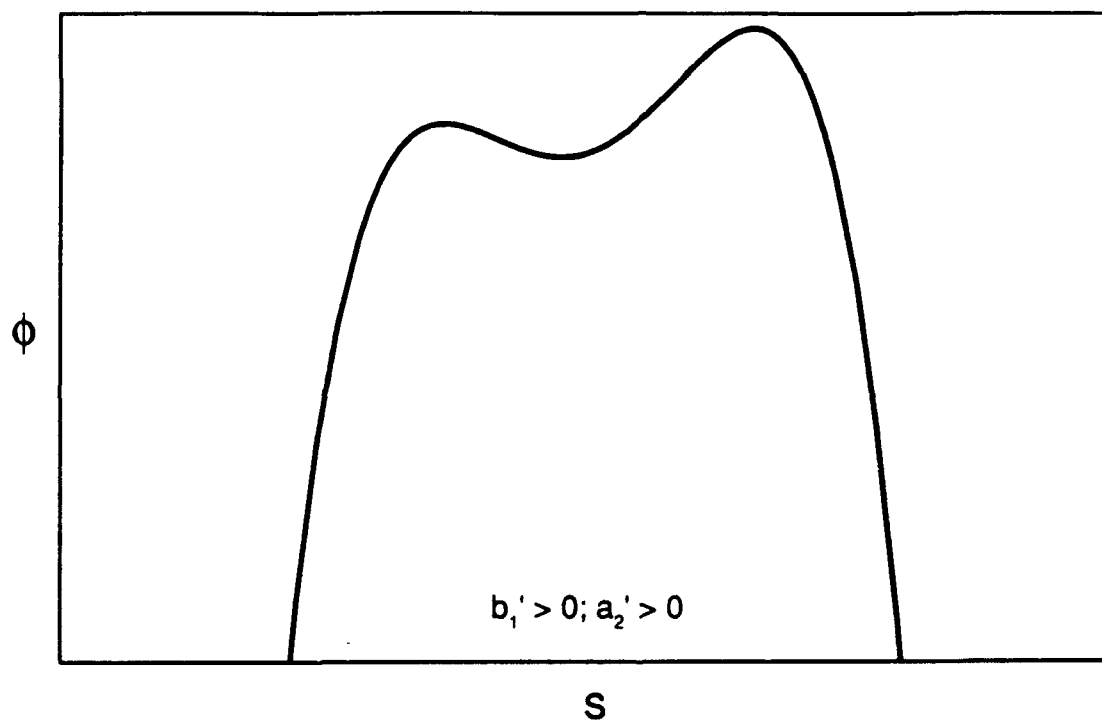
Figure 7) The general shape of the distance function of the transverse cusp caustic diffraction integral after the evaluation of the x dependence when $b_1' > 0$, $a_2' > 0$, $U_e > 0$, and $V_e < 0$.
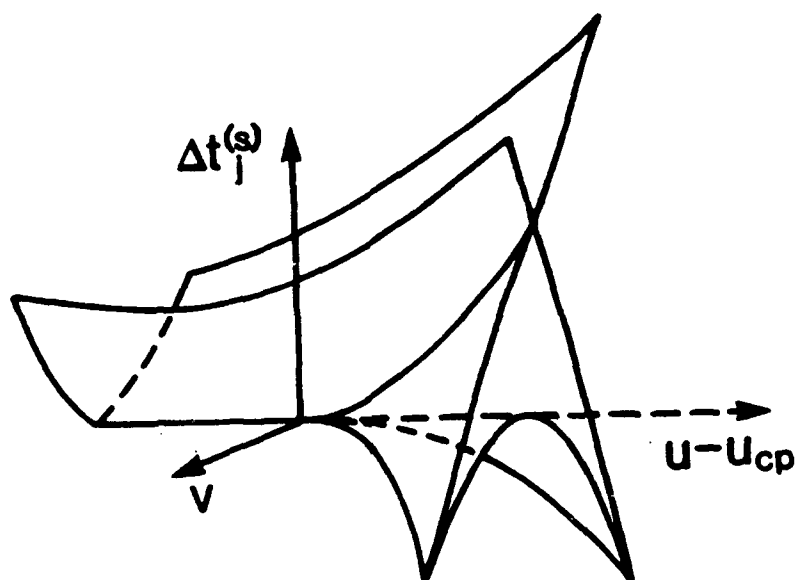
Figure 8) The travel time surface of the transverse cusp caustic has the same general shape

as the singular surface of the next higher codimension catastrophe, the swallow tail shown.
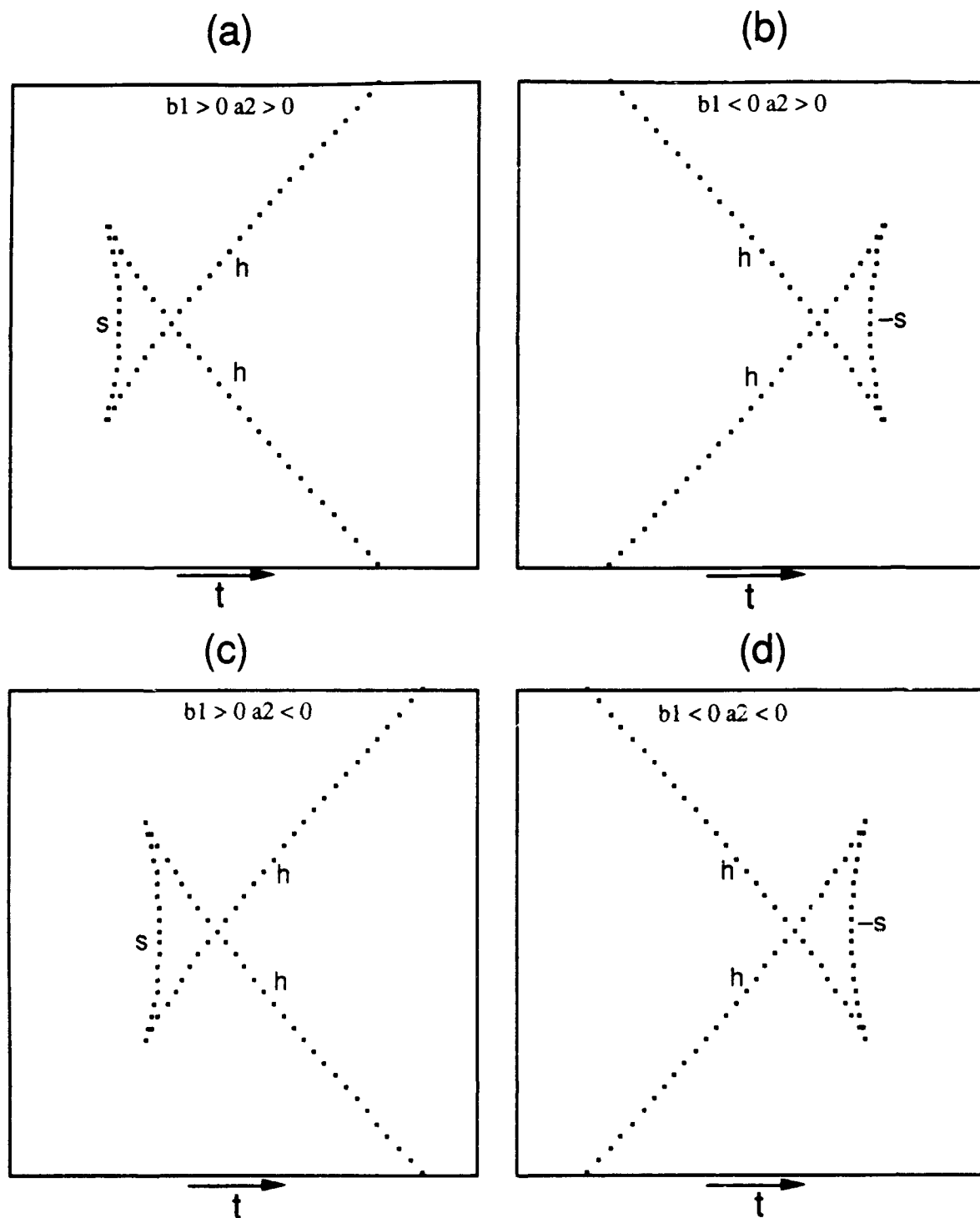
Figure 9) The orientation of the travel time surface along the time axis depends on the sign

of b_1' (a) $b_1' > 0$, $a_2' > 0$; (b) $b_1' < 0$, $a_2' > 0$; (c) $b_1' > 0$, $a_2' < 0$; (d) $b_1' < 0$, $a_2' < 0$.

The tail of the travel time surface is formed by the first two arrivals in (a) and (c) and the

last two arrivals in (b) and (d). The situations shown in (b) - (d) are discussed in Sec. 4.4.
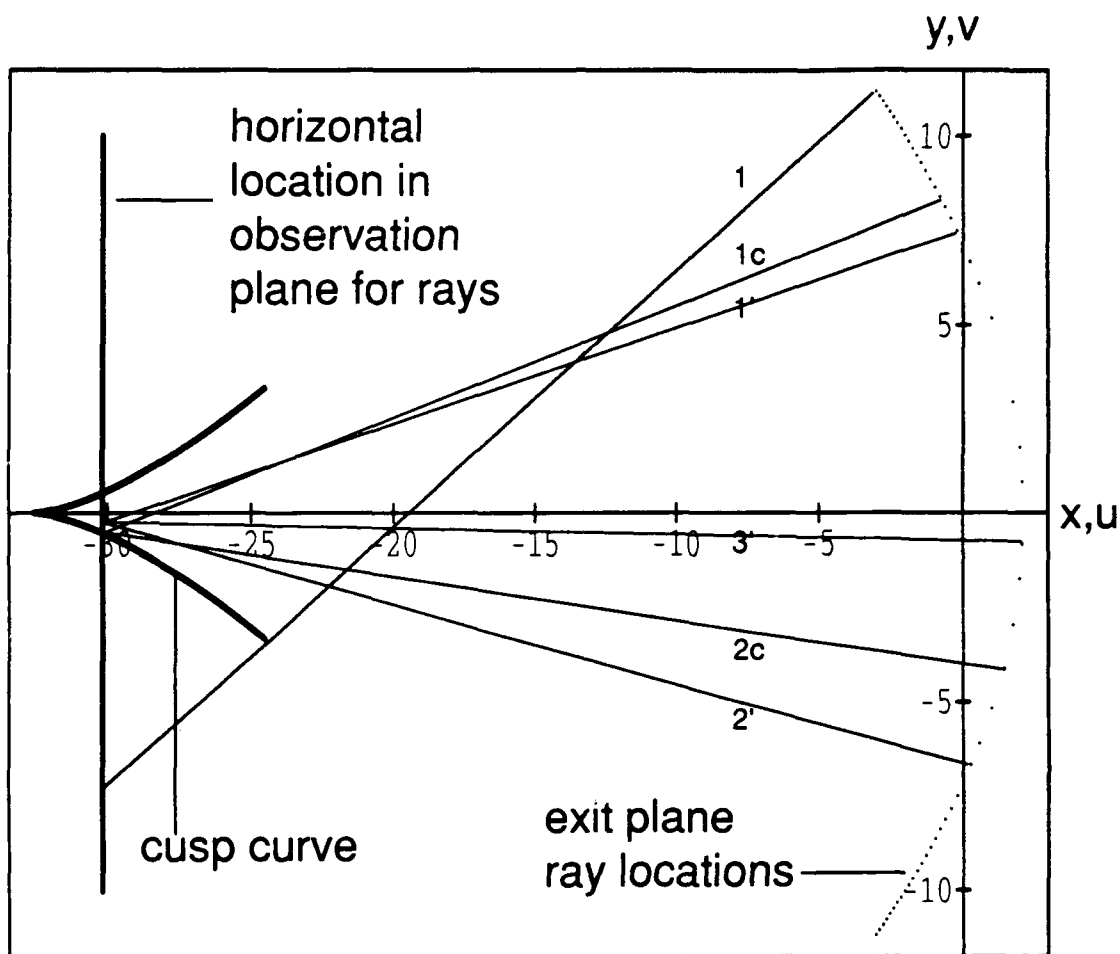
Figure 10) The relative location of rays in the exit plane that pass through a vertical cut in the observation plane when $b_1' > 0$ and $a_2' > 0$. Ray 1 passes through the cut below the cusp curve in the observation plane. Rays 1c and 2c pass through the lower branch of the cusp curve, with ray path 1c being the longer path to the cusp curve. Rays 1', 2', and 3' pass through a point inside the cusp curve below the symmetry axis, with the ray paths from shortest to longest being 3', 2', and 1'.

B. EXPERIMENTAL MEASUREMENT OF THE ARRIVAL SEQUENCE FOR A TRANSVERSE CUSP CAUSTIC PRODUCED BY REFLECTION FROM A CURVED SURFACE

Figure 11 shows two cuts through the travel time time surface of a TCC produced by scattering a point source of sound from a curved metal surface with the general shape given by Eq. (9). The surface height was measured on a grid of points and the data fit to Eq. (9) giving $h_1 = -0.00031$ cm^{-1} and $h_2 = -0.00117$ cm^{-2}. As h_1 and h_2 were both negative, the parameters b_1' and a_2' were both positive for all z_e. With b_1' and a_2' both positive the sequence of the $s(t)$ and $h(t)$ type arrivals given by Sec. 3.A is, one $h(t)$ type arrival outside the cusp curve and inside the cusp curve one early $s(t)$ type arrival and two later $h(t)$ type arrivals.

The travel time cuts shown in Fig. 11 were produced by selecting a horizontal position in the observation plane and collecting time traces at equispaced vertical positions. The time traces could then be displayed in a waterfall format showing the arrival times of the signals in the observation plane. Figure 11a is a cut taken outside the cusp curve (for present the case of $a_2' > 0$ this means that $U_e < U_{ec}$) and 11b is a cut taken well inside the cusp curve ($U_e > U_{ec}$). Figure 12 shows the arrivals of signals propagating along ray paths that pass through the horizontal symmetry axis of the TCC. The first and last time traces in Fig. 12 come from traces 21 in Figs. 11a and 11b respectively and the rest come from cuts made along equispaced horizontal positions between the horizontal positions of Figs. 11a and 11b. The cusp point of the TCC is located near the position corresponding to time trace 2 in Fig. 12. Inside the cusp curve there appear to be only two arrivals, however along the symmetry axis of the TCC the late arrival is due to the simultaneous arrival of two signals that have the same path length but originate on different points of the wavefront.

The reflection coefficient of the reflecting surface was approximated to be near unity using the oblique incidence mass law found in Pierce [20]. This approximation assumes that

Figure 11) (a) Time traces taken along a vertical cut through in the observation plane for a horizontal location outside the cusp curve. The waterfall display of the time traces shows the arrival times of the single signal propagating along the single ray path from the wavefront to points outside the cusp curve in the observation plane.
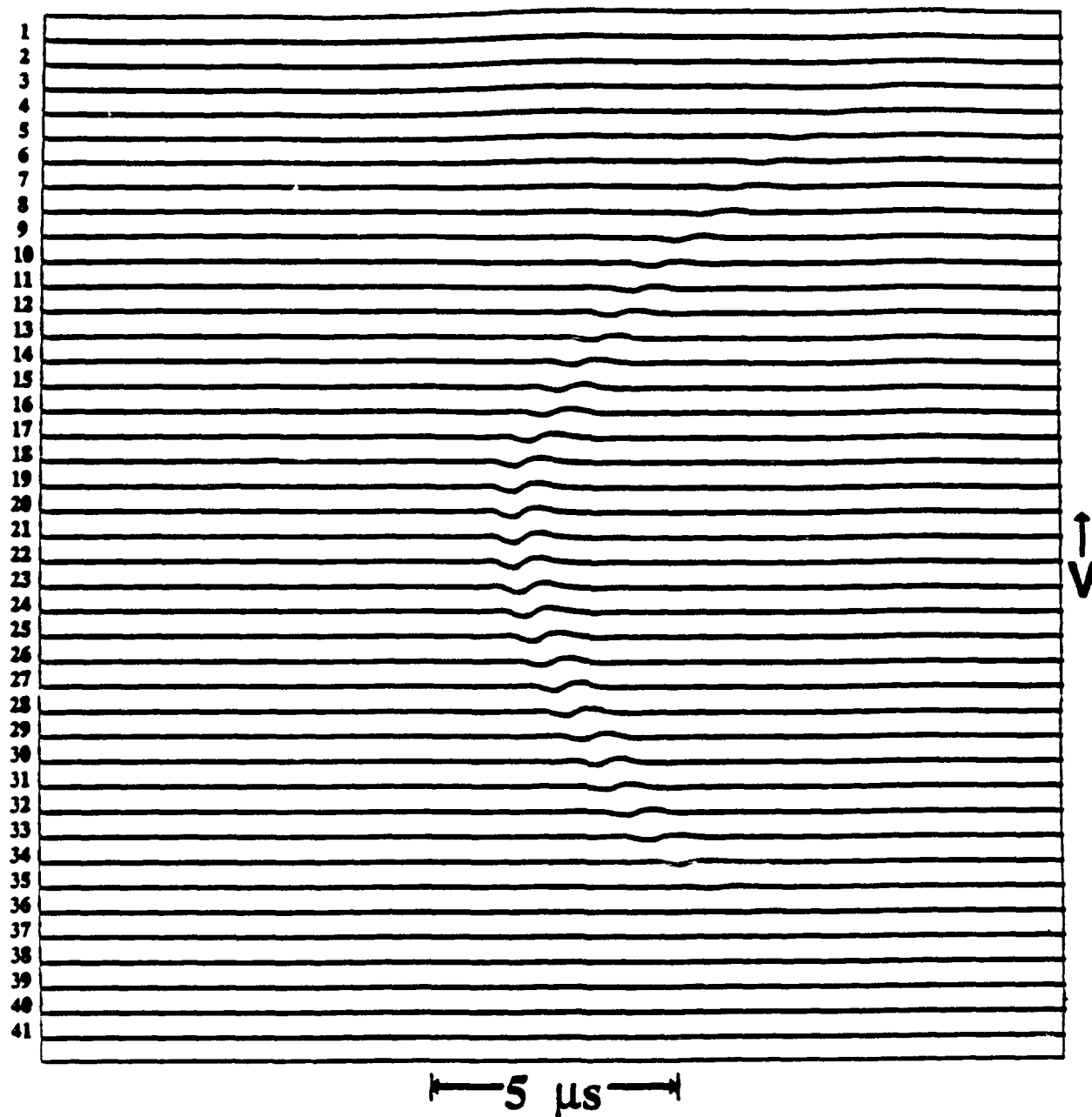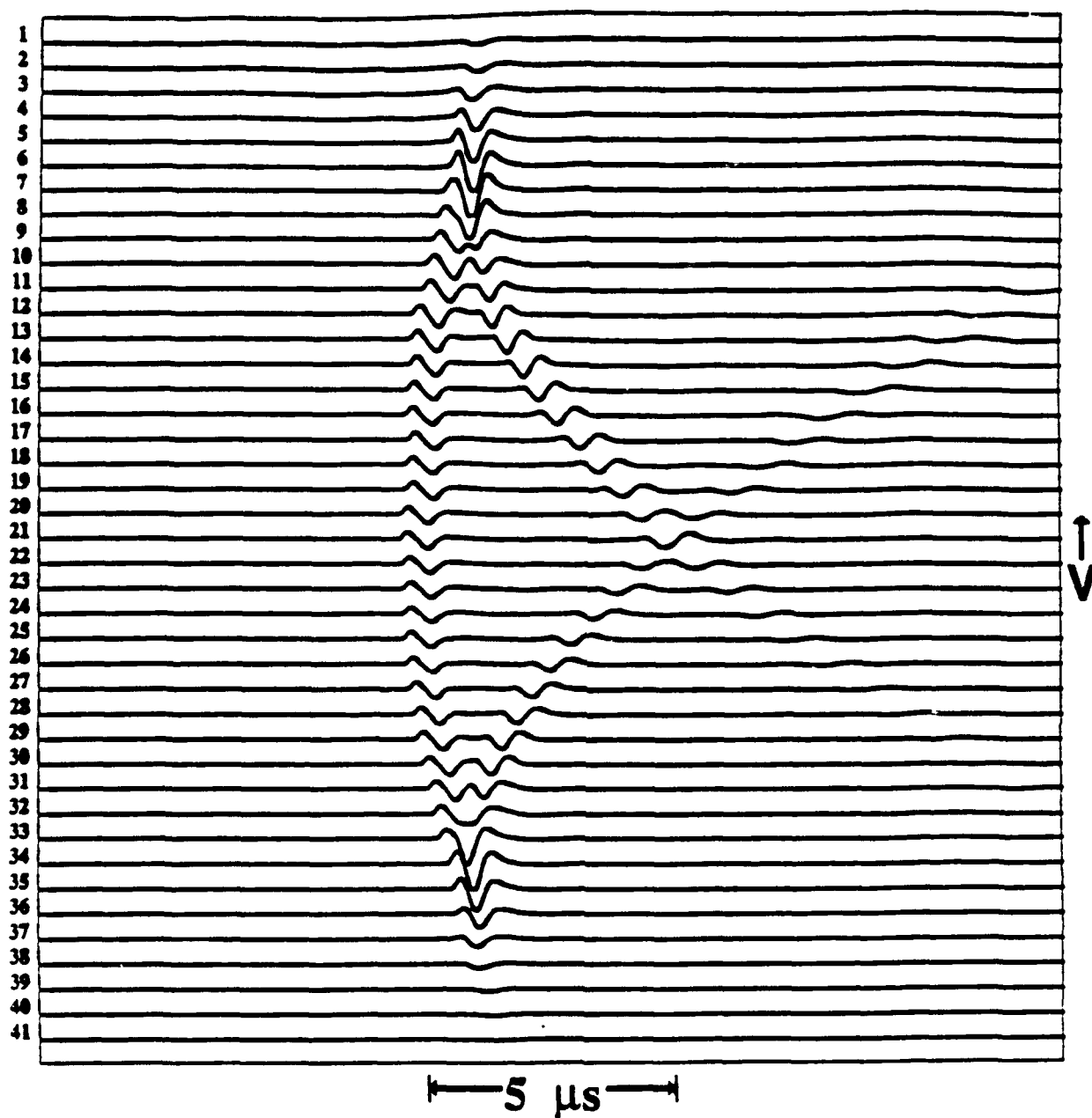
Figure 11) (b)Time traces taken along a vertical cut through in the observation plane for a horizontal location inside the cusp curve. The waterfall display of the time traces shows the arrival times of the signals that propagate along the ray paths from the wavefront to points outside the cusp curve in the observation plane. Note the tail of the travel time surface arrives first.

the wavelength of sound in the scattering surface $\lambda_s \gg 4l_s$ where l_s is the thickness of the

slab, $l_s = 15$ mil $= 0.38$ mm. Measurements of the reflection coefficient, discussed in

Chapter 2 Appendix C, estimated $r \approx 1$ for the range of spectral components of the

transients used. The reflection coefficient was real and positive and there was no phase

advance of the signal due to the reflection from the surface. The reflected signals were due

to a single reflection from the front surface of the reflector which had the proper shape to

form a TCC and there was no problem with reflections from the back of reflector.

The shapes of the observed pulses in Fig. 12 were compared with the the shape of

the incident pulse used in the experiment, Fig. 13. The incident pulse was produced by a

Sonic Instruments Inc. ultrasonic transducer type CBA 10-1. The transducer has a 1/4 in

diameter and has a heavily damped resonance at 10 MHz. The transducer was driven by a

Smith Kline Instruments medical ultrasound driver that was modified to be triggered at a

low repetition rate. The pulse provided by the driver was approximately a 70 V spike with

a rise time on the order of nanoseconds and an exponential tail $\approx 3\mu s$ long. The pulse

produced by the CBA 10-1 is shown in Fig. 13. This signal was measured at a distance of

1 m from the source transducer by another CBA 10-1 used as the receiver in this

experiment. The driving signal was a unipolar spike while the measured source signal is

bipolar. The bipolar shape of the source pulse is due to two unipolar contributions [21], one

a direct signal from the planar face of the transducer, the second an inverted contribution

from an effective ring source lying along the transducer perimeter. In the near field these

two signals are separated in time. In the far field the two signals arrive vary near in time

producing the bipolar signal shown in Fig. 13.

Figure 14 shows the individual signals from the first and last time traces in Fig. 12

along with the HT of each signal calculated using the algorithm described in Sec. 2.B.

Figure 14a is the single arrival outside the cusp curve in the observation plane shown in the

first trace of Fig. 12, while Fig. 14b is its HT. Comparing Figs. 14a and 13, the single

signal arriving outside the cusp curve in the observation plane has a different shape from
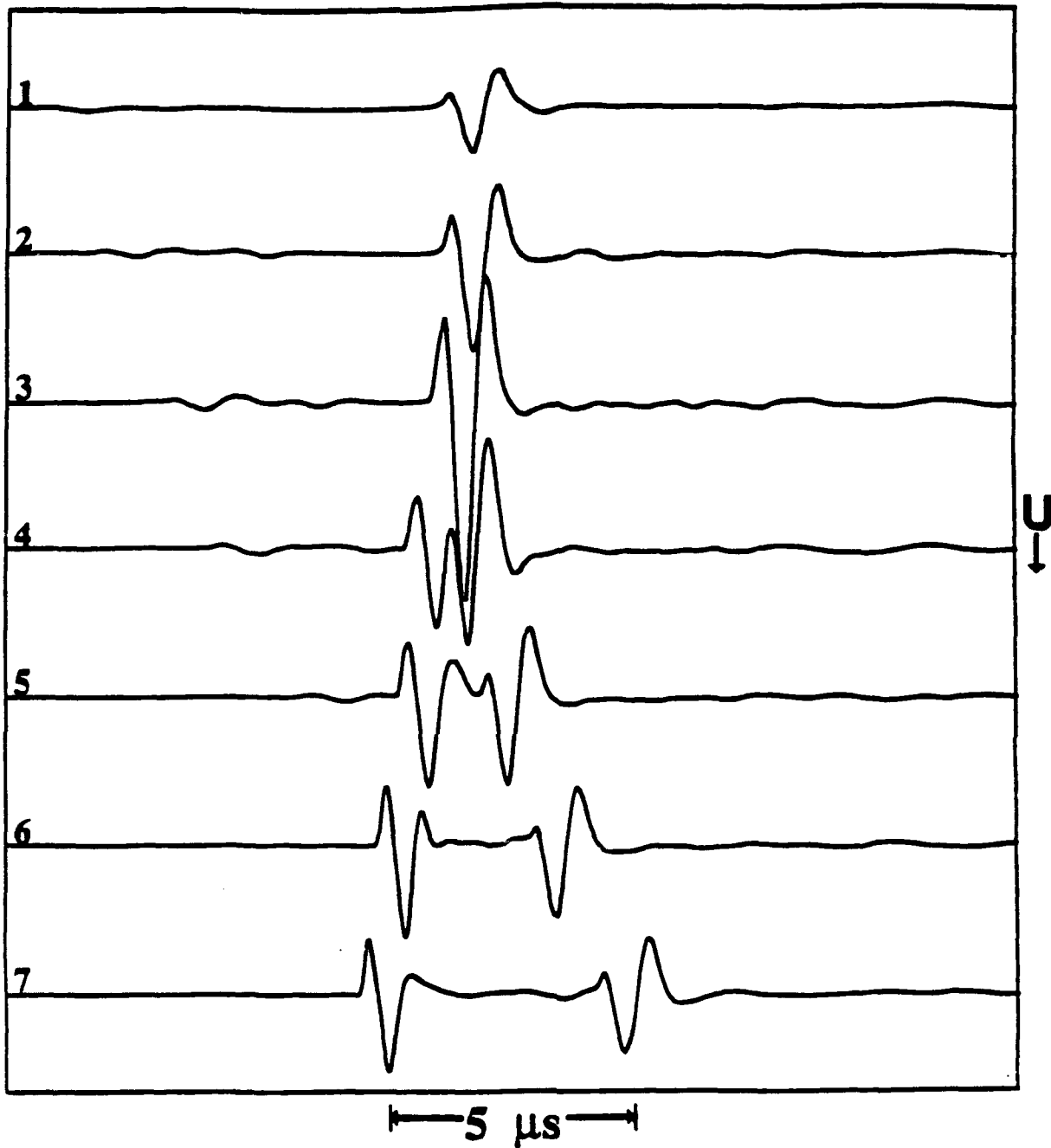
Figure 12) A horizontal cut through the travel time surface along the symmetry axis of the transverse cusp caustic. Trace 1 corresponds to trace 21 in Fig.17a and trace 7 to trace 21 in Fig. 17b. The location of the arête is approximately the location at which trace 2 was collected. The later arrival in traces 4-7 is due the simultaneous arrival of two signals from different portions of the wavefront.
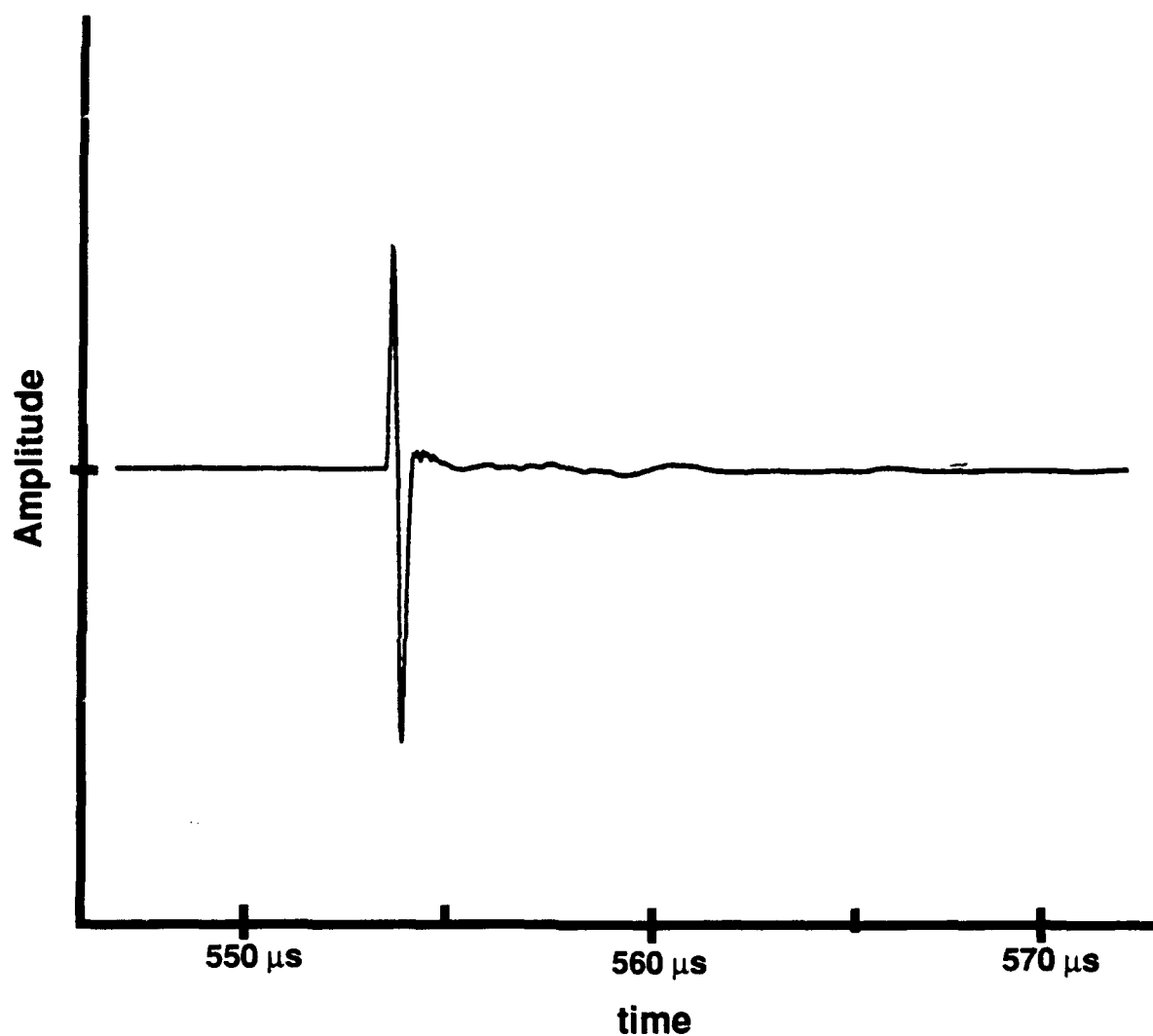
Figure 13) A representative source pulse used in the time domain experiments. Note that this pulse is a causal pulse with a sharp turn on and no precursor on the begging of the pulse. The bipolar shape of the pulse is due to the superposition of a direct signal from the source transducer surface and an inverted signal from an effective ring source lying along the transducer perimeter. This time trace was taken by pointing the receiving transducer at the source transducer about 1 m away.

Figure 14) (a) The single pulse in Fig. 18 trace 1. This pulse has the shape of the Hilbert transform of the source pulse. (b) The Hilbert transform of (a) this pulse has the shape of −1 times the shape of the source pulse. (c) The single early pulse in Fig. 18 trace 7. This pulse has the shape of the source pulse. (d) The Hilbert transform of (c), this pulse has the shape of (a). Note the precursor showing up prior to the expected arrival time of the ray in the Hilbert transform. (e) The simultaneous second arrival in Fig. 18 trace 7. These pulses have the shape of (a), (d), and the Hilbert transform of the source pulse. (f) The Hilbert transform of (e), this pulse has the shape of −1 times the source pulse.
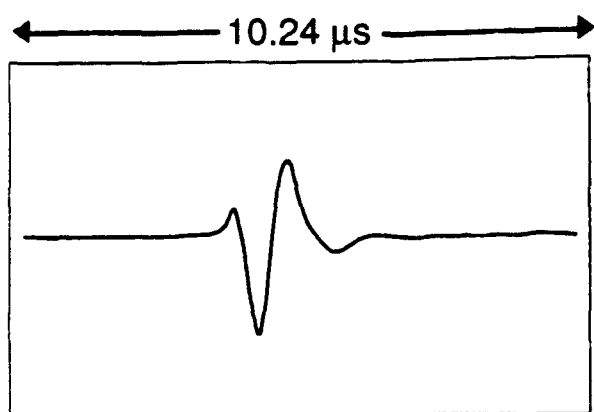
(a)
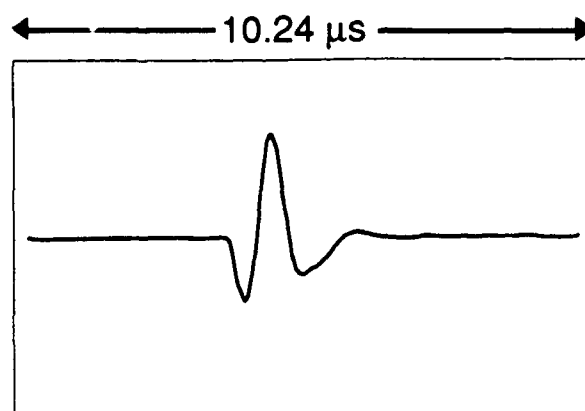
(b)
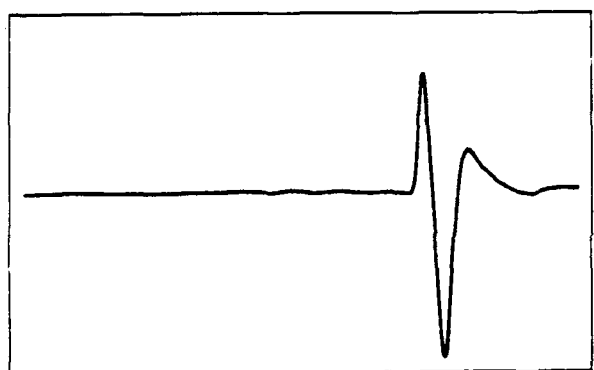
(c)
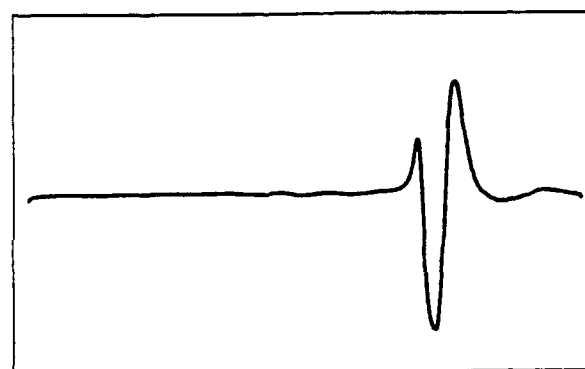
(d)
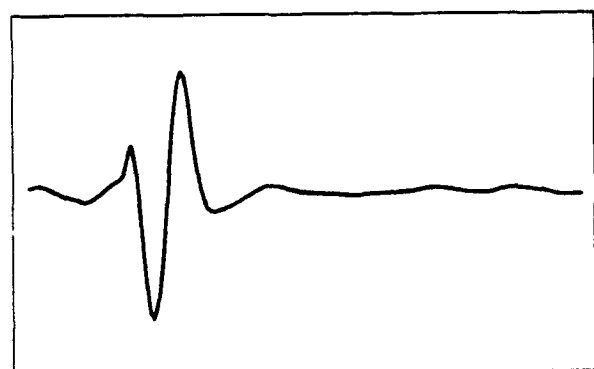
(e)

(f)
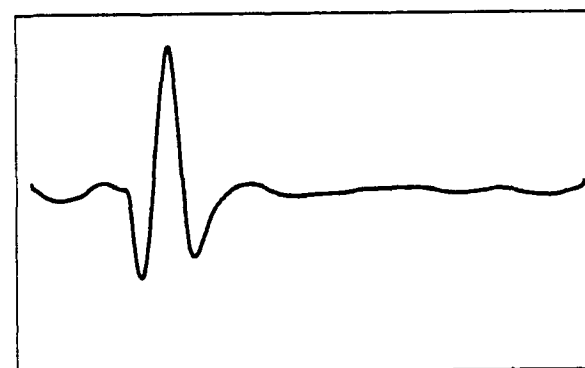
the source signal. When Figs. 14b and 13 are compared the two signals appear to have similar shapes differing by a factor of -1. If the shape of the incident signal, Fig. 13, is an s(t) type shape, then the shape of the HT of Fig. 14a is a $-s(t)$ type shape. The skew-reciprocal nature of the HT suggests then, that Fig. 14a has the shape of the HT of the incident signal shape and is an h(t) type arrival.

Figure 14c shows the single early arrival at the point along the symmetry axis inside the cusp curve corresponding to the last time trace in Fig. 12. This arrival has the same shape as the source pulse in Fig. 13. Thus the pulse in Fig. 14c is an s(t) type arrival and Fig. 14d, which is the HT of 14c, is an h(t) type arrival. Comparing Figs. 14a and 14d confirms the assumption made using the skew-reciprocal nature of the HT that Fig. 14a is an h(t) type arrival. Figure 14e is the simultaneous later arrival at the same point inside the cusp curve corresponding to the last trace in Fig. 12. Both of the arrivals in Fig. 14e appear to have the same general shape of the signals in Figs. 14a and 14d. Thus both of these late arrivals are h(t) type arrivals and the HT of Fig. 14e, Fig. 14f, is a $-s(t)$ type shape.

By the comparison of Figs. 13 and 14a-f, the sequence and type of arrivals for a TCC wavefront with $b_1' > 0$ and $a_2' > 0$ is given. The single arrival outside the cusp curve in the observation plane, Fig. 14a, is an h(t) type arrival. Inside the cusp curve the single early arrival is an s(t) type arrival, while the simultaneous late arrivals are both h(t) type arrivals. This sequence of the type of the arrivals agrees with the analysis of the relationship between b_1' and a_2' and the ray paths that touch the caustic surface given in Sec. 3.A. It was assumed in that analysis that there was no phase shift on reflection. Were there a phase advance of $\pi/2$ on reflection, the expected arrival sequence inside the cusp curve would have been h(t), $- s(t)$, $- s(t)$. As none of the signal were $- s(t)$ type arrivals, the assumption that there was no phase advance associated with the reflection was valid.

4.4 THE EFFECT OF THE WAVEFRONT PARAMETERS a_2' AND b_1' ON THE ARRIVAL SEQUENCE OF THE TRANSVERSE CUSP

It can be seen from Eqs. (11)-(13) that the parameter b_3' has no effect on the shape of the caustic other then to locate the cusp point. The important parameters for determining the shape of the caustic and the arrival sequence are a_2' and b_1' as they determine the rate at which the caustic opens and the orientation of the travel time surface. In Eq. (12), a_2' controls the direction along which the caustic opens. For a_2' negative the caustic opens along the negative U_e direction (Figs. 15a and 16a). When a_2' is positive the caustic opens along the positive U_e direction (Figs. 17a and 18a). Inspection of Fig. 9 shows, however, that the parameter a_2' has no effect on the arrival sequence. It only affects the spatial orientation of the caustic surface and the opening rate of the surface.

The effect of b_1' on the caustic shape is more subtle then just a sign change as with a_2'. Once the reflecting surface shape is known the parameter a_2' is fixed. However b_1' depends on the surface and on z and z_s through the expression

$$b_1' = -2h_1 + \frac{1}{2z_e} , \tag{17}$$

where $z_e = (1/z + 1/z_s)^{-1}$. Thus the opening rate D_T will be affected through b_1' by a change in either the source or observation distances. The variations in z_e, and thus the shape of the caustic and travel time surfaces, discussed below can be attributed to changes in either z or z_s. Thus the caustic surface may be traced by fixing an observation plane and moving the source plane. The dependence of b_1' and b_3' on z and z_s is symmetric .

The sign of the surface parameter h_1 has a large affect on the shape of the caustic surface through the dependence of b_1' on h_1. When $h_1 < 0$, b_1' will always be positive for positive values of z_e. In the reflection problem being discussed both z and z_s were always positive so z_e was always positive. Thus for $h_1 < 0$, b_1' goes from $+\infty$ when $z_e = 0$, to

$b_1' = -2h_1 > 0$ for $z_e = \infty$. This gives values for D_T from 0 to $-2h_2/27h_1^2$ as z_e goes from 0 to ∞. When $h_1 > 0$, b_1' goes from $+\infty$ when $z_e = 0$ to $-2h_1 < 0$ when $z_e = \infty$, passing through $b_1' = 0$ at $z_e = z_c$ where $z_c = 1/4h_1$. As $b_1' \to 0$, D_T, which goes as $1/b_1'^2$, diverges rapidly. For $z_e < z_c$ the $|D_T|$ goes from 0 to ∞ as z_e goes from 0 to z_c while for $z_e > z_c$, $|D_T|$ goes from ∞ at $z_e = z_c$ to $|D_T| = |2h_2/27h_1^2|$ at $z_e = \infty$.

Figures 15a-18a show the general shapes of the caustic surface associated with a TCC in a plane for: (15a) $b_1' > 0$, $a_2' < 0$; (16a) $b_1' < 0$, $a_2' < 0$; (17a) $b_1' > 0$, $a_2' > 0$; and (18a) $b_1' < 0$, $a_2' > 0$. Each figure was calculated using a value of $h_1 > 0$ to show the effect of the sign change of b_1' on the caustic surface by simply increasing z_e. In both (15a) and (16a), the caustic surface opens along the negative U_e direction due to $a_2' < 0$. In (15a) the opening rate begins to diverge as U_e increases, while in (15a) the opening rate decreases as U_e increases. The value z_c is located between the z_e values used in the two calculated surfaces shown, as near z_c the opening rate becomes so large as to dominate the plot of the surface. Figures (17a) and (18a) show calculated surfaces with $a_2' > 0$. As in (15a), the opening rate of the surface in (17a) increases rapidly as z_e increases and b_1' goes to zero. The opening rate in (18a) decreases rapidly as b_1' becomes more negative, as in (16a).

Figures (15b) -(18b), shown below the associated caustic surface, show the calculated locations of rays in the exit plane that pass through points along a vertical cut through a transverse cusp curve in an observation plane at the effective horizontal point $|(U_e - U_{ec})| = 0.1191$. These figures show the effect of the change in sign of b_1' on the spatial orientation of the ray locations in the exit plane relative to the caustic surface. Comparing Figs 15b and 17b and Figs. 16b and 18b along with Eq. (10) shows that a change in the sign of a_2' simply reflects the wavefront and associated caustic through the vertical axis. The change between Figs 15b and 17b and Figs. 16b and 18b is the sign of a_2' which gives the opposite spatial orientation for the caustic surface and the ray locations for each figure.

The effect of the change in sign of b_1' is seen when Figs. 15b and 16b and Figs. 17b and 18b are compared. Each pair of figures has the same sign for a_2' but opposite signs for b_1'. When b_1' is negative, the parabola described by the locations of the rays in the exit plane that passes through a vertical cut in a transverse observation plane opens along the same direction as the caustic surface. When b_1' is positive, the parabola opens along the opposite direction as the caustic. The effect of the sign change in b_1' on the travel time surface is shown in Fig. 9. The four cuts through travel time surfaces inside the caustic differ in only the signs of b_1' and a_2'. Note that the sign of a_2' has no effect on the temporal orientation of the travel time surface. However, a change in the sign of b_1' inverts the travel time surface in time. The effect on ϕ' given in Eq. (16) of a negative b_1' is seen in Fig. 19, where ϕ' is calculated with b_1' equal to the negative of that used in Fig. 7 and all the other parameters unchanged. In Fig. 19 the calculated reduced distance function contains two minima and one maximum. Using the analysis given in Appendix A, the extrema of the reduced distance function give the arrival sequences, marked in Fig. 9, of one $h(t)$ type arrival outside the caustic and inside two early $h(t)$ type arrivals and one later $-s(t)$ type arrival. Figure 20 shows the projection of the cusp curve and ray locations onto the same plane similar to that shown in Fig. 10 except with $b_1' < 0$. Where the ray paths in Fig. 10 originate inside the cusp curve in the plane of projection, for Fig. 20 the ray paths originate outside the cusp curve.

It is the spatial orientation of the ray locations that determines the arrival sequence. The distance function given in Eq. (16) will have three extrema: two maxima and one minimum or two minima and one maximum depending on the sign of b_1'. The arrival sequence associated with the signs of b_1' are: for $b_1' > 0$ shh inside the caustic and h outside the caustic, for $b_1' < 0$ hh–s inside the caustic and h outside the caustic. The arrival sequence is not affected by a_2'.

Figure 15) (a) The caustic surface when $b_1' > 0$ and $a_2' < 0$. The divergence of the opening rate as z increases is due to the surface parameter h_1 being positive. (b) The orientation of the rays in the exit plane that pass through a vertical cut through the cusp curve in the observation plane. The parabola formed by the ray locations in the exit plane opens opposite the direction of the caustic surface.

(a)

(b)
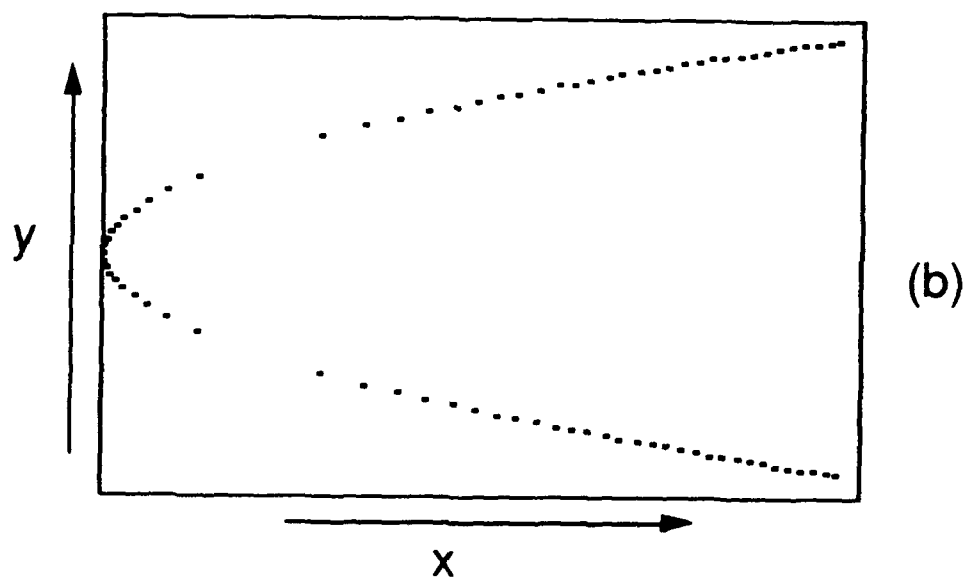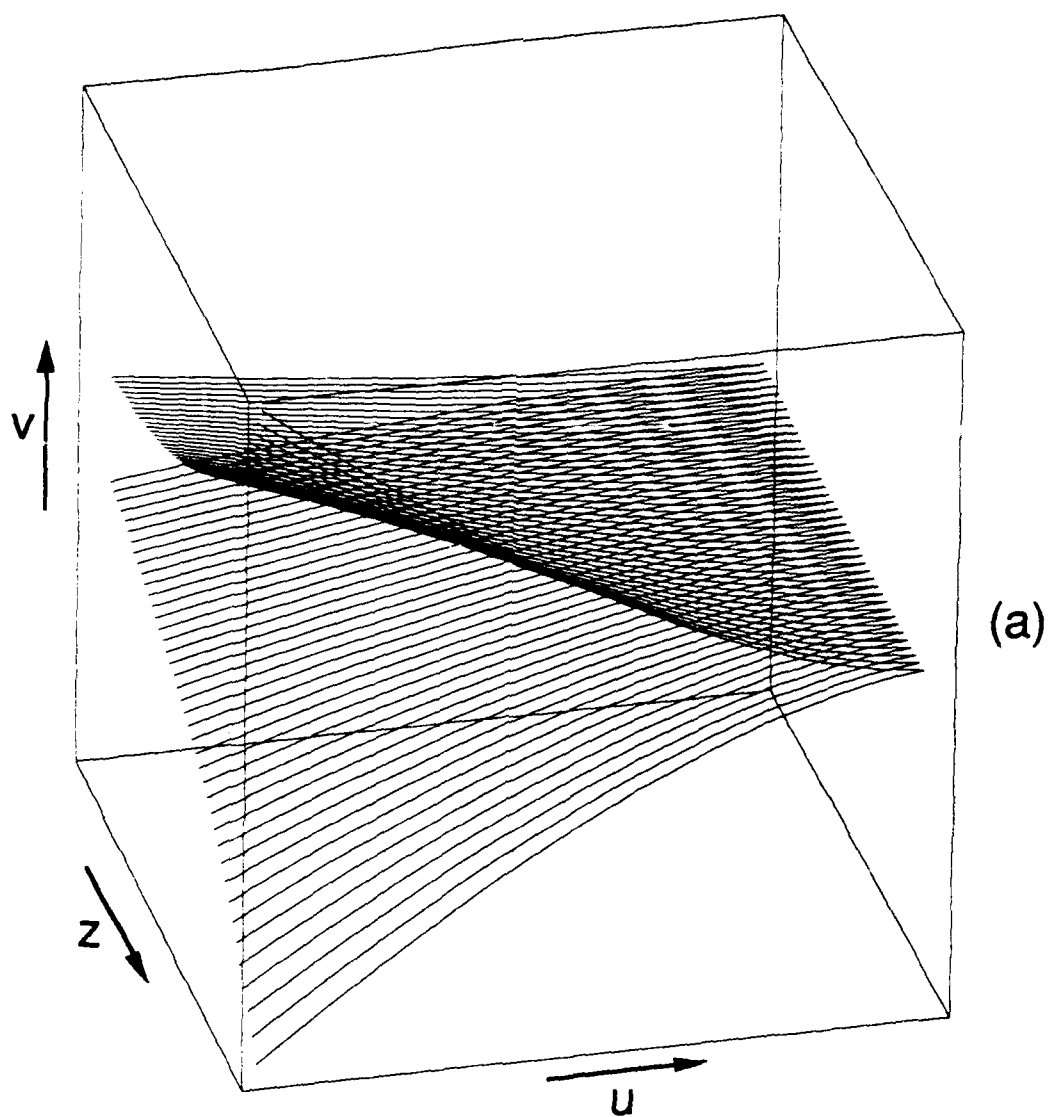
Figure 16) (a) The caustic surface when $b_1' < 0$ and $a_2' < 0$. The divergence of the

opening rate as z increases is due to the surface parameter h_1 being positive. (b) The

orientation of the rays in the exit plane that pass through a vertical cut through the cusp

curve in the observation plane. The parabola formed by the ray locations in the exit plane

opens along the direction of the caustic surface.

(a)

(b)
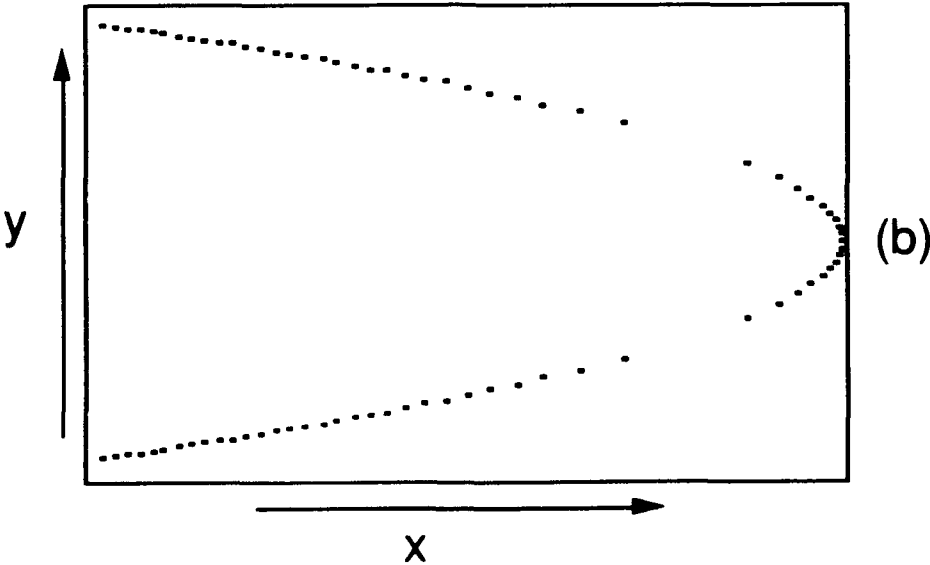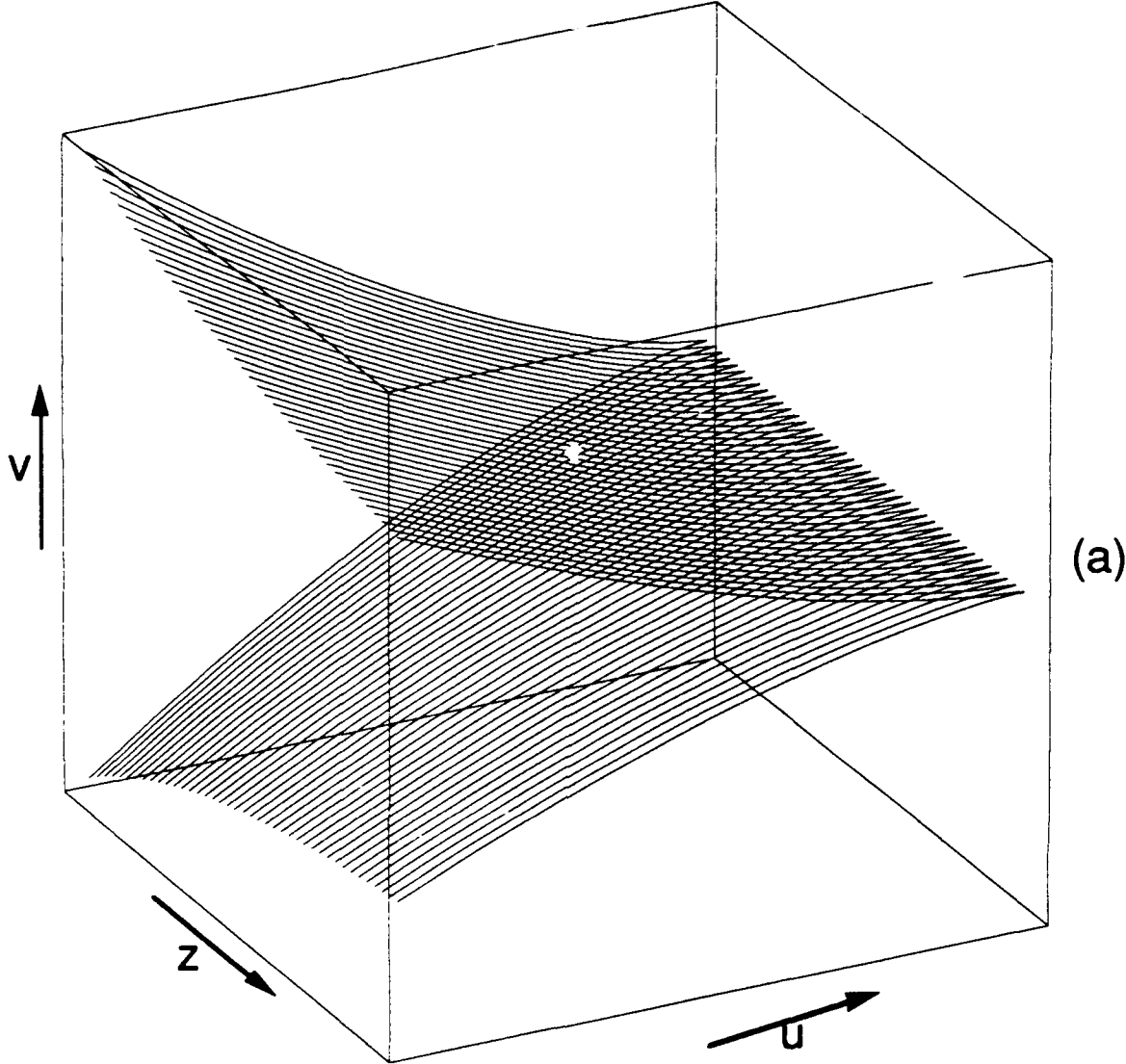
Figure 17) (a) The caustic surface when $b_1' > 0$ and $a_2' > 0$. The divergence of the opening rate as z increases is due to the surface parameter h_1 being positive. (b) The orientation of the rays in the exit plane that pass through a vertical cut through the cusp curve in the observation plane. The parabola formed by the ray locations in the exit plane opens opposite the direction of the caustic surface.

(a)

(b)
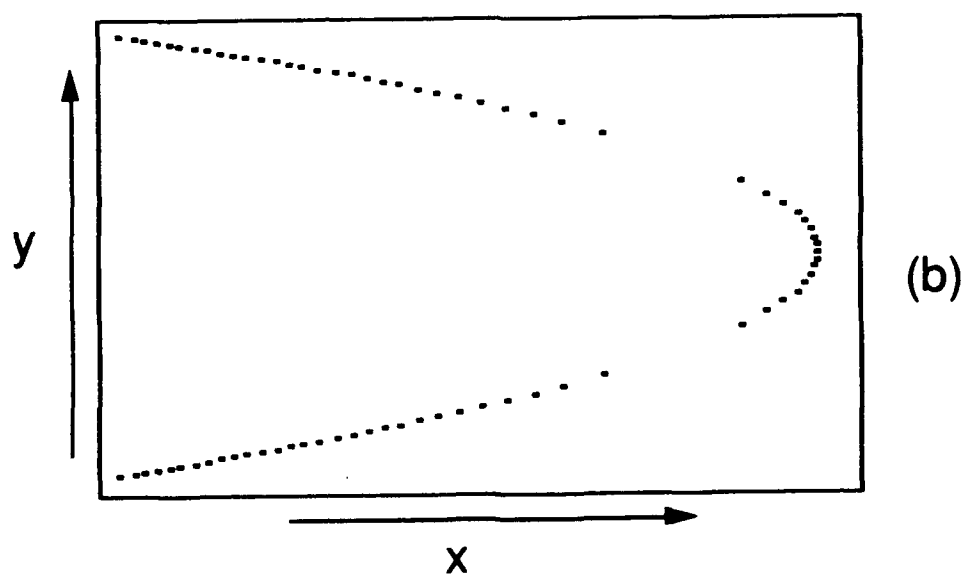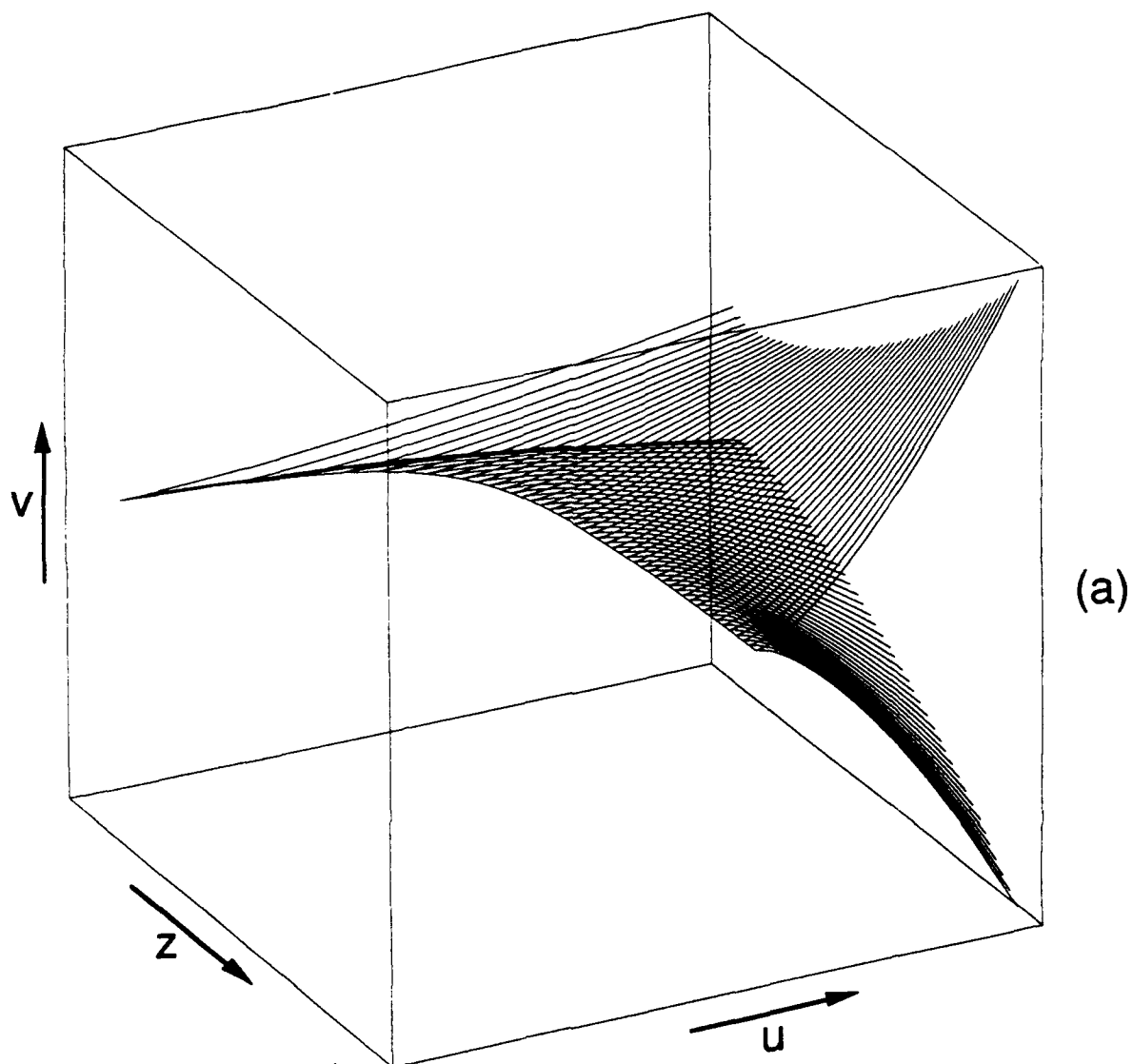
Figure 18) (a) The caustic surface when $b_1' < 0$ and $a_2' > 0$. The divergence of the opening rate as z increases is due to the surface parameter h_1 being positive. (b) The orientation of the rays in the exit plane that pass through a vertical cut through the cusp curve in the observation plane. The parabola formed by the ray locations in the exit plane opens along the direction of the caustic surface.

(a)

(b)
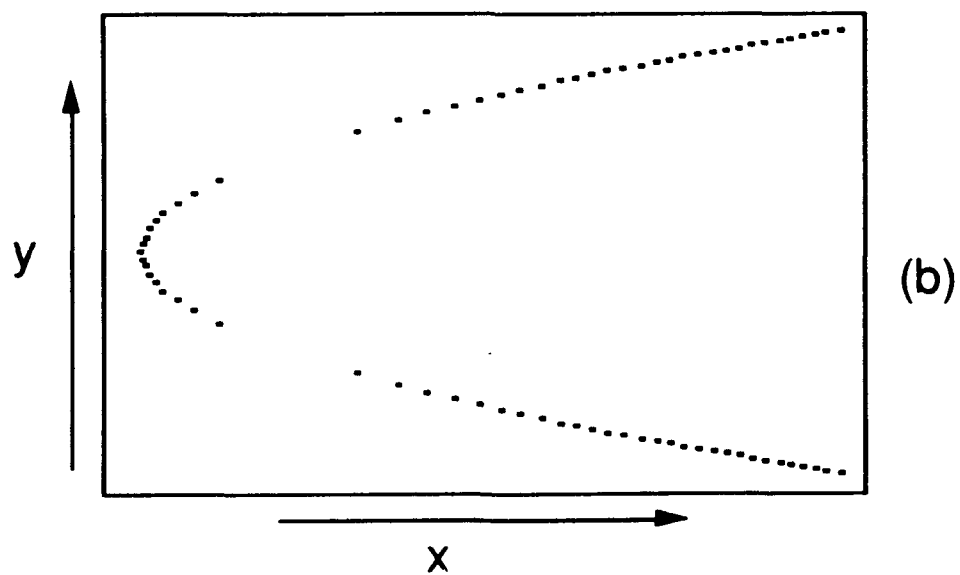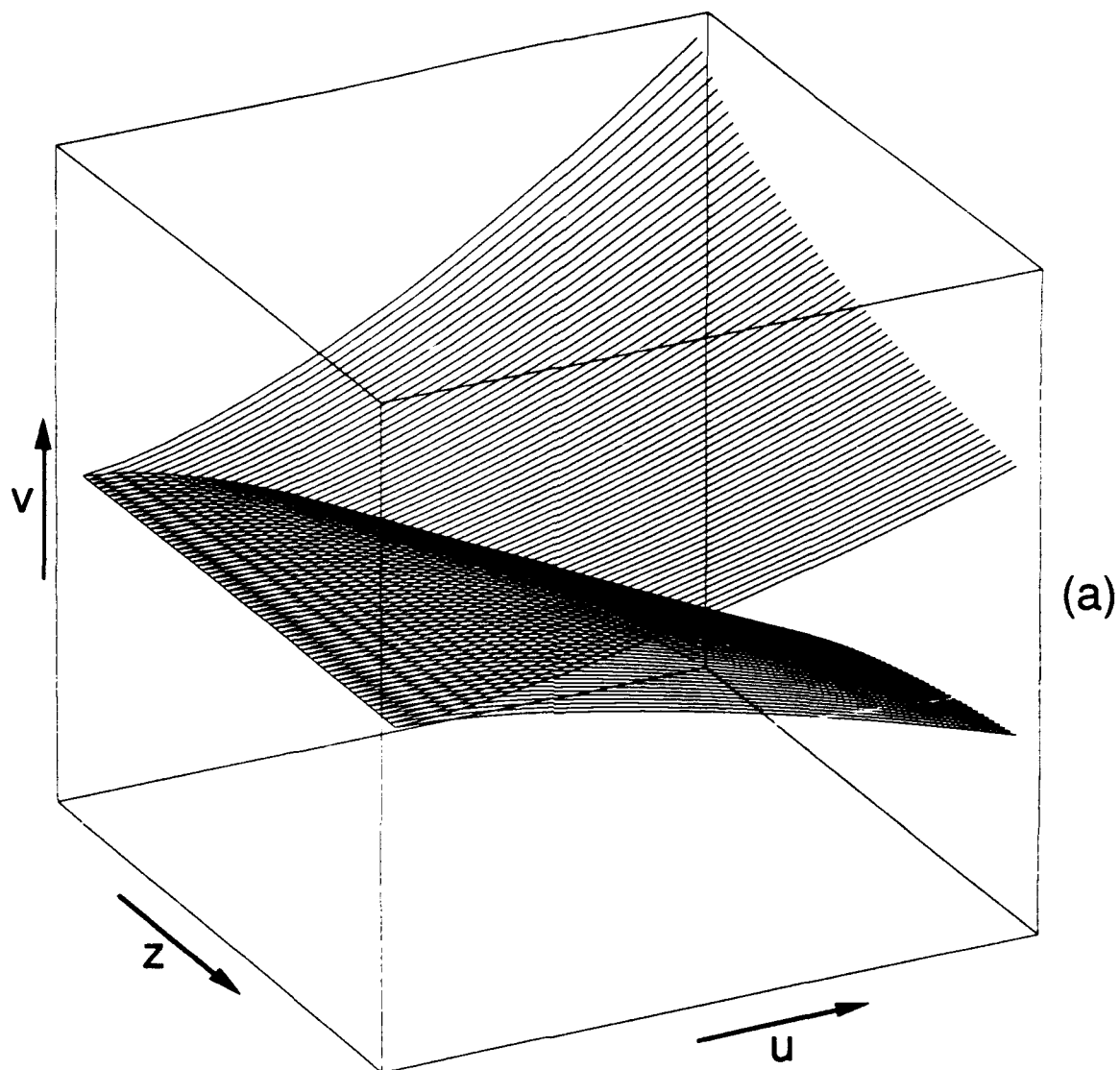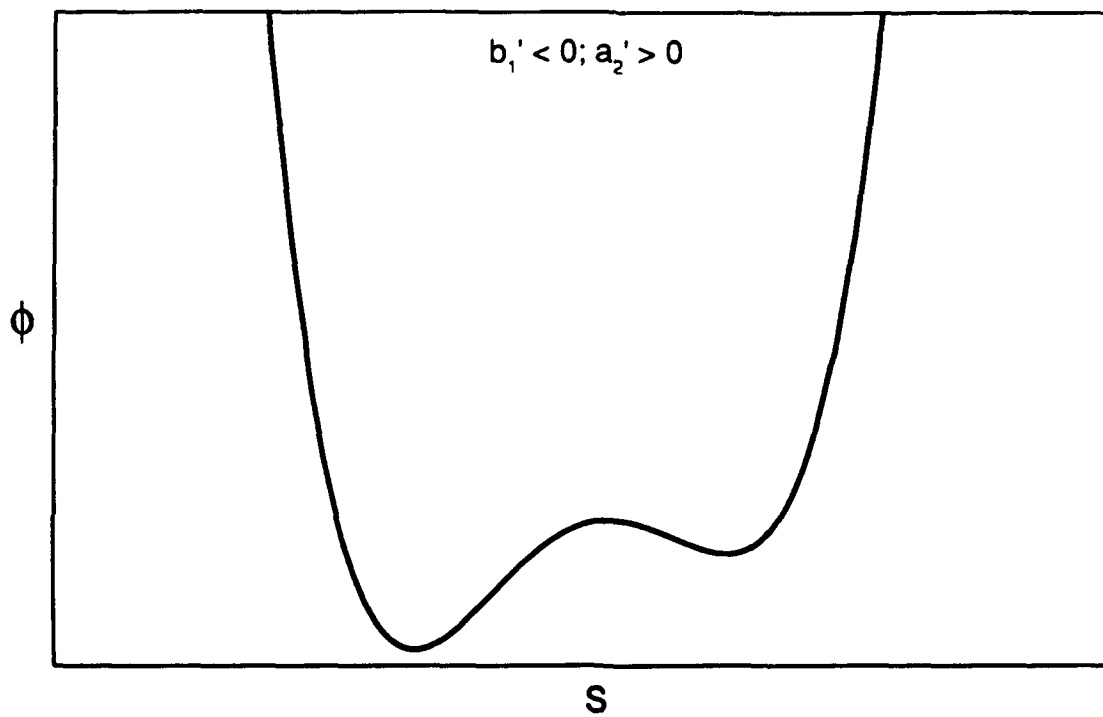
Figure 19) The general shape of the distance function of the transverse cusp caustic

diffraction integral after the evaluation of the x dependence when $b_1' = - b_1'$ from Fig. 7

and a_2', U_e, and V_e are unchanged from Fig. 7.
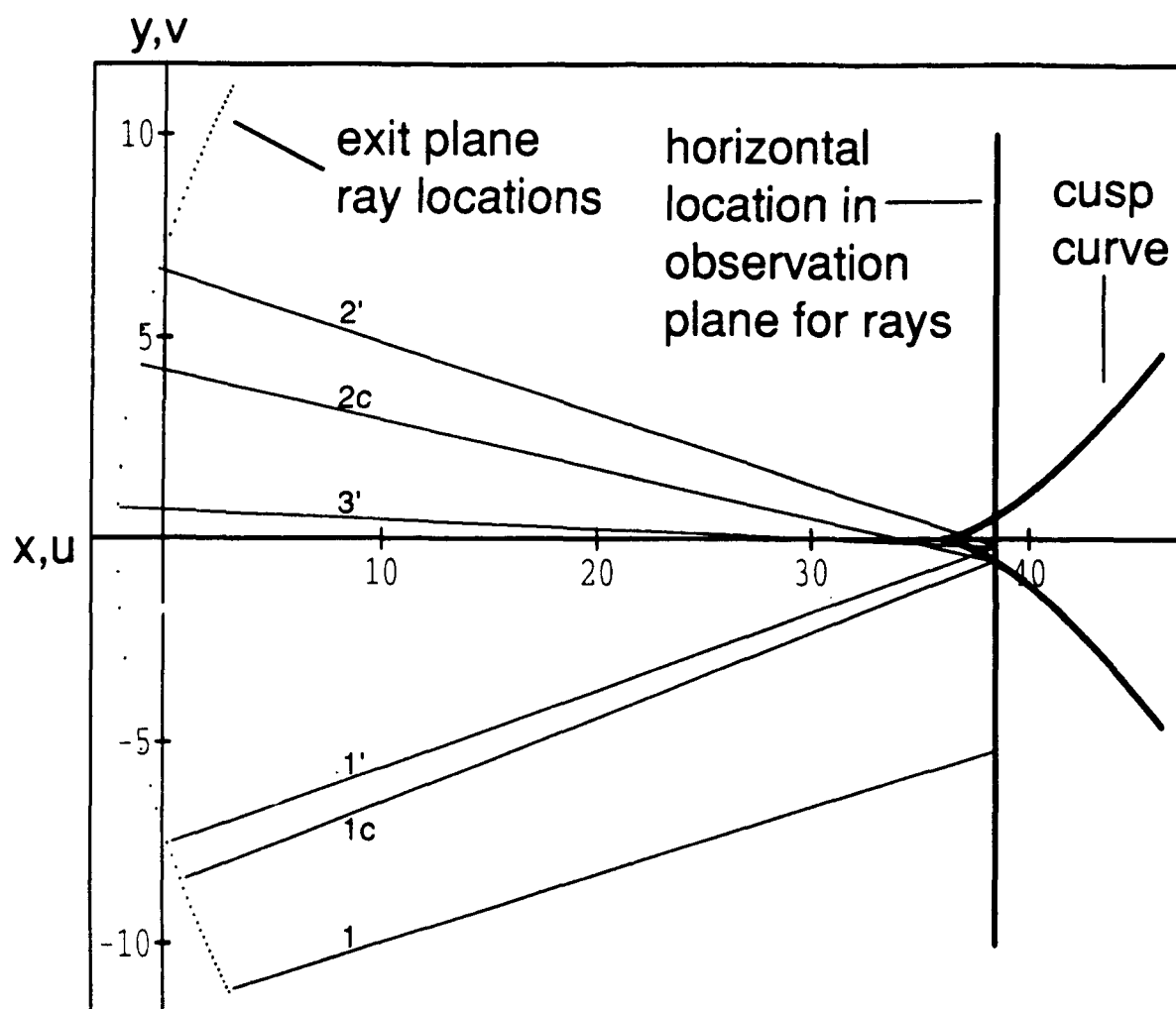
Figure 20) The relative location of rays in the exit plane that pass through a vertical cut in the observation plane when $b_1' < 0$ and $a_2' > 0$. Ray 1 passes through the cut below the cusp curve in the observation plane. Rays 1c and 2c pass through the lower branch of the cusp curve, with ray path 1c being the shorter path to the cusp curve. Rays 1', 2', and 3' pass through a point inside the cusp curve below the symmetry axis, with the ray paths from longest to shortest being 3', 2', and 1'.

4.5 DISCUSSION AND CONCLUSION

The experiments discussed in Sec. 4.3 show that whether an echo had touched a caustic or not prior to reaching the observation plane could be established from its shape. Furthermore, the identification of the echoes in the sequence was in agreement with predictions. The theory for other surface parameters from which a TCC can be produced was discussed in Sec. 4.4. The results are related to the more general aspects of identifying arrivals discussed here in Sec. 4.5.

Figure 21 shows the longitudinal cusp caustic formed by the reflection of a plane wave from a circular surface. The longitudinal cusp caustic opens opposite the direction of propagation of the wavefront forming the caustic. It is clear from Fig. 21 that inside the caustic there will be one early $s(t)$ type arrival and two later $h(t)$ type arrivals, while the one ray left outside the caustic will have touched the caustic and be an $h(t)$ type arrival. Figure 22 shows the opposite orientation for the longitudinal cusp caustic, opening along the direction of propagation. From the three rays shown (A, B, and C) the orientation of the rays arriving inside the caustic is two early $s(t)$ type arrivals and one later $h(t)$ type arrival, while outside the caustic none of the rays will have reached the caustic and there is one $s(t)$ type arrival.

When Figs. 21 and 22 are compared to Figs. 10 and 20 the following is evident. For $b_1' > 0$ the TCC has a spatial orientation relative to the ray paths similar to that of the longitudinal cusp caustic shown in Fig. 21 while for $b_1' < 0$ the TCC has a spatial orientation similar to that of the longitudinal cusp caustic in Fig. 22. The difference in the spatial orientations of the ray locations in the exit plane relative to the caustic surfaces can be seen as follows: for $b_1' > 0$ rays originate inside the caustic and move out and for $b_1' < 0$ rays originate outside the caustic and move in. Considering the orientation of the ray locations relative to the caustic surfaces shown in Figs. 15-18, when $b_1' > 0$ the sequence of the $s(t)$ and $h(t)$ type arrivals is that of a longitudinal cusp caustic opening opposite the direction of propagation, Fig. 21. When $b_1' > 0$ there will be one $h(t)$ arrival outside the

cusp curve, and inside the cusp curve there will be one early s(t) type arrival and two later h(t) type arrivals. For $b_1' < 0$ it is anticipated that the sequence of the arrivals for the TCC is that of a longitudinal cusp caustic that opens along the direction of propagation, Fig. 22. However for the TCC produced by reflection from a surface described by Eq. (9) each arrival will have an extra $\pi/2$ phase advance due to touching the caustic close to the reflector. Thus for $b_1' < 0$ there will be one h(t) type arrival outside the cusp curve, and inside the cusp curve two early h(t) type arrivals and one later −s(t) type arrival.

The experimental data shown in Sec. 3.B was obtained from a wavefront with b_1' > 0 and a_2' > 0. The single arrival outside the cusp curve in the observation plane is an h(t) type arrival. Inside the cusp curve in the observation plane the arrivals have the sequence, one s(t) then two h(t) type arrivals. As b_1' > 0 and a_2' > 0 for this wavefront the observed arrival orientations are those expected from the analysis given in Sec. 3.A. From observations of the locations of rays in the exit plane made by positioning an anti-reflection tile in front of the reflecting surface and knowledge of the location of the cusp curve in the observation plane, the orientation of the ray locations in the exit plane relative to the cusp curve in the observation plane was verified to be that shown in Figs. 10 and (17b) for b_1' > 0 and a_2' > 0.

The sequence of the arrivals shown by the data appears to violate the restrictions imposed by Brown and Tappert [15]. However, the restrictions of Brown and Tappert apply to wavefields that are not aperture limited. Since the size of the reflecting surface used was finite, the reflected wavefront was aperture limited. Echoes from the edge of the reflector were not clearly seen either because of their low amplitude or because their time of arrival was outside the time window considered. The low amplitude may be partially a consequence of the weak directionality of the source and receiver. Brown and Tappert state that for aperture limited wavefields the restrictions given in Sec. 2.B may not hold. This does not, however, reconcile the expected behavior of the caustics discussed in Sec. 4,

unless the aperture free TCC with $b_1' > 0$ or $b_1' < 0$ is always imbedded in a higher order caustic with at least two earlier $s(t)$ type arrivals then the arrivals of the TCC.
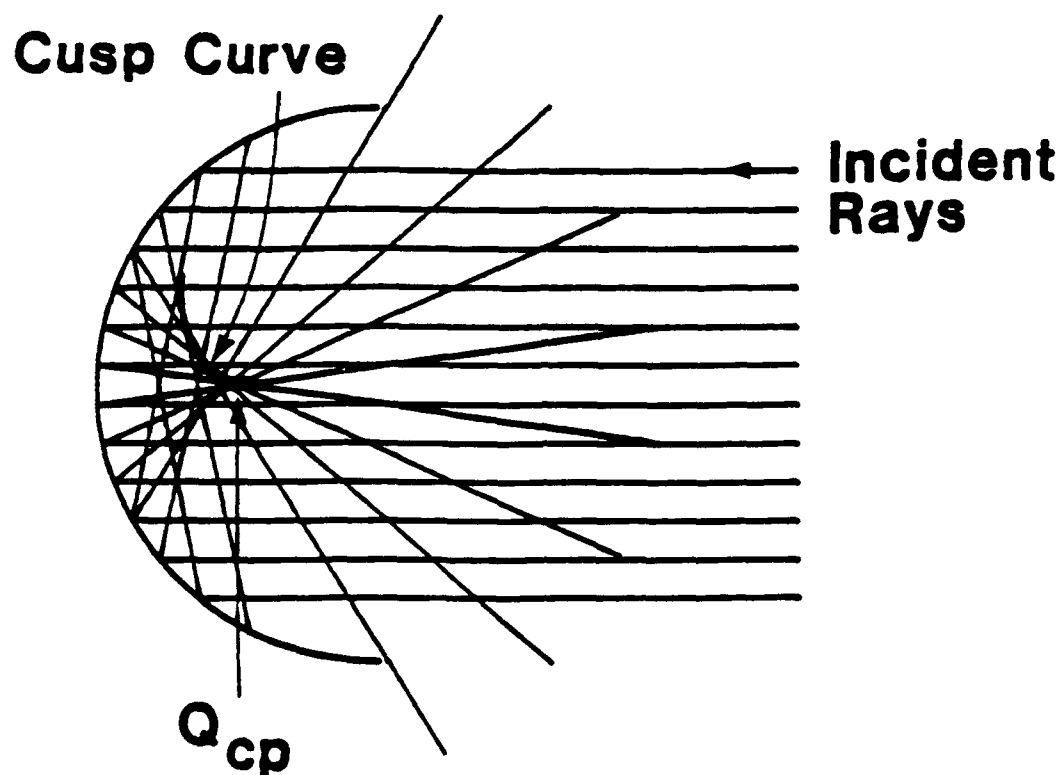
Figure 21) The longitudinal cusp caustic formed by the reflection of a plane wave from a semi-circular surface. The longitudinal cusp caustic in this figure opens opposite the direction of propagation of the reflected wavefront. The rays from the upper and lower portions of the wavefront travel a longer distance to reach points inside the caustic thus the arrival time sequence of signals inside the caustic is s(t), h(t), h(t). Outside the caustic the single ray must have touched the caustic and is thus an h(t) type arrival.
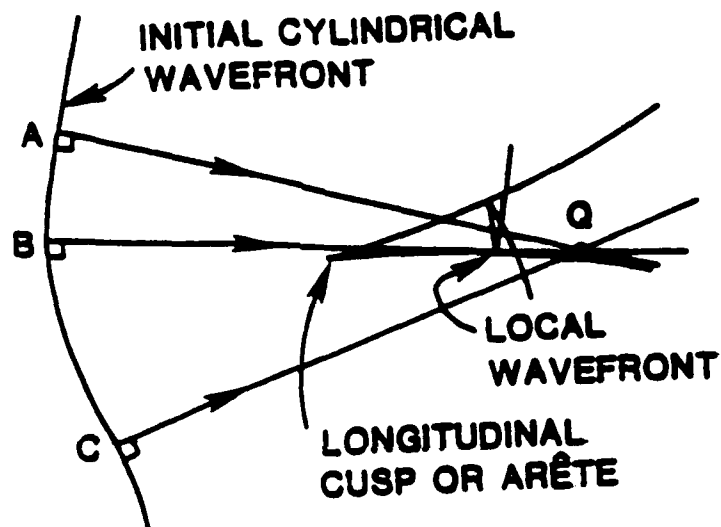
Figure 22) An example of a wavefront that forms a longitudinal cusp caustic that opens along the direction of propagation. The arrival scheme for the signals propagating along the ray paths A, B, and C in this figure inside the caustic is s(t), s(t), h(t), where the upper and lower ray paths from this wavefront to points in the caustic are shorter distances then the center ray path. Outside the caustic none of the rays have reached the caustic and the single arrival will be an s(t) type arrival.

APPENDIX A

THE RELATION OF THE MAXIMA AND MINIMA OF THE DISTANCE FUNCTION TO THE RAYS THAT TOUCH THE CAUSTIC

Consider the surface formed by the distance function for points in the exit plane to a point in the observation plane. The ray condition defines the location of rays in the exit plane as the extrema of the distance function. In a small region about a ray in the exit plane there will be two principle directions x' and y' associated with the curvature of the distance function at that point. When the ray location is the origin of the principle coordinates (x' = 0, y' = 0), a Taylor expansion of the distance function about the ray gives

$$\phi(x',y',U_e,V_e) \approx \phi(0,0,U_e,V_e) + \frac{\partial^2\phi}{\partial x'^2} x'^2 + \frac{\partial^2\phi}{\partial y'^2} y'^2 . \tag{A1}$$

There are then three possibilities for the type of the extrema of the distance function at the ray: Both second partial derivatives are positive and the distance function increases in either direction relative to the ray location; the ray is located at a minimum of ϕ. The second partial derivatives have opposite signs so that the distance function increases along one coordinate and decreases along the other; the ray is located at a saddle point of ϕ. Or, both second derivatives are negative and the distance function decreases in either direction from the ray location; the ray is located at a maximum of ϕ.

Dangelmayr and Güttinger[22] show that, relative to a ray located at a minimum of ϕ, the spectral components of a ray located at a saddle point of ϕ are phase advanced by a factor of $\pi/2$. The spectral components of a ray located at a maximum of ϕ are phase advanced relative to a ray located at a minimum of ϕ by a factor of π. This relation of the phases of the three possibilities shows that a ray at a minimum of the distance function will not have touched a caustic prior to arriving in the observation plane. A ray located at a saddle point of ϕ will have touched one caustic prior to arriving in the observation plane. A

ray located at a maximum of ϕ will have touched two caustics prior to arriving in the observation plane.

For the transverse cusp caustic the analysis given in Chapter 1 for a reflecting surface with $h_1 < 0$ forms only one caustic surface for $z > 0$. A second virtual caustic surface is formed for $z < 0$, however, for the reflection problem under consideration a ray will never touch this caustic. Thus only two of the above possibilities should be evident in reflected signals. A ray from the surface will either not have touched a caustic, or it will have touched only one caustic and its spectral components will be phase advanced by $\pi/2$. The coordinates (x,y) in the exit plane are not necessarily the principle coordinates and thus the identification of the type of extremum of the distance function is not as easy as that given in the discussion that follows Eq. (A1), though the relationship between the types of extremum and how many times a ray touches a caustic is the same.

For a general three dimension surface defined by $z = f(x,y)$, the extremum are given by $\partial f/\partial x = 0$ and $\partial f/\partial y = 0$. The type of the extremum is identified by [23,24]

$$\text{maximum:} \quad H(x,y) > 0 \text{ and } \quad \partial^2 f/\partial x^2 < 0 \qquad (A2)$$

$$\text{minimum:} \quad H(x,y) > 0 \text{ and } \quad \partial^2 f/\partial x^2 > 0 \qquad (A3)$$

$$\text{saddle:} \quad H(x,y) < 0, \qquad (A4)$$

where $H = (\partial^2 f/\partial x^2)(\partial^2 f/\partial y^2) - (\partial^2 f/\partial x\partial y)^2$ and in terms of the principle coordinates $\partial^2 f/\partial x\partial y = 0$. This can be related to the reduced distance function $\phi(x,y,U_e,V_e)$ in Eq. (10) by letting $\phi = f$. By using the ray condition $\partial\phi/\partial x = 0$ to find $x(y)$, ϕ can be written in the form of Eq. (16). The extrema of Eq. (16) are classified by: a maximum when $d^2\phi/ds^2 < 0$, an inflection point when $d^2\phi/ds^2 = 0$, and a minimum when $d^2\phi/ds^2 > 0$. The hessian, H, and $d^2\phi/ds^2$ are related by $H = 2b_1'K(d^2\phi/ds^2)$, where $K = |a_2'|/2|b_1'|^{1/2}$ is a positive number and thus will not affect the sign of H. Whether or not a ray touches a caustic prior to arriving in the observation plane is then given by the signs of b_1' and $d^2\phi/ds^2$.

For the surface parameters of the reflecting surface used in the experiments $b_1' > 0$ for all z_e and the discussion below follows from the analysis of the extremum identifications given above. As $\partial^2\phi/\partial x^2 = 2b_1' > 0$ at all observation points, for a ray to have touched a caustic $\phi(s,U_e,V_e)$ must be at a maximum in terms of s $(\partial^2\phi/\partial s^2 < 0)$. From the relation $H = 2b_1'K(\partial^2\phi/\partial s^2)$, $H < 0$ and the ray is located at a saddle point of the distance function. When $\partial^2\phi/\partial s^2 > 0$, at a minimum of $\phi(s,U_e,V_e)$, $H > 0$ and with $\partial^2\phi/\partial x^2 = 2b_1' > 0$ the ray is at a minimum of the distance function and will not touch the caustic. Thus the maxima of Eq. (16) will define rays that touch one caustic and the minima define rays that do not touch a caustic when $b_1' > 0$.

When $h_1 > 0$ it can be argued that there will be two caustic surfaces for $z > 0$, one of which is located near the reflector in the region where $b_1' > 0$. As z_e increases, b_1', which starts out positive, becomes negative. When $b_1' < 0$, $\partial^2\phi/\partial x^2 = 2b_1' < 0$ and the extrema of $\phi(s,U_e,V_e)$ will define either a saddle point or a maximum. Thus it follows from Fig. 19 and the sign of $\partial^2\phi/\partial x^2$ that two of the rays come from saddle points of ϕ and one comes from a maximum of ϕ. As the each ray leaves the exit plane they will touch the caustic formed when b_1' is positive (close to the reflecting surface) prior to reaching the caustic formed when b_1' is negative (far from the reflecting surface). Thus the analogy between the TCC when $b_1' < 0$ and the axial cusp caustic, Fig. 22, given in Sec. 4.5 still holds though the signals associated with the TCC will have the arrival sequence hh–s due to having touched the caustic formed when $b_1' > 0$.

References

1)   A. D Pierce, *Acoustics, An Introduction to its Principles and Applications*, (McGraw-Hill, New York, 1981), pp 468-469.

2)   D. P. Hill, "Phase shift and pulse distortion in body waves due to internal caustics," Bull. Seism. Soc. Am., **64**, 1733-1742, (1974).

3)   M. G. Brown, "The transient wave fields in the vicinity of cuspoid caustics," J. Acoust. Soc. Am. **70**, 1427-1436 (1986).

4)   I Tolstoy, "Phase changes and pulse deformation in acoustics," J. Acoust. Soc. Am., **44**, 675-683,(1968).

5)   G. L. Choy and P. G. Richards, "Pulse distortion and Hilbert transformation in multiply reflected and refracted body waves," Bull. Seism. Soc. Am., **65**, 55-70, (1975).

6)   M. V. Berry and C. Upstill, "Catastrophe optics: Morphologies of caustics and their diffraction patterns," in *Progress in Optics*, ed E. Wolf (North Holland, Amsterdam, 1980), Vol. 18, pp 257-346.

7)   M. G. Brown and F. D. Tappert, "Catastrophe theory, caustics and traveltime diagrams in seismology," Geophys. J. R. astr. Soc., **88**, 217-229, (1987).

8)   ref 1, Ch. 4.

9)   T. Pearcey, "The structure of an electromagnetic field in the neighbourhood of a cusp of a caustic," Philos. Mag. **37**, 311-317, (1946).

10)   P. L. Marston, "Transverse cusp diffraction catastrophe: Some pertinent wavefronts and a Pearcey approximation to the wave fields," J. Acoust. Soc. Am. **81**, 226-232, (1987).

11)   J. H. Ansell, "Legendre functions, the Hilbert transform and surface waves on spheres," Geophys. J. R. astr. Soc., **32**, 95-117, (1973).

12)   E. C. Tichmarsh, *Introduction to the Theory of Fourier Integrals*, (Oxford at the Claredon, 1937), pp 119-151.

13)   B. F. Cron and A. H. Nuttall, "Phase distortion of a pulse caused by bottom reflection," J. Acoust. Soc. Am., **37**, 486-492, (1965).

14)   ref. 1, pp 135-137.

15)   M. G. Brown and F. D. Tappert, "Causality, caustics and the structure of transient wave fields," J. Acoust. Soc. Am., **80**, 251-255, (1986);M. G. Brown, *ibid*, **80**, 1851(E), (1986).

16)   L. B. Felsen, "Novel ways of tracking rays," J. Opt. Soc. Am. A, **2**, 954-963, (1985).

17)   L. B. Felsen, "Evanescent waves," J. Opt. Soc. Am., **66**, 751-760, (1976).

18) L. B. Felsen, "Geometric theory of diffraction, evanescent waves, complex rays and Gaussian beams," Geophys. J. R. astr. Soc., **79**, 77-88, (1984).

19) R. W. Boyd, "Intuitive explanation of the phase anomaly of focused light beams," J. Opt. Soc. Am., **70**, 877-880, (1980).

20) ref. 1, pp 143-144.

21) M. R. Layton, E. F. Carome, H. D. Hardy and J. A. Bucaro, "Effects of diffraction on stress pulse propagation," J. Acoust. Soc. Am., **64**, pp 250-256, (1978).

22) G. Danglemayr and W. Güttinger, "Topological approach to remote sensing," Geophys. J. R. astr. Soc.,**71**,pp 79-126, (1982). The sine convention used for the principle radii in the discussion above is the opposite of that used by Danglemayr and Güttinger.

23) P. T. Saunders, *An Introduction to Catastrophe Theory*, (Cambridge University Press, New York, 1985), p 22.

24) M. G. Brown, "The transient wave fields in the vicinity of the elliptic, hyperbolic, and parabolic umbilic caustics," J. Acoust. Soc. Am., **79**, 1385-1401, (1986).

This page is intentionally blank.

CHAPTER FIVE
COMPUTER SOFTWARE

5.1 THE CALCULATION OF THE PEARCEY FUNCTION

The basic algorithm used to calculate the Pearcey function $P(w_2, w_1)$ was provided by F. J. Wright [1]. This algorithm was modified to run on the IBM3090 with the quadrature routine being included in the algorithm, as opposed to using the IMSL library, for convenience. The integrand of the Pearcey function $\exp(i\psi)$ with

$$\psi = \frac{s^4}{4} + w_2\frac{s^2}{2} + w_1 s . \tag{1}$$

is highly oscillatory away from the stationary points of the phase. The use of standard quadrature routines to evaluate the Pearcey function gives inaccurate answers due to the highly oscillatory nature of the integrand. A general outline of the method used by the algorithm to compute $P(w_2,w_2)$ and the inaccuracy of the method for points far from the cusp point are discussed below. The method used to evaluate $P(w_2,w_2)$ is also used to Berry *et al.* to evaluate the diffraction integral describing the elliptic umbilic diffraction catastrophe [2].

To evaluate the Pearcey function, the integral is split into three separate integrals

$$P(w_2,w_1) = \int_{-\infty}^{\infty}\exp(i\psi)\,ds = \int_{-\infty}^{B}\exp(i\psi)\,ds + \int_{B}^{A}\exp(i\psi)\,ds + \int_{A}^{\infty}\exp(i\psi)\,ds. \tag{2}$$

The limits B and A are set to include all of the stationary points s_i of the integrand where

$$\frac{\partial\psi}{\partial s}\Big|_{s_i} = s_i^3 + w_2 s_i + w_1 = 0. \tag{3}$$

Both of the outer integrals contain the region where the integrand $\exp(i\psi)$ is highly oscillatory and are evaluated using an asymptotic approximation. The asymptotic series is produced by a repeated integration by parts of the outer integrals starting with

$$\exp(i\psi) = \frac{1}{i\psi'}[i\psi' \exp(i\psi)] = \frac{1}{i\psi'}\frac{d\exp(i\psi)}{ds} . \tag{4}$$

With $\psi(s = \pm\infty) = \infty$, the first three terms in the asymptotic series are

$$i\frac{\exp[i\psi(A)]}{\psi'(A)} - i\frac{\exp[i\psi(B)]}{\psi'(B)} , \tag{5a}$$

$$\frac{\psi''(A)}{[\psi'(A)]^3}\exp[i\psi(A)] - \frac{\psi''(B)}{[\psi'(B)]^3}\exp[i\psi(B)] , \tag{5b}$$

$$i\left\{ \frac{\psi'''(A)}{[\psi'(A)]^4} - \frac{3[\psi''(A)]^2}{[\psi'(A)]^5} \right\}\exp[i\psi(A)]$$

$$-i\left\{ \frac{\psi'''(B)}{[\psi'(B)]^4} - \frac{3[\psi''(B)]^2}{[\psi'(B)]^5} \right\}\exp[i\psi(B)], \tag{5c}$$

where $\psi' = d\psi/ds$. The center definite integral is evaluated using a standard quadrature routine as it contains all the stationary points of the phase and near the cusp point does not oscillate rapidly.

As the observation point moves far from the cusp point, the approximation to the Pearcey function given above begins breakdown. The reason for this breakdown is discussed below. For points near the cusp point the stationary points of the phase are close together and the integrand in this region is not highly oscillatory. As the observation point moves away from the cusp point the stationary points move further apart. The region between the stationary points becomes highly oscillatory when there is a large separation between the stationary points, thus the quadrature routine used to approximate the definite integral returns inaccurate results. Figures 1- 6 show calculations of

$$\cos\left(\frac{s^4}{4} + w_2\frac{s^2}{2} + w_1s\right), \qquad \sin\left(\frac{s^4}{4} + w_2\frac{s^2}{2} + w_1s\right), \tag{6a,b}$$

and Eq. (3) showing the stationary points, where $\partial\psi/\partial s = 0$. From Figs. 1- 6 it can be seen that the oscillatory nature of the integrand begins to dominate the region between the stationary points of the phase as the observation point moves away from the cusp point.

Thus, far from the cusp point the quadrature routine will not return accurate values for the

center definite integral and the approximation of the Pearcey function begins to breakdown.

The code used to calculate the Pearcey function follows.

```
*** PROGRAM TITLE: CANONICAL CUSP DIFFRACTION CATASTROPHE
**           MAGNITUDE CONTOUR DATA GENERATOR
***
*
*
*
*** PROGRAM INTENT
*** THIS PROGRAM GENERATES A RECTANGULAR GRID OF CANONICAL
*** CUSP
*** DIFFRACTION CATASTROPHE MAGNITUDES FOR PLOTTING BY
*** CUSPCON SAS.
*** CUSPCON USES COMPLEX FUNCTION CUSPDC AND WRITES THE
*** OUTPUT FILE
*** CUSPCON DATA.

*** MAIN


      INTEGER IDIVS
      REAL V(400), U(300), MAGC(400,300), MAX, K, B1
      COMMON /PARAMS/ B1 , K
      COMMON /COORD/ U, V, MX, MY
      COMMON /LEVEL/ MAX, MAGC, NX, NY

      MAXMAG = 0.0

      CALL POINTS

      CALL MAG

      CALL RAS

      END




      SUBROUTINE MAG

      REAL U(400), V(300), MAX, MAGC(400,300), UC, B1, K
      COMPLEX C, CUSPDC, CPH
      COMMON /PARAMS/ B1 , K
      COMMON /COORD/ U, V, MX, MY
      COMMON /LEVEL/ MAX, MAGC, NX, NY
```

```
      WRITE(*,*) NX, NY
      WRITE(*,*) MX, MY
      NY = MY
      NX = MX
      WRITE(*,*) NX, NY
      WRITE(*,*) MX, MY

      DO 12 IY1=1,NY
           DO 13 IX1=1,NX
                UC = V(IY1) - 10.0
                IF (U(IX1).LT.UC) THEN
                MAGC(IX1,IY1) = 0.0
                GO TO 13
                ENDIF
                C = CUSPDC(U(IX1), V(IY1))
                MAGC(IX1,IY1) = SQRT(REAL(C)**2 + IMAG(C)**2)
                IF (MAGC(IX1,IY1).GT.MAX) MAX=MAGC(IX1,IY1)
13         CONTINUE
12    CONTINUE

      WRITE(*,*) MAX,N

      RETURN
      END




*** CUSPDC RETURNS THE CANONICAL CUSP DIFFRACTION CATASTROPHE
*** AT (U, V) TO AN ESTIMATED ACCURACY OF 0.001.
*** AN EARLIER VERSION WAS TESTED ON THE QMC2988 BY F. J. WRIGHT
*** FOR - 8 <= U <= 4 AND 0 <= V <= 6.

      COMPLEX FUNCTION CUSPDC(U, V)

      REAL A, B, C1, RT2PI, START, U, U3, UU, V, VV
      COMPLEX QUAD, TAILS, SERIES
      COMMON /COORDS/ UU, VV
      DATA RT2PI /1.4142136/
      DATA C1   /10./
      DATA START /5./
*** START MAY NEED INCREASING FOR LARGE NEGATIVE U AND LARGE V
*** (TOO LARGE A VALUE MERELY REDUCES EFFICIENCY).

      UU = U
      VV = ABS(V)


*** SET STARTING VALUES FOR NEWTON-RAPHSON ITERATION FOR
*** CUTOFFS:
*** LOWER CUTOFF B IS ALWAYS < 0 AND NEVER GIVES ANY PROBLEM -
*** JUST TAKE STARTING VALUE SUFFICIENTLY LARGE AND NEGATIVE.
      B = - START
*** UPPER CUTOFF A DEPENDS CRITICALLY ON SHAPE OF THE DERIVATIVE
```

```
*** OF THE PHASE FUNCTION, WHICH DEPENDS ON U AND V.
      IF (U .GT. 0) THEN
            A = SIGN(START, C1 - VV)
      ELSE
      U3 = - U / 3.
      A = SIGN(START, C1 - VV + 2. * U3 * SQRT(U3))
      END IF

      TAILS = SERIES(A, C1) - SERIES(B,- C1)

*** CUSPDC HAS AN ACCURACY OF 0.001 SINCE TAILS + QUAD'S IS 0.002.
      CUSPDC = (TAILS + QUAD(B, A)) / RT2PI

      RETURN
      END


*** FUNCTION SERIES(S, +/-C1) EVALUATES THE TAIL OF THE INTEGRAL
*** USING ASYMPTOTIC SERIES TO AN ESTIMATED ACCURACY OF 0.0005
*** AND ALSO RETURNS THE OPTIMAL CUTOFF S.

      COMPLEX FUNCTION SERIES(S, PMC1)

      REAL ASTEP, C2, C3, COR, P, P1, P2, P3, PHI, PMC1,
     +    STEP, T, T1, T1SQ, T2, T3, U, V, S
      COMMON /COORDS/ U, V
      DATA ASTEP /0.02/
      DATA C2    /0.01/
      DATA C3    /0.0005/

*** DERIVATIVES OF THE PHASE FUNCTION
      P(S)  = S * (S * (S * S/4 + U/2) + V)
      P1(S) = S * (S * S + U) + V
      P2(S) = 3. * S * S + U
      P3(S) = 6. * S
*** PMC = +/-C1
*** ASTEP = MAGNITUDE OF THE OPTIMIZATION STEP
      STEP = SIGN(ASTEP, PMC1)

*** SOLVE P1(S) - PMC1 = 0 FOR INITIAL CUTOFF, USING NEWTON-
RAPHSON:
1        COR = (P1(S) - PMC1) / P2(S)
      S = S - COR
      IF (ABS(COR) .GT. ASTEP) GOTO 1

*** EVALUATE SERIES STEPPING OUT AS NECESSARY:
      GOTO 20
10    S = S + STEP
*** TERM 1:
20    T1 = 1. / P1(S)
      T1SQ = T1 * T1
      T = P2(S) * T1SQ
*** TERM 2:
      T2 = T * T1
```

```
        IF (ABS(T2) .GT. C2) GOTO 10
*** TERM 3:
        T3 = P3(S) * T1SQ * T1SQ - 3. * T * T * T1
        IF (ABS(T3) .GT. C3) GOTO 10

        PHI = P(S)
        SERIES = CMPLX(COS(PHI), SIN(PHI)) * CMPLX(T2, T1 + T3)
        RETURN
        END



*** FUNCTION QUAD(B, A) EVALUATES BY QUADRATURE THE CENTER
RANGE OF
*** THE INTEGRAL TO AN ESTIMATED ACCURACY OF 0.001.

        COMPLEX FUNCTION QUAD(B, A)

        REAL A, B, COSPHI, QI, QR
        EXTERNAL COSPHI, SINPHI, GQUAD

*** THIS IS AN ADAPTIVE QUADRATURE ROUTINE FROM THE 'IMSL'
LIBRARY.
        CALL GQUAD(B,A,COSPHI,QR)
        CALL GQUAD(B,A,SINPHI,QI)
        QUAD = CMPLX(QR, QI)
        RETURN
        END



        REAL FUNCTION COSPHI(S)
        REAL U, V, S
        COMMON /COORDS/ U, V
        PHI(S) = S *(S *(S * S/4. + U/2.) + V)
        COSPHI = COS(PHI(S))
        RETURN
        ENTRY SINPHI(S)
        SINPHI = SIN(PHI(S))
        RETURN
        END
C
C
        SUBROUTINE GQUAD
C       ..................................................
C   PURPOSE
C       TO COMPUTE INTERGRAL(FCT(X), SUMMED OVER X FROM XL TO XU)
C
C       USAGE
C          CALL GQUAD(XL,XU,FCT,Y)
C       PARAMETER FCT REQUIRES AN EXTERNAL STATEMENT
C
C       PARAMETERS
C       XL - DOUBLE PRECISION LOWER BOUND OF THE INTEGRAL.
C       XU - DOUBLE PRECISION UPPER BOUND OF THE INTEGRAL.
```

```
C      FCT - THE NAME OF THE DOUBLE PRECISION EXTERNAL FUNCTION
C      SUBPROGRAM USED.
C      Y   - THE RESULTING DOUBLE PRECISION INTEGRAL VALUE.
C
C      REMARKS
C      NONE
C
C      SUBROUTINES AND FUNCTION SUBPROGRAMS REQUIRED
C      THE EXTERNAL DOUBLE PRECISION FUNCTION SUBPROGRAM FCT
C      MUST BE SUPPLIED BY THE USER
C
C      METHOD
C      EVALUATION IS DONE BY MEANS OF A 32-POINT GUAS QUADRATURE
C      FORMULA, WHICH INTERGRATES POLYNOMIALS UP TO DEGREE 63
C      EXACTLY.
C      FROM THE FORTRAN COOKBOOK IN THE OUTER OFFICE.
C
C      .................................................................
C
       SUBROUTINE GQUAD(XL,XU,FCT,Y)
C
C
       REAL XL, XU, Y, A, B, C, FCT
       EXTERNAL FCT
C
       A = 0.5D0 * (XL + XU)
       B = XU - XL
       C = 0.49863193092474078D0 * B
       Y = 0.35093050047350483D-2 * ( FCT(A+C) + FCT(A-C))
       C = 0.49280575577263417D0 * B
       _ = Y + 0.81371973654528835D-2 * (FCT(A+C) + FCT(A-C))
       C = 0.48238112779375322D0 * B
       Y = Y + 0.12696032654631030D-1 * (FCT(A+C) + FCT(A-C))
       C = 0.46745303796886984D0 * B
       Y = Y + 0.17136931456510717D-1 * (FCT(A+C) + FCT(A-C))
       C = 0.44816057788302606D0 * B
       Y = Y + 0.21417949011113340D-1 * (FCT(A+C) + FCT(A-C))
       C = 0.42468380686628499D0 * B
       Y = Y + 0.25499029631188088D-1 * (FCT(A+C) + FCT(A-C))
       C = 0.39724189798397120D0 * B
       Y = Y + 0.29342046739267774D-1 * (FCT(A+C) + FCT(A-C))
       C = 0.36609105937014484D0 * B
       Y = Y + 0.32911111388180923D-1 * (FCT(A+C) + FCT(A-C))
       C = 0.33152213346510760D0 * B
       Y = Y + 0.36172897054424253D-1 * (FCT(A+C) + FCT(A-C))
       C = 0.29385787862038116D0 * B
       Y = Y + 0.39096947893535153D-1 * (FCT(A+C) + FCT(A-C))
       C = 0.25344995446611470D0 * B
       Y = Y + 0.41655962113473378D-1 * (FCT(A+C) + FCT(A-C))
       C = 0.21067563806531767D0 * B
       Y = Y + 0.43826046502201906D-1 * (FCT(A+C) + FCT(A-C))
       C = 0.16593430114106382D0 *B
       Y = Y + 0.45586939347881942D-1 * (FCT(A+C) + FCT(A-C))
       C = 0.11964368112606854D0 * B
```

```
Y = Y + 0.46922199540402283D-1 * (FCT(A+C) + FCT(A-C))
C = 0.72235980079139825D-1 * B
Y = Y + 0.47819360039637430D-1 * (FCT(A+C) + FCT(A-C))
C = 0.24153832843869158D-1 * B
Y = B * (Y + 0.48270044257363900D-1 * (FCT(A+C) + FCT(A-C)))
RETURN
END




      SUBROUTINE POINTS

      REAL U(400), V(300), SQ2, X2, Y1
      REAL D, UL, UH, VL, VH, SPACEV, SPACEU, I, J
      INTEGER N, IU, IV, MX, MY
      COMMON /COORD/ U, V, MX, MY

      CALL PARAM(D,X2,Y1,Z,SQ2)

      READ(7,*) UL, UH
      READ(7,*) VL, VH
      READ(7,*) MX, MY

      WRITE(10,8) UL, UH
      WRITE(10,9) VL, VH
8     FORMAT('UL=', 1F10.5, '  UH=', 1F10.5)
9     FORMAT('VL=', 1F10.5, '  VH=', 1F10.5)

      DIVS = MY
      SPACEV = (VH-VL)/DIVS
      DIVS = MX
      SPACEU = (UH - UL)/DIVS

      IX = 0
      IY = 0

      DO 10 J = VL, VH, SPACEV
           IY = IY + 1
           V(IY) = J * Y1
10    CONTINUE

      DO 11 I = UL, UH, SPACEU
           IX = IX + 1
           U(IX) = I * X2
11    CONTINUE

      RETURN
      END
```

```
         SUBROUTINE RAS

         REAL MAX, MAGC(400,300), NORFAC
         INTEGER NX, NY, IRAS, N, IX, IY
         COMMON /LEVEL/ MAX, MAGC, NX, NY

         WRITE(*,*) MAX
         NORFAC = 255.0 / MAX
         WRITE(9,1) NX
         WRITE(9,1) NY

         DO 3 IY = 1, NY
               DO 2 IX = 1, NX
                     IRAS = NINT(NORFAC * MAGC(IX,IY))
                     WRITE(9,1) IRAS
1                    FORMAT(1I5)
2              CONTINUE
3        CONTINUE
         RETURN
         END


         SUBROUTINE PARAM(D ,X2,Y1,Z,SQ2)

         REAL  Z,ZS,F,CS,UP,UA,VP,VA,C1,C2,C3,SQ2,ZE,B1,B2,A2,K,AB1,Y1
         REAL X1,X2,D
         COMMON /PARAMS/ B1 , K

         READ(7,*) Z, ZS
         READ(7,*) F, CS
         READ(7,*) C1, C2 , C3
         WRITE(*,*) Z, ZS
         WRITE(*,*) F, CS
         WRITE(*,*) C1, C2 , C3


         SQ2 = 1.4142136

         ZE = 1/(1/Z + 1/ZS)
         B1 = -2.0*C1 + 1/(2.0*ZE)
         B3 = -2.0*C3 + 1/(2.0*ZE)
         A2 = -2.0*C2
C        A2 = 27.0 * B1**2 * D / 4.0
C        C2 = A2 / 2.0
         K = 6.2831853*F / CS
         AB1 = ABS(B1)
         Y1 = (SQRT( SQRT( AB1 * K**3) / A2) / Z)*(AB1/B1)
         X1 = -2.0*B1*B3/A2
         X2 = SQRT(K/AB1) / Z
         D = (4.0*A2) / (B1 * B1 * 27.0)
         WRITE(10,20) D
```

```
20        FORMAT('THE UNITLESS OPENING RATE IS: ', 1F10.5)
          D = D / Z
          WRITE(10,30) D
30        FORMAT('THE OPENING RATE FOR THE PICTURE IS: ',1F10.5)
          WRITE(10,1) B1, B3
          WRITE(10,2) F, CS
          WRITE(10,3) Z, ZS
          WRITE(10,4) A2, K
          WRITE(10,5) X2, Y1
          WRITE(10,6) UA, UP
          WRITE(10,7) VA, VP
          WRITE(10,8) C1, C2
1         FORMAT('B1=', 1F10.5, '  B3=', 1F10.5)
2         FORMAT('F =', 1G10.5, '  CS=', 1G10.5)
3         FORMAT('Z =', 1F10.5, '  ZS=', 1F10.5)
4         FORMAT('A2=', 1F10.5, '  K =', 1F10.5)
5         FORMAT('X2=', 1F10.5, '  Y1=', 1F10.5)
6         FORMAT('UA=', 1F10.5, '  UP=', 1F10.5)
7         FORMAT('VA=', 1F10.5, '  VP=', 1F10.5)
8         FORMAT('C1=', 1F10.5, '  C2=', 1F10.5)

          RETURN
          END
```

Figure 1) (a) A calculation of $\cos(s^4/4 + w_2 s^2/2 + w_1 s)$ and $\partial\psi/\partial s$ for $w_2 = 2.0$ and $w_1 = 0$. (b) A calculation of $\sin(s^4/4 + w_2 s^2/2 + w_1 s)$ and $\partial\psi/\partial s$ for $w_2 = 2.0$ and $w_1 = 0$.

Figure 2) (a) A calculation of $\cos(s^4/4 + w_2s^2/2 + w_1s)$ and $\partial\psi/\partial s$ for $w_2 = 10.0$ and $w_1 = 0$. (b) A calculation of $\sin(s^4/4 + w_2s^2/2 + w_1s)$ and $\partial\psi/\partial s$ for $w_2 = 10.0$ and $w_1 = 0$.

Figure 3) (a) A calculation of $\cos(s^4/4 + w_2 s^2/2 + w_1 s)$ and $\partial \psi/\partial s$ for $w_2 = 20.0$ and

$w_1 = 0$. (b) A calculation of $\sin(s^4/4 + w_2 s^2/2 + w_1 s)$ and $\partial \psi/\partial s$ for $w_2 = 20.0$ and
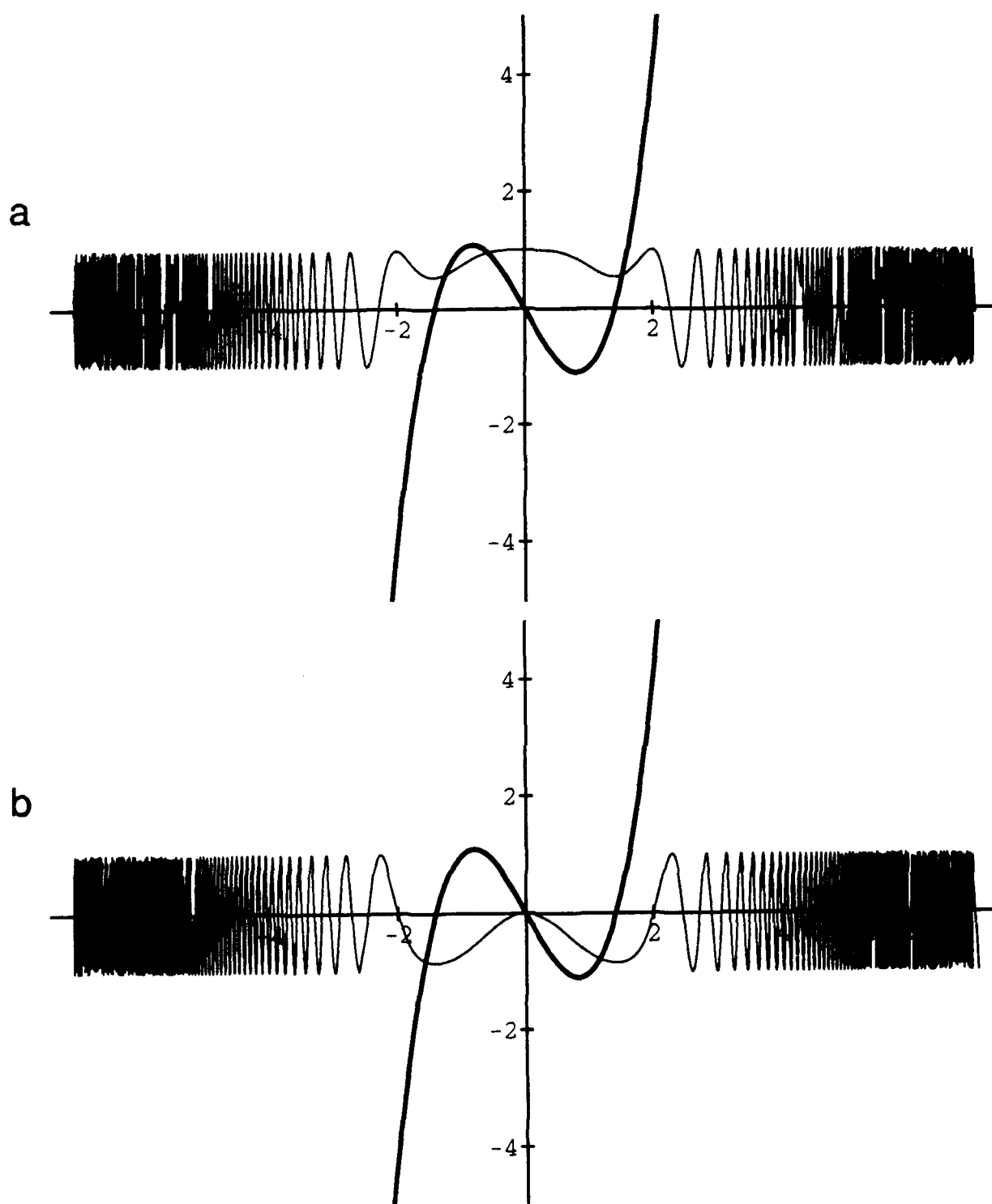
$w_1 = 0$.

Figure 4) (a) A calculation of $\cos(s^4/4 + w_2 s^2/2 + w_1 s)$ and $\partial\psi/\partial s$ for $w_2 = 5.0$ and $w_1 = 5.0$. (b) A calculation of $\sin(s^4/4 + w_2 s^2/2 + w_1 s)$ and $\partial\psi/\partial s$ for $w_2 = 5.0$ and $w_1 = 5.0$.

Figure 5) (a) A calculation of $\cos(s^4/4 + w_2s^2/2 + w_1s)$ and $\partial\psi/\partial s$ for $w_2 = 10.0$ and $w_1 = 5.0$. (b) A calculation of $\sin(s^4/4 + w_2s^2/2 + w_1s)$ and $\partial\psi/\partial s$ for $w_2 = 10.0$ and $w_1 = 5.0$.
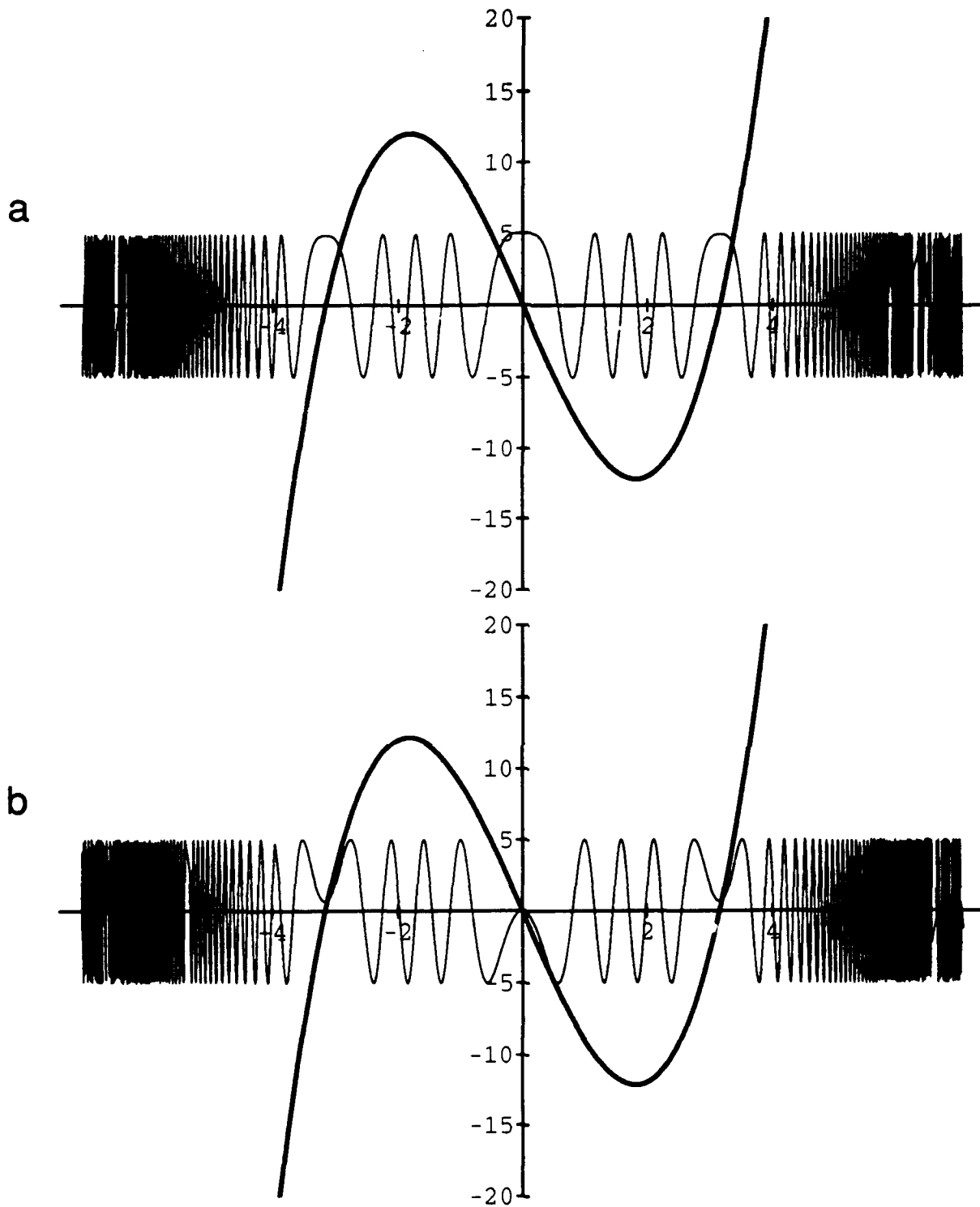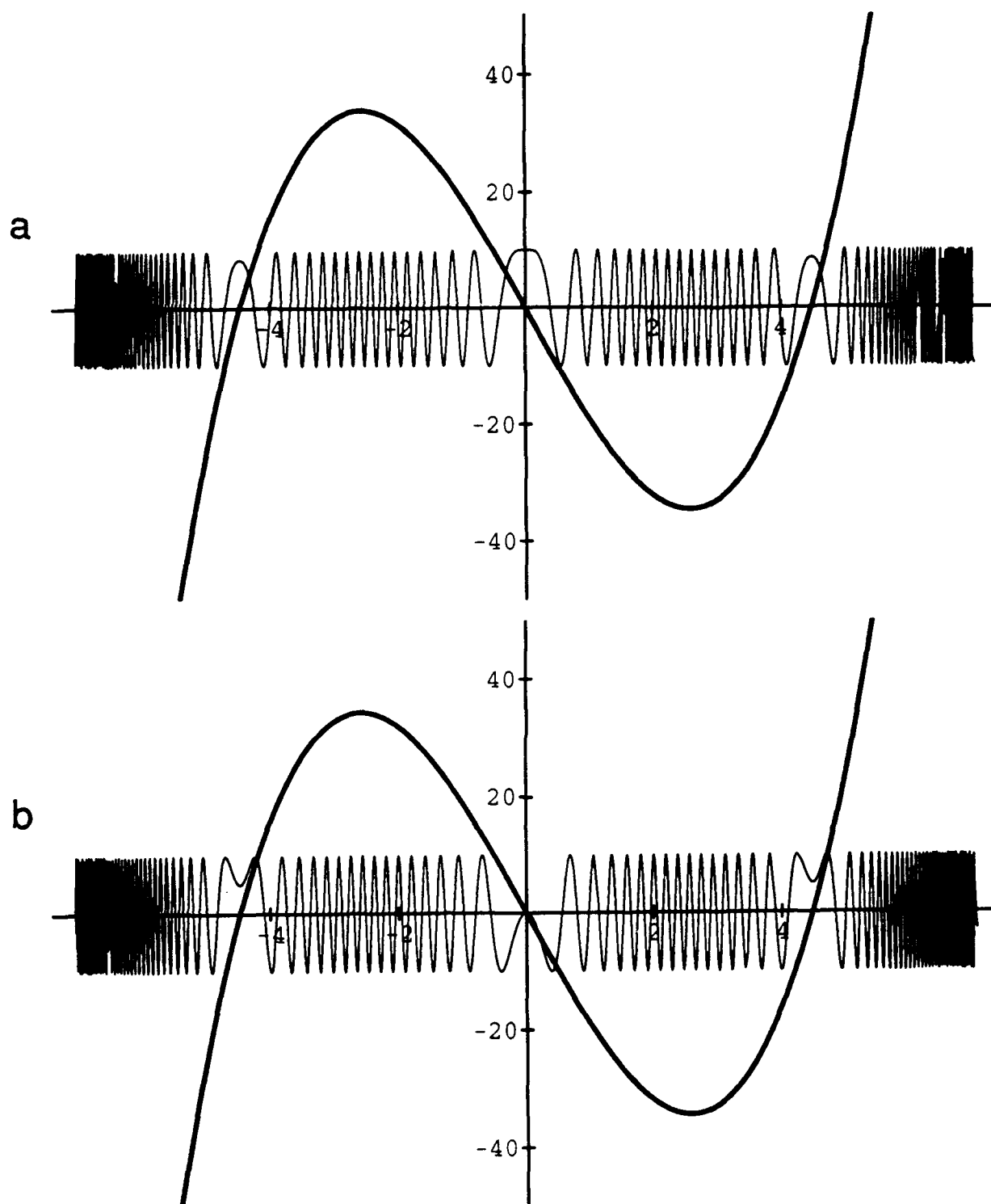
Figure 6) (a) A calculation of $\cos(s^4/4 + w_2s^2/2 + w_1s)$ and $\partial\psi/\partial s$ for $w_2 = 20.0$ and $w_1 = 5.0$. (b) A calculation of $\sin(s^4/4 + w_2s^2/2 + w_1s)$ and $\partial\psi/\partial s$ for $w_2 = 20.0$ and $w_1 = 5.0$.
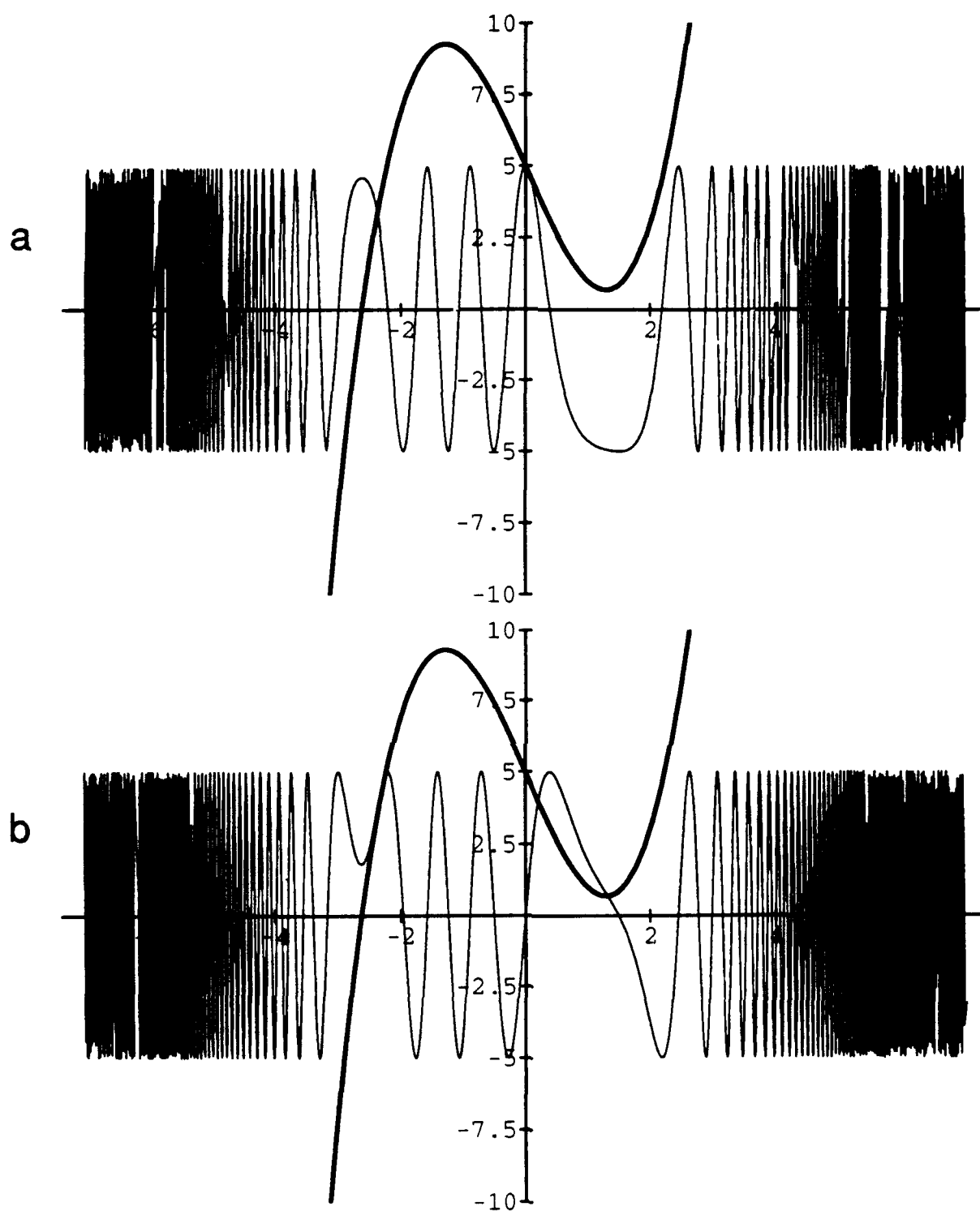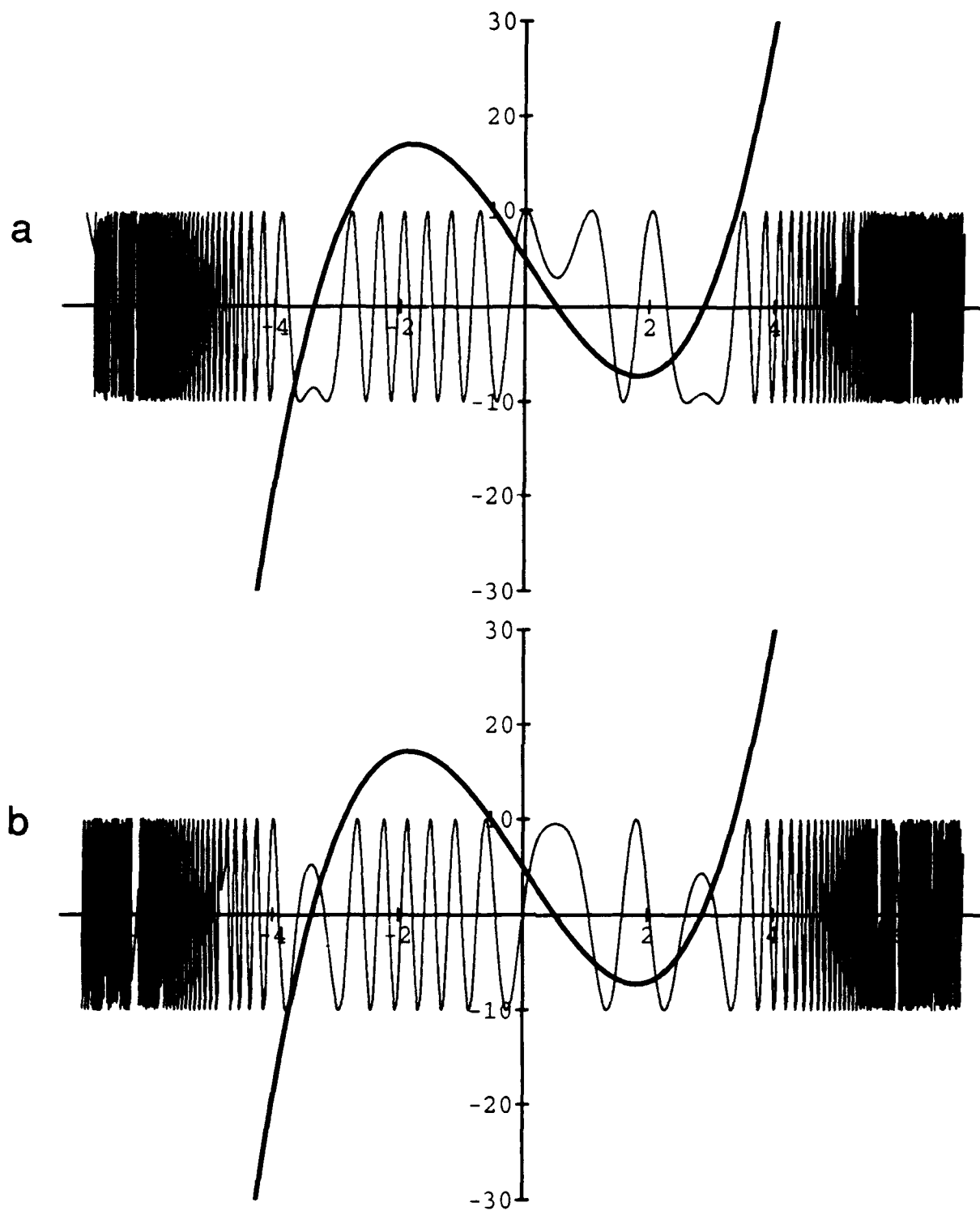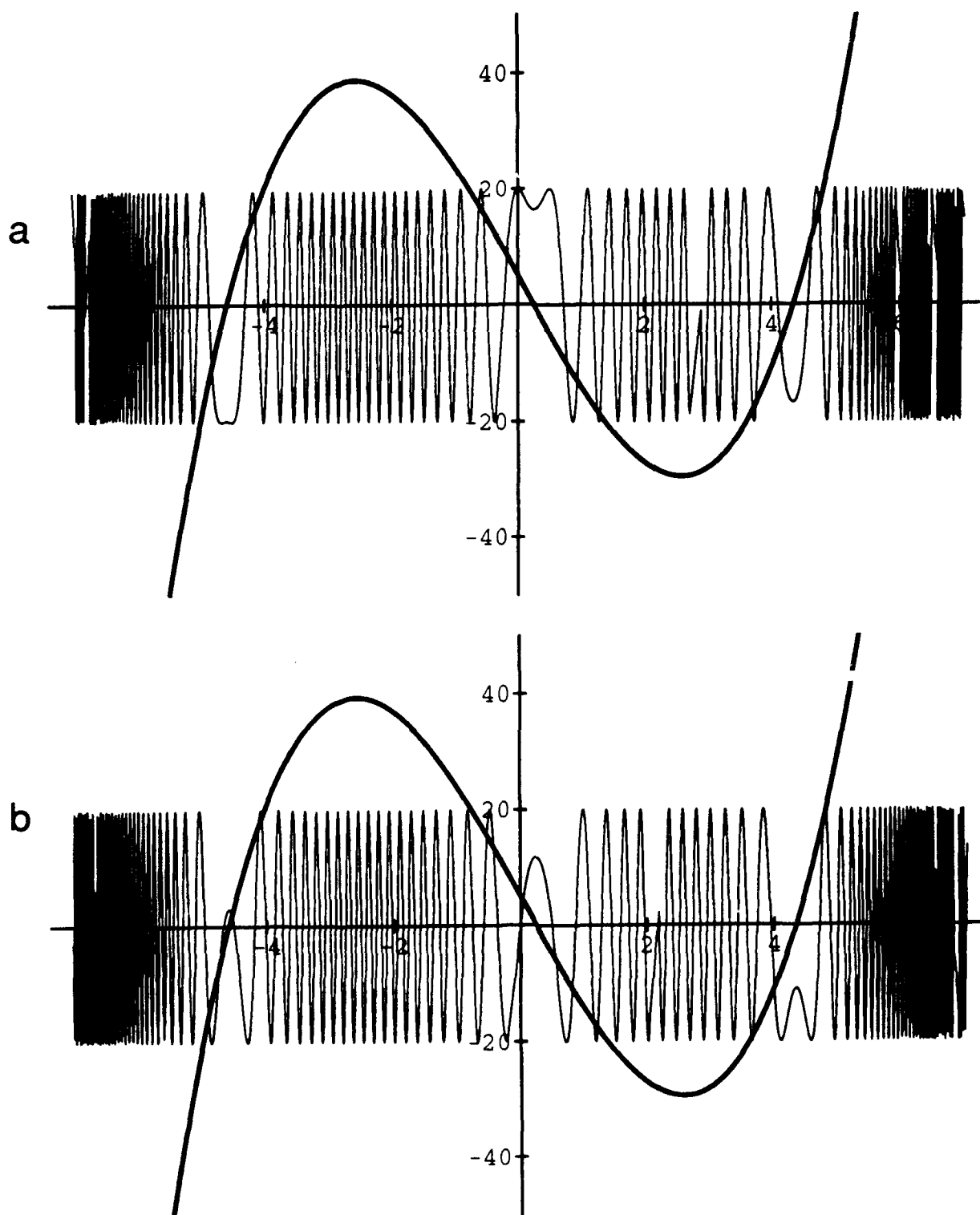
5.2 THE ALGORITHM USED TO CALCULATE THE LOCATION OF RAYS IN THE EXIT PLANE AND THE TRAVEL TIME SURFACE

The general method used in this algorithm was described in Appendix A of Chapter 3. The code follows.

```
        REAL*8 V, U, B1, THIRD, A2, DET, UTILDE, VTILDE, B3, UC
        REAL*8 H1, H3
        INTEGER ZERO, THREE, I
        COMPLEX*16 SQRT3
        COMMON/DATA/U,V,A2,B1
        COMMON/DAT2/ SQRT3, THIRD

        ZERO = 0
        THREE = 3

        THIRD = 1.0D0 / 3.0D0
        SQRT3 = DCMPLX(0.0D0, DSQRT(3.0D0))
CCCC  SURFACE PARAMETERS FOR H1 = -0.00031/CM               CCCC
CCCC                H2 = -0.00117/CM/CM                      CCCC
CCCC                Z = 68 CM                                CCCC
CCCC                ZS = 170 CM                              CCCC
CCCC  TAKEN FROM TDS DATA OF 11-01-90                        CCCC
        H1 = -0.00031
        H3 = -0.0194
        Z = 68
        ZS = 170
        B1 = -2*H1 + 1/(2*Z) + 1/(ZS*2)
        B3 = -2*H3 + 1/(2*Z) + 1/(2*ZS)
        A2 = 0.00234D0
        UC = -2.0D0*B3*B1/A2

CCCC  CALCULATE TRAVEL TIMES ALONG CUTS THROUGH             CCCC
CCCC  HORIZONTAL                                            CCCC
CCCC  POSITIONS GIVEN BY U - UC = ...                       CCCC


        DO 100 I = 1, 7
        U = -0.0397 + (I-1)*0.0397
        UTILDE = -U / A2

CCCC  LIMITS REPRESENT VERTICAL LIMITS OF DATA 11-01-90     CCCC
        DO 10  V = -0.159D0, 0.000D0, 0.00795D0
            VTILDE = V * B1 / (2.0D0 * A2**2)
            DET = VTILDE**2 + UTILDE**3 / 27.0D0
            CALL FINDTIME(VTILDE, UTILDE, DET,ZERO,I)
10      CONTINUE

        DO 20  V = 0.00795D0, 0.160D0, 0.00795D0
            VTILDE = V * B1 / (2.0D0 * A2**2)
```

```
                DET = VTILDE**2 + UTILDE**3 / 27.0D0
                CALL FINDTIME(VTILDE, UTILDE, DET,THREE,I)
20      CONTINUE

100     CONTINUE
        END


        SUBROUTINE FINDTIME(VTILDE, UTILDE, DET, MF,I)
        REAL*8 VTILDE, UTILDE, DET, THIRD, AR, BR
        REAL*8 U, X, Y, A2, B1, V, Y1, X1
        INTEGER CMPL, ONE, TWO, THREE, MF, M, I
        COMPLEX*16 A, B, APB, AMB, SQRT3
        COMMON/DATA/U,V,A2,B1
        COMMON/DAT2/ SQRT3, THIRD

        ONE = 1
        TWO = 2
        THREE = 3

        IF (DET.LT.0.0D0) THEN
                A = DCMPLX(-VTILDE, DSQRT(DABS(DET)))
                IF (REAL(A).LT.0.0D0) THEN
                        A = -1*((-A)**THIRD)
                ELSE
                A = A**THIRD
                ENDIF
                B = DCMPLX(-VTILDE, -DSQRT(DABS(DET)))
                IF (REAL(B).LT.0.0D0) THEN
                        B = -1*(-B)**THIRD
                ELSE
                        B = B**THIRD
                ENDIF
                CMPL = 1
        ELSE
                AR = -VTILDE + DSQRT(DET)
                AR = SIGN(1.0D0,AR)*(SIGN(1.0D0,AR)*AR)**THIRD
                BR = VTILDE + DSQRT(DET)
                BR = -1*SIGN(1.0D0,BR)*(SIGN(1.0D0,BR)*BR)**THIRD
                A = DCMPLX(AR,0.0D0)
                B = DCMPLX(BR,0.0D0)
                CMPL = 0
        ENDIF

        APB = A + B

        Y1 = REAL(APB)
        X1 = (U - A2*Y1**2)/(2.0D0*B1)
        M = ONE + MF
        CALL TIME(M,X1,Y1,U,V,I,B1)

        IF (CMPL.EQ.1) THEN
                AMB = (A - B)*SQRT3*0.5D0
```

```
            Y = -REAL(APB)/2.0D0 + REAL(AMB)
            X = (U-A2*Y**2)/(2.0D0*B1)
            M = TWO + MF
            CALL TIME(M,X,Y,U,V,I,B1)

            Y = -REAL(APB)/2.0D0 - REAL(AMB)
            X = (U-A2*Y**2)/(2.0D0*B1)
            M = THREE + MF
            CALL TIME(M,X,Y,U,V,I,B1)
      ENDIF
      RETURN
      END




      SUBROUTINE TIME(WHICH,X,Y,U,V,I,B1)
      REAL*8 C, X, Y, Z, ZS, A2, B1, PHI, ATIME, U, V
      REAL*8 US, VS, B3, A4, A5, R, RS, H1, H3
      INTEGER  WHICH, I

      C = 0.148D6
      Z = 68.0D0
      ZS = 170.0D0
      H1 = -0.00031
      H3 = -0.0194
      B1 = -2*H1 + 1/(2*Z) + 1/(ZS*2)
      B3 = -2*H3 + 1/(2*Z) + 1/(2*ZS)
      A2 = 0.00234D0
      US = -15.0D0
      VS = 0.0D0
      UC = -2.0D0*B3*B1/A2
      UT = U + UC - US/ZS
      VT = V - VS/ZS
      R = DSQRT(Z*Z*(1 + UT*UT + VT*VT))
      RS = DSQRT(ZS*ZS + US*US + VS*VS)
      PHI = B1*X**2 + A2*X*Y**2 + B3*Y**2 - X*(U + UC) - Y*V
CCCC  THE TIME IS CALCULATED IN MICRO SECONDS               CCCC
C     ATIME = 1000000*(R + RS + PHI)/C
      ATIME = 1000000*PHI/C
C     ATIME = 1000000*(R + RS)/C
      WRITE(16, 40) ATIME, V
 100  FORMAT(3F15.5)
      RETURN
      END
```

5.3 THE ALGORITHM USED TO CALCULATE THE HILBERT

TRANSFORM OF A DIGITIZED TIME RECORD

The outline of this program is given in Table II of Chapter 4. The code follows.

```
        INTEGER N, I
        PARAMETER (N=1024)
        REAL A(N),RSEQ(N),TWOPI
        COMPLEX SEQ(N),COEF(N),X(N),IM
        REAL RWKSP(6179)
        COMMON/WOkKSP/RWKSP
        CALL IWKIN(5179)
        TWOPI = 2.0*CONST('PI')
        IM = CMPLX(0.0,1.0)
        DO 10 I = 1,N
CCCC            The algorithm can be used to calculate the Hilbert transform of a signal
CCCC            numerically produced on the computer as well as a data signal input from an
CCCC            external file
                A(I) = SIN(I*TWOPI/64)
C               A(I) = 0.0
C               IF ((I.GE.480).AND.(I.LE.544)) A(I) = SIN((I-480)*TWOPI/64)
                IF ((I.GE.  0).AND.(I.LE.200)) A(I) = 0
                IF ((I.GE.700).AND.(I.LE.1024)) A(I) = 0
                X(I) = CMPLX(A(I),0.0)
10      CONTINUE
        CALL FFTCF(N,X,COEF)
        DO 20 I = 1,N/2
                COEF(I) = IM*COEF(I)
                COEF(I+N/2) = -IM*COEF(I+N/2)
20      CONTINUE
        CALL FFTCB(N,COEF,SEQ)
        DO 30 I=1,N
                SEQ(I) = SEQ(I)/N
                RSEQ(I) = REAL(SEQ(I))
30      CONTINUE
        WRITE(8,100) (I,A(I),I=1,N)
        WRITE(9,100) (I,RSEQ(I),I=1,N)
100     FORMAT(1X,I7,7X,F15.3)
        WRITE(10,101)
        WRITE(10,102)
        WRITE(10,103) (I,X(I),COEF(I),SEQ(I),I=1,N)
101     FORMAT(7x,
        +'The transform of the single arrival touching the caustic')
102     FORMAT(4X,'INDEX',7X,'INPUT',8X,'FORWARD  TRANSFORM',2X,
        +'BACKWARD TRANSFORM')
103     FORMAT(I7,4X,'(',F6.3,',',F6.3,')',
        +4X,'(',F6.3,',',F6.3,')',
        +4X,'(',F6.3,',',F6.3,')')
104     FORMAT(1X,I7,7X,F15.3,7X,F15.3)
        END
```

References

1)   F. J. Wright (private communication).

2)   M. V. Berry, J. F. Nye, and F. J. Wright, "The elliptic umbilic diffraction
      catastrophe," Philos. Trans. R. Soc. London, Ser. A **291**, 453-484, (1979).

TECHNICAL REPORT DISTRIBUTION, UNCLASSIFIED CONTRACT

Defense Technical Information Center Comeron Station Alexandria, VA 22314	2 one-sided copies
L. E. Hargrove Physics Division, Code 1112 Office of Naval Research 800 N. Quincy Street Arlington, VA 22217-5000	1 two-sided copy
C. K. Frederickson Department of Physics and Astronomy University of Mississippi University, MS 38677	1 two-sided copy
K. L. Williams University of Washington Applied Physics Laboratory 1013 E. 40th Street Seattle, WA 98195	1 two-sided copy